Universität Rostock

Traditio et Innovatio

Trajectory-based approaches to vibronic spectroscopy of molecular systems

Kumulative Dissertation

zur Erlangung des akademischen Grades

doctor rerum naturalium (Dr. rer. nat.)

der Mathematisch-Naturwissenschaftlichen Fakultät
der Universität Rostock

vorgelegt am 25. Mai 2018 in Rostock

von

SVEN KARSTEN,

geb. am 16. Februar 1989 in Kyritz

https://doi.org/10.18453/rosdok_id00002484

DISSERTATION

MATHEMATISCH-NATURWISSENSCHAFTLICHE FAKULTÄT

Gutachter:

Prof. Dr. Oliver Kühn, Universität Rostock, Institut für Physik

Prof. Dr. Mario Barbatti, Aix-Marseille Université, Institut de Chimie Radicalaire

Prof. Dr. Eitan Geva, University of Michigan, Department of Chemistry

Jahr der Einreichung: 2018

Jahr der Verteidigung: 2019

Abstract

The measurement of the vibronic spectrum, from the ultra-violet/visible to the X-ray range, provides a microscopic insight into the dynamical processes in molecular systems. However, the interpretation of the experimental data requires a suitable theoretical support. Since the direct ansatz, i.e. propagating a wave packet in the time domain, becomes rapidly unfeasible for complex systems, it is often necessary to employ classical or classical-like approximations. In the case of vibronic spectroscopy, such an attempt is particularly challenging, as there is no direct classical analogue for the occurring time evolution. A popular compromise is thus to neglect the nuclear dynamics and to obtain the spectrum via single-point calculations in the static picture, thereby losing any dynamical information.

The goal of this thesis is to bridge the gap between the two extrema via trajectory-based approximations to the nuclear quantum dynamics. To this end, a generalized time-correlation function is introduced, which contains many well-known correlation functions as special cases and furthermore enables the construction of (in principle) infinitely many new ones.

Employing the generalized formalism as a starting point, the nuclear quantum dynamics is approximated in the framework of imaginary-time path integrals. The presented derivation is performed in the spirit of the standard ring-polymer molecular dynamics and, thus, the developed methodology recovers important quantum effects. It is demonstrated for model systems, that this method can indeed lead to improved numerical protocols if compared to well-established ones. Importantly, the commonly known dynamical classical limit approach, which profits from a particularly low computational effort, is identified as a special limiting case of the path-integral method. This ansatz is applied to the (non-)linear X-ray spectrum of gas-phase and bulk water, where the comparison to the static approximation reveals the importance of taking time-correlated nuclear effects into account.

Alternatively to the dynamics of the ring polymer that suffers from artificial oscillations, the generalized time-correlation function is approximated via the Matsubara dynamics, which is extended to vibronic transitions. It turns out that, in contrast to the aforementioned approximations, this method yields the exact absorption spectrum for a harmonic oscillator system. Nevertheless, the Matsubara dynamics is not directly applicable to realistic systems, since the infamous sign problem inhibits a proper statistical convergence. To circumvent this issue, an *ad-hoc* modification of the method is suggested, yielding not only an adequate approximation to the vibronic spectra of considered model systems but also providing accurately the thermal Wigner function.

Zusammenfassung

Die Messung des vibronischen Spektrums, vom ultravioletten/sichtbaren bis hin zum Röntgenbereich, erlaubt einen mikroskopischen Einblick in die dynamischen Prozesse von molekularen Systemen. Die Interpretation der gemessenen Daten erfordert jedoch die Unterstützung durch eine geeignete Theorie. Da der direkte Ansatz über das Propagieren eines Wellenpaketes in der Zeitdomäne sehr schnell unpraktikabel wird, ist es für komplexe Systeme oft nötig, von klassischen oder ähnlichen Näherungen auszugehen. Im Falle von vibronischen Spektren stellt sich dieses Vorhaben als besonders herausfordernd dar, da es kein direktes klassiches Analogon für die hier auftretende Zeitentwicklung der Kerne gibt. Ein beliebter Ansatz ist daher, die Kerndynamik zu vernachlässigen und das Spektrum aus Einzelpunktberechnungen im statischen Bild zu gewinnen, was jedoch zum Verlust jeglicher dynamischer Information führt.

Diese Arbeit hat das Ziel eine Brücke zwischen den beiden Extremen zu schlagen und bedient sich dafür des Formalismus' der trajektorienbasierten Näherungen an die Quantendynamik. Als Ausgangspunkt einer solchen Näherung wird eine verallgemeinerte Zeitkorrelationsfunktion eingeführt, die bereits bekannte Korrelationsfunktionen als Spezialfälle enthält und darüber hinaus die Konstruktion von (prinzipiell) unendlich vielen neuen ermöglicht.

In Anlehnung an die Ringpolymer-Molekulardynamik werden die Kerne zunächst mithilfe von Imaginärzeit-Pfadintegralmethoden über quasi-klassische Bewegungsgleichungen propagiert, wodurch wichtige Quanteneffekte berücksichtigt werden können. Es zeigt sich an Modellsystemen, dass diese Methode, im Vergleich zu bereits existierenden Ansätzen, tatsächlich zu verbesserten numerischen Protokollen führen kann. Als besonderer Spezialfall des Pfadintegralansatzes ergibt sich die bestens bekannte Methode des dynamisch-klassischen Grenzfalls, welche aufgrund des besonders geringen numerischen Aufwands direkt für die Berechnung (nicht-)linearer Röntgenspektren von gasförmigem und flüssigem Wasser eingesetzt wird. Der Vergleich mit den Ergebnissen der rein statischen Näherung lässt erkennen, wie wichtig eine akkurate Einbeziehung von zeitlich korrelierten Kerneffekten für die Interpretation des Spektrums ist.

Alternativ zur Dynamik eines Ringpolymers, welche durch künstliche Oszillationen gestört ist, wird das vibronische Spektrum mithilfe der Matsubaradynamik ausgewertet, die für diesen Zweck verallgemeinert wird. Es stellt sich heraus, dass dieser Ansatz im Gegensatz zu den vorher erwähnten Näherungen das exakte Absorptionsspektrum eines harmonischen Modellsystems wiedergibt. Nichtsdestoweniger ist diese Methode nicht direkt auf realistische Systeme anwendbar, da sich durch das berüchtigte Vorzeichenproblem praktisch kaum statistische Konvergenz erreichen lässt. Abhilfe schafft eine zweckmäßige Modifikation, die nicht nur die Spektren adäquat wiedergibt, sondern auch die thermische Wignerfunktion angemessen verfügbar macht.

Table of abbreviations & Glossary

ACL averaged classical limit.
Semi-classical approximation to the standard correlation function. The occurring classical dynamics is with respect to the average of initial- and final-state potentials.

BOA Born-Oppenheimer approximation

CMD centroid molecular dynamics

DCL dynamical classical limit.
Classical approximation to the standard correlation function. The occurring classical dynamics and statistics are exclusively determined by the initial-state potential.

DFT density functional theory

DOF degree of freedom

EOM equation of motion

IR infra-red

MD molecular dynamics

MO molecular orbital

NRPMD nonadiabatic ring-polymer molecular dynamics

PES potential energy surface

PI path integral

SCF shift correction factor.
Prefactor that relates the Fourier transform of the generalized time-correlation function to the desired absorption spectrum. The abbreviation is not to be confused with the common one for self-consistent field.

QM quantum mechanical

RIXS resonant inelastic X-ray scattering

RPMD ring-polymer molecular dynamics.
The common extension of imaginary-time path-integral techniques to real-time problems. The nuclear quantum dynamics is approximated via the motion of a classical object consisting of beads connected by harmonic springs, i.e. the ring polymer.

SACL Schofield averaged classical limit.

Semi-classical approximation to the Schofield correlation function, which is a real-valued function of time. The occurring classical dynamics as well as the density correspond to the average of initial- and final-state potentials.

SCL statical classical limit.

Static approximation to the dynamical classical limit. The spectrum is approximated via a sampling of stick spectra evaluated at the relevant nuclear configurations.

TCF time-correlation function

TRPMD thermostatted ring-polymer molecular dynamics

XAS X-ray absorption spectrum

XFEL X-ray free-electron laser

Contents

1 Introduction

Understanding the dynamics of complex many-body systems is one of the most demanding challenges in theoretical chemistry and molecular physics. With the ongoing development of powerful light sources and precise detection devices within the recent decades, experimentalists achieved a spectacular progress in (non-)linear spectroscopic techniques for various frequency ranges.[1–3] When complemented by proper theoretical models and methods, the resulting vibrational, electronic and especially vibronic spectra, provide comprehensive information about the interplay between electrons and nuclei forming the molecular systems of interest.[4–7] This offers insights into the dynamical processes on an atomistic level that is often not available by means of the experiment only. In turn, the theoretical models can be tested for their applicability via comparing the results of computer simulations to the experimentally obtained data. Thus, the investigation of (non-)linear spectra by experimental and theoretical means is a prominent approach to gain more understanding on relevant chemical and physical mechanisms.

The success of (non-)linear X-ray spectroscopy. Since their discovery in 1895 by Röntgen,[8] X-rays (with energies from hundred to several thousand electron volts) allowed scientists to examine the microscopic details of crystals[9] but also of molecules in the gas phase[10,11] and liquids.[12–15] For the two latter cases, the success of the X-ray spectroscopy is mainly due to three aspects, making it particularly interesting for the present purpose. First, it is especially useful for obtaining highly local information on the system in question.[16] Here, the so-called core-excited states play the key role, since the corresponding core orbitals are inherently localized on a particular atom. This is in contrast to the lower-energy ultraviolet/visible spectroscopy, where the interaction between light and matter usually involves delocalized valence molecular orbitals (MOs). Second, due to the energetic separation of the core levels of different elements, a specific kind of atoms can be investigated or identified by tuning the X-ray frequency properly. Third, combining the spatial resolution and the elemental sensitivity with an ultrafast X-ray source enables following charge dynamics and excitations in materials.[6,17] Importantly, only the progress in developing proper light sources within the recent years has made all of these points accessible.[18,19] Especially the disentanglement of electronic and nuclear contributions in the spectrum requires a high instrumental resolution as it will be discussed later.

Early X-ray sources, as used by Röntgen himself, employed the so-called Bremsstrahlung (engl. deceleration radiation) of cathode rays hitting anode targets in vacuum tubes[8] yielding incoherent light of relatively low intensity. Unfortunately, the laser technique, developed in the 1960s, has not been available for the X-ray range. The short lifetime of core holes and the high cross section for X-ray absorption in matter complicate the generation of a stable population inversion as it is necessary for the conventional laser technique.[20] Consequently,

a monochromatic and coherent source of X-rays along with high field intensities and a high instrumental resolution has been outside reach for a long period of time. Synchrotron radiation, being also a kind of Bremsstrahlung in high-energy particle experiments and, thus, originally considered as a loss, has been recognized as a powerful tool for performing experiments in chemistry, biology and condensed matter physics.[21] Exploiting complex relativistic effects that emerge if electron bunches are aligned in a particle accelerator, enabled lately the construction of the X-ray free-electron laser (XFEL),[22] which yields a coherent electromagnetic field with a tunable frequency and pulses with an ultrashort duration. Without actually utilizing an active medium, this facility transfers the benefits of conventional laser techniques to the X-ray range. In parallel, high harmonic generation sources have been developed, yielding also proper X-ray pulses though at a considerably lower intensity than that produced by XFELs. Owing to the increasing spectral resolution, the X-ray experiments can now reveal fine spectral structures such as vibronic progressions. The creation of suitable X-ray sources thus paved the way to examine microscopic interaction mechanisms in complex molecular systems by means of linear and, especially, non-linear spectroscopies.[18,19]

If the applied electromagnetic fields are weak compared to those inside an atom or a molecule, the response to the applied light is linear and reveals valuable information on the core-excited states and their transition dipoles.[1,2] The measurement of the linear X-ray absorption spectrum (XAS) probes those electronic transitions, where a core electron is excited to the unoccupied MOs. Particular examples of linear X-ray spectroscopies are near-edge X-ray absorption fine structure[16] techniques that examine the low-energy region of the spectrum, whereas the extended X-ray absorption fine structure[23] refers to higher-energy spectral features. At higher field intensities, a non-linear response emerges, carrying much more information than the linear response.[1,2] Different contributions to the non-linear signal can be addressed by various spectroscopic techniques. Specifically, resonant inelastic X-ray scattering (RIXS) can be used to detect the emission signal resulting from the spontaneous refill of a core hole by electrons from occupied MOs, providing detailed information on the electronic structure of samples being in different aggregation states.[24,25]

Along with the improvement of X-ray sources and detection devices, not only electronic but also vibronic transitions can be resolved in today's experiments.[26,27] Although X-ray scattering processes occur during few femtoseconds due to the rapid decay of the core-excited states, fingerprints of ultrafast nuclear dynamics and coherences could be observed in spectra. For instance, the inclusion of vibronic effects in RIXS spectra has been found essential for the correct assignment of spectral features in simple model systems.[28,29] Further, dissociative dynamics on the short timescale of the RIXS process[30–32] has also been found important. It is noteworthy that in Ref. 33, vibrationally resovled inelastic X-ray scattering has been even considered as a complementary technique to the conventional infra-red (IR) and vibrational Raman spectroscopies. Moreover, the RIXS spectra of liquid water and alcohols initiated active debates in the last decade due to the splitting of the $1b_1$ band, which is not

observed in the photoelectron spectra.[14,34–36] Remarkably, this peculiar effect received controversial interpretation resulting in six hypotheses,[15] with four of them involving different aspects of nuclear dynamics, such as ultrafast dissociation and H-bond dynamics. At this point it becomes evident, that a full understanding of such complicated effects requires a robust and feasible theoretical treatment of nuclear vibrational effects in X-ray spectroscopy and, thus, this thesis is dedicated to this topic. However, since the mathematical expressions to describe the interaction between matter and light are independent on the spectral range, the following discussion on theoretical approaches applies not only to X-ray but to vibronic spectroscopy in general.

State-of-the-art approaches to theoretical vibronic spectroscopy. Nowadays, computer simulations serve as a bridge between the experimental observations and the theoretical models describing the underlying dynamics. Due to the rapid increase of the computational capabilities in the last decades, one is able to investigate ever more complex systems by means of simulations. However, to describe the interaction between the molecular system and the applied light exactly, one would have to solve the full Schrödinger equation coupled to the electromagnetic field equations. Due to the infamous curse of dimensionality of quantum dynamics, such an approach is not feasible for realistic systems and it is thus necessary to develop strategies and approximations that can circumvent this issue. From the theoretical standpoint, there exist two limiting strategies to simulate vibronic spectra, that is static and time-dependent approaches, offering very distinct possibilities with respect to numerical approximations.

In the static picture, the exact description would require the solution of the time-independent Schrödinger equation for the electronic degrees of freedom (DOFs) as well as for the nuclear ones, where the latter approach is only feasible for rather small molecules,[37] leaving e.g. systems in the condensed phase outside reach. Thus, a very common approach is to perform the so-called single-point calculations, see left panel of Fig. 1 for a sketch. After separating the electronic and nuclear DOFs and sacrificing any vibronic coupling, i.e. employing the Born-Oppenheimer approximation (BOA), the electronic structure is obtained for a single (typically equilibrium) nuclear configuration. The excited state properties such as energies and transition dipoles are then represented in form of a stick spectrum, approximating the exact one. Although dubbed here as the simplest approach, it should be stressed that already a single electronic-structure calculation can be an extremely demanding task for many-body systems. Fortunately, the underlying solvers for the electronic time-independent Schrödinger equation became increasingly accurate and performant with the development of elaborate quantum-chemical methods in recent years.[38,39] For ground state properties, density functional theory (DFT) is a well-established approach,[40] but there is still no universal strategy for treating excited-state problems for large systems. Nevertheless, several methods exist that are able to tackle this challenge. A simplistic quasi-one-electron

approach readily employing the Kohn-Sham MOs obtained via ground-state DFT can still yield surprisingly good results for excited state properties as has been demonstrated for various kinds of systems.[28,41–44] Approaches that are capable to treat the general case accurately are based on e.g. variants of configuration interaction,[45] the perturbation theory[46] as well as the coupled cluster[47,48] technique. However, the numerical effort increases drastically if compared to the aforementioned one-electron approximation. Alternatively, one can follow the multi-configurational self-consistent field ansatz to treat complex systems, in particular the restricted active space self-consistent field method[49] together with a state-interaction treatment of spin-orbit effects can provide accurate results if complemented sufficiently by "chemical intuition".[50] Recently, also the algebraic diagrammatic construction[51,52] and the restricted open-shell configuration interaction singles[53] methods have been implemented in state-of-the-art quantum chemical program packages. Importantly, the consideration of X-ray induced transitions particularly challenges these electronic structure methods, since the whole plethora of states up to the highly excited core-ones has to be taken into account. Hence, in order to simulate X-ray spectra, the chosen quantum chemistry method has to be based on a very efficient algorithm that still yields proper results. Unfortunately, independently on the level of the employed quantum chemistry, the single-point approach clearly ignores any nuclear dynamics and statistics. Thus, spectral broadening and line shapes can only be included on a phenomenological level.[1]

Leaving the realm of time-independent techniques, one can find the other common approach to vibronic spectra in the time domain. In contrast to single-point calculations, the idea is to obtain a numerically exact solution for the problem by performing nuclear wave packet dynamics on the electronic potential energy surfaces (PESs), as depicted in the right panel of Fig. 1. This strategy has been proposed already in 1978 by Heller[54] and has been used extensively since then.[37,55–57] The increasing success of this ansatz is again due to the growth of computer capabilities but it also owes to the development of smart algorithms. Especially the multi-configurational time-dependent Hartree method[58] has proven its applicability to systems with many nuclear DOFs in plenty of applications.[59–62] However, such a wave-packet propagation usually requires an expensive pre-computation of many-dimensional PESs which can rapidly become a drawback for two reasons. First, the calculation of the PESs themselves requires an individual electronic structure calculation for each relevant nuclear configuration. Their number grows exponentially with the dimensionality of the problem and so does the computational effort; eventually the curse of dimensionality strikes. Second, if the PESs cannot be easily parametrized into a functional form, as it is generally the case for complex systems, the information for all the points has to be stored in some way. For chemically relevant molecular systems, the required memory would quickly exceed the available storage resources, being again a manifestation of the curse. In order to avoid such a barrier, usually just a few nuclear DOFs are taken into account explicitly while the rest is included via a system-bath partitioning.[63,64] However, such a distinction has to

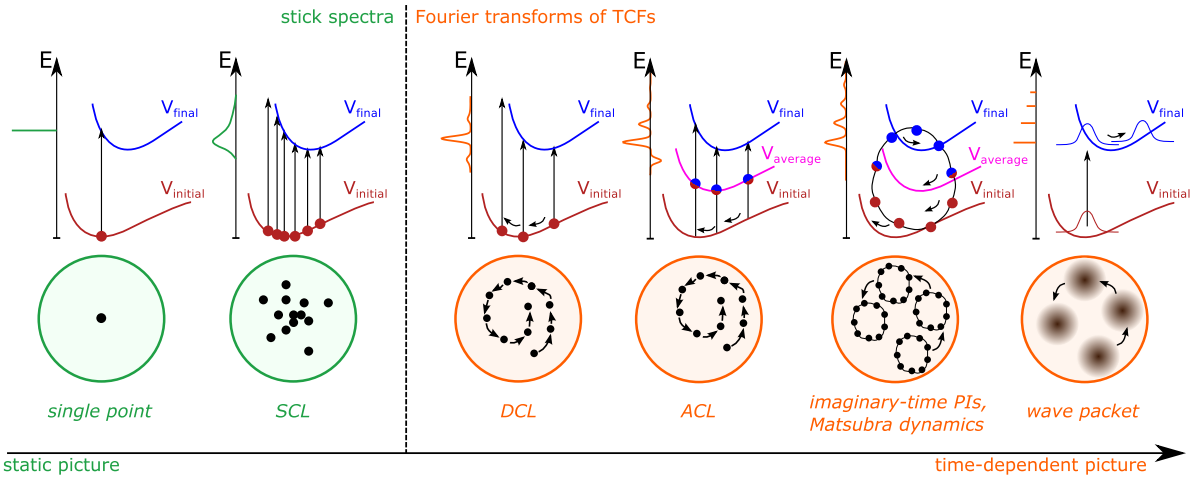

Figure 1: Overview of the methodologies that are considered to bridge the gap between the common static and time-dependent approaches. The circles represent the nuclear configuration space and the small black arrows indicate real-time evolution. The arrows in between the PESs correspond to the electronic energy gap and the approximated spectra are symbolically plotted along the energy axes.

be done carefully and is often very problem-specific. To conclude, as a price for its accuracy, the wave-packet propagation is limited to rather small systems or requires a non-trivial reduction of dimensionality.

Building a bridge between the common static and time-dependent approaches. Ideally, there would be a method that combines the advantages of the two limiting strategies, i.e. the single-point calculations and the time-dependent ansatz in a practical and efficient way. To be precise, such an approach should treat the electronic problem via the well-established quantum-chemistry tools accompanied by a feasible but accurate treatment of the nuclear DOFs without facing the curse of dimensionality. Several attempts to bridge this gap have been made as it will be discussed in the following.

If one starts from the single-point calculations, as the limiting static approach (left panel in Fig. 1), a step towards treating nuclear vibration levels can be done by taking the curvature of the PES into account. Subsequently, assuming shifted harmonic potentials for the initial and final electronic states yields the Franck-Condon model for vibronic progressions.[2,38,57,65] Still, this approach is not applicable to systems with strongly anharmonic excited states or for cases where bond formation or cleavage, and/or pronounced conformational changes are significant. Alternatively, one can sample nuclear distributions e.g. via classical molecular dynamics (MD) methods[2,66] also referred to as the statical classical limit (SCL), see Fig. 1. It leads to a more realistic description of conformational and environmental effects[67–69] than a single-point calculation, but still lacks information about time-correlated nuclear motion and thus, for instance, is not capable of reproducing vibronic progressions that can be crucial for the spectral line shape. To account for static quantum nuclear effects, quasi-classical imaginary-time path integral (PI) MD simulations[70–72] can serve as a basis for the sampling procedure. Here, one exploits the isomorphism between the quantum me-

chanical (QM) partition function and a configuration integral for a purely classical object consisting of beads connected by harmonic springs. How these PI methods can be employed to treat real-time quantum effects is discussed below and in the following sections.

Switching to the time domain has the great advantage that the quantum expressions are more similar to the classical ones, i.e. the Heisenberg time evolution has a direct correspondence to Hamilton's classical equations of motion (EOMs). Thus, it is more straightforward to deduce reasonable classical-like approximations leading to nuclear dynamics in form of trajectories. In contrast to the wave-packet approach, the PESs then can be calculated on the fly. Hence, there is no need to store and to know the full surface and the curse of dimensionality is not directly faced. Consequently, the time-dependent picture is the preferred choice to approach the complex dynamics of molecular systems. During the last decades, plenty of methods have been developed that can treat nuclear dynamics on multiple electronic PESs also beyond the BOA. For instance, there are surface hopping methods,[73–75] mean-field (Ehrenfest) dynamics,[76] multiple spawning techniques,[77,78] nonadiabatic direct-dynamics,[79,80] classical and semiclassical mapping approaches,[81–83] the exact factorization perspective,[84,85] and Bohmian dynamics[86], see, e.g., Refs. 87–89 for review. However, the majority of them are addressing the rates of non-adiabatic transitions, while mostly leaving the problem of vibronic spectra aside.

Thus, the goal of this thesis is to bridge the aforementioned gap between the exact time-dependent approach and the purely static one with the focus being on vibronic spectroscopy. In order to turn to (non-)linear spectroscopic observables, the exact time-independent expressions can be rewritten in terms of time-correlation functions (TCFs) by employing the Fourier transform. Since TCFs naturally take time-correlation effects into account[1,2,90–92] and profit from the aforementioned benefits of a time-dependent ansatz, the TCF formulation has served as the starting point here, see Sec. 2.1. In particular, in [SK1] and [SK2], the so-called dynamical classical limit (DCL)[1,2] has been applied to (non-)linear X-ray spectroscopy, where this approach is not commonly used, especially for the RIXS spectrum. Here, after employing the interaction representation, the nuclear dynamics is approximated by classical trajectories that are exclusively determined by the adiabatic ground-state PES as it is depicted in Fig. 1. However, this contradicts to some extent the correct quantum picture, where the nuclear wave packet evolves explicitly on the excited PES. Therefore, it leads to the loss of information about the excited-state dynamics and can cause wrong frequencies and shapes of the vibronic progressions in certain physical situations.[93,94] Moreover, the nuclei are treated as point particles, sacrificing their quantum nature, in particular zero-point energy and tunneling effects. This leads to wrong dynamics if light atoms, shallow PESs and/or isotope substitutions are involved, as it has been shown on numerous examples starting from small molecules in gas phase to biomolecules.[95–98] Still, the DCL possesses various profitable features when it comes to an efficient numerical protocol for treating complex systems and it can be readily applied to non-linear TCFs, see Sec. 2.3.2. Importantly, it pro-

vides more information on the line shape than obtained by the static SCL approach to X-ray spectroscopy, in particular to XAS and especially in the case of RIXS spectra as it has been discussed in [SK1] and [SK2] and is summarized in this thesis, see Sec. 3.1. However, in order to get closer to the correct quantum picture, a method that explicitly accounts for excited states' dynamics is needed.

In particular, one can derive a semiclassical approximation to the absorption cross-section that leads to the dynamics that is performed on the arithmetic mean of the ground- and excited-state PESs, hence referred to as the averaged classical limit (ACL) method, see Ref. 99 and Fig. 1. Following the same line of reasoning for the non-linear spectrum leads to the known expression derived by Shi and Geva.[100,101] Although the ACL approach is in quite good agreement with the exact results for simple model systems,[93,94,100,101] it produces artificial negativities in the spectrum and still yields purely classical dynamics that might be an insufficient approximation to the quantum one.

As it has been already mentioned, imaginary-time PIs provide perhaps the most elegant and robust solution for inclusion of static quantum effects by means of trajectory-based approaches.[66,70,102,103] The common extension of imaginary-time PI techniques to real-time problems, the ring-polymer molecular dynamics (RPMD) method,[104] yields quasi-classical dynamics in an extended classical phase space and has enjoyed success in simulating chemical reaction rates and approximating IR spectra for the condensed phase, see e.g. Refs. 105,106 for review. The beauty of this approach lies in the fact that it captures important quantum effects while it can be treated efficiently via standard classical MD algorithms. For the case of multiple electronic PESs, two similar extensions to standard RPMD, referred to as nonadiabatic ring-polymer molecular dynamics (NRPMD) have been developed[107,108] based on the mapping approach introduced by Stock and Thoss.[87,109] This method allows for nonadiabatic dynamics involving several electronic states and is thus a suitable method for simulating vibronic spectra, given an efficient simulation protocol is provided.[110] However, the convergence with respect to the number of mapping variables, representing the electronic DOFs, could be an issue for larger systems and it is not yet fully understood what will happen if this number approaches infinity. Several PI approaches for many PESs without using mapping variables were attempted[111–115] most of them addressing nonadiabatic effects on static properties or reaction rates via surface hopping methods. Still, none of them has been applied for simulating vibronic spectra.

In order to achieve the declared goal, a practical formalism for simulating optical absorption spectra in the adiabatic limit without employing mapping variables has been suggested in [SK3] and is presented in Sec. 2.2. In contrast to the RPMD and NRPMD methods that are based on the Kubo-transformed TCF, the presented formalism involves a generalized TCF, having the Kubo TCF itself as well as several other common approximations to vibronic spectra as limiting cases. This new flexible ansatz has been motivated by the observation that for a practical evaluation of vibronic spectra, the Kubo TCF either becomes non-tractable by

MD methods or has to be decomposed into the contributions that do not have the beneficial properties of the original TCF, in particular they are no more real functions of time. This poses the question whether the choice of the Kubo TCF as the starting point for simulating vibronic spectra is as unambiguous as it is in IR spectroscopy.[92,104,116] As it will be presented in Sec. 2.3.1, the imaginary-time shifted TCF, being the cornerstone of the generalized formalism, can be approximated in the spirit of the standard RPMD method, thereby accounting for nuclear quantum dynamics on multiple adiabatic PESs via quasi-classical trajectories, see Fig. 1 for a sketch. Remarkably, also the DCL method follows from the generalized TCF and is thus presented in the following as a special case leading to a particularly simple numerical protocol. Most importantly, the generalized formalism offers the possibility to construct in principle infinitely many new TCFs that might lead to superior numerical protocols if compared to the well-established ones, see Sec. 3.2.

Although the quasi-classical dynamics suggested in [SK3] represents a step forward to the nuclear quantum dynamics on multiple electronic PESs, it suffers from artificial harmonic spring oscillations, similarly to the ground-state RPMD method.[117] During the last years, several perspectives have been suggested on how to deduce improved approximations to vibrational quantum nuclear dynamics employing the so-called Matsubara dynamics.[118–120] This methodology is based on the fact that only smooth imaginary-time paths contribute to canonical thermal averages, whereas jagged or discontinuous paths are sufficiently suppressed by the Boltzmann operator. By assuming that the path remains smooth even if it undergoes real-time dynamics, i.e. the Matsubara approximation, one can rigorously derive classical-like EOMs that conserve the quantum Boltzmann distribution. Although the Matsubara dynamics ansatz yields a reasonable approximation to the Kubo TCF for smaller systems, it is not yet applicable to many-dimensional problems due to the infamous sign problem. Still, it has been shown that popular methods such as RPMD,[104] thermostatted ring-polymer molecular dynamics (TRPMD)[121] as well as centroid molecular dynamics (CMD)[122] can be viewed as feasible approximations to the Matsubara dynamics.[118,119] Thus, it is natural to expect that other even more powerful approximations to nuclear quantum dynamics can be derived on the basis of the Matsubara dynamics making this approach particularly promising. However, so far this approach has not been employed for vibronic spectra.

In [SK4] and Sec. 2.3.3 it is presented how the imaginary-time shifted TCF and, thus, spectroscopic observables can be approximated via the Matsubara dynamics, thereby generalizing the existing methodology to the multi-PES regime (as sketched in Fig. 1). As opposed to all aforementioned classical-like approximations, this method restores the exact quantum TCF for a system consisting of two displaced harmonic oscillators. Moreover, a modified Matsubara method is deduced as an *ad-hoc* ansatz to simulate the standard correlation function without suffering from the sign problem. Importantly, this method samples directly the thermal Wigner function of the harmonic oscillator and is capable to approximate the vibronic absorption spectrum of an anharmonic system accurately, see Sec. 3.3.

2 Developed methodology to approximate vibronic spectra

The theoretical and methodological achievements derived in detail in [SK1], [SK2], [SK3] and [SK4] are presented in a compact way in this section. As it has been stated in the Introduction, the presented formalism should serve as a bridge between a full quantum treatment in time domain and a purely static approximation via single-point calculations.

2.1 Background theory: (Non-)linear spectra in terms of time-correlation functions

In this section, the absorption amplitude, being the key quantity of linear spectroscopy, is reformulated in terms of a quantum TCF. A more detailed derivation can be found in [SK2] and an alternative route involving response functions is presented in [SK1]. The derivation of the non-linear TCF from the two-dimensional amplitude is presented here only in brief with all the details written out in the given references and the associated Supplements. It should be stressed that although the formalism presented therein is dedicated to describe X-ray spectra, it is applicable to vibronic spectroscopy in general and, thus, the presentation here is not bound to a certain spectral range.

If the intensity of the light is sufficiently low and the considered wavelength is much larger than the dimensions of the system, one can employ first-order perturbation theory in combination with the dipole approximation yielding Fermi's Golden rule.[2] The resulting expression describes the system being excited from an initial molecular eigenstate $|\gamma\rangle$ with the energy ϵ_γ to a final state $|\phi\rangle$ with energy ϵ_ϕ by interacting with a single photon having an angular frequency Ω and a polarization vector $\mathfrak{e}$, see left panel in Fig. 2. According to that, the absorption spectrum is proportional to the absorption amplitude that can be written down as

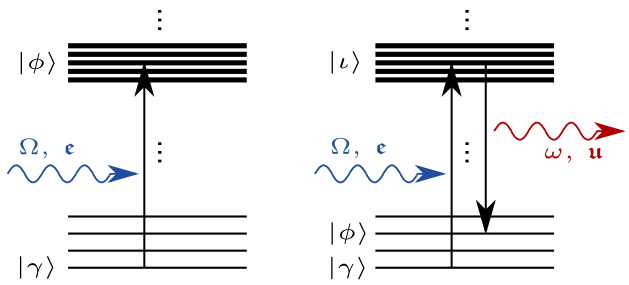

Figure 2: Schematic sketch of XAS (left) and RIXS (right) processes, see text.

$$S_0(\Omega) = \sum_{\gamma,\phi} \frac{\mathrm{e}^{-\beta\epsilon_\gamma}}{Z} \left|\langle\phi|\hat{d}|\gamma\rangle\right|^2 \delta\left(\Omega - (\epsilon_\phi - \epsilon_\gamma)/\hbar\right) \quad , \tag{1}$$

where $\beta := 1/(k_\mathrm{B}T)$ is the inverse temperature, k_B is the Boltzmann constant, $Z := \sum_\gamma \exp\left[-\beta\epsilon_\gamma\right]$ is the canonical partition function, and $\hat{d}$ is dipole operator projected on the polarization vector. The Dirac δ-function ensures the energy conservation during the process.

In order to formulate the time-domain version of Eq. (1), the δ-function is represented as the time integral[54]

$$\delta(\Omega) = \frac{1}{2\pi}\int_{-\infty}^{\infty} \mathrm{d}t\, \mathrm{e}^{-\mathrm{i}\Omega t} \quad . \tag{2}$$

Using the fact that $|\gamma\rangle$ and $|\phi\rangle$ are molecular eigenstates, one can replace the corresponding energies by the molecular Hamiltonian $\hat{H}$, evoking the Boltzmann operator and a Heisenberg time evolution of the dipole operator. The resulting expression takes the desired form of a Fourier transformed quantum TCF

$$S_0(\Omega) = \int_{-\infty}^{\infty} \mathrm{d}t\, \mathrm{e}^{-\mathrm{i}\Omega t} C_0(t) \quad , \quad C_0(t) = \frac{1}{Z}\mathrm{tr}\left[\mathrm{e}^{-\beta\hat{H}}\hat{d}(0)\hat{d}(t)\right] \quad , \tag{3}$$

where tr[•] represents a trace in the molecular Hilbert space.

The description of the two-dimensional non-linear spectrum requires including higher terms in the perturbation theory.[1] The contribution that corresponds to the spontaneous emission of light after the excitation is described by the Kramers-Heisenberg expression[123]

$$R(\Omega,\omega) = \sum_{\gamma,\phi}\frac{\mathrm{e}^{-\beta\epsilon_\gamma}}{Z}\left|\sum_{\iota}\frac{\langle\phi|\hat{d}|\iota\rangle\langle\iota|\hat{d}|\gamma\rangle}{\Omega-(\epsilon_\iota-\epsilon_\gamma)/\hbar+\mathrm{i}\Gamma_\iota}\right|^2 \delta\left(\Omega-\omega-(\epsilon_\phi-\epsilon_\gamma)/\hbar\right) \quad , \tag{4}$$

which is referred to as the RIXS amplitude if X-ray spectroscopy is concerned. Here, the system is first excited from the initial state $|\gamma\rangle$ to an intermediate state $|\iota\rangle$ by absorbing light with a frequency Ω and a polarization vector components $\mathfrak{e}$, see right panel in Fig. 2. Second, the system transits from the state $|\iota\rangle$ to the final state $|\phi\rangle$ by emitting light with the frequency ω and the polarization vector $\mathfrak{u}$. The dephasing rate Γ_ι is responsible for a finite lifetime of the state $|\iota\rangle$, which enables non-radiative relaxation mechanisms, such as the Auger one,[124] by assuming a simple mono-exponential decay. Following the same steps towards the linear TCF presented above, the integral representation of a δ-function, Eq. (2), is employed and on top the denominator in Eq. (4) is rewritten as[1]

$$\frac{1}{\omega\pm\mathrm{i}\Gamma_\alpha} = \mp\mathrm{i}\int_0^{\infty}\mathrm{d}t\,\mathrm{e}^{\pm\mathrm{i}\omega t}\mathrm{e}^{-\Gamma_\alpha t} \quad . \tag{5}$$

Finally, the non-linear spectrum can be written as a Fourier transform of a multi-time correlation function

$$R(\Omega,\omega) = \frac{1}{2\pi Z}\int_{-\infty}^{\infty}\mathrm{d}t\,\mathrm{e}^{-\mathrm{i}(\Omega-\omega)t}\int_0^{\infty}\mathrm{d}\tau_1\,\mathrm{e}^{\mathrm{i}\omega\tau_1}\int_0^{\infty}\mathrm{d}\tau_2\,\mathrm{e}^{-\mathrm{i}\omega\tau_2}\mathrm{tr}\left[\mathrm{e}^{-\beta\hat{H}}\hat{d}(0)\hat{\Delta}(\tau_2)\hat{d}(\tau_2)\hat{d}(t+\tau_1)\hat{\Delta}(\tau_1)\hat{d}(t)\right] \quad , \tag{6}$$

where $\hat{\Delta}(t) := \sum_\alpha \exp[-\Gamma_\alpha t]|\alpha\rangle\langle\alpha|$ stems from the mono-exponential decay.

Equations (3) and (6) constitute time-domain formulations of the linear and non-linear spectral amplitudes. As it has been described in the Introduction, these can serve as starting points to approximate the nuclear quantum dynamics via classical-like trajectory-based techniques.

2.2 Generalized time-correlation function

Before focusing directly on approximating the nuclear quantum dynamics, see Sec. 2.3, the previously developed linear time-domain expression is employed to formulate a generalized TCF as described in detail in [SK3]. As it turns out, employing this new general TCF, instead of directly approximating $C_0(t)$ in Eq. (3), can yield an improved numerical protocol. Moreover, due to its intrinsic flexibility, the developed formalism includes many well-established and popular variants of quantum correlation functions as limiting cases. The non-linear counterpart of such a generalized TCF will be the subject of future research, see Sec. 4 and is thus not derived here. Still, the multi-dimensional spectrum and the corresponding TCF are considered theoretically as a particular case, see Sec. 2.3.2, and its application to the X-ray spectrum of water is extensively discussed in the results part, Sec. 3.1.

It is well known that in the case of purely vibrational transitions, as considered e.g. in IR spectroscopy, many quantum TCFs can be defined, all carrying the same information.[92,116] However, with respect to a (quasi-)classical approximation, the choice of a particular TCF can yield improved results if compared to others. Justified by symmetry properties and an isomorphism between the classical and the QM linear response function, the Kubo-transformed TCF, $C_\mathrm{K}(t) = \beta^{-1}\int_0^\beta \mathrm{d}\lambda\, C_0(t+\mathrm{i}\lambda\hbar)$,[125] is the preferred choice. Nevertheless, in [SK3] it has been shown that for a *practical* consideration of *vibronic* transitions the choice of the Kubo transformed TCF might not be unambiguous. Thus a more flexible ansatz for finding a suitable correlation function has been suggested. At its heart is the integrand of the Kubo-transformed TCF, i.e. the imaginary-time shifted TCF

$$C_\lambda(t) := C_0(t+\mathrm{i}\lambda\hbar) = \frac{1}{Z}\mathrm{tr}\left[\mathrm{e}^{-(\beta-\lambda)\hat{H}}\hat{d}(0)\mathrm{e}^{-\lambda\hat{H}}\hat{d}(t)\right] \ , \tag{7}$$

with the shift λ being a real number between 0 and β, where the quantity $\hbar\beta$ is usually referred to as the imaginary time. The relation between the Fourier transforms of $C_\lambda(t)$ and $C_0(t)$ reads

$$S_\lambda(\Omega) = \mathrm{e}^{-\lambda\Omega\hbar}S_0(\Omega) \ , \tag{8}$$

see [SK3]. Integrating both sides of this equation over λ immediately reproduces the relation between the absorption spectrum and the well-known Kubo-transformed TCF. In contrast,

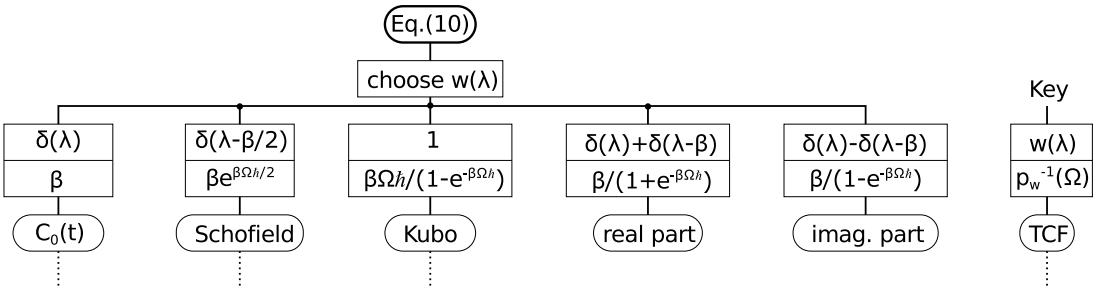

Figure 3: Sketch of the developed formalism with particular choices of the weighting function $w(\lambda)$, leading to the well-established TCFs. The two choices on the right correspond to the real and imaginary part of the complex $C_0(t)$, respectively. The legend on the right hand side deciphers the employed convention. The dashed lines below the first three TCFs imply that further approximations to them will be discussed in the following, see Sec. 2.3, in particular Fig. 4.

employing an arbitrary weighting function $w(\lambda)$ for this integration, such that

$$\underbrace{\frac{1}{\beta}\int_0^\beta \mathrm{d}\lambda\, w(\lambda) S_\lambda(\Omega)}_{=:\bar{S}_w(\Omega)} = \underbrace{\frac{1}{\beta}\int_0^\beta \mathrm{d}\lambda\, w(\lambda)\mathrm{e}^{-\lambda\Omega\hbar}}_{=:p_w(\Omega)} S_0(\Omega) \quad \Longleftrightarrow \quad S_0(\Omega) = p_w^{-1}(\Omega)\bar{S}_w(\Omega) \tag{9}$$

enables the construction of in principle infinitely many different TCFs that could be more suitable for (quasi-)classical approximations to vibronic spectra. To reiterate, the idea is to find a reasonable approximation to each $C_\lambda(t)$ in combination with a proper choice of $w(\lambda)$ to construct the generalized TCF

$$\bar{C}_w(t) := \frac{1}{\beta}\int_0^\beta \mathrm{d}\lambda\, w(\lambda) C_\lambda(t) \ , \tag{10}$$

which is a time-domain version of $\bar{S}_w(\Omega)$, rather than to approximate the desired lineshape function, $S_0(\Omega)$, directly. The prefactor $p_w^{-1}(\Omega)$ in Eq. (9) compensates the performed shift in the imaginary time and is thus referred to as the shift correction factor (SCF).

Naturally, setting $w(\lambda) = 1$ and $w(\lambda) = \delta(\lambda)$ restore the Kubo-transformed TCF and the dipole autocorrelation function itself, respectively. Setting $w(\lambda)$ differently leads to other TCFs as it will be discussed in Sec. 3.2 and is sketched in Fig. 3. In order to profit from this flexibility, the TCF that is optimal for the vibronic transition under study has to be determined by numerical or ideally by profound physical considerations.

2.3 Trajectory-based approximations to nuclear quantum dynamics

As it has been already stated in the Introduction, the great benefit of the time-domain formulation, i.e. a reformulation via TCFs, is the possibility to deduce classical-like approximations to the quantum dynamics, since the Heisenberg time evolution has a direct correspondence

in classical mechanics. In order to separate electronic and nuclear DOFs, the BOA is assumed in the following. The electronic part of the trace in Eq. (7) can then be evaluated in the adiabatic electronic basis $|a\rangle$ yielding

$$C_\lambda(t) = \frac{1}{Z}\sum_{a,b}\mathrm{Tr}\left[\mathrm{e}^{-(\beta-\lambda)\hat{H}_a}\hat{D}_b^a\mathrm{e}^{-\lambda\hat{H}_b}\mathrm{e}^{\mathrm{i}\hat{H}_b t/\hbar}\hat{D}_a^b\mathrm{e}^{-\mathrm{i}\hat{H}_a t/\hbar}\right] \ , \tag{11}$$

where Tr[•] stands for a trace in the nuclear Hilbert space only, $\hat{H}_a$ corresponds to the nuclear Hamiltonian with the potential $\hat{V}_a$ of the a-th electronic eigenstate and $\hat{D}_b^a := \langle a|\hat{d}|b\rangle$ is the transition dipole moment. The drawback of this separation becomes immediately apparent if one considers the case $a \neq b$, i.e. a truly vibronic transition. The resulting time evolution in Eq. (11) is then no longer of Heisenberg form and, thus, there is no direct classical analogue which could serve as a base for any classical approximation. Still, as it will be presented in the following, taking this expression as a starting point leads to several approximations to the adiabatic nuclear quantum dynamics via trajectory methods.

2.3.1 Imaginary-time path-integral techniques

The first approach, developed in detail in [SK3], is formulated in the spirit of RPMD,[104] which is proven to capture important aspects of the quantum dynamics in the case of pure nuclear transitions, e.g. in IR spectroscopy.[95] However, the protocol presented here differs drastically from RPMD due to the presence of multiple electronic states. Still, by setting $\hat{H}_b = \hat{H}_a$ and restricting to the Kubo transformed TCF, the standard RPMD expressions are recovered and, thus, the protocol derived here can be viewed as a generalization of the well-established single-PES method. The concrete relation to the so-called NRPMD[107,110] that employs mapping variables[109] to describe nuclear quantum dynamical processes on multiple PESs is not yet fully understood. Nevertheless, it is conjectured that the method suggested here corresponds to an *adiabatic* version of NRPMD in the limit of infinitely many mapping variables if $w(\lambda) = 1$, i.e. the Kubo TCF, is considered, see Fig. 4 for an illustration of the relation between the methods.

In the canonical fashion of imaginary-time PI techniques, the correlation function in question, here $C_\lambda(t)$, Eq. (11), is first considered at $t = 0$ only. Note that for the sake of brevity a single transition from an initial adiabatic electronic state g to a final one f of a two-level system is considered in the following. The generalization to the case of many states is straightforward. First, the nuclear trace is evaluated in the eigenstate basis of the position operator and the imaginary time is equidistantly discretized into P slices, such that $\lambda \equiv l\beta/P$ with $l = 0, 1, \ldots, P$. Consequently, the two left exponentials in Eq. (11) can be factorized into $P - l$ and l parts, respectively. In between these factors, one inserts unities as integrals over the so-called bead coordinates $\boldsymbol{R}_i$, collectively represented by the configuration $\mathbb{R} = (\boldsymbol{R}_0, \ldots \boldsymbol{R}_{P-1})^{\mathrm{T}}$, referred to as the ring polymer. Employing the symmetric Trotter

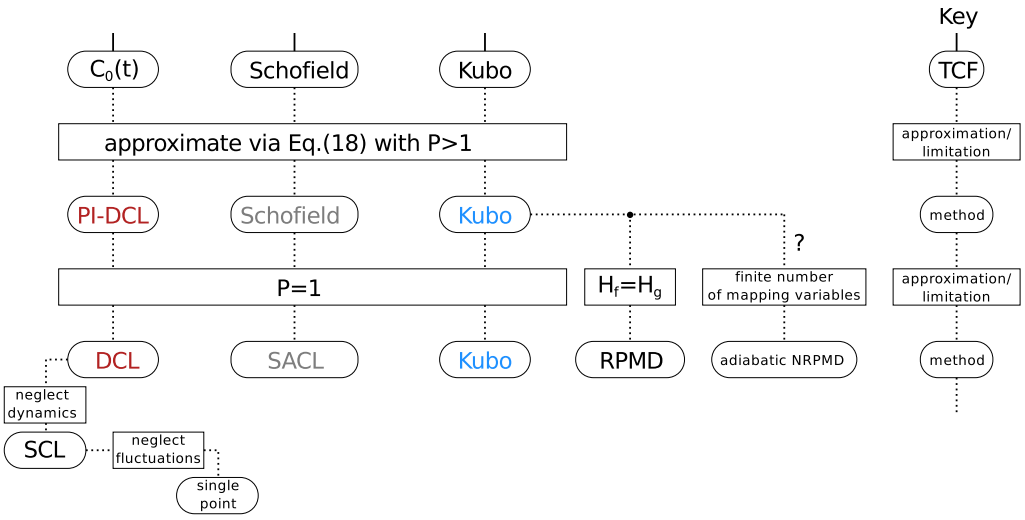

Figure 4: Continuation of Fig. 3. It is shown which methods result from the approximation in Eq. (18) for particular choices of $w(\lambda)$. The legend on the right hand side deciphers the employed convention. The methods that are indicated by color are compared against each other in Sec. 3.2.

factorization, which becomes exact in the limit $P \to \infty$, the QM trace turns out to be isomorphic to the classical configuration-space integral

$$C_{\lambda \equiv l\beta/P}(0) = \lim_{P\to\infty} \frac{\mathcal{N}_P}{Z} \int \mathrm{d}\mathbb{R}\, \mathrm{e}^{-\beta U_l(\mathbb{R})} D_f^g(\boldsymbol{R}_l) D_g^f(\boldsymbol{R}_0) \ , \tag{12}$$

where $\mathcal{N}_P$ is a known normalization constant and it is noted that l and λ are used synonymously throughout the thesis. The effective ring-polymer potential

$$U_l(\mathbb{R}) := K(\mathbb{R}) + \frac{1}{P}\left[\sum_{k=0}^{l} \eta_k V_f(\boldsymbol{R}_k) + \sum_{k=l}^{P} \eta_k V_g(\boldsymbol{R}_k)\right] \tag{13}$$

contains the kinetic spring term $K(\mathbb{R})$ which connects neighboring beads via harmonic springs as in standard RPMD. Note that it has the same form for all electronic states considered, since its origin lies in the kinetic energy operator. In contrast, the potential part of $U_l(\mathbb{R})$ consists of *different* contributions from *different* electronic states, where η_k is equal to $1/2$ if k corresponds to the first or the last summand, to 0 if there is only one summand, which is the case if $l = 0, P$, and to 1 in all other cases. Importantly, each value of l defines a particular PES and thus a particular *realization* of the ring polymer, undergoing different statistics and dynamics as will become clear later. An example of such a realization is illustrated in Fig. 5.

One sees that there are two sets of beads, which "feel" either the upper or the lower PES, indicated by the blue and the red color, respectively. Additionally, the 0-th and the l-th beads are influenced by the averaged potential, symbolized by both colors at a time. The presence of the two distinguishable sets of beads breaks the cyclic symmetry of the ring polymer which is in stark contrast to the standard RPMD. Following the steps in [SK3], one obtains the

desired (and still exact) relation for $\bar{C}_w(0)$ as

$$\bar{C}_w(0) = \lim_{P\to\infty} \frac{1}{P} \sum_{l=0}^{P} \eta_l w(\lambda) \xi_\lambda \left\langle D_f^g(\boldsymbol{R}_l) D_g^f(\boldsymbol{R}_0) \right\rangle_\lambda \ , \tag{14}$$

where the imaginary-time integration in Eq. (10) is discretized via the trapezoidal rule and $\langle \bullet \rangle_\lambda$ stands for an average with respect to the Boltzmann density of the l-th realization. The factors

$$\xi_\lambda := \frac{\exp\left[-\int_0^\lambda \langle \hat{V}_f - \hat{V}_g \rangle_\mu \mathrm{d}\mu\right]}{1+\exp\left[-\int_0^\beta \langle \hat{V}_f - \hat{V}_g \rangle_\mu \mathrm{d}\mu\right]} \tag{15}$$

weight each summand in Eq. (14) individually. Since they are exclusively determined by the quantum Boltzmann statistics, they are dubbed as *intrinsic* weights, which is in opposition to the arbitrary factors $w(\lambda)$ that can be viewed as *external* weights. Importantly, due to the particular form of Eq. (15), the intrinsic weights can be calculated conveniently and numerically exactly via an imaginary-time PI sampling.

Having the $t = 0$ expression at hand, the problem remains how to approximate the nuclear quantum dynamics, in particular, how to estimate the non-classical time evolution in Eq. (11), which is inherent to vibronic transitions. In [SK3], the following ansatz has been proposed. First, an effective Hamiltonian $\hat{H}_\lambda$ is defined such that it corresponds to the effective potential $U_l(\mathbb{R})$, Eq. (13), for each point in the imaginary time $\lambda = l\beta/P$. Second, employing the interaction representation,[1,2] the propagator belonging to the a-th state with $a = g, f$ is rewritten as

$$\mathrm{e}^{-\mathrm{i}\hat{H}_a t/\hbar} = \mathrm{e}^{-\mathrm{i}\hat{H}_\lambda t/\hbar} \exp_+\left\{-\frac{\mathrm{i}}{\hbar}\int_0^t [\hat{H}_a(\tau) - \hat{H}_\lambda]\mathrm{d}\tau\right\} \ , \tag{16}$$

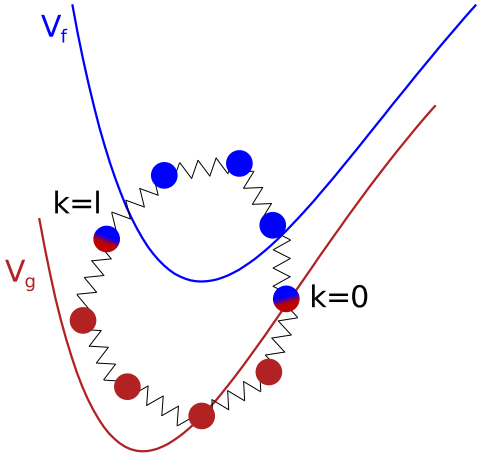

Figure 5: Sketch of the effective ring-polymer potential, Eq. (13) for the case $P = 9$ and $l = 4$, where the 0-th and the l-th bead are marked. The PESs V_g and V_f are shown in red and blue, respectively. The color of the beads that "feel" one of the PESs is chosen accordingly.

where the time argument represents a time evolution with respect to $\hat{H}_\lambda$ and $\exp_+$ is the time-ordered exponential. The important outcome of this reformulation is that all operators appearing in Eq. (11) undergo a Heisenberg-type time evolution. This permits to approximate the dynamics generated by $\hat{H}_\lambda$ via the quasi-classical dynamics of the ring polymer with respect to the classical Hamilton function

$$H_\lambda(\mathbb{R},\mathbb{P}) = \frac{1}{2P}\mathbb{P}^{\mathrm{T}}\mathbb{M}^{-1}\mathbb{P} + U_l(\mathbb{R}) \ . \tag{17}$$

The operators are then replaced by their classical counterparts and, thus, the time ordering becomes irrelevant. The momenta of the ring polymer $\mathbb{P}$ are introduced as conjugate variables to the coordinates $\mathbb{R}$ in the usual RPMD fashion and $\mathbb{M}$ is the diagonal nuclear mass matrix. Finally, the desired generalized TCF is approximated as

$$\bar{C}_w(t) \approx \lim_{P\to\infty} \frac{1}{P} \sum_{l=0}^{P} \eta_l w(\lambda) \xi_\lambda \left\langle D_f^g(\boldsymbol{R}_l) D_g^f(\boldsymbol{R}_0(t)) \mathrm{e}^{\mathrm{i}/\hbar \int_0^t [V_f(\boldsymbol{R}_0(\tau)) - V_g(\boldsymbol{R}_0(\tau))] \mathrm{d}\tau} \right\rangle_\lambda \quad , \tag{18}$$

which is main theoretical result of this section.

In order to evaluate the TCF, the following simulation protocol can be applied, where the practical value of P is a convergence parameter. First, for each value of $l = 0, 1, \ldots, P$ the coordinates and momenta of the ring polymer are sampled from the corresponding density determined by H_λ, Eq. (17), e.g. by using the Langevin thermostat.[126] The electronic energy gap, $V_f - V_g$, is evaluated on the fly such that the intrinsic weights, ξ_λ, can be calculated according to Eq. (15). Second, the Hamilton EOMs are solved with respect to H_λ for each summand in Eq. (18) which requires in general *ab-initio* MD simulations[66] accompanied with a proper electronic-structure method, see Sec. 1. Importantly, since the order and the phase of the adiabatic electronic states are ambiguous in quantum-chemical calculations, it becomes obligatory to trace the states. For instance, the number of states that are relevant for X-ray spectra of realistic molecular systems can become readily larger than several hundreds. Thus, the tracing procedure has to be realized in a fully automated manner, as carried out in [SK1] and [SK2]. Third, the electronic gap as well as transition dipole moments are evaluated along the resulting trajectories and plugged into the generalized TCF, Eq. (18). Finally, the contributions from all values of l are summed over by employing a proper weighting function, yielding e.g. the standard TCF, the Kubo transformed or the Schofield function,[127] see Fig. 4. Note that since the density and the dynamics are generated by the same Hamiltonian, this protocol leaves the density stationary at all times and excludes problems such as the infamous zero-point energy leakage.[128] Additionally, this stationarity enables averaging along trajectories, on top of the averaging with respect to the initial conditions thereby greatly improving the statistical convergence. The generalization to a larger number of states amounts to considering each transition separately according to Eq. (18) and summing the results over.

To summarize, a quasi-classical approximation to the generalized TCF has been proposed employing imaginary-time PI techniques. In contrast to the standard RPMD, the generalized TCF is built from multiple realizations of the ring polymer, each experiencing an individual effective potential, Eq. (13), featuring different fractions of the initial- and the final-state PESs. In the next section it will be shown that restricting to the particular realization with $\lambda = 0$ yields the well-known DCL expression for a single bead, i.e. a classical point particle.

2.3.2 Particular limiting cases: the dynamical and statical classical limits

As it has been stated in Sec. 2.2, setting $w(\lambda) = \delta(\lambda)$ for the generalized TCF restores the correlation function $C_0(t)$ itself. Although a (quasi-)classical approximation to the original correlation function might not lead to optimal results, this choice still possesses various beneficial features as it will be discussed in the following.

Applying the approximation scheme derived in the previous section with $w(\lambda) = \delta(\lambda)$ results in a realization, where the ring polymer is exclusively influenced by the initial-state potential V_g, see Eq. (13) with $l = 0$. The resulting TCF is determined by ground-state trajectories starting from the corresponding Boltzmann distribution independently on the excited state, see Eq. (18) with the imposed settings. The important consequence is that, although hidden by the compact notation, the very same trajectories can be used to evaluate the TCFs for *all* transitions that contribute to the full spectrum, making this approach particularly attractive for treating complex systems. The last statement can be additionally supported, since a parametrized ground-state potential in the form of a force field exists for many systems such that the trajectories can be conveniently obtained via molecular mechanics simulations. Further, sacrificing the nuclear quantum effects by setting $P = 1$ converts the generalized TCF with the imposed weighting function into the commonly known DCL[1,2,93,94] (and, thus, the case $P > 1$ is referred to as PI-DCL), see Fig. 4. This purely classical approach also yields a feasible protocol to treat the non-linear spectrum as it has been demonstrated for RIXS in [SK1] and [SK2] with the results being summarized in Sec. 3.1. It should be stressed that especially the computational effort for multi-dimensional spectra is enormously reduced by using a common set of ground-state trajectories for all transitions, since their possible number grows exponentially with the order of the spectrum.

Unfortunately, the advantage of the DCL, i.e. an exclusive use of ground-state dynamics, is at the same time its drawback. In this case, the system's time evolution is not affected by the excited-state PESs. This contradicts the correct quantum picture, where the nuclear wave packet evolves explicitly on these PESs.[2,54] Thus, it can be already foreseen that such an approximation might yield incorrect dynamical information and the contributions from realizations with $\lambda > 0$ are required, see Sec. 3.2 and Sec. 3.3.

The SCL follows from the DCL by removing the nuclear dynamics as such, as it has been mentioned in the Introduction and is sketched in Fig. 4. The static spectrum follows from a sampling of the relevant nuclear configuration space, thereby accounting for conformational and environmental effects[67–69] that form the spectral line shape. However, it lacks information about time-correlated nuclear motion and, thus, it is not capable to reproduce e.g. vibronic progressions. Still, the comparison between the results obtained from the DCL and the SCL can be employed to identify and analyze vibronic transitions that are sensitive to time-correlated nuclear effects, as carried out in [SK1], [SK2] and Sec. 3.1. Contracting the sampling to a particular (typically the equilibrium) nuclear configuration, finally yields

the single-point calculation protocol that, despite being most simplistic, is also a popular method to describe spectra, where electronic transitions are involved,[38] see Introduction. Another more accurate trajectory-based approach via the so-called Matsubara dynamics is presented in the following section.

2.3.3 Matsubara dynamics and the modified Matsubara method

In this section it is demonstrated how the imaginary-time shifted TCF and, thus, the vibronic spectrum can be approximated in terms of the Matsubara dynamics, see [SK4] for details. As opposed to the approximations described in Sec. 2.3.1 and Sec. 2.3.2, this approach recovers the exact TCF, $C_\lambda(t)$, for two shifted harmonic oscillators in the Condon approximation.

The starting point of the derivation is the exact imaginary-time shifted TCF, Eq. (11), considered at an *arbitrary* time instance t, which is in contrast to Sec. 2.3.1, where $t = 0$ has been imposed. For the sake of brevity, we restrict ourselves to a one-dimensional system, described by $\hat{x}$ and $\hat{p}$, and two discrete electronic states g and f; the generalization to a more-dimensional multi-level system is straightforward. Similarly to common PI techniques, described in Sec. 2.3.1, the nuclear trace is evaluated in the eigenstate basis of $\hat{x}$ and the imaginary time is discretized. Subsequently, in between the Boltzmann factors, $\exp[-\beta\hat{H}_a/P]$ with $a = g, f$, one inserts unities that correspond to *pairs* of variables $x_i^\pm$, that are transformed to midpoint and difference variables, i.e. x_i and Δ_i, respectively, see Fig. 6 for a sketch. Note that the x_i play a similar role as the bead positions depicted in Fig. 5 in Sec. 2.3.1. Importantly, apart from the case $i = 0$, each unity $\hat{1} = \exp[\mathrm{i}\hat{\mathscr{H}}_i t]\exp[-\mathrm{i}\hat{\mathscr{H}}_i t]$ is realized as a Heisenberg time evolution with respect to an arbitrary Hamiltonian $\hat{\mathscr{H}}_i = \hat{p}^2/2m + \hat{V}_i(\hat{x})$, see Fig. 6, where m is the nuclear mass and particular choices for the potentials $\hat{V}_i$ will be discussed later. Finally, the TCF can be written in the form of a classical-like phase-space integral over the positions $\boldsymbol{x} = (x_0, \ldots, x_{P-1})$ and momenta $\boldsymbol{p} = (p_0, \ldots, p_{P-1})$

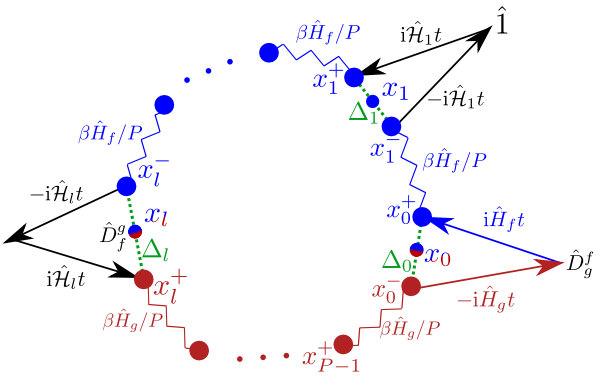

Figure 6: Visualization of the structure of the correlation function in Eqs. (19). The jagged lines and straight arrows represent imaginary- and real-time propagations with length β/P and t, respectively. The red and the blue color indicates the interaction with respect to initial and final electronic states, correspondingly.

$$C_\lambda(t) = \int \mathrm{d}\boldsymbol{x} \int \mathrm{d}\boldsymbol{p}\, A_l(\boldsymbol{x},\boldsymbol{p}) B_l(\boldsymbol{x},\boldsymbol{p},t) \ , \tag{19}$$

where the momentum variables have been introduced via Fourier transforms with respect to the difference variables and the factors $A_l(\boldsymbol{x},\boldsymbol{p})$ and $B_l(\boldsymbol{x},\boldsymbol{p},t)$ will be considered in the following.

The time-independent part, $A_l(\boldsymbol{x},\boldsymbol{p})$ in Eq. (19), that contains matrix elements of the Boltzmann operator, is further evaluated by employing the symmetric Trotter factorization. Alternatively to Ref. 118, the Matsubara dynamics is derived in this thesis via a *local* harmonic approximation to the physical potential, i.e.

$$V_a(x_i^{\pm}) \approx V_a(x_i) \pm \frac{\partial V_a}{\partial x_i}\frac{\Delta_i}{2} + \frac{1}{2}\frac{\partial^2 V_a}{\partial x_i^2}\left(\frac{\Delta_i}{2}\right)^2 \quad , \tag{20}$$

and a local linear approximation to the transition dipole. This ultimately enables analytical integration over the difference variables and, hence, only the classical-like position and momentum variables, $\boldsymbol{x}$ and $\boldsymbol{p}$, respectively, remain relevant. The next important step towards the Matsubara dynamics is to employ the normal mode coordinates of the free-particle ring polymer,[103,117] $\boldsymbol{Q} := \mathbb{T}\boldsymbol{x}/\sqrt{P}$ and $\boldsymbol{\Pi} := \mathbb{T}\boldsymbol{p}/\sqrt{P}$, where the orthogonal transformation matrix $\mathbb{T}$ represents the discrete Fourier transform with respect to the imaginary time.[118] In order to avoid problems with terms that diverge as P increases, one restricts the normal modes to the M lowest, so-called Matsubara modes, where $M \ll P$, see Fig. 7 for a sketch. Practically it implies that only smooth imaginary-time paths significantly contribute to the TCF for all times t and that integrals corresponding to the non-Matsubara modes in Eq. (19) can be performed analytically. Finally, one can write down the time-independent part in the Matsubara approximation as

$$\tilde{A}_l(\boldsymbol{Q},\boldsymbol{\Pi}) \approx \frac{\bar{M}!^2}{2\pi\hbar^M Z} D_f^g(x_l(\boldsymbol{Q}))\mathrm{e}^{-\beta[\tilde{H}_l(\boldsymbol{Q},\boldsymbol{\Pi})+\mathrm{i}\boldsymbol{\Pi}^{\mathrm{T}}\mathbb{W}\boldsymbol{Q}]} \quad , \tag{21}$$

where the anti-symmetric anti-diagonal matrix $\mathbb{W}$ contains the well-known Matsubara frequencies $\omega_r = 2\pi r/\beta\hbar$ and $\bar{M} := (M-1)/2$. For the sake of brevity, $\boldsymbol{Q}$ and $\boldsymbol{\Pi}$ represent the Matsubara modes only and $\tilde{A}_l(\boldsymbol{Q},\boldsymbol{\Pi}) := P^P A_l(\boldsymbol{x}(\boldsymbol{Q}),\boldsymbol{p}(\boldsymbol{\Pi}))$ with P^P stemming from the substitution of the Cartesian volume element by the normal-mode one. The classical Hamilton function in Eq. (21), $\tilde{H}_l(\boldsymbol{Q},\boldsymbol{\Pi}) := \boldsymbol{\Pi}^{\mathrm{T}}\boldsymbol{\Pi}/2m + \tilde{U}_l(\boldsymbol{Q})$, is determined by the effective ring-polymer potential for multiple PESs, Eq. (13), *without* the spring term.

The time-dependent part, $B_l(\boldsymbol{x},\boldsymbol{p},t)$ in Eq. (19), is built up from the matrix elements of the real-time propagators that contain $\hat{\mathscr{H}}_i$. Employing properties of the Wigner transform,[99,129,130] one can show that for $P\to\infty$ the time evolution of $\tilde{B}_l(\boldsymbol{Q},\boldsymbol{\Pi},t) = B_l(\boldsymbol{x}(\boldsymbol{Q}),\boldsymbol{p}(\boldsymbol{\Pi}),t)$ is *exactly* given by the classical-like Liouvillian

$$\lim_{P\to\infty}\hat{\tilde{\mathscr{L}}}_l(\boldsymbol{Q},\boldsymbol{\Pi}) = \frac{1}{m}\boldsymbol{\Pi}^{\mathrm{T}}\nabla_{\boldsymbol{Q}} - [\nabla_{\boldsymbol{Q}}^{\mathrm{T}}\tilde{\mathscr{U}}_l(\boldsymbol{Q})]\nabla_{\boldsymbol{\Pi}} + \frac{\mathrm{i}}{\hbar}[V_f(x_0(\boldsymbol{Q})) - V_g(x_0(\boldsymbol{Q}))] \quad , \tag{22}$$

where $\mathscr{U}_l(\boldsymbol{x}) := [V_f(x_0)+V_g(x_0)]/2P + \sum_{i=1}^{P-1}\mathscr{V}_i(x_i)/P$ contains the yet unspecified potentials $\mathscr{V}_i$ that stem from the $\hat{\mathscr{H}}_i$. Importantly, neither an additional approximation nor any $\hbar\to 0$ limit has been applied but crucial has been the application of the Matsubara approximation which has removed the problematic divergent terms.

Putting together both parts, $A_l(\boldsymbol{x},\boldsymbol{p})$ and $B_l(\boldsymbol{x},\boldsymbol{p},t)$, yields the Matsubara approximation to the imaginary-time shifted correlation function

$$C_\lambda(t) \approx \frac{\bar{M}!^2}{2\pi\hbar^M Z}\int \mathrm{d}\boldsymbol{Q}\int \mathrm{d}\boldsymbol{\Pi}\, \mathrm{e}^{-\beta[\tilde{H}_l(\boldsymbol{Q},\boldsymbol{\Pi})+\mathrm{i}\boldsymbol{\Pi}^{\mathrm{T}}\mathbb{W}\boldsymbol{Q}]} \\ \times D_f^g(x_l(0))D_g^f(x_0(t))\exp\left\{\frac{\mathrm{i}}{\hbar}\int_0^t [V_f(x_0(\tau))-V_g(x_0(\tau))]\mathrm{d}\tau\right\}\ , \tag{23}$$

where the time evolution obeys the classical-like EOMs

$$\dot{\boldsymbol{Q}} = \frac{\boldsymbol{\Pi}}{m}, \quad \dot{\boldsymbol{\Pi}} = -\nabla_{\boldsymbol{Q}}\tilde{\mathscr{U}}_l(\boldsymbol{Q})\ . \tag{24}$$

These last two equations represent one of the main theoretical results in [SK4]. Importantly, the developed protocol is a generalization of the existing Matsubara dynamics method to multi-PES spectroscopy, since the single-PES case can be addressed by considering the Kubo transformed TCF and additionally imposing that the adiabatic electronic states coincide, see Fig. 8. However, two concerns are yet unresolved.

First, one has to find a reasonable choice for the potentials $\mathscr{V}_i$, which has been put forward in [SK4] with the following two suggestions as the outcome. The so-called *equilibrium method* is designed to keep the density as stationary as possible to avoid problems like zero-point energy leakage and artificial negativities in the spectrum, see [SK3]. Unfortunately, the stationarity cannot be completely achieved and, moreover, this choice seems to be incompatible with the Matsubara approximation, which implies taking only smooth imaginary-time paths into account. The latter deficiency can be circumvented by the alternative *average method*, where all beads are propagated with respect to the average of the initial- and final-state Hamiltonians. The resulting EOMs conserve the cyclic symmetry of imaginary-time path, leading to dynamics that are compatible with the Matsubara approximation at the price of non-stationarity. In this thesis only two choices for the potentials are suggested, nonetheless, the presented formalism offers in principle infinitely many possible approaches to vibronic spectroscopy that might or might not lead to efficient simulation protocols.

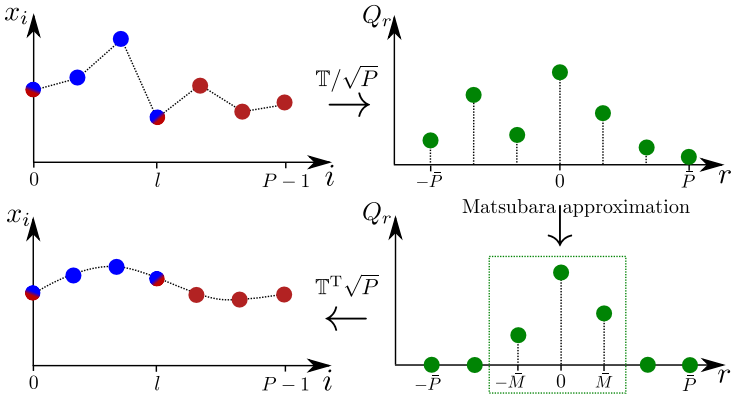

Figure 7: A sketch illustrating how the Matsubara approximation affects an imaginary-time path. An arbitrary jagged imaginary-time path (upper left) is transformed to the normal modes' coordinates via the matrix $\mathbb{T}$ (upper right). After restricting to the M lowest modes (bottom right), i.e. the Matsubara approximation, one obtains a smooth path via the back transform (bottom left). Note that the normal mode index r runs over $-\bar{P},\ldots,\bar{P}$, where, similarly to $\bar{M}$, $\bar{P} := (P-1)/2$.

The second and more severe concern is the presence of the imaginary part $\mathbf{\Pi}^{\mathrm{T}}\mathbb{W}\boldsymbol{Q}$ in the exponent in Eq. (23), which is responsible for the infamous sign problem plaguing the Matsubara dynamics methods. This imaginary part can be removed by transforming the Matsubara momentum to the complex plane.[118] Unfortunately, the resulting dynamics feature unstable complex trajectories yielding similar statistical convergence issues as the sign problem itself. For single-PES studies, one common ansatz to finally avoid the sign problem is to simply neglect the imaginary contributions to the dynamics leading directly to the well-known RPMD method. If vibronic spectroscopy is considered, this approximation leads to a RPMD-like method for multiple PESs that coincides with the one presented in [SK3] and Sec. 2.3.1 for the open interval $\lambda \in]0,\beta[$ if the equilibrium method is considered, see Fig. 8. Thus, for these values of λ, the quasi-classical methodology introduced in Sec. 2.3.1 can be viewed as an approximation to the Matsubara dynamics presented here. In contrast for the set $\lambda \in \{0,\beta\}$, such a relation is not given, since the dynamics that is described here features the averaged potential $[V_f(x_0)+V_g(x_0)]/2P$ for the 0-th bead, which is not present in Sec. 2.3.1. Consequently for $\lambda = 0$, the equilibrium and average versions of the Matsubara method as well as its RPMD-like approximation have the ACL as their common $P \to 1$ limit instead of the DCL, compare Fig. 4 and Fig. 8.

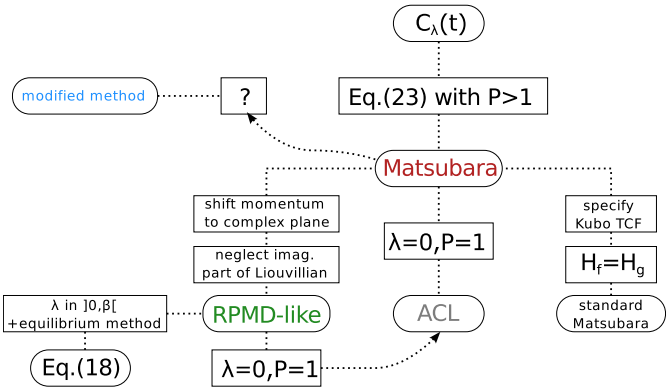

Figure 8: Overview of the methods that result from the approximation in Eq. (23) for different values of λ and P. The legend can be found on the right hand side of Fig. 4. The methods that are indicated by color are compared against each other in Sec. 3.3.

Yet another method that is suitable to accurately simulate the standard correlation function, $C_0(t)$, without suffering from the sign problem has been suggested in [SK4]. In contrast to the aforementioned RPMD-like ansatz, this *modified Matsubara method* is not a systematic approximation to the Matsubara dynamics, but is rather deduced from a comparison of analytical expressions for a harmonic oscillator system. At the heart of the method is the *ad-hoc* modification of the complex exponent in Eq. (23), such that

$$\frac{1}{2m}\mathbf{\Pi}^{\mathrm{T}}\mathbf{\Pi}+\tilde{U}_0(\boldsymbol{Q})+\mathrm{i}\mathbf{\Pi}^{\mathrm{T}}\mathbb{W}\boldsymbol{Q}\mapsto\frac{1}{2m}\mathbf{\Pi}^{\mathrm{T}}(1+\mathbb{W}^{\mathrm{T}}\mathbb{Y}^{-1}(\boldsymbol{Q})\mathbb{W})\mathbf{\Pi}+\tilde{U}_0(\boldsymbol{Q})+\frac{1}{2}m\boldsymbol{Q}^{\mathrm{T}}\mathbb{W}^{\mathrm{T}}\mathbb{W}\boldsymbol{Q}\ , \tag{25}$$

while keeping the original EOMs from Eq. (24) for the real-time propagation. The key quantity is the position-dependent matrix $\mathbb{Y}(\boldsymbol{Q})$, which maps the curvature of the ground-state

potential along the imaginary-time path onto the Matsubara modes, i.e.

$$\mathbb{Y}(\boldsymbol{Q}) := \frac{1}{m}\mathbb{T}\left(\frac{\partial^2 V_g}{\partial x_i^2}\delta_{ij}\right)\mathbb{T}^{\mathrm{T}} \quad . \tag{26}$$

For two shifted harmonic oscillators, this modification leads to a standard TCF, $C_0(t)$, that is equal to the one obtained by the original Matsubara method, see [SK4]. Hence, both methods restore the exact QM spectrum for this particular model. Importantly, since the modified density is strictly real, the sign problem does not occur and, thus, the statistical convergence behavior is strikingly improved with respect to the original method. Moreover, the suggested modified method accurately samples the thermal Wigner function and provides a reasonable approximation to vibronic absorption spectra of anharmonic model systems, as it will be demonstrated in Sec. 3.3. However, as a word of caution it should be noted that the inverse $\mathbb{Y}^{-1}$ becomes ill-defined at points where the second derivative of the ground-state PES vanishes and that the modified density can become unbound if $V_g(x)$ possesses regions with a negative curvature.

It remains to be seen whether this new but heuristic simulation protocol can be viewed as a systematic approximation to the orignal Matsubara method, see Fig. 8. In order to clarify this relation, it would be desirable to find a rigorous mathematical route from the original Matsubara method to the modified one. Such a derivation may also shed light on the relation to the known Feynman-Kleinert Quasi-Classical Wigner method.[131]

3 Numerical applications

3.1 Applying the dynamical classical limit to (non-)linear X-ray spectra of water

As it has been already stated in Sec. 2.3.2, the somewhat simplistic DCL method may constitute a pragmatic choice for complex realistic systems due to its comparably low cost and good scaling with the number of DOFs. It has been demonstrated in [SK1], [SK2] that it can serve as a basis for a qualitative analysis, proving the importance of accurately accounting for dynamical nuclear effects in theoretical X-ray spectroscopy. Especially for the non-linear RIXS spectrum, the common static description via the SCL can lead to wrong line shapes and intensities as it is exemplified in the following for the oxygen K-edge spectra of gas phase and bulk water at ambient temperature. It should be stressed that the focus is put on the comparison between the SCL and the DCL methods and, thus, the differences due to nuclear dynamics rather than on the peculiarities of the water spectra themselves. Note that the same datasets have been used for both methods.

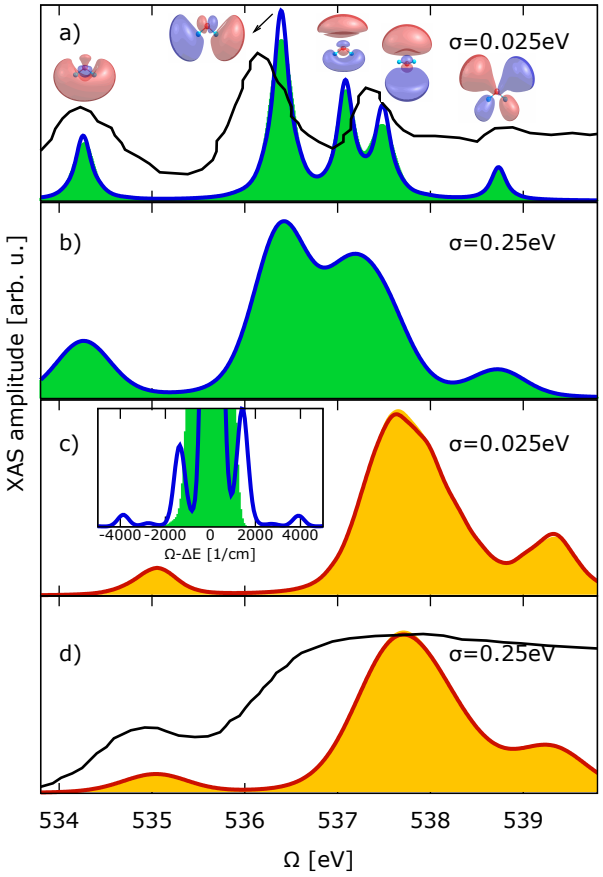

Figure 9: XAS amplitudes for gas phase water, panels a,b) and for bulk water, panels c,d). The black line represents the respective experimental data from Ref. 13. The blue and red lines depict the DCL results, whereas the filled green and yellow curves correspond to the SCL method. The unoccupied MOs of a water molecule to which the transition is performed are visualized next to the corresponding peaks. Inset zooms on the transition corresponding to the lowest energy in the gas phase with the imposed infinite lifetime, where the frequency axis is shifted by the peak position $\Delta E = 534.3$ eV.

3.1.1 The X-ray absorption spectrum

The results for the XAS amplitude obtained via various simulation setups and strategies are discussed and compared against each other, where all the computational details are given in [SK1] and [SK2]. In Fig. 9, the XAS amplitudes for gas phase and bulk water resulting from the SCL and the DCL approaches for a rather small (0.025 eV) and a larger (0.25 eV) width σ of the excitation pulse are shown. With-

out any fitting, the computed curves for the gas phase and the bulk system are in qualitative agreement with experimental data,[13] depicted by solid black curves therein. A comparison between the SCL and DCL results for the gas phase and the small linewidth, Fig. 9a), reveals subtle but evident differences in the peak intensities. Their origin can be clearly traced back to dynamical effects by assuming an infinite lifetime of the final core-excited states within the simulation, see inset. The observed side bands can be directly related to the vibrational modes of the water molecule, in particular to the bending and stretching ones, which have in the employed force field frequencies of $\approx 1500\,\mathrm{cm}^{-1}$ and $\approx 3800\,\mathrm{cm}^{-1}$, respectively. Naturally these side bands cannot be recovered by the SCL method due to the aforementioned intrinsic limitations of this static approach, see Sec. 2.3.2. However, all the differences vanish at the large spectral pulse width, see Fig. 9b). One can show that the two spectra cover the same area and, thus, increasing the width of the convoluted Gaussian naturally eliminates the differences between the two approaches. The same comparison is performed for bulk water, see panels c) and d) in Fig. 9. Here, the differences between the methods are negligibly small for both pulse widths as well as for an hypothetic infinite lifetime of the core-excited states, see Sec. VI in Supplement of [SK2]. This suggests that XAS is not a very sensitive observable for nuclear dynamical effects.

To resume, correlated nuclear dynamics does not affect XAS amplitudes significantly for bulk water under any circumstances. However, differences for the gas phase can be seen if the pulse widths and/or lifetime broadening of the final states are particularly small. As it has been pointed out in the Introduction, the RIXS amplitude contains more information and, hence, the fingerprints of nuclear dynamical effects are more prominent, as will be shown in the following section.

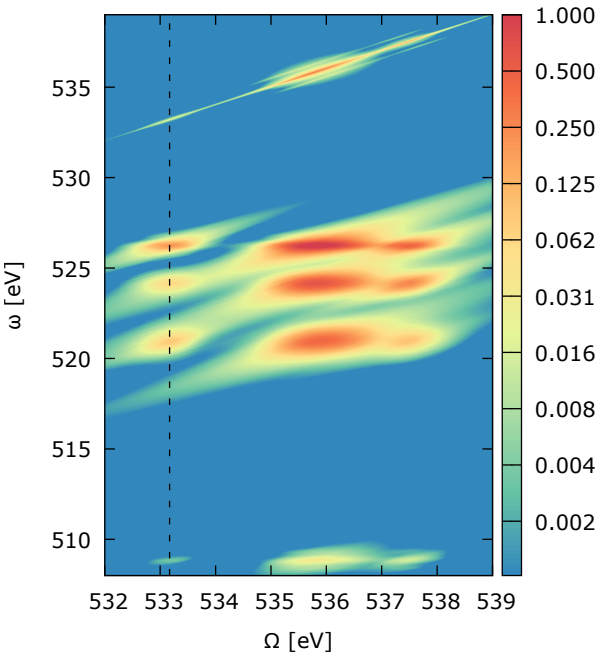

Figure 10: Two-dimensional RIXS spectrum for bulk water (small pulse width) obtained by means of the DCL method, see Sec. 2.3.2. The dashed vertical line indicates the position of the cut depicted in Fig. 11.

3.1.2 The resonant inelastic X-ray scattering

In Fig. 10, a two-dimensional spectrum is shown for bulk water obtained via the DCL method. Since it is hard to make a quantitative analysis on its basis, a particular cut corresponding to the lowest absorption frequency is considered, see vertical line in Fig. 10; note that the particular excitation frequencies are different for the gas phase (534.2 eV) and bulk (535.0 eV) cases. Note further that the features revealed by cuts at different excitation

frequencies are qualitatively similar, as it can be seen in [SK1] and [SK2].

In Fig. 11, the aforementioned cut is divided into three spectral ranges that are examined for various simulation setups. The peaks can be related to spontaneous emissions from the intermediate (core-excited) state to final (ground or valence-excited) ones, see the respective water MOs from which the emission takes place in panels a). The simulated spectra qualitatively reproduce the experimental data, taken from Refs. 132 and 34 and depicted by black lines in panels b2) and d2). Note that no experimental data has been available for the transitions shown in the left and right columns. In panels a1)-a3) significant differences between the methods become evident in case of the small pulse width. For all peaks, prominent vibronic structures being almost symmetric around the maximum can be observed with the frequencies easily attributed to vibrational modes of the water molecule, see, e.g., the inset where the progression of the bending mode is clearly visible. Although the fine structures cannot be detected employing a larger excitation bandwidth, see panels b) therein, differences in intensity remain for the elastic and for the peak around 526 eV in panel b2). Moreover, the energetically lowest transition in panel b1) possesses a pronounced peak structure when computed via the DCL method and, thus, this transition turns out to be very sensitive to nuclear dynamical effects.

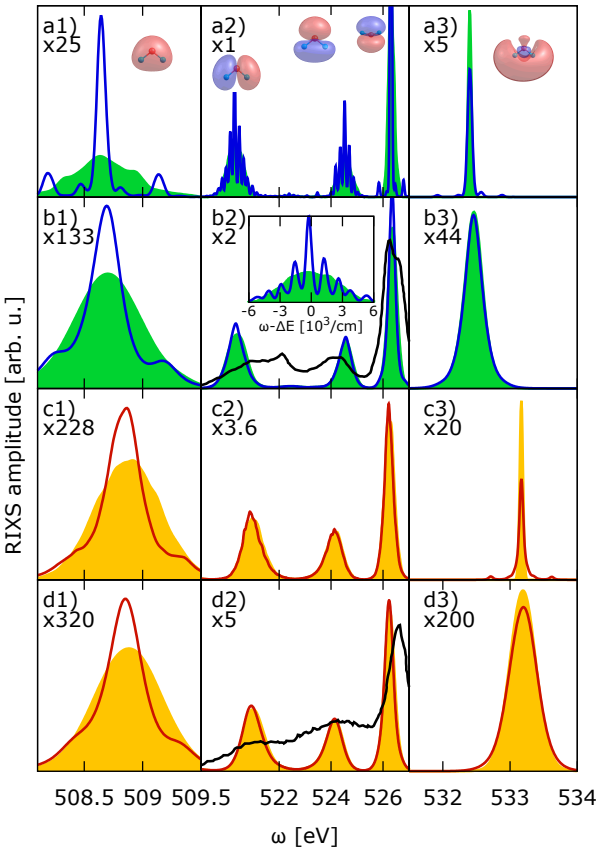

Figure 11: Cuts through RIXS spectra for various simulation scenarios. The excitations frequencies are fixed at 534.2 eV and 535.0 eV for the gas phase and the bulk, respectively. The color code and the panel structure are the same as in Fig. 9. Panels a) and c) correspond to $\sigma = 0.025$ eV whereas b) and d) to $\sigma = 0.25$ eV. Each panel is split into three sub-panels according to the spectral ranges that exhibit intensity (note multiplicative factors therein), see Fig. 10. The black line represents the respective experimental data for the gas phase and for the bulk system from Refs. 132 and 34, respectively. Inset zooms on the left peak in panel a2) with $\Delta E = 520.2$ eV.

In contrast to the linear spectrum, i.e. XAS, the results for the condensed phase still feature noticeable differences between the methods for all pulse widths considered, see panels c1), c3), d1) and d3). This underlines the statement that non-linear RIXS spectra are more sensitive to time-correlated nuclear effects. Most importantly, one sees clear traces of nuclear dynamics at all realistic experimental conditions considered. In particular, the static approach is naturally not able to reproduce any vibronic progression and the intensity of the

elastic peak is overestimated whereas the inelastic peak height is underestimated.

The origin of these differences has been extensively analyzed in [SK2] and will be briefly summarized in the following. Employing the Condon approximation and a simple harmonic model, the magnitude of the deviation between the static and the dynamical approach can be connected to the high- and low-frequency contributions to the fluctuations of the electronic gap, i.e. the spectral density.[1,2] The conclusion is that, the more a vibronic transition involves faster nuclear motion and, thus, higher vibrational modes, the larger the discrepancy between the SCL and DCL method becomes.

In this section it has been demonstrated that the DCL indeed represents a step forward over the more common SCL approach to X-ray spectroscopy. Due to its simplicity, the DCL method can be readily applied to study the non-linear spectra of complex systems on a qualitative basis. In particular, via a comparison to the purely static approach, it can be used to identify those transitions that are particularly sensitive to nuclear dynamical and time-correlation effects. However, it might become unreliable when it comes to a quantitative analysis, since the approximation can cause wrong frequencies and shapes of the vibronic progressions. The quantum dynamics are approximated more accurately within the formalisms presented in Sec. 2.3.1 and Sec. 2.3.3, as it will be demonstrated in the following sections.

3.2 Applying the generalized methodology to model systems

As it has been discussed in Sec. 2.2, the generalized formalism does not only restore common TCFs, see Fig. 3, it furthermore enables "tailoring" completely new ones that might lead to improved numerical protocols. As a first step to investigate the opportunities given by this flexibility, a one-dimensional model system consisting of two displaced Morse oscillators has been considered at two different temperatures in [SK3]. The chosen ground-state potential mimics an isolated OH bond of a water molecule, where the parameters are adopted from Ref. 133. In order to examine various scenarios, a moderate displacement (0.22 au) and a large one (0.5 au) have been used in combination with equal dissociation energies but different stiffness parameters α for the two oscillators, where the stiffness of the excited-state PES is reduced by a factor of 0.86 with respect to the ground-state one.

3.2.1 Common weighting functions

First, the spectra obtained by the methods that stem from common choices of the weighting function, namely PI-DCL, DCL, ACL, Schofield, Schofield averaged classical limit (SACL) and Kubo are compared against each other in Fig. 12, see Fig. 4 for a sketch and [SK3] for a detailed description of all the methods. Since the numerically exact results are available for such a model system, one can directly judge on the ability of each method to reproduce the correct QM spectrum. To start, the comparison for the moderately displaced PESs is per-

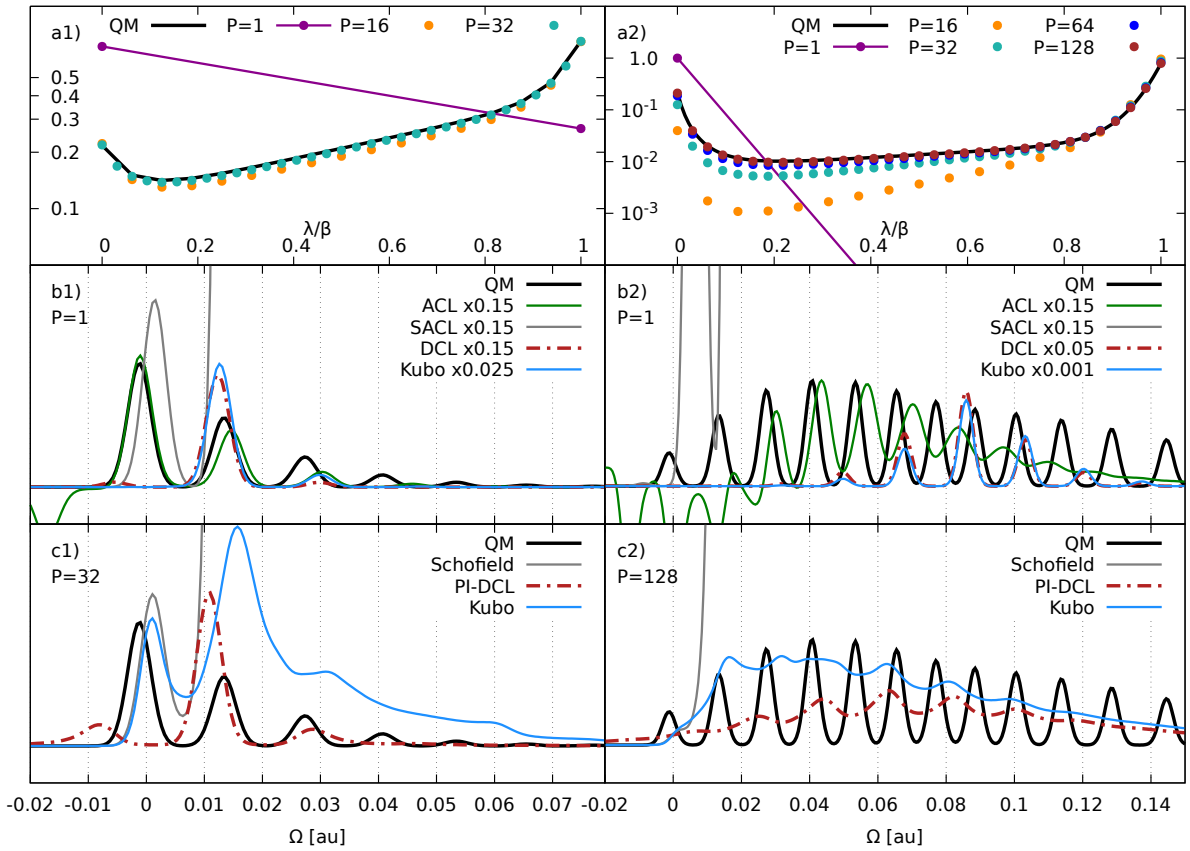

Figure 12: The two-level system at 300 K, left: moderate shift of 0.22 au and right: large shift of 0.5 au, see text. Panels a) intrinsic weights, ξ_λ, b)-c) absorption spectra for $P = 1, 32, 128$, see the legend therein.

formed (left column) for ambient temperature. The intrinsic weights, ξ_λ defined in Eq. (15), can be used to examine the convergence with respect to the number of beads, see panel a1) therein. It becomes immediately apparent that the weights for $P = 1$ (the classical limit for the nuclei) are qualitatively wrong. Complete convergence to the exact quantum result is reached at $P = 32$, which is a manifestation of the fact that imaginary-time PI methods correctly describe static quantities. These numbers of beads are also typical for reaching convergence for ground-state properties of water at ambient conditions.[128,134]

Turning to the absorption spectra depicted in Fig. 12b1)-c1), one sees that the QM spectrum reveals a Franck-Condon progression with a Huang-Rhys factor smaller than 0.5, meaning that the maximal intensity is located at the 0-0 transition.[2] For the case $P = 1$, panel b1), DCL and Kubo results are very similar, however, both methods fail completely to reproduce the exact spectrum in this parameter regime. In particular, the maximum is not at the correct 0-0 transition and the peak heights are dramatically overestimated (note the scaling factor). The vibronic progression is almost not present and features wrong frequencies and a symmetrical shape, as it has been discussed for the DCL before, see Sec. 3.1, [SK1] and [SK2]. In contrast, the ACL results are in better agreement with the exact ones, apart from the scaling and a slight difference in the fundamental frequency. The artificial negativity that can be

observed to the left of the 0-0 transition is an intrinsic feature of this method, as it has been shown in [SK3]. Finally, the numerical spectra obtained from the SACL method, i.e. classical limit of the Schofield method, suffer from an uncontrollable intensity growth due to the SCF. As it can be seen in Fig. 3 and Fig. 13, this factor grows exponentially with frequency, where a solution for this problem is suggested in Sec. 3.2.2.

Increasing the number of beads to $P = 32$, see panel c1), the PI-DCL method yields reasonable amplitudes but still wrong spectral shapes. This supports the statement that the pure ground-state dynamics cannot reproduce the spectra, which significantly dependent on the peculiarities of the excited state. As they include contributions from the beads evolving on the PES of the excited state, the Kubo results improve a lot with respect to the spectral structure. Still, the shape is not correct, which in principle can be healed by a different choice of the SCF, see Sec. 3.2.2. Again, the spectra stemming from the Schofield function grow uncontrollably with frequency due to the SCF that is independent on the number of beads.

In order to investigate a regime, where the vibronic progressions are more pronounced, the model system with the large displacement of the PESs, i.e. 0.5 au, is considered, see right panels in Fig. 12. The convergence of the intrinsic weights can be observed for $P = 128$ beads, which is significantly more than for the moderately displaced system. This is intuitively expected, since a larger number of beads is needed to account for the increased displacement of the PESs as can be understood from Fig. 5. The spectra obtained by the Kubo and the DCL method for $P = 1$, see panel b2), exhibit again dramatically overestimated intensities and rather symmetric lineshapes, whereas the ACL spectra are qualitatively better, though suffer increasingly from the negativities. When the number of beads is increased to $P = 128$, panel c2), the Kubo spectrum features an improved envelop with respect to the results for $P = 1$. However, the peaks are much broader than in the QM reference and they are not at the correct positions. The PI-DCL amplitudes are getting more reasonable but the shape and peak positions still do not fit to the QM result and the Schofield spectra are again numerically unstable. Practically, there is no qualitative difference in terms of the performance of each method with $P > 1$ for the two regimes considered, which supports the assertion that the Kubo transform is not superior to the other methods if vibronic spectra are considered.

3.2.2 Possible improvements

As it is has been discussed in the previous section, the common approaches to vibronic spectra, do not necessarily lead to optimal results for the considered model systems. For instance, the ACL reproduces the lineshapes generally quite well, but suffers from the rather severe problem of negativities due to non-equilibrium dynamics. The equilibrium version of ACL, i.e. the SACL, does not have this deficiency but, unfortunately, the respective SCF (depicted in Fig. 13b)) leads to a numerical instability for spectra. It thus seems natural to opt for a more moderate SCF while having SACL-like dynamics, which can be readily realized by the generalized formalism, since the external weighting function $w(\lambda)$ can be chosen arbitrarily.

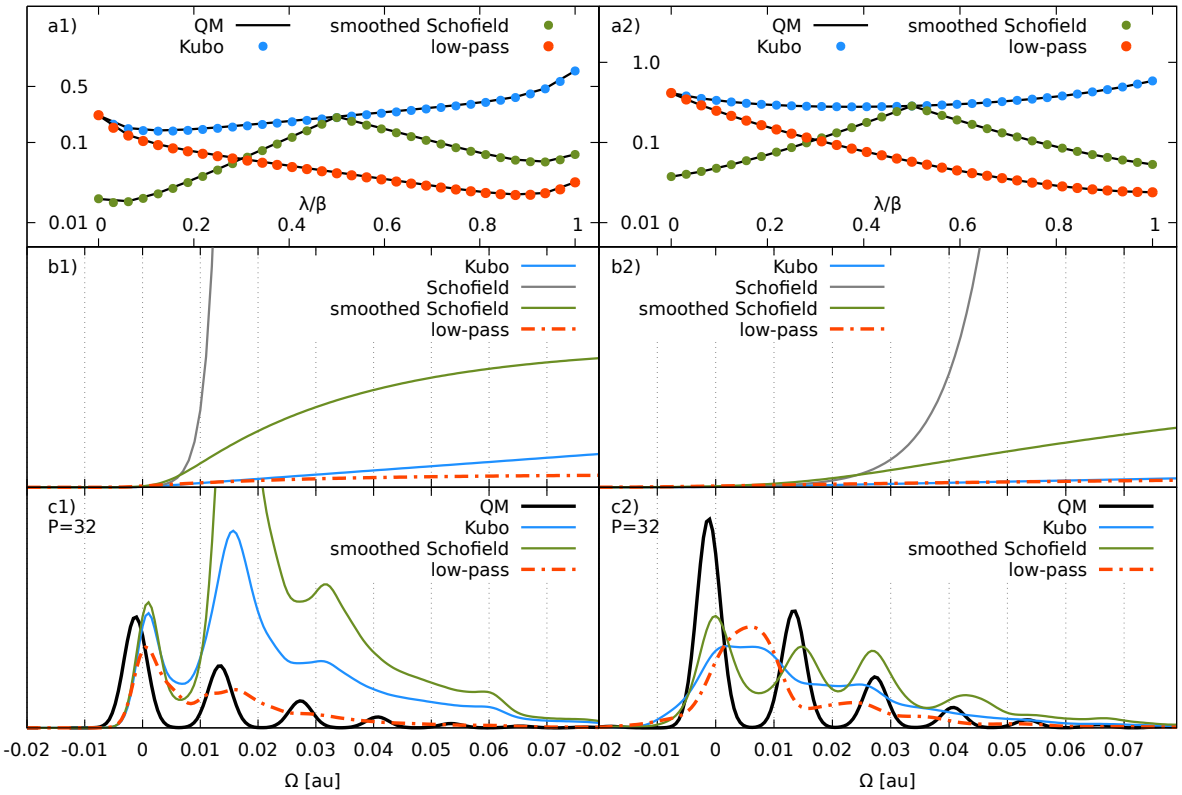

Figure 13: The two-level system with the moderate shift of 0.22 au; left: at $T = 300\,\mathrm{K}$ and right: at $T = 1117.6\,\mathrm{K}$, see text. The smoothing for the Schofield function $\beta\varepsilon = 4.8$, and for the low-pass filter $\beta\varepsilon = 3.2$. Panels a) filtered intrinsic weights, $\xi_\lambda \cdot w(\lambda)$, b) SCFs, c) absorption spectra for $P = 32$.

One possibility is to choose $w(\lambda) = \exp[-|\lambda - \beta/2| \cdot \epsilon]$, which "smooths" the delta peak around $\beta/2$ (corresponding to the Schofield TCF), where the width can be controlled by the value of ϵ. It can be clearly seen in Fig. 13b) that the resulting SCFs (green curves) indeed exhibit a significantly lower magnitude for higher frequencies. Another reasonable choice follows from the conclusion that Kubo yields an acceptable envelop for the vibronic progressions, but suffers from overestimated intensities for higher frequencies. It is supposed that this deficiency is due to over-pronounced contributions with large λ, thus, suggesting $w(\lambda) = \exp[-\lambda\epsilon]$, which suppresses the unwanted contributions to spectra and can be hence considered as a low-pass filter. The resulting *filtered* intrinsic weights, $\xi_\lambda \cdot w(\lambda)$, are depicted in the upper panels of Fig. 13.

The respective spectra for the system with the small displacement between the PESs are shown in the lower panels of Fig. 13 for two different temperatures. At lower temperatures (larger β), panel c1), the low-pass filter appears to be preferable. Specifically, it removes the overpronounced high frequency contributions that spoiled the Kubo results, whereas the smoothed Schofield filter emphasizes these contributions even more and is thus not usable for this regime. However, the fine structures in the spectrum obtained by the low-pass filter are broader than those in the exact spectrum. Switching to the higher temperature case, right column of Fig. 13, the low-pass does not improve over the Kubo results, whereas the

smoothed Schofield filter reveals the fine spectral structure with a decent quality without any negativities. In both cases the smoothed Schofield spectra exhibit reasonable intensities, as it is implied by the choice of the external weight.

To summarize, the present study suggests that a non-standard form of $w(\lambda)$ *can* be beneficial in comparison to common choices with respect to quality and numerical stability. However, a universal recipe for choosing the weighting function is hard to formulate for the general case and requires further investigations, see Sec. 4.

3.3 Performance of the Matsubara dynamics and the modified method

It has been demonstrated in [SK4] that the suggested Matsubara dynamics approach to vibronic spectra as well as the modified method recover the exact TCF for a system consisting of two displaced harmonic oscillators in the Condon approximation. To reiterate, this in contrast to all (quasi-)classical approximations presented in Sec. 2.3.1 and Sec. 2.3.2. In order to investigate a more realistic scenario (beyond the harmonic case), the focus is on two displaced anharmonic oscillators given by quartic expansions of the Morse potential at ambient temperature. The parameters for the electronic ground state are again adopted from Ref. 133. Similarly to [SK3] and Sec. 3.2, the excited-state PES differs from the ground-state one by a displacement of 0.22 au and a lower stiffness, whereas the dissociation energies are equal.

3.3.1 Static properties of the methods

Before discussing the vibronic spectra, the peculiarities of the modified Matsubara method, as introduced in Sec. 2.3.3, are considered. It has been demonstrated in [SK4] that the modification suggested in Eq. (25) yields the exact sampling of the Wigner function for the harmonic oscillator. In Fig. 14, the ability of the modified Matsubara method to reproduce the exact Wigner function of the anharmonic system is investigated. In panel a) therein, one can see the classical Boltzmann function for the electronic ground state. It is not surprising that the classical density is much more localized than the exact Wigner function seen in panel d); note the different scales for the color bars in the different panels. In panel b), the absolute value of the complex density corresponding to the original Matsubara method, Eq. (23), is shown for $P = 45$. This is effectively nothing else than the classical Boltzmann distribution, but for a temperature that is P times higher than in the classical case, panel a). For the present model this implies a temperature of 13500 K and, hence, the density covers a phase-space volume that is much larger than the classical one and significantly larger than the correct QM one. Only the cancellation due to the complex phase in the Matsubara density removes the irrelevant contributions to the observables. This *indirect* sampling of the correct distribution is at the heart of the sign problem and is thus responsible for the insufficient convergence of the original Matsubara method. In contrast, the modified method ap-

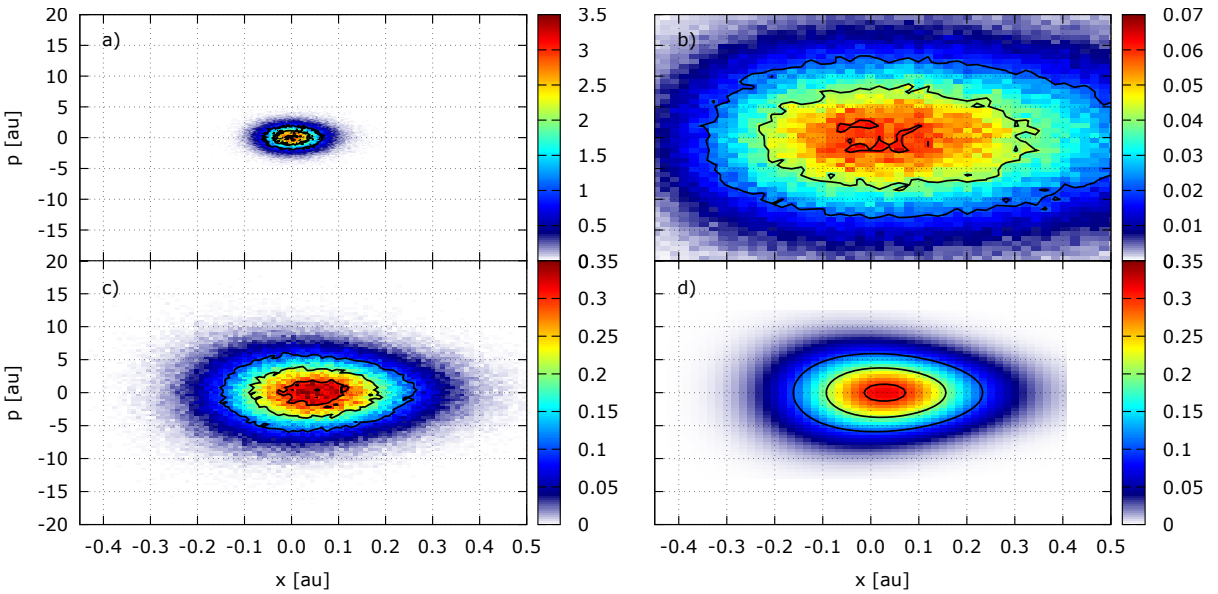

Figure 14: Phase-space probability densities for the anharmonic model system sampled by the considered methods. Panel a) the classical Boltzmann distribution; panel b) the absolute value of the complex Matsubara density and panel c) the modified density, both with $P = 45$; panel d) the exact Wigner function.

proximates the exact thermal Wigner function *directly* with a remarkable accuracy, see panel c). Importantly, it is even able to reproduce the "egg shape" of the correct Wigner function, which is an inherently quantum-statistical effect, since it requires the coupling of positions and momenta in the density, which is not present in the classical case.

3.3.2 The vibronic absorption spectrum for an anharmonic system

After discussing static properties of the methods, the dynamical observables of interest, i.e. vibronic absorption spectra, are considered for the anharmonic system in Fig. 15. It should be noted that the focus is put on the case $\lambda = 0$ only, since in [SK4] it has been concluded, that none of the methods presented in Sec. 2.3.3 can practically reproduce the exact imaginary-time shifted TCF for the case $\lambda \in]0, \beta[$. In particular, the equilibrium Matsubara method converges formally to the exact result but is suffering from the sign problem. The RPMD-like method (see Sec. 2.3.3 and Fig. 8) does not lead to an acceptable approximation to the quantum TCF, and unfortunately, the modified Matsubara method has been derived just for $\lambda = 0$ and naive use of this modification for $\lambda > 0$ expectedly fails. Still, the expressions that have been derived in this thesis for a general value of λ might serve as a basis for future work, see Sec. 4.

Figure 15 is structured such that the results from the equilibrium and average methods, see Sec. 2.3.3, are depicted in left and right columns, respectively. Although setting $M = P$ contradicts the assumption of the Matsubara approximation, it has been concluded in [SK4] that only this choice leads to reasonable results for the equilibrium method. Moreover, for the model systems considered therein, it has been demonstrated that there is no apparent

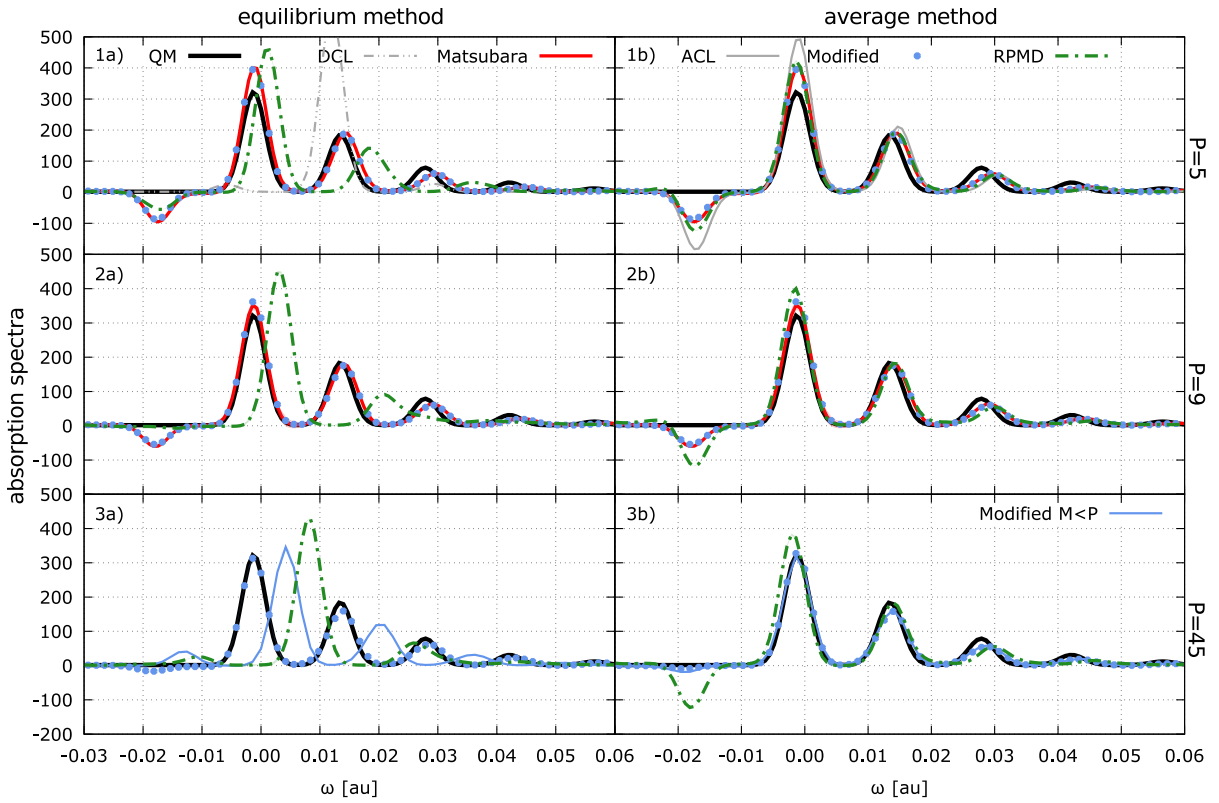

Figure 15: Absorption spectra for two displaced anharmonic oscillators at 300K. The left column, panels a), exhibits the results of the equilibrium methods whereas panels b) contain the results of the average methods for $M = P$. The first row, panels 1), exhibits the results for $M = P = 5$, apart from the DCL and ACL curves which correspond to $M = P = 1$. The second row, panels 2), features $M = P = 9$ and panels 3) show $M = P = 45$. The thin blue lines in the lower row represent the setup $M = 25, P = 45$.

advantage of using $M \ll P$ instead of $M = P$ for the average method. Thus the setup with $M = P$ is still considered in the following.

Starting with the description of the QM spectrum in Fig. 15, one recognizes a typical Franck-Condon progression with a maximal intensity that is located at the 0-0 transition. Switching to the approximations in panel 1a), the common DCL method neither yields the correct spectral shape nor the correct peak positions, as it has been observed before, see Refs. 93,94, [SK3] and Sec. 3.2. In contrast, the result obtained with the ACL method, see panel 1b), is in much better agreement with the QM one. However, a significant negative intensity below the 0-0 transition is present, which is again a consequence of the non-stationary dynamics featured by this method.

Employing more modes and beads, i.e. $M = P = 5$ in panels 1) of Fig. 15, the modified method still coincides with the Matsubara method although this is generally not expected for an anharmonic case. Both methods lead to a negative intensity to the left of the 0-0 transition, having a smaller amplitude than the one produced by the ACL and RPMD-like methods. For the latter, the average method, see panel 1b), performs significantly better than its equilibrium counterpart depicted in panel 1a).

Increasing M and P to nine improves the quality of the modified and the Matsubara method, which are still surprisingly similar, as it can be seen in panels 2) of Fig. 15. Nevertheless, as a consequence of the sign problem, the Matsubara method has required ten times more trajectories than the modified one to yield statistically converged results. Importantly, the artificial negativity is smaller by a factor of two than that for the case $M = P = 5$. The average version of the RPMD-like approach, see panel 2b), improves further with respect to the peak intensities, whereas the negative intensity has not changed notably. The opposite can be observed in panel 2a) for the equilibrium RPMD-like method, where the negativity is removed completely, whereas the overall agreement with the QM curve becomes worse.

It appears to be impossible to practically reach statistical convergence for the Matsubara method, if the number of beads and modes is increased to 45, even employing 10^6 trajectories and, thus, no results are shown. The average version of the RPMD-like method does not improve significantly in this case and the same can be observed for its equilibrium counterpart, see panels 3). The modified Matsubara method converges again without any issues, while coming quite close to the exact QM curve. Importantly, the artificial negativity vanishes almost completely. As it has been stated in the beginning of this subsection, there is no apparent advantage of setting $M = 25 < P = 45$ in comparison to $M = P = 45$ when considering the average methods, see the solid line in panel 3b). In contrast, the equilibrium method fails for $M < P$, as it can be seen in panel 3a).

To conclude, Matsubara and modified Matsubara methods nearly coincide for all cases, where the Matsubara method reaches statistical convergence. One can therefore expect for the general case that both would tend to very similar results in the limit $M, P \to \infty$. In comparison to the more common methods, i.e. DCL, ACL, as well as to the RPMD-like ansatz, the modified Matsubara method yields much more accurate results, especially with respect to the negativities below the 0-0 transition. Interestingly, setting $M < P$, that is compatible with the Matsubara approximation, does not yield any benefit in comparison to the case where $M = P$ if the average method is considered. However, this is by no means the ultimate conclusion and the impact of such a setup has to be investigated carefully, in particular using more complex systems featuring problems such as zero-point energy leakage.

4 Conclusions and outlook

This thesis is dedicated to bridging the gap between a numerically exact approach to vibronic spectra via wave-packet propagation and a purely static approximation via single-point calculations. For that purpose, a versatile formalism for simulating optical absorption spectra has been suggested. In contrast to common approaches to spectroscopy, that are mostly based on the Kubo-transformed time-correlation function (TCF), the presented formalism involves a generalized correlation function, having the Kubo TCF itself as well as various other known correlation functions as limiting cases. Beyond that, the formalism offers the possibility to construct in principle infinitely many new TCFs that might lead to superior numerical protocols if compared to the established ones. Practically, the generalization is done via employing an arbitrary weighting function and the imaginary-time shifted TCF, where the latter can be directly related to the desired vibronic absorption spectrum in the Fourier space. Employing this TCF as the starting point, the spectral amplitude has been approximated in the framework of classical(-like) trajectory-based methods, which is particularly challenging, since there is no classical analogue of the time evolution on multiple potential energy surfaces (PESs). However, this ansatz yielded several feasible simulation protocols that are capable to bridge the aforementioned gap.

In the spirit of the standard ring-polymer molecular dynamics (RPMD) method, the exact time evolution has been approximated by the quasi-classical dynamics of the ring polymer, thereby recovering important nuclear quantum effects. Importantly, in contrast to the existing RPMD ansatz for single-PES problems, the presented methodology features dynamics on several PESs simultaneously as an inherent feature of vibronic transitions. It has been demonstrated that the quasi-classical dynamics improves on the purely classical one, e.g. the dynamical classical limit (DCL), when employing commonly known TCFs such as the Kubo transformed. Moreover, by exploiting the flexibility of the generalized formalism, some of the results could be further improved upon choosing a more complicated weighting function form, i.e. the low-pass filter as well as the smoothed Schofield one. This elucidates the attractive possibilities provided by the generalized formalism and motivates searching for an optimal weighting function, suited for a specific problem or even for the general case. Ideally, finding such an optimum should be supported by a physical foundation, which, however, requires a general understanding that may be obtained via an extensive analysis for various complex systems in different parameter regimes.

It has been shown that the well-established DCL follows as a limiting case of the quasi-classical method by employing a particular weighting function. In that case, the nuclear dynamics is approximated by classical trajectories that are exclusively determined by the adiabatic ground-state PES, independently on the considered transition. This leads to a particularly simple numerical protocol that is readily applicable to non-linear spectra of more complex systems. However, the consequence is a loss of information about the excited-state

dynamics, leading to incorrect features in the simulated vibronic spectrum. Still, the comparison between the results obtained from the DCL and the statical classical limit (SCL) (i.e. the sampling), has been employed to identify and analyze vibronic transitions that are sensitive to nuclear dynamical effects. It has been exemplified for gas-phase and bulk water that the DCL recovers more information on X-ray spectra than the sampling approach, which is e.g. not capable to reproduce any vibronic progression. Moreover, it has turned out that the non-linear resonant inelastic X-ray scattering (RIXS) amplitude is much more sensitive to nuclear correlation effects than the linear X-ray absorption spectrum (XAS). This observation strongly suggests to extend the developed generalized formalism as well as the quasi-classical dynamics approximation to the realm of non-linear spectroscopy.

Although the presented quasi-classical method captures important nuclear quantum effects and is thus more accurate than a purely classical description, the ring-polymer dynamics suffers from artificial harmonic spring oscillations. This fact has motivated to approximate the imaginary-time shifted TCF alternatively via the Matsubara dynamics, which has led to a generalization of the existing single-PES methodology. Here, the quantum dynamics has been approximated via classical-like equations of motion (EOMs) for a smooth imaginary-time path that does not feature artificial spring motions. The developed expressions leave a great flexibility in choosing the particular potentials $\mathcal{V}_i$ and the generated dynamics, thereby providing an exciting perspective for future investigations. By employing two particular suggestions for the dynamics, the Matsubara ansatz formally restores the exact quantum TCF for a system consisting of two displaced harmonic oscillators. Importantly, this is in contrast to all aforementioned classical-like approximations and, thus, the suggested Matsubara method to simulate vibronic spectra represents a significant step towards the declared goal. Still, its direct practical application to complex systems is inhibited by the infamous sign problem, causing an insufficient statistical convergence. In order to circumvent this issue, a modified Matsubara method to simulate the standard correlation function has been deduced as an *ad-hoc* solution via a comparison of analytical expressions for a harmonic oscillator model system. This method has been demonstrated to yield absorption spectra that are of the same adequate quality as the ones obtained from the Matsubara dynamics approach, whereas the convergence behavior is excellent. Moreover, it has turned out that the modified method samples the thermal Wigner functions of the considered model systems accurately. Hence, this method is a promising starting point, not only for simulating vibronic spectra, but for classical-like approximations to nuclear quantum dynamics in general. However, due to numerical instabilities for concave regions of the potential, it remains to be seen if this *ad-hoc* method is applicable to arbitrary realistic systems. Since the suggested modification yields an adequate approximation to the standard TCF only, this method is not yet compatible with the generalized formalism. Thus, the ultimate goal would be to deduce a similar modification for the genuine imaginary-time shifted correlation function, which would enable to profit from the flexibility of generalized TCF

as well as from the quality of the approximated spectra. The derived Matsubara dynamics approximation to vibronic spectra may serve as a basis for such an attempt.

To conclude, by employing trajectory-based approaches to vibronic spectroscopy as the framework for this thesis, some of the most severe difficulties and deficiencies of the more common methods have been avoided. Thus, the developed formalisms represent a step forward to simulating spectroscopic observables of complex molecular systems via feasible and practical protocols. Offering on top exciting perspectives for future research, the presented methodologies are a valuable contribution to the realm of theoretical tools that may help physicists to obtain deeper insights into the fascinating world of molecular dynamics.

5 Bibliography

[1] S. MUKAMEL, *Principles of nonlinear optical spectroscopy*, Oxford University Press, Oxford, 1995.

[2] V. MAY and O. KÜHN, *Charge and energy transfer dynamics in molecular systems*, Wiley-VCH, Weinheim, 2011.

[3] P. HAMM and M. ZANNI, *Concepts and methods of 2D infrared spectroscopy*, Cambridge University Press, Cambridge, 2011.

[4] H. Y. HWANG, S. FLEISCHER, N. C. BRANDT, B. G. PERKINS JR., M. LIU, K. FAN, A. STERNBACH, X. ZHANG, R. D. AVERITT, and K. A. NELSON, A review of non-linear terahertz spectroscopy with ultrashort tabletop-laser pulses, *J. Mod. Opt* **62**, 1447 (2015).

[5] M. CHO, Coherent two-dimensional optical spectroscopy., *Chem. Rev.* **108**, 1331 (2008).

[6] C. MILNE, T. PENFOLD, and M. CHERGUI, Recent experimental and theoretical developments in time-resolved X-ray spectroscopies, *Coord. Chem. Rev.* **277-278**, 44 (2014).

[7] S. M. TEICHMANN, F. SILVA, S. L. COUSIN, M. HEMMER, and J. BIEGERT, 0.5-keV Soft X-ray attosecond continua, *Nat. Commun.* **7**, 11493 (2016).

[8] W. C. RÖNTGEN, Ueber eine neue Art von Strahlen, *Ann. Phys.* **300**, 1 (1898).

[9] A. KOTANI and S. SHIN, Resonant inelastic x-ray scattering spectra for electrons in solids, *Rev. Mod. Phys.* **73**, 203 (2001).

[10] J. D. BIGGS, Y. ZHANG, D. HEALION, and S. MUKAMEL, Two-dimensional stimulated resonance Raman spectroscopy of molecules with broadband x-ray pulses, *J. Chem. Phys.* **136**, 174117 (2012).

[11] S. MUKAMEL, D. HEALION, Y. ZHANG, and J. D. BIGGS, Multidimensional attosecond resonant X-ray spectroscopy of molecules: lessons from the optical regime, *Annu. Rev. Phys. Chem.* **64**, 101 (2013).

[12] A. NILSSON and L. PETTERSSON, Perspective on the structure of liquid water, *Chem. Phys.* **389**, 1 (2011).

[13] K. M. LANGE, A. KOTHE, and E. F. AZIZ, Chemistry in solution: recent techniques and applications using soft X-ray spectroscopy., *Phys. Chem. Chem. Phys.* **14**, 5331 (2012).

[14] L. WEINHARDT, M. BLUMC, O. FUCHS, A. BENKERT, F. MEYERB, M. BAR, J. D. DENLINGER, W. YANG, F. REINERT, and C. HESKE, RIXS investigations of liquids, solutions, and liquid/solid interfaces, *J. Electron Spectrosc.* **188**, 111 (2013).

[15] J. A. SELLBERG, T. A. MCQUEEN, H. LAKSMONO, S. SCHRECK, M. BEYE, D. P. DEPONTE, B. KENNEDY, D. NORDLUND, R. G. SIERRA, D. SCHLESINGER, T. TOKUSHIMA, I. ZHOVTOBRIUKH, S. ECKERT, V. H. SEGTNAN, H. OGASAWARA, K. KUBICEK, S. TECHERT, U. BERGMANN, G. L. DAKOVSKI, W. F. SCHLOTTER, Y. HARADA, M. J. BOGAN, P. WERNET, A. FÖHLISCH, L. G. M. PETTERSSON, and A. NILSSON, X-ray emission spectroscopy of bulk liquid water in "no-man's land", *J. Chem. Phys.* **142**, 044505 (2015).

[16] J. STÖHR, *NEXAFS spectroscopy*, volume 25, Springer Science & Business Media, Berlin, 2013.

[17] T. PFEIFER, C. SPIELMANN, and G. GERBER, Femtosecond x-ray science, *Rep. Prog. Phys.* **69**, 443 (2006).

[18] A. M. LINDENBERG, S. L. JOHNSON, and D. A. REIS, Visualization of Atomic-Scale Motions in Materials via Femtosecond X-Ray Scattering Techniques, *Annu. Rev. Mater. Res.* (2017).

[19] M. CHERGUI and E. COLLET, Photoinduced Structural Dynamics of Molecular Systems Mapped by Time-Resolved X-ray Methods, *Chem. Rev.* **117**, 11025 (2017).

[20] M. DUGUAY and P. RENTZEPIS, SOME APPROACHES TO VACUUM UV AND X-RAY LASERS, *Appl. Phys. Lett.* **10**, 350 (1967).

[21] M. PERLMAN, E. ROWE, and R. WATSON, Synchrotron radiation-light fantastic, *Phys. Today* **27**, 30 (1974).

[22] J. ULLRICH, A. RUDENKO, and R. MOSHAMMER, Free-electron lasers: new avenues in Mol. Phys. and photochemistry, *Annu. Rev. Phys. Chem.* **63**, 635 (2012).

[23] D. KONINGSBERGER and R. PRINS, *X-ray absorption: principles, applications, techniques of EXAFS, SEXAFS, and XANES*, John Wiley and Sons, New York, 1988.

[24] F. DE GROOT and A. KOTANI, *Core level spectroscopy of solids*, CRC press, Boca Raton, 2008.

[25] B. WINTER and M. FAUBEL, Photoemission from Liquid Aqueous Solutions, *Chem. Rev.* **106**, 1176 (2006).

[26] J. E. RUBENSSON, F. HENNIES, and A. PIETZSCH, High-resolution resonant inelastic soft x-ray scattering applied to liquids, *J. Electron Spectros.* **188**, 79 (2013).

[27] R. GUILLEMIN, S. CARNIATO, L. JOURNEL, W. C. STOLTE, T. MARCHENKO, L. E. KHOURY, E. KAWERK, M. N. PIANCASTELLI, A. C. HUDSON, D. W. LINDLE, and M. SIMON, A review of molecular effects in gas-phase KL X-ray emission, *J. Electron Spectros.* **188**, 53 (2013).

[28] F. HENNIES, S. POLYUTOV, I. MINKOV, A. PIETZSCH, M. NAGASONO, F. GEL'MUKHANOV, L. TRIGUERO, M.-N. PIANCASTELLI, W. WURTH, H. ÅGREN, and A. FÖHLISCH, Nonadiabatic effects in resonant inelastic x-ray scattering, *Phys. Rev. Lett.* **95**, 163002 (2005).

[29] M. P. LJUNGBERG, L. G. M. PETTERSSON, and A. NILSSON, Vibrational interference effects in x-ray emission of a model water dimer: Implications for the interpretation of the liquid spectrum, *J. Chem. Phys.* **134**, 044513 (2011).

[30] R. BOHINC, M. ŽITNIK, K. BUČAR, M. KAVČIČ, L. JOURNEL, R. GUILLEMIN, T. MARCHENKO, M. SIMON, and W. CAO, Dissociation of chloromethanes upon resonant σ_* excitation studied by x-ray scattering, *J. Chem. Phys.* **139**, 134302 (2013).

[31] A. PIETZSCH, Y.-P. SUN, F. HENNIES, Z. RINKEVICIUS, H. O. KARLSSON, T. SCHMITT, V. N. STROCOV, J. ANDERSSON, B. KENNEDY, J. SCHLAPPA, A. FÖHLISCH, J.-E. RUBENSSON, and F. GEL'MUKHANOV, Spatial quantum beats in vibrational resonant inelastic soft X-ray scattering at dissociating states in oxygen, *Phys. Rev. Lett.* **106**, 153004 (2011).

[32] F. HENNIES, A. PIETZSCH, M. BERGLUND, A. FÖHLISCH, T. SCHMITT, V. STROCOV, H. O. KARLSSON, J. ANDERSSON, and J.-E. RUBENSSON, Resonant inelastic scattering spectra of free molecules with vibrational resolution, *Phys. Rev. Lett.* **104**, 193002 (2010).

[33] W. DONG, H. WANG, M. M. OLMSTEAD, J. C. FETTINGER, J. NIX, H. UCHIYAMA, S. TSUTSUI, A. Q. R. BARON, E. DOWTY, and S. P. CRAMER, Inelastic X-ray scattering of a transition-metal complex ($FeCl_4^-$): vibrational spectroscopy for all normal modes, *Inorg. Chem.* **52**, 6767 (2013).

[34] K. M. LANGE and E. F. AZIZ, The hydrogen bond of water from the perspective of soft X-ray spectroscopy., *Chem. Asian J.* **8**, 318 (2013).

[35] S. SCHRECK, A. PIETZSCH, K. KUNNUS, B. KENNEDY, W. QUEVEDO, P. S. MIEDEMA, P. WERNET, and A. FÖHLISCH, Dynamics of the OH group and the electronic structure of liquid alcohols, *Struct. Dyn.* **1**, 054901 (2014).

[36] T. FRANSSON, Y. HARADA, N. KOSUGI, N. A. BESLEY, B. WINTER, J. J. REHR, L. G. M. PETTERSSON, and A. NILSSON, X-ray and electron spectroscopy of water, *Chem. Rev.* **116**, 7551 (2016).

[37] R. SCHINKE, *Photodissociation Dynamics*, Cambridge University Press, Cambridge, 1995.

[38] S. GRIMME, Calculation of the Electronic Spectra of Large Molecules, in *Rev. Comput. Chem.*, volume 20, chapter 3, pp. 153–218, John Wiley & Sons, Inc., 2004.

[39] C. J. CRAMER, *Essentials of computational chemistry: theories and models*, John Wiley & Sons, Chichester, 2013.

[40] W. KOCH and M. C. HOLTHAUSEN, *A chemist's guide to density functional theory*, John Wiley & Sons, Weinheim, 2015.

[41] L.-Å. NÄSLUND, M. CAVALLERI, H. OGASAWARA, A. NILSSON, L. G. M. PETTERSSON, P. WERNET, D. C. EDWARDS, M. SANDSTRÖM, and S. MYNENI, Direct evidence of orbital mixing between water and solvated transition-metal ions: an oxygen 1s XAS and DFT study of aqueous systems, *J. Phys. Chem. A* **107**, 6869 (2003).

[42] N. LEE, T. PETRENKO, U. BERGMANN, F. NEESE, and S. DEBEER, Probing valence orbital composition with iron Kß X-ray emission spectroscopy, *J. Am. Chem. Soc.* **132**, 9715 (2010).

[43] B. LASSALLE-KAISER, T. T. BORON, V. KREWALD, J. KERN, M. A. BECKWITH, M. U. DELGADO-JAIME, H. SCHROEDER, R. ALONSO-MORI, D. NORDLUND, T. C. WENG, D. SOKARAS, F. NEESE, U. BERGMANN, V. K. YACHANDRA, S. DEBEER, V. L. PECORARO, and J. YANO, Experimental and computational X-ray emission spectroscopy as a direct probe of protonation states in oxo-bridged MnIV dimers relevant to redox-active metalloproteins, *Inorg. Chem.* **52**, 12915 (2013).

[44] C. J. POLLOCK, K. GRUBEL, P. L. HOLLAND, and S. DEBEER, Experimentally quantifying small-molecule bond activation using valence-to-core X-ray emission spectroscopy, *J. Am. Chem. Soc.* **135**, 11803 (2013).

[45] C. D. SHERRILL and H. F. SCHAEFER III, The configuration interaction method: Advances in highly correlated approaches, in *Adv. Quantum Chem.*, volume 34, pp. 143–269, Elsevier, 1999.

[46] C. MØLLER and M. S. PLESSET, Note on an approximation treatment for many-electron systems, *Phys. Rev.* **46**, 618 (1934).

[47] J. ČÍŽEK, On the correlation problem in atomic and molecular systems. Calculation of wavefunction components in Ursell-type expansion using quantum-field theoretical methods, *J. Chem. Phys.* **45**, 4256 (1966).

[48] S. CORIANI, O. CHRISTIANSEN, T. FRANSSON, and P. NORMAN, Coupled-cluster response theory for near-edge x-ray-absorption fine structure of atoms and molecules, *Phys. Rev. A* **85**, 022507 (2012).

[49] P. A. MALMQVIST, A. RENDELL, and B. O. ROOS, The restricted active space self-consistent-field method, implemented with a split graph unitary group approach, *J. Phys. Chem.* **94**, 5477 (1990).

[50] S. I. BOKAREV, M. DANTZ, E. SULJOTI, O. KÜHN, and E. F. AZIZ, State-dependent electron delocalization dynamics at the solute-solvent interface: soft-x-ray absorption spectroscopy and Ab initio calculations, *Phys. Rev. letters* **111**, 083002 (2013).

[51] A. DREUW and M. WORMIT, The algebraic diagrammatic construction scheme for the polarization propagator for the calculation of excited states, *Wiley Interdiscip. Rev. Comput. Mol. Sci.* **5**, 82 (2015).

[52] D. R. REHN, A. DREUW, and P. NORMAN, Resonant Inelastic X-ray Scattering Amplitudes and Cross Sections in the Algebraic Diagrammatic Construction/Intermediate State Representation (ADC/ISR) Approach, *J. Chem. Theory Comput.* **13**, 5552 (2017).

[53] D. MAGANAS, S. DeBEER, and F. NEESE, Restricted Open-Shell Configuration Interaction Cluster Calculations of the L-Edge X-ray Absorption Study of TiO2 and CaF2 Solids, *Inorg. Chem.* **53**, 6374 (2014).

[54] E. J. HELLER, Photofragmentation of symmetric triatomic molecules: Time dependent picture, *J. Chem. Phys.* **68**, 3891 (1978).

[55] S.-Y. LEE and E. J. HELLER, Time-dependent theory of Raman scattering, *J. Chem. Phys.* **71**, 4777 (1979).

[56] K. GIESE, M. PETKOVIĆ, H. NAUNDORF, and O. KÜHN, Multidimensional quantum dynamics and infrared spectroscopy of hydrogen bonds, *Phys. Rep.* **430**, 211 (2006).

[57] M. WÄCHTLER, J. GUTHMULLER, L. GONZÁLEZ, and B. DIETZEK, Analysis and characterization of coordination compounds by resonance Raman spectroscopy, *Coord. Chem. Rev.* **256**, 1479 (2012).

[58] H.-D. MEYER, U. MANTHE, and L. S. CEDERBAUM, The multi-configurational time-dependent Hartree approach, *Chem. Phys. Lett.* **165**, 73 (1990).

[59] M. H. BECK, A. JÄCKLE, G. WORTH, and H.-D. MEYER, The multiconfiguration time-dependent Hartree (MCTDH) method: a highly efficient algorithm for propagating wavepackets, *Phys. Rep.* **324**, 1 (2000).

[60] H.-D. MEYER and G. A. WORTH, Quantum molecular dynamics: propagating wavepackets and density operators using the multiconfiguration time-dependent Hartree method, *Theor. Chem. Acc.* **109**, 251 (2003).

[61] H.-D. MEYER, F. GATTI, and G. A. WORTH, *Multidimensional Quantum Dynamics: MCTDH Theory and Applications*, Wiley-VCH, Weinheim, 2009.

[62] H.-D. MEYER, Studying molecular quantum dynamics with the multiconfiguration time-dependent Hartree method, *Wiley Interdiscip. Rev. Comput. Mol. Sci.* **2**, 351 (2012).

[63] R. ZWANZIG, *Nonequilibrium statistical mechanics*, Oxford University Press, New York, 2001.

[64] U. WEISS, *Quantum dissipative systems*, volume 13, World scientific, Singapore, 2012.

[65] M. SCHRÖTER, S. IVANOV, J. SCHULZE, S. POLYUTOV, Y. YAN, T. PULLERITS, and O. KÜHN, Exciton-vibrational coupling in the dynamics and spectroscopy of Frenkel excitons in molecular aggregates, *Phys. Rep.* **567**, 1 (2015).

[66] D. MARX and J. HUTTER, *Ab initio molecular dynamics: basic theory and advanced methods*, Cambridge University Press, Cambridge, 2009.

[67] M. ONČÁK, L. SCISTIK, and P. SLAVÍČEK, Can theory quantitatively model stratospheric photolysis? Ab initio estimate of absolute absorption cross sections of ClOOCl, *J. Chem. Phys.* **133** (2010).

[68] N. K. JENA, I. JOSEFSSON, S. K. ERIKSSON, A. HAGFELDT, H. SIEGBAHN, O. BJÖRNEHOLM, H. RENSMO, and M. ODELIUS, Solvent-dependent structure of the I_3^- ion derived from photoelectron spectroscopy and ab initio molecular dynamics simulations, *Chem. Eur. J.* **21**, 4049 (2015).

[69] L. WEINHARDT, E. ERTAN, M. IANNUZZI, M. WEIGAND, O. FUCHS, M. BÄR, M. BLUM, J. D. DENLINGER, W. YANG, E. UMBACH, M. ODELIUS, and C. HESKE, Probing hydrogen bonding orbitals: resonant inelastic soft X-ray scattering of aqueous NH 3, *Phys. Chem. Chem. Phys.* **17**, 27145 (2015).

[70] R. P. FEYNMAN and A. R. HIBBS, *Quantum Mechanics and Path Integrals*, McGraw-Hill, New-York, 1965.

[71] D. MARX and M. PARRINELLO, Ab initio path integral molecular dynamics: Basic ideas, *J. Chem. Phys.* **104**, 4077 (1996).

[72] C. P. SCHWARTZ, J. S. UEJIO, R. J. SAYKALLY, and D. PRENDERGAST, On the importance of nuclear quantum motions in near edge x-ray absorption fine structure spectroscopy of molecules, *J. Chem. Phys.* **130**, 184109 (2009).

[73] J. C. TULLY and R. K. PRESTON, Trajectory Surface Hopping Approach to Nonadiabatic Molecular Collisions: The Reaction of H^+ with D_2, *J. Chem. Phys.* **55**, 562 (1971).

[74] F. PLASSER, R. CRESPO-OTERO, M. PEDERZOLI, J. PITTNER, H. LISCHKA, and M. BARBATTI, Surface hopping dynamics with correlated single-reference methods: 9H-adenine as a case study, *J. Chem. Theory Comput.* **10**, 1395 (2014).

[75] M. BARBATTI, M. RUCKENBAUER, F. PLASSER, J. PITTNER, G. GRANUCCI, M. PERSICO, and H. LISCHKA, Newton-X: a surface-hopping program for nonadiabatic molecular dynamics, *Wiley Interdiscip. Rev. Comput. Mol. Sci.* **4**, 26 (2014).

[76] J. C. TULLY, Mixed quantum-classical dynamics, *Faraday Discuss.* **110**, 407 (1998).

[77] M. BEN-NUN, J. QUENNEVILLE, and T. J. MARTÍNEZ, Ab Initio Multiple Spawning: Photochemistry from First Principles Quantum Molecular Dynamics, *J. Phys. Chem. A* **104**, 5161 (2000).

[78] B. G. LEVINE and T. J. MARTÍNEZ, Isomerization Through Conical Intersections, *Annu. Rev. Phys. Chem.* **58**, 613 (2007).

[79] G. A. WORTH, M. A. ROBB, and I. BURGHARDT, A novel algorithm for non-adiabatic direct dynamics using variational Gaussian wavepackets, *Faraday Discuss.* **127**, 307 (2004).

[80] G. W. RICHINGS and G. A. WORTH, Multi-state non-adiabatic direct-dynamics on propagated diabatic potential energy surfaces, *Chem. Phys. Lett.* (2017).

[81] H.-D. MEYER and W. H. MILLER, A classical analog for electronic degrees of freedom in nonadiabatic collision processes, *J. Chem. Phys.* **70**, 3214 (1979).

[82] G. STOCK and M. THOSS, Semiclassical Description of Nonadiabatic Quantum Dynamics, *Phys. Rev. Lett.* **78**, 578 (1997).

[83] S. BONELLA and D. F. COKER, Semi-classical implementation of mapping Hamiltonian methods for general non-adiabatic problems, *Chem. Phys.* **268**, 189 (2001).

[84] A. ABEDI, N. T. MAITRA, and E. K. U. GROSS, Exact Factorization of the Time-Dependent Electron-Nuclear Wave Function, *Phys. Rev. Lett.* **105**, 123002 (2010).

[85] F. AGOSTINI, S. K. MIN, A. ABEDI, and E. K. U. GROSS, Quantum-Classical Nonadiabatic Dynamics: Coupled- vs Independent-Trajectory Methods, *J. Chem. Theory Comput.* **12**, 2127 (2016).

[86] B. F. CURCHOD and I. TAVERNELLI, On trajectory-based nonadiabatic dynamics: Bohmian dynamics versus trajectory surface hopping, *J. Chem. Phys.* **138**, 184112 (2013).

[87] G. STOCK and M. THOSS, Classical Description of Nonadiabatic Quantum Dynamics, *Adv. Chem. Phys.* **131**, 243 (2005).

[88] J. C. TULLY, Perspective: Nonadiabatic dynamics theory, *J. Chem. Phys.* **137**, 22A301 (2012).

[89] I. TAVERNELLI, Nonadiabatic Molecular Dynamics Simulations: Synergies between Theory and Experiments, *Acc. Chem. Res.* **48**, 792 (2015).

[90] C. LAWRENCE and J. SKINNER, Vibrational spectroscopy of HOD in liquid D_2O. II. Infrared line shapes and vibrational Stokes shift, *J. Chem. Phys.* **117**, 8847 (2002).

[91] E. HARDER, J. D. EAVES, A. TOKMAKOFF, and B. BERNE, Polarizable molecules in the vibrational spectroscopy of water, *Proc. Nat. Acad. Sci.* **102**, 11611 (2005).

[92] S. D. IVANOV, A. WITT, and D. MARX, Theoretical spectroscopy using molecular dynamics: theory and application to CH5(+) and its isotopologues., *Phys. Chem. Chem. Phys.* **15**, 10270 (2013).

[93] S. A. EGOROV, E. RABANI, and B. J. BERNE, Vibronic spectra in condensed matter: A comparison of exact quantum mechanical and various semiclassical treatments for harmonic baths, *J. Chem. Phys.* **108**, 1407 (1998).

[94] E. RABANI, S. A. EGOROV, and B. J. BERNE, A comparison of exact quantum mechanical and various semiclassical treatments for the vibronic absorption spectrum: The case of fast vibrational relaxation, *J. Chem. Phys.* **109**, 6376 (1998).

[95] S. D. IVANOV, O. ASVANY, A. WITT, E. HUGO, G. MATHIAS, B. REDLICH, D. MARX, and S. SCHLEMMER, Quantum-induced symmetry breaking explains infrared spectra of CH5+ isotopologues, *Nat. Chem.* **2**, 298 (2010).

[96] A. WITT, S. D. IVANOV, and D. MARX, Microsolvation-Induced Quantum Localization in Protonated Methane, *Phys. Rev. Lett.* **110**, 083003 (2013).

[97] M. H. M. OLSSON, P. E. M. SIEGBAHN, and A. WARSHEL, Simulations of the large kinetic isotope effect and the temperature dependence of the hydrogen atom transfer in lipoxygenase., *J. Am. Chem. Soc.* **126**, 2820 (2004).

[98] J. GAO and D. G. TRUHLAR, Quantum Mechanical Methods for Enzyme Kinetics, *Annu. Rev. Phys. Chem.* **53**, 467 (2002).

[99] N. E. SHEMETULSKIS and R. F. LORING, Semiclassical theory of the photon echo: application to polar fluids, *J. Chem. Phys.* **97**, 1217 (1992).

[100] Q. SHI and E. GEVA, A comparison between different semiclassical approximations for optical response functions in nonpolar liquid solutions., *J. Chem. Phys.* **122**, 064506 (2005).

[101] Q. SHI and E. GEVA, A comparison between different semiclassical approximations for optical response functions in nonpolar liquid solution. II. The signature of excited state dynamics on two-dimensional spectra., *J. Chem. Phys.* **129**, 124505 (2008).

[102] L. SCHULMAN, *Techniques and Applications of Path Integration*, Dover Publications, Inc., Mineola, New York, 2005.

[103] M. E. TUCKERMAN, *Statistical mechanics: theory and molecular simulation*, Oxford University Press, Oxford, 2010.

[104] I. R. CRAIG and D. E. MANOLOPOULOS, Quantum statistics and classical mechanics: real time correlation functions from ring polymer molecular dynamics., *J. Chem. Phys.* **121**, 3368 (2004).

[105] S. HABERSHON, D. E. MANOLOPOULOS, T. E. MARKLAND, and T. F. MILLER III, Ring-polymer molecular dynamics: quantum effects in chemical dynamics from classical trajectories in an extended phase space, *Annu. Rev. Phys. Chem.* **64**, 387 (2013).

[106] M. CERIOTTI, W. FANG, P. G. KUSALIK, R. H. MCKENZIE, A. MICHAELIDES, M. A. MORALES, and T. E. MARKLAND, Nuclear Quantum Effects in Water and Aqueous Systems: Experiment, Theory, and Current Challenges, *Chem. Rev.* **116**, 7529 (2016).

[107] J. O. RICHARDSON and M. THOSS, Communication: Nonadiabatic ring-polymer molecular dynamics, *J. Chem. Phys.* **139**, 031102 (2013).

[108] N. ANANTH, Mapping variable ring polymer molecular dynamics: A path-integral based method for nonadiabatic processes, *J. Chem. Phys.* **139**, 124102 (2013).

[109] M. THOSS and G. STOCK, Mapping approach to the semiclassical description of nonadiabatic quantum dynamics, *Phys. Rev. A* **59**, 64 (1999).

[110] J. O. RICHARDSON, P. MEYER, M.-O. PLEINERT, and M. THOSS, An analysis of nonadiabatic ring-polymer molecular dynamics and its application to vibronic spectra, *Chem. Phys.* **482**, 124 (2016).

[111] C. D. SCHWIETERS and G. A. VOTH, Extension of path integral quantum transition state theory to the case of nonadiabatic activated dynamics, *J. Chem. Phys.* **111**, 2869 (1999).

[112] M. H. ALEXANDER, Path-integral simulation of finite-temperature properties of systems involving multiple, coupled electronic states, *Chem. Phys. Lett.* **347**, 436 (2001).

[113] J. SCHMIDT and J. C. TULLY, Path-integral simulations beyond the adiabatic approximation, *J. Chem. Phys.* **127**, 094103 (2007).

[114] P. SHUSHKOV, R. LI, and J. C. TULLY, Ring polymer molecular dynamics with surface hopping, *J. Chem. Phys.* **137**, 22A549 (2012).

[115] J. LU and Z. ZHOU, Path integral molecular dynamics with surface hopping for thermal equilibrium sampling of nonadiabatic systems, *J. Chem. Phys.* **146**, 154110 (2017).

[116] R. RAMIREZ, T. LÓPEZ-CIUDAD, P. KUMAR P, and D. MARX, Quantum corrections to classical time-correlation functions: hydrogen bonding and anharmonic floppy modes., *J. Chem. Phys.* **121**, 3973 (2004).

[117] A. WITT, S. D. IVANOV, M. SHIGA, H. FORBERT, and D. MARX, On the applicability of centroid and ring polymer path integral molecular dynamics for vibrational spectroscopy., *J. Chem. Phys.* **130**, 194510 (2009).

[118] T. J. H. HELE, M. J. WILLATT, A. MUOLO, and S. C. ALTHORPE, Boltzmann-conserving classical dynamics in quantum time-correlation functions: "Matsubara dynamics", *J. Chem. Phys.* **142**, 134103 (2015).

[119] T. J. HELE, M. J. WILLATT, A. MUOLO, and S. C. ALTHORPE, Communication: Relation of centroid molecular dynamics and ring-polymer molecular dynamics to exact quantum dynamics, *J. Chem. Phys.* **142**, 191101 (2015).

[120] T. J. HELE, On the relation between thermostatted ring-polymer molecular dynamics and exact quantum dynamics, *Mol. Phys.* **114**, 1461 (2016).

[121] M. ROSSI, M. CERIOTTI, and D. E. MANOLOPOULOS, How to remove the spurious resonances from ring polymer molecular dynamics., *J. Chem. Phys.* **140**, 234116 (2014).

[122] J. CAO and G. A. VOTH, A new perspective on quantum time correlation functions, *J. Chem. Phys.* **99**, 10070 (1993).

[123] H. KRAMERS and W. HEISENBERG, Über die Streuung von Strahlung durch Atome, in *Original Scientific Papers Wissenschaftliche Originalarbeiten*, pp. 354–381, Springer, 1985.

[124] T. CARLSON, *Photoelectron and Auger spectroscopy*, Springer Science & Business Media, New York, 2013.

[125] R. KUBO, Statistical-mechanical theory of irreversible processes. I. General theory and simple applications to magnetic and conduction problems, *J. Phys. Soc. Jpn.* **12**, 570 (1957).

[126] G. BUSSI and M. PARRINELLO, Accurate sampling using Langevin dynamics, *Phys. Rev. E* **75**, 056707 (2007).

[127] P. SCHOFIELD, Space-Time Correlation Function Formalism for Slow Neutron Scattering, *Phys. Rev. Lett.* **4**, 239 (1960).

[128] S. HABERSHON, T. E. MARKLAND, and D. E. MANOLOPOULOS, Competing quantum effects in the dynamics of a flexible water model, *J. Chem. Phys.* **131**, 024501 (2009).

[129] E. WIGNER, On the Quantum Correction For Thermodynamic Equilibrium, *Phys. Rev.* **40**, 749 (1932).

[130] A. M. DE ALMEIDA, The Weyl representation in classical and quantum mechanics, *Phys. Rep.* **295**, 265 (1998).

[131] K. K. SMITH, J. A. POULSEN, G. NYMAN, and P. J. ROSSKY, A new class of ensemble conserving algorithms for approximate quantum dynamics: Theoretical formulation and model problems, *J. Chem. Phys.* **142**, 244112 (2015).

[132] L. WEINHARDT, A. BENKERT, F. MEYER, M. BLUM, R. G. WILKS, W. YANG, M. BÄR, F. REINERT, and C. HESKE, Nuclear dynamics and spectator effects in resonant inelastic soft x-ray scattering of gas-phase water molecules., *J. Chem. Phys.* **136**, 144311 (2012).

[133] F. PAESANI, W. ZHANG, D. A. CASE, T. E. CHEATHAM, and G. A. VOTH, An accurate and simple quantum model for liquid water., *J. Chem. Phys.* **125**, 184507 (2006).

[134] S. D. IVANOV, A. WITT, M. SHIGA, and D. MARX, Communications: On artificial frequency shifts in infrared spectra obtained from centroid molecular dynamics: Quantum liquid water., *J. Chem. Phys.* **132**, 031101 (2010).

A Own contributions to the manuscripts

Peer reviewed publications

[SK1]: SVEN KARSTEN, SERGEI D. IVANOV, SAADULLAH G. AZIZ, SERGEY I. BOKAREV, and OLIVER KÜHN, Nuclear Dynamical Correlation Effects in X-ray Spectroscopy from a Theoretical Time-Domain Perspective, *Journal of Physical Chemistry Letters* **8**, 992 (2017)
My contribution: I have developed the working expressions leading to the numerical protocol that has been implemented by me. I have performed the numerical simulations and produced the presented figures. I have drafted the article after the results have been interpreted together with the coauthors. Subsequently, the text has been iterated to its final form by me and the coauthors.

[SK2]: SVEN KARSTEN, SERGEY I. BOKAREV, SAADULLAH G. AZIZ, SERGEI D. IVANOV, and OLIVER KÜHN, A time-correlation function approach to nuclear dynamical effects in X-ray spectroscopy, *Journal of Chemical Physics* **146**, 224203 (2017)
My contribution: Using the protocol developed in [SK1], I have performed all numerical simulations and produced the presented figures. I have interpreted the results, drafted the article and iterated the text to its final stage together with the coauthors.

[SK3]: SVEN KARSTEN, SERGEI D. IVANOV, SERGEY I. BOKAREV, and OLIVER KÜHN, Quasiclassical approaches to vibronic spectra revisited, *Journal of Chemical Physics* **148**, 102337 (2018)
My contribution: I have developed the employed theoretical expressions leading to the presented numerical protocol that has been implemented by me. I have performed the numerical simulations and produced the figures. Together with the coauthors, I have interpreted the results, drafted the article and iterated the text.

Additional manuscripts

[SK4]: SVEN KARSTEN, SERGEI D. IVANOV, SERGEY I. BOKAREV, and OLIVER KÜHN, Simulating vibronic spectra via Matsubara dynamics: coping with the sign problem, *arXiv:* 1805.06195 [physics.chem-ph] (2018)
My contribution: I have derived the presented theoretical expressions and implemented the resulting numerical methods. I have performed the numerical simulations and created the figures. After interpreting the results, I have drafted the text iterated it to its final stage together with the coauthors.

B Peer reviewed publications

[SK1] Nuclear Dynamical Correlation Effects in X-ray Spectroscopy from a Theoretical Time-Domain Perspective

SVEN KARSTEN, SERGEI D. IVANOV, SAADULLAH G. AZIZ, SERGEY I. BOKAREV, and OLIVER KÜHN

Reprinted with permission from S. KARSTEN, S. D. IVANOV, S. G. AZIZ, S. I. BOKAREV, and O. KÜHN, *Journal of Physical Chemistry Letters* **8**, 992 (2017).

THE JOURNAL OF PHYSICAL CHEMISTRY Letters

Letter

pubs.acs.org/JPCL

Nuclear Dynamical Correlation Effects in X-ray Spectroscopy from a Theoretical Time-Domain Perspective

Sven Karsten,[†] Sergei D. Ivanov,*[,†] Saadullah G. Aziz,[‡] Sergey I. Bokarev,*[,†] and Oliver Kühn[†]

[†]Institute of Physics, University of Rostock, Albert-Einstein-Str. 23-24, 18059 Rostock, Germany

[‡]Chemistry Department, Faculty of Science, King Abdulaziz University, 21589 Jeddah, Saudi Arabia

Supporting Information

ABSTRACT: To date X-ray spectroscopy has become a routine tool that can reveal highly local and element-specific information on the electronic structure of atoms in complex environments. Here, we focus on nuclear dynamical correlation effects in X-ray spectra and develop a rigorous time-correlation function method employing ground state classical molecular dynamics simulations. The importance of nuclear correlation phenomena is demonstrated by comparison against the results from the conventional sampling approach performed on the same data set for gas phase water. In contrast to the first-order absorption, second-order resonant inelastic scattering spectra exhibit pronounced fingerprints of nuclear motions. The developed methodology is not biased to a particular electronic structure method and, owing to its generality, can be applied to, e.g., X-ray photoelectron and Auger spectroscopies.

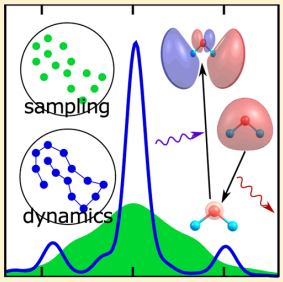

Constant increase in spectral resolution and rapid development of various spectroscopies, covering broad energy ranges from radio frequencies to extra hard radiation, open new horizons for molecular science to investigate more and more intricate phenomena. When it comes to obtaining highly local and element-specific information on the electronic structure, X-ray spectroscopies stand out.[1] Popular variants include first-order X-ray absorption spectra (XAS) and second-order resonant inelastic X-ray scattering (RIXS) techniques. The former focuses on the electronic transitions where a core electron is excited to the manifold of unoccupied molecular orbitals (MOs), whereas the latter detects the emission signal resulting from a refill of a core-hole by electrons occupying valence MOs. Although X-ray spectroscopy usually targets electronic transitions, the vibrational ones as well as the accompanying nuclear dynamics have recently received growing attention.[2−9] Remarkably, the RIXS spectra of liquid water and alcohols initiated active ongoing debates in the past decade,[10−12] with controversial interpretations, among others, involving different aspects of nuclear dynamics; see ref 13 for a review.

From a theoretical standpoint, there exist two strategies to simulate electronic spectra. Clearly, the best approach possible is to perform wavepacket quantum dynamics numerically exactly.[14−17] However, it is limited to small systems and requires expensive precomputation of many-dimensional potential energy surfaces for typically large numbers of highly excited electronic states relevant for X-ray spectra. Any attempt to apply it to large systems can only be made feasible via a reduction of dimensionality, that is, by introducing low-dimensional models, which could be a severe approximation on its own.

The other approach is to treat the system in question in full complexity and to perform single point electronic structure calculations combined with models such as the multimode Brownian oscillator one to include broadening on a phenomenological level.[18] A substantial improvement is to sample nuclear distributions in the phase space via molecular dynamics (MD) methods,[19−21] leading to a more realistic description of conformational and environmental effects[22−25] although lacking information about correlated nuclear motion. Here we propose an extension of this state-of-the-art approach to XAS and RIXS spectra based on time-correlation functions obtained from the time evolution provided by electronic ground-state MD simulations, analogous to infrared and UV−vis spectroscopies.[18,21,26−29] Being a representative of trajectory-based methods, which became extremely popular in theoretical physical chemistry in the last decades, it even opens the possibility to incorporate nuclear quantum effects.[20,30]

At first glance it might appear that the ultrafast core-hole dynamics triggered by an X-ray excitation should be essentially decoupled from the nuclear dynamics, which takes place on time scales longer than 10 fs. In other words, sampling uncorrelated nuclear distributions should be sufficient for the purpose of X-ray spectroscopy. However, the central message of this Letter is that this is not the case; that is, nuclear correlation effects can play a significant role for the proper description of lineshapes. We exemplify this on oxygen K-edge spectra of gas-phase water by comparison against the results of the aforementioned sampling approach on the same data set.

Received: January 6, 2017
Accepted: February 3, 2017
Published: February 3, 2017

DOI: 10.1021/acs.jpclett.7b00037
J. Phys. Chem. Lett. 2017, 8, 992−996

We would like to stress that we are not aiming at the peculiarities of the water spectra and rather use water as a convenient model system to study nuclear correlation effects. Importantly, only RIXS, being a second-order process, appears sensitive to them, much like nonlinear optical spectra provide more detailed insight into the underlying dynamical processes.[18,19]

Theory. The XAS process consists of exciting the system from an initial state $|g\rangle$ to a final core-excited state $|f\rangle$ by absorbing light with angular frequency Ω and polarization e; see left panel in Figure 1. Similarly, in RIXS the system is first excited to a

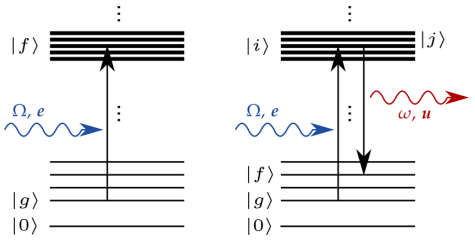

Figure 1. Schematic sketch of XAS (left) and RIXS (right) processes, see text.

core-excited intermediate state $|i\rangle$ or $|j\rangle$ and then transits to the valence final state $|f\rangle$ by emitting light with the frequency ω and polarization u; see right panel therein.

The derivation of the spectral amplitudes corresponding to both processes, taking explicit correlated nuclear dynamics into account, is sketched below; see the Supporting Information for a complete derivation. The starting point for the XAS amplitude, $\mathcal{X}(\Omega)$, is the Fourier-transformed linear response function.[18] The time evolution of the transition dipole moments involved is exactly recast with respect to the electronic ground state via the interaction representation. As a consequence, the electronic energy gaps between the ground state and the other states appear in the formalism. To develop a practical recipe involving classical MD methods, the dynamical classical limit is taken for the nuclear degrees of freedom. Finally, the resulting XAS amplitude possesses the form of the Fourier transform of a time-correlation function being a classical canonical average with respect to the electronic ground state Hamilton function, H_0.

The same steps are undertaken to derive the RIXS amplitude, $\mathcal{R}(\Omega, \omega)$. However, the starting point here is the Raman part of the spontaneous light emission signal expressed via the corresponding third-order response function. Note that the lifetimes of the intermediate states due to Auger process are introduced phenomenologically via a monoexponential decay and are assumed to depend on the corresponding electronic level only.

The final expressions for the spectral amplitudes in atomic units read

$$\mathcal{X}(\Omega) = \int_{-\infty}^{\infty} \mathrm{d}t\ \mathrm{e}^{\mathrm{i}\Omega t} \langle \mathcal{W}_g(0) M_f^{g\eta}(t) e_\eta e^{\xi} M_{\xi g}^{f}(0) \rangle \tag{1}$$

and

$$\begin{aligned} \mathcal{R}(\Omega, \omega) = & \int_{-\infty}^{\infty} \mathrm{d}t\ \mathrm{e}^{\mathrm{i}\Omega t} \int_{-\infty}^{\infty} \mathrm{d}\tau_1\ \mathrm{e}^{-\mathrm{i}\omega(t+\tau_1)} \int_{-\infty}^{\infty} \mathrm{d}\tau_2\ \mathrm{e}^{\mathrm{i}\omega\tau_2} \\ & \times \langle \mathcal{W}_g(0) M_j^{g\zeta}(t) e_\zeta \Delta_j(\tau_1) u^\nu M_{\nu f}^{j}(t+\tau_1) \\ & \times M_i^{f\eta}(\tau_2) u_\eta \Delta_i(\tau_2) e^{\xi} M_{\xi g}^{i}(0) \rangle \end{aligned} \tag{2}$$

where Greek letters stand for Cartesian components of the respective vectors and Einstein notation for summing over indices that appear in sub- and superscript is implied. Here the "dressed" transition dipole moments are introduced as

$$M_{\xi g}^{f}(t) := D_{\xi g}^{f}(t) \exp[\mathrm{i} \int_0^t \mathrm{d}\tau\ \Delta E_{fg}(\tau)] \tag{3}$$

where $D_{\xi g}^{f}$ are the elements of the transition dipole moment vectors from $|g\rangle$ to $|f\rangle$ and $\Delta E_{fg}(\tau)$ is the respective electronic energy gap, time-evolved with respect to H_0. Furthermore, $\Delta_i(\tau) := \theta(\tau) \exp[-\Gamma_i \tau]$ is the damping function, where Γ_i is the lifetime broadening of the intermediate state $|i\rangle$ and $\theta(\tau)$ is the Heaviside step function. Additionally, the spectra are convoluted with a Gaussian of width σ along the Ω axis to account for the bandwidth of the excitation pulse. Finally, the weighting function is defined as

$$\mathcal{W}_g(t) := \mathrm{e}^{-\Delta E_{g0}(t)/k_\mathrm{B}T} / \langle \sum_g \mathrm{e}^{-\Delta E_{g0}(0)/k_\mathrm{B}T} \rangle \tag{4}$$

with k_B being the Boltzmann constant and $\langle ... \rangle$ here and in eqs 1 and 2 standing for the classical canonical average with respect to H_0. We note in passing that eqs 1 and 2 can be derived starting from the Fermi's Golden rule and the Kramers–Heisenberg expression, respectively.[31] Note further that from the practical standpoint it is more convenient to evaluate eqs 1 and 2 in the frequency domain, as explained in detail in the Supporting Information. Importantly, this transformation changes a coupled multitime integral in eq 2 into decoupled single-variable integrations.

Computational Details. The MD simulations have been performed using Gromacs version 4.6.5,[33] employing the anharmonic qSPC/Fw water model with a Morse O–H potential.[34] A set of 140 uncorrelated initial conditions has been sampled from an *NVT* MD run at 300 K further serving as starting points for *NVE* trajectories. The trajectories have been 0.5 ps long with a time step of 0.5 fs, yielding a spectral resolution of ~8 meV. The electronic Schrödinger equation for each MD snapshot has been solved via ground-state density functional theory with the PBE functional[35] using ORCA version 3.0.3.[36] The def2-QZVPP basis set[37] together with (5s5p)/[1s1p] generally contracted Rydberg functions on oxygen have been used. Such a small Rydberg basis does not allow one to reproduce the high-energy tail of the absorption spectrum[38] but enables the description of the lowest states just above the core-excitation threshold. The energies of the valence and core-excited states have been approximated by the differences of the respective Kohn–Sham orbital energies; the corresponding dipole transition moments have been calculated with respect to these orbitals.[39] This approximation is known to yield a reasonable compromise between accuracy and efficiency.[2,38−41] Note that the separation between the electronic states makes nonadiabatic effects negligible. To preserve the continuous time evolution of the dressed dipoles, the entire manifold of relevant electronic levels has been traced along the MD trajectories in a fully automated manner.[31] The excitation Gaussian line width and the uniform Lorentzian lifetime broadening have been chosen as σ = 0.05 eV and Γ =

DOI: 10.1021/acs.jpclett.7b00037
J. Phys. Chem. Lett. 2017, 8, 992−996

0.25 fs^{-1}, respectively.[42,43] The data have been averaged over the molecular orientations assuming the orthogonality of e and u, which corresponds to a typical experimental setup, and the spectra have been shifted *globally* by 24.8 eV on the absorption axis and 23.3 eV on the emission axis such that the peak structure roughly matches the experimental data.[32,44] Note that both the sampling and time-correlation approaches employ the same data sets for the consistency of comparison. For further computational details, see the Supporting Information.

Results. The XAS amplitudes (Figure 2) are in fairly good agreement with the experimental data[32] shown as the black solid line. We would like to reiterate that we do not aim at quantitatively reproducing and analyzing experimental data with the rather simple model employed. Instead, the focus is on the nuclear correlation effects, manifesting themselves as the differences between the results of the sampling and correlation approaches.

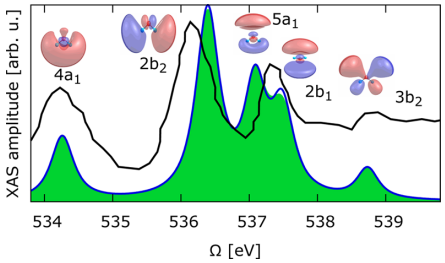

Figure 2. XAS amplitudes for gas phase water. The black line represents the respective experimental data from ref 32. The blue line depicts the time-correlation approach results according to eq 1, whereas the filled green curve corresponds to the sampling method. The unoccupied MOs to which the transition is performed are shown and assigned near the respective spectral peaks.

The first two absorption peaks in Figure 2 correspond to the $1s_O \rightarrow \sigma^*(2s)$ $[1a_1 \rightarrow 4a_1]$ and $1s_O \rightarrow \sigma^*(2p)$ $[1a_1 \rightarrow 2b_2]$ transitions, whereas the other three stem from the Rydberg $1s_O \rightarrow 3p_O$ $[1a_1 \rightarrow 5a_1, 2b_1, 3b_2]$ ones, as is illustrated by the target unoccupied MOs displayed near the respective spectral peaks therein. Apparently, XAS amplitudes feature only subtle differences in intensities between the sampling and the correlation approach. This suggests that XAS is not a very sensitive observable for nuclear correlation effects.

Figure 3 shows a 2D RIXS spectrum obtained via the correlation approach, eq 2. Although it gives an overall impression about the spectral shape, it is hard to make quantitative analysis on its basis. Therefore, we consider a particular cut for a fixed excitation frequency $\Omega = 536.4$ eV that corresponds to the $1s_O \rightarrow \sigma^*(2p)$ $[1a_1 \rightarrow 2b_2]$ XAS transition, see Figure 2 and vertical line in Figure 3. Three spectral ranges marked with horizontal lines in Figure 3 are shown in Figure 4. They contain peaks related to transitions from the intermediate (core-excited) states to final (ground or valence-excited) ones; see the respective orbitals from which the core-hole refill takes place. Despite the simple electronic structure method employed, the RIXS results also qualitatively reproduce experimental data; see black solid line in panel b.[44] Note that the experimental data corresponding to those in panels a and c are not available to us.

Most importantly, the RIXS spectrum obtained via the time-correlation approach exhibits clear traces of nuclear dynamical

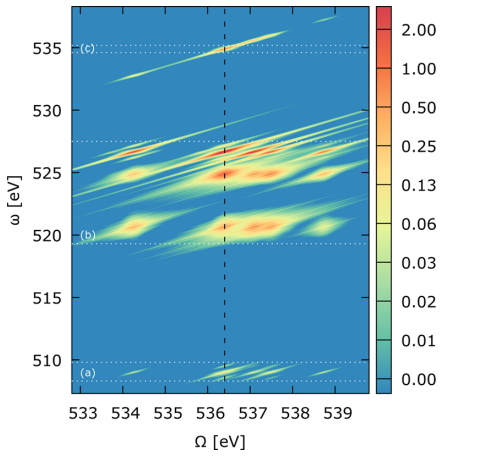

Figure 3. 2D RIXS spectrum, $\mathcal{R}(\Omega, \omega)$, of gas-phase water obtained by means of the time-correlation approach, eq 2; note the log scale for intensities depicted with color. The dashed vertical line indicates the position of the cut depicted in Figure 4. The three pairs of dotted horizontal lines indicate the three spectral regions corresponding to panels a–c in Figure 4.

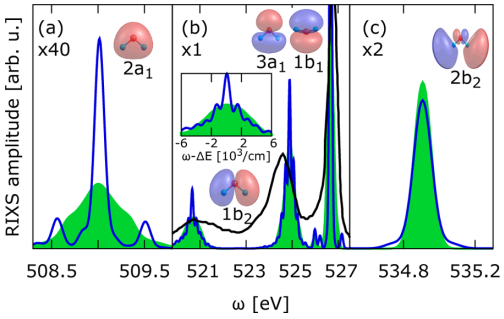

Figure 4. Cut-through RIXS spectrum in Figure 3 at $\Omega = 536.4$ eV. The color code is the same as in Figure 2. Panels depict three relevant spectral ranges. The black line represents the respective experimental data from ref 24. Inset zooms on the left peak in panel b that corresponds to $\sigma(2p) \rightarrow 1s_O$ $[1b_2 \rightarrow 1a_1]$ transition with $\Delta E = 520.7$ eV.

effects as compared with the sampling one. First, the two spectra possess notably different lineshapes. For instance, the vibronic structure, which is not present in the sampling spectra by construction, is clearly visible for inelastic features in Figure 4a,b. In particular, the sidebands for peaks at 509.0 and 526.7 eV correspond to the O–H stretching mode with the frequency 3800 cm^{-1} ≈ 0.47 eV. Furthermore, the electronic transitions at 520.7 (see inset) and 524.9 eV are coupled to the bending vibrational mode having the frequency of ≈ 1500 cm^{-1}.

Second, the sampling approach exhibits higher intensity of the elastic peak (Figure 4c) and lower intensities of the inelastic ones with respect to the correlation method, although both techniques employ the same statistics. The origin of the differences in intensities can be mainly traced back to the complex exponential of the gap fluctuations in the dressed transition dipoles (see eq 3), as shown in detail elsewhere.[31] Since the expression in eq 2 contains energy gap fluctuations

DOI: 10.1021/acs.jpclett.7b00037
J. Phys. Chem. Lett. 2017, 8, 992–996

between *different* pairs of electronic states, we believe that this makes RIXS spectra more sensitive to nuclear dynamical correlation effects. In contrast, the absorption spectrum, eq 1, depends only on the initial−final gap fluctuations.

Conclusions and Outlook. A simulation protocol allowing for nuclear correlation phenomena in X-ray spectra has been developed. This rigorously derived method intrinsically exploits classical molecular dynamics in the electronic ground state together with a phenomenological dephasing model for core-excited states. As a word of caution, using the latter model leaves cases that exhibit intricate large-amplitude dynamics in the excited state, for example, ultrafast dissociation,[43,45,46] outside reach. From this viewpoint, both liquid and gaseous water systems are not very suitable to reproduce nuclear effects in full complexity. Still, because the effects in question are elucidated as the differences between the two methods applied to the same data set, the particular model system is not important for the present purpose. The consequences of the dynamical classical limit, employed here, have been extensively studied by Berne et al.[47,48] This approximation can cause wrong frequencies and shapes of the vibronic progressions in certain physical situations. Importantly, it can only lead to a *suppression* of the vibronic progressions, and hence the strength of the vibronic effects discussed here can be even stronger. Overall, the developed technique provides an improvement on the description of nuclear dynamical correlation effects in X-ray spectra with respect to state-of-the-art approaches. These effects have been demonstrated to be essential for X-ray spectroscopy via the comparison against the conventional sampling approach results for gas phase water. In particular, RIXS, being a two-photon process, has turned out to be a sensitive technique for the effects in question. In contrast, XAS, being a one-photon process, exhibits almost no traces of the underlying nuclear dynamics. Interestingly, static (sampling) and dynamic (correlation) nuclear phenomena have been disentangled from each other experimentally, employing RIXS with excitation pulses strongly detuned from the resonance.[11] Thus a theoretical prediction of fine nuclear effects may further stimulate respective high-resolution experiments. Note that it is not clear how to single out nuclear correlation effects by means of a wavepacket propagation method, whereas they come out naturally via trajectory-based approaches, for example, the one employed here.

Remarkably, the developed methodology is rather universal and does not conceptually depend on the accompanying electronic structure method. Furthermore, a similar strategy can be applied to the related photon-in/electron-out techniques, such as photoelectron and Auger spectroscopies. We believe that these developments are especially important in view of the recently suggested nonlinear X-ray techniques[49,50] that are foreseen to be even more informative and sensitive than the conventional RIXS approach.

■ ASSOCIATED CONTENT

Supporting Information

The Supporting Information is available free of charge on the ACS Publications website at DOI: 10.1021/acs.jpclett.7b00037.

Computational details, derivation of time-domain expressions from first- and third-order response functions, and derivation of the expressions for XAS and RIXS in Fourier space. (PDF)

■ AUTHOR INFORMATION

Corresponding Authors

*S.D.I.: E-mail: sergei.ivanov@uni-rostock.de.
*S.I.B.: E-mail: sergey.bokarev@uni-rostock.de.

ORCID

Sergei D. Ivanov: 0000-0002-6631-4868

Notes

The authors declare no competing financial interest.

■ ACKNOWLEDGMENTS

We acknowledge financial support by the Deanship of Scientific Research (DSR), King Abdulaziz University, Jeddah, grant No. D-003-435 (S.I.B., O.K.), and the Deutsche Forschungsgemeinschaft KU 952/10-1 (S.K., O.K.), IV 171/2-1 (S.D.I.). Special thanks go to Fabian Gottwald for technical assistance with the MD simulations of water.

■ REFERENCES

(1) Stöhr, J. *NEXAFS Spectroscopy*; Springer Science & Business Media, 2013; Vol. 25.
(2) Hennies, F.; Polyutov, S.; Minkov, I.; Pietzsch, A.; Nagasono, M.; Gel'mukhanov, F.; Triguero, L.; Piancastelli, M.-N.; Wurth, W.; Ågren, H.; et al. Nonadiabatic effects in resonant inelastic x-ray scattering. *Phys. Rev. Lett.* **2005**, *95*, 163002.
(3) Ljungberg, M. P.; Pettersson, L. G. M.; Nilsson, A. Vibrational interference effects in x-ray emission of a model water dimer: Implications for the interpretation of the liquid spectrum. *J. Chem. Phys.* **2011**, *134*, 044513.
(4) Rubensson, J. E.; Hennies, F.; Pietzsch, A. High-resolution resonant inelastic soft x-ray scattering applied to liquids. *J. Electron Spectrosc. Relat. Phenom.* **2013**, *188*, 79−83.
(5) Guillemin, R.; Carniato, S.; Journel, L.; Stolte, W. C.; Marchenko, T.; Khoury, L. E.; Kawerk, E.; Piancastelli, M. N.; Hudson, A. C.; Lindle, D. W.; et al. A review of molecular effects in gas-phase KL X-ray emission. *J. Electron Spectrosc. Relat. Phenom.* **2013**, *188*, 53−61.
(6) Dong, W.; Wang, H.; Olmstead, M. M.; Fettinger, J. C.; Nix, J.; Uchiyama, H.; Tsutsui, S.; Baron, A. Q. R.; Dowty, E.; Cramer, S. P. Inelastic X-ray scattering of a transition-metal complex ($FeCl_4^-$): vibrational spectroscopy for all normal modes. *Inorg. Chem.* **2013**, *52*, 6767−6769.
(7) Bohinc, R.; Žitnik, M.; Bučar, K.; Kavčič, M.; Journel, L.; Guillemin, R.; Marchenko, T.; Simon, M.; Cao, W. Dissociation of chloromethanes upon resonant σ excitation studied by x-ray scattering. *J. Chem. Phys.* **2013**, *139*, 134302.
(8) Pietzsch, A.; Sun, Y.-P.; Hennies, F.; Rinkevicius, Z.; Karlsson, H. O.; Schmitt, T.; Strocov, V. N.; Andersson, J.; Kennedy, B.; Schlappa, J.; et al. Spatial quantum beats in vibrational resonant inelastic soft X-ray scattering at dissociating states in oxygen. *Phys. Rev. Lett.* **2011**, *106*, 153004.
(9) Hennies, F.; Pietzsch, A.; Berglund, M.; Föhlisch, A.; Schmitt, T.; Strocov, V.; Karlsson, H. O.; Andersson, J.; Rubensson, J.-E. Resonant inelastic scattering spectra of free molecules with vibrational resolution. *Phys. Rev. Lett.* **2010**, *104*, 193002.
(10) Lange, K. M.; Aziz, E. F. The hydrogen bond of water from the perspective of soft X-ray spectroscopy. *Chem. - Asian J.* **2013**, *8*, 318−327.
(11) Schreck, S.; Pietzsch, A.; Kunnus, K.; Kennedy, B.; Quevedo, W.; Miedema, P. S.; Wernet, P.; Föhlisch, A. Dynamics of the OH group and the electronic structure of liquid alcohols. *Struct. Dyn.* **2014**, *1*, 054901.
(12) Fransson, T.; Harada, Y.; Kosugi, N.; Besley, N. A.; Winter, B.; Rehr, J. J.; Pettersson, L. G. M.; Nilsson, A. X-ray and electron spectroscopy of water. *Chem. Rev.* **2016**, *116*, 7551−7569.
(13) Sellberg, J. A.; Mcqueen, T. A.; Laksmono, H.; Schreck, S.; Beye, M.; Deponte, D. P.; Kennedy, B.; Nordlund, D.; Sierra, R. G.;

DOI: 10.1021/acs.jpclett.7b00037
J. Phys. Chem. Lett. 2017, 8, 992−996

Schlesinger, D.; et al. X-ray emission spectroscopy of bulk liquid water in "no-man's land. *J. Chem. Phys.* **2015**, *142*, 044505.
(14) Sałek, P.; Baev, A.; Gel'mukhanov, F.; Ågren, H. Dynamical properties of X-ray Raman scattering. *Phys. Chem. Chem. Phys.* **2003**, *5*, 1−11.
(15) Wächtler, M.; Guthmuller, J.; González, L.; Dietzek, B. Analysis and characterization of coordination compounds by resonance Raman spectroscopy. *Coord. Chem. Rev.* **2012**, *256*, 1479−1508.
(16) Couto, R. C.; Guarise, M.; Nicolaou, A.; Jaouen, N.; Chiuzbăian, G. S.; Lüning, J.; Ekholm, V.; Rubensson, J.-E.; Såthe, C.; Hennies, F.; et al. Coupled electron-nuclear dynamics in resonant $1\sigma \rightarrow 2\pi$ x-ray Raman scattering of CO molecules. *Phys. Rev. A: At., Mol., Opt. Phys.* **2016**, *93*, 032510.
(17) Couto, R. C.; Cruz, V. V.; Ertan, E.; Eckert, S.; Fondell, M.; Dantz, M.; Kennedy, B.; Schmitt, T.; Pietzsch, A.; Guimarães, F. F.; et al. Selective gating to vibrational modes through resonant X-ray scattering. *Nat. Commun.* **2017**, *8*, 12725−12734.
(18) Mukamel, S. *Principles of Nonlinear Optical Spectroscopy*; Oxford University Press: Oxford, U.K., 1995.
(19) May, V.; Kühn, O. *Charge and Energy Transfer Dynamics in Molecular Systems*; Wiley-VCH: Weinheim, Germany, 2011.
(20) Marx, D.; Hutter, J. *Ab Initio Molecular Dynamics: Basic Theory and Advanced Methods*; Cambridge University Press: Cambridge, U.K., 2009.
(21) Ivanov, S. D.; Witt, A.; Marx, D. Theoretical spectroscopy using molecular dynamics: theory and application to CH_5^+ and its isotopologues. *Phys. Chem. Chem. Phys.* **2013**, *15*, 10270−10299.
(22) Sun, Y.-P.; Hennies, F.; Pietzsch, A.; Kennedy, B.; Schmitt, T.; Strocov, V. N.; Andersson, J.; Berglund, M.; Rubensson, J.-E.; Aidas, K.; et al. Intramolecular soft modes and intermolecular interactions in liquid acetone. *Phys. Rev. B: Condens. Matter Mater. Phys.* **2011**, *84*, 132202.
(23) Jena, N. K.; Josefsson, I.; Eriksson, S. K.; Hagfeldt, A.; Siegbahn, H.; Björneholm, O.; Rensmo, H.; Odelius, M. Solvent-dependent structure of the I_3^- ion derived from photoelectron spectroscopy and ab initio molecular dynamics simulations. *Chem. - Eur. J.* **2015**, *21*, 4049−4055.
(24) Weinhardt, L.; Ertan, E.; Iannuzzi, M.; Weigand, M.; Fuchs, O.; Bär, M.; Blum, M.; Denlinger, J. D.; Yang, W.; Umbach, E.; et al. Probing hydrogen bonding orbitals: resonant inelastic soft X-ray scattering of aqueous NH 3. *Phys. Chem. Chem. Phys.* **2015**, *17*, 27145−27153.
(25) Leetmaa, M.; Ljungberg, M.; Lyubartsev, A.; Nilsson, A.; Pettersson, L. Theoretical approximations to X-ray absorption spectroscopy of liquid water and ice. *J. Electron Spectrosc. Relat. Phenom.* **2010**, *177*, 135−157.
(26) Heller, E. J. Photofragmentation of symmetric triatomic molecules: Time dependent picture. *J. Chem. Phys.* **1978**, *68*, 3891.
(27) Lee, S.; Heller, E. J. Time-dependent theory of Raman scattering. *J. Chem. Phys.* **1979**, *71*, 4777−4788.
(28) Lawrence, C.; Skinner, J. Vibrational spectroscopy of HOD in liquid D_2O. II. Infrared line shapes and vibrational Stokes shift. *J. Chem. Phys.* **2002**, *117*, 8847−8854.
(29) Harder, E.; Eaves, J. D.; Tokmakoff, A.; Berne, B. Polarizable molecules in the vibrational spectroscopy of water. *Proc. Natl. Acad. Sci. U. S. A.* **2005**, *102*, 11611−11616.
(30) Tuckerman, M. E. *Statistical Mechanics: Theory and Molecular Simulation*; Oxford University Press: Oxford, U.K., 2010.
(31) Karsten, S.; Bokarev, S. I.; Aziz, S. G.; Ivanov, S. D.; Kühn, O. A time-correlation function approach to nuclear dynamical effects in X-ray spectroscopy. *arXiv:1611.05025 [physics.chem-ph]*.
(32) Lange, K. M.; Kothe, A.; Aziz, E. F. Chemistry in solution: recent techniques and applications using soft X-ray spectroscopy. *Phys. Chem. Chem. Phys.* **2012**, *14*, 5331−5338.
(33) Hess, B.; Kutzner, C.; van der Spoel, D.; Lindahl, E. GROMACS 4: Algorithms for highly efficient, load-balanced, and scalable molecular simulation. *J. Chem. Theory Comput.* **2008**, *4*, 435−447.
(34) Paesani, F.; Zhang, W.; Case, D. A.; Cheatham, T. E.; Voth, G. A. An accurate and simple quantum model for liquid water. *J. Chem. Phys.* **2006**, *125*, 184507.
(35) Perdew, J. P.; Burke, K.; Ernzerhof, M. Generalized gradient approximation made simple. *Phys. Rev. Lett.* **1996**, *77*, 3865−3868.
(36) Neese, F. The ORCA program system. *Wiley Interdiscip. Rev. Comput. Mol. Sci.* **2012**, *2*, 73−78.
(37) Weigend, F.; Ahlrichs, R. Balanced basis sets of split valence, triple zeta valence and quadruple zeta valence quality for H to Rn: Design and assessment of accuracy. *Phys. Chem. Chem. Phys.* **2005**, *7*, 3297−3305.
(38) Näslund, L.-Å.; Cavalleri, M.; Ogasawara, H.; Nilsson, A.; Pettersson, L. G. M.; Wernet, P.; Edwards, D. C.; Sandström, M.; Myneni, S. Direct evidence of orbital mixing between water and solvated transition-metal ions: an oxygen 1s XAS and DFT study of aqueous systems. *J. Phys. Chem. A* **2003**, *107*, 6869−6876.
(39) Lee, N.; Petrenko, T.; Bergmann, U.; Neese, F.; DeBeer, S. Probing valence orbital composition with iron Kß X-ray emission spectroscopy. *J. Am. Chem. Soc.* **2010**, *132*, 9715−9727.
(40) Lassalle-Kaiser, B.; Boron, T. T.; Krewald, V.; Kern, J.; Beckwith, M. A.; Delgado-Jaime, M. U.; Schroeder, H.; Alonso-Mori, R.; Nordlund, D.; Weng, T. C.; et al. Experimental and computational X-ray emission spectroscopy as a direct probe of protonation states in oxo-bridged MnIV dimers relevant to redox-active metalloproteins. *Inorg. Chem.* **2013**, *52*, 12915−12922.
(41) Pollock, C. J.; Grubel, K.; Holland, P. L.; Debeer, S. Experimentally quantifying small-molecule bond activation using valence-to-core X-ray emission spectroscopy. *J. Am. Chem. Soc.* **2013**, *135*, 11803−11808.
(42) Milne, C.; Penfold, T.; Chergui, M. Recent experimental and theoretical developments in time-resolved X-ray spectroscopies. *Coord. Chem. Rev.* **2014**, *277−278*, 44−68.
(43) Hjelte, I.; Piancastelli, M. N.; Fink, R. F.; Björneholm, O.; Bässler, M.; Feifel, R.; Giertz, A.; Wang, H.; Wiesner, K.; Ausmees, A.; et al. Evidence for ultra-fast dissociation of molecular water from resonant Auger spectroscopy. *Chem. Phys. Lett.* **2001**, *334*, 151−158.
(44) Weinhardt, L.; Benkert, A.; Meyer, F.; Blum, M.; Wilks, R. G.; Yang, W.; Bär, M.; Reinert, F.; Heske, C. Nuclear dynamics and spectator effects in resonant inelastic soft x-ray scattering of gas-phase water molecules. *J. Chem. Phys.* **2012**, *136*, 144311.
(45) Pietzsch, A.; Hennies, F.; Miedema, P. S.; Kennedy, B.; Schlappa, J.; Schmitt, T.; Strocov, V. N.; Föhlisch, A. Snapshots of the fluctuating hydrogen bond network in liquid water on the sub-femtosecond timescale with vibrational resonant inelastic x-ray scattering. *Phys. Rev. Lett.* **2015**, *114*, 088302.
(46) Harada, Y.; Tokushima, T.; Horikawa, Y.; Takahashi, O.; Niwa, H.; Kobayashi, M.; Oshima, M.; Senba, Y.; Ohashi, H.; Wikfeldt, K. T.; et al. Selective probing of the OH or OD stretch vibration in liquid water using resonant inelastic soft-X-ray scattering. *Phys. Rev. Lett.* **2013**, *111*, 1−5.
(47) Egorov, S. A.; Rabani, E.; Berne, B. J. Vibronic spectra in condensed matter: A comparison of exact quantum mechanical and various semiclassical treatments for harmonic baths. *J. Chem. Phys.* **1998**, *108*, 1407−1422.
(48) Rabani, E.; Egorov, S. A.; Berne, B. J. A comparison of exact quantum mechanical and various semiclassical treatments for the vibronic absorption spectrum: The case of fast vibrational relaxation. *J. Chem. Phys.* **1998**, *109*, 6376−6381.
(49) Biggs, J. D.; Zhang, Y.; Healion, D.; Mukamel, S. Two-dimensional stimulated resonance Raman spectroscopy of molecules with broadband x-ray pulses. *J. Chem. Phys.* **2012**, *136*, 174117.
(50) Mukamel, S.; Healion, D.; Zhang, Y.; Biggs, J. D. Multidimensional attosecond resonant X-ray spectroscopy of molecules: lessons from the optical regime. *Annu. Rev. Phys. Chem.* **2013**, *64*, 101−127.

DOI: 10.1021/acs.jpclett.7b00037
J. Phys. Chem. Lett. 2017, 8, 992−996

Supporting information for: Nuclear Dynamical Correlation Effects in X-ray Spectroscopy from a Theoretical Time-domain Perspective

Sven Karsten[1],[†] Sergei D. Ivanov[1],[*,†] Saadullah G. Aziz[2],[†] Sergey I. Bokarev[1],[*,†] and Oliver Kühn[1†]

[1]*Institute of Physics, University of Rostock, Albert-Einstein-Str. 23-24, 18059 Rostock, Germany, and* [2]*Chemistry Department, Faculty of Science, King Abdulaziz University, 21589 Jeddah, Saudi Arabia*

E-mail: sergei.ivanov@uni-rostock.de; sergey.bokarev@uni-rostock.de

Contents

[*]To whom correspondence should be addressed
[†1]Institute of Physics, University of Rostock, Albert-Einstein-Str. 23-24, 18059 Rostock, Germany
[‡2]Chemistry Department, Faculty of Science, King Abdulaziz University, 21589 Jeddah, Saudi Arabia

1 Computational details

The MD simulations have been performed for a gas phase water molecule using the GROMACS program package ver. 4.6.5[S1] employing the anharmonic qSPC/Fw water model with a Morse potential for the O-H intra-molecular potential.[S2] The "standard protocol"[S3] for calculating spectra in the canonical ensemble has been used, that is a set of 140 uncorrelated initial conditions, which is sufficient to obtain converged results, has been generated from an NVT MD run with the target temperature of 300 K imposed by the Langevin thermostat. These initial conditions have been further used as starting points for simulating microcanonical (NVE) trajectories, each 0.5 ps with MD timestep of 0.5 fs. The spectra calculated along the NVE trajectories have been averaged to yield the desired canonical ensemble result.

The time-independent electronic Schrödinger equation has been solved for each MD snapshot at the level of the ground state density functional theory with the Perdew-Burke-Ernzerhof functional[S4] using the ORCA ver. 3.0.3 program package.[S5] Tight SCF convergence criteria (10^{-7} Hartree) and a standard grid (ORCA grid3) have been employed. The def2-QZVPP basis set for oxygen and hydrogen[S6] together with (5s5p)/[1s1p] generally contracted Rydberg functions on oxygen have been used. Rydberg contractions have been obtained as atomic natural orbitals[S7,S8] constructed of primitives with universal exponents (see Ref. S9). The energies of the singly-excited valence and core states have been approximated by the differences of the respective Kohn-Sham orbital energies; the corresponding dipole transition moments have been calculated with respect to these orbitals.[S10]

In order to mimic the finite width of the exciting light pulse given by the experimental conditions, the XAS amplitudes and RIXS spectra are convoluted with normalized Gaussian functions $\exp[-\Omega^2/(2\sigma^2)]/(\sqrt{2\pi\sigma^2})$ along the excitation axis, Ω, with $\sigma =$

0.05 eV.[S11] Additionally, the XAS amplitude is convoluted with normalized Lorentzian functions $\Gamma/\pi \cdot [\Gamma^2 + \Omega^2]^{-1}$ taking into account the finite lifetime of the core-excited final states, $\Gamma = 0.25\,\mathrm{fs}^{-1}$.[S12] The same Γ has been used for all final states entering the XAS amplitude as well as for all intermediate states entering the RIXS amplitude, where the finite lifetime is already accounted for by construction.

The number of considered states that contribute to the spectra is determined by the absorption and emission frequency range of interest, here $\Omega \in [532.8, 540.8]\,\mathrm{eV}$ and $\omega \in [507.3, 538.3]\,\mathrm{eV}$ requiring the consideration of 31 states. Note that all the spectra have been shifted *globally* by 24.8 eV such that the peak structure in XAS approximately matches the experimental data for gas phase water.[S13]

2 Derivation of time-domain expression from 3rd order nonlinear response function

Taking the Raman part (R_3) of the expression for the spontaneous light emission (SLE) given in 9.12a (p. 269 of Ref. S14) with the corresponding third-order response function defined in Eq. (7.12) (p. 198 therein), one gets

$$S_{\mathrm{SLE}}(\omega_{\mathrm{L}}, \omega_{\mathrm{S}}) = 2\mathrm{Re} \int_0^\infty \mathrm{d}t_1 \int_0^\infty \mathrm{d}t_2 \int_0^\infty \mathrm{d}t_3 \exp[-\mathrm{i}\omega_{\mathrm{L}} t_1 - \mathrm{i}(\omega_{\mathrm{L}} - \omega_{\mathrm{S}})t_2 + \mathrm{i}\omega_{\mathrm{S}} t_3]$$
$$\times \langle \hat{V}_{ge} \exp[\mathrm{i}\hat{H}_e t_1/\hbar] \hat{V}_{eg} \exp[\mathrm{i}\hat{H}_g (t_2 + t_3)/\hbar] \hat{V}_{ge} \exp[-\mathrm{i}\hat{H}_e t_3/\hbar] \hat{V}_{eg} \exp[-\mathrm{i}\hat{H}_g (t_1 + t_2)/\hbar] \hat{\rho}_g \rangle \tag{S1}$$

Here, ω_{L} and ω_{S} are the frequencies of the absorbed and emitted photons, that is Ω and ω in our notation, respectively. The equation above is restricted to the case of an electronic two-level system; the extension to a multi-level system is straightforward and will be performed later below. In the following atomic units will be employed, that is $\hbar = 1$. In order to get

the proper time arguments one can perform the rearrangements

$$\exp[\mathrm{i}\hat{H}_g(t_2+t_3)] = \exp[-\mathrm{i}\hat{H}_g t_1]\exp[\mathrm{i}\hat{H}_g(t_1+t_2+t_3)] \tag{S2}$$

$$\exp[-\mathrm{i}\hat{H}_e t_3] = \exp[-\mathrm{i}\hat{H}_e(t_1+t_2+t_3)]\exp[\mathrm{i}\hat{H}_e(t_1+t_2)] \ , \tag{S3}$$

yielding

$$\begin{aligned} S_{\mathrm{SLE}}(\Omega,\omega) = 2\mathrm{Re}\int_0^\infty \mathrm{d}t_1 \int_0^\infty \mathrm{d}t_2 \int_0^\infty \mathrm{d}t_3 \exp[-\mathrm{i}\Omega t_1 - \mathrm{i}(\Omega-\omega)t_2 + \mathrm{i}\omega t_3] \\ \times \langle \hat{V}_{ge}\exp[\mathrm{i}\hat{H}_e t_1]\hat{V}_{eg}\exp[-\mathrm{i}\hat{H}_g t_1]\exp[\mathrm{i}\hat{H}_g(t_1+t_2+t_3)]\hat{V}_{ge}\exp[-\mathrm{i}\hat{H}_e(t_1+t_2+t_3)] \\ \times \exp[\mathrm{i}\hat{H}_e(t_1+t_2)]\hat{V}_{eg}\exp[-\mathrm{i}\hat{H}_g(t_1+t_2)]\hat{\rho}_g\rangle \ . \end{aligned} \tag{S4}$$

One sees that the interaction terms, $\hat{V}_{eg}$ and $\hat{V}_{ge}$ are now embraced with the Heisenberg time evolution operators that form pairs with same times. Introducing a new time variable $t := t_1 + t_2$ leads to

$$\begin{aligned} S_{\mathrm{SLE}}(\Omega,\omega) = 2\mathrm{Re}\int_0^\infty \mathrm{d}t_1 \int_0^\infty \mathrm{d}t \int_0^\infty \mathrm{d}t_3 \exp[-\mathrm{i}\Omega t_1 - \mathrm{i}(\Omega-\omega)(t-t_1) + \mathrm{i}\omega t_3] \\ \times \langle \hat{V}_{ge}\exp[\mathrm{i}\hat{H}_e t_1]\hat{V}_{eg}\exp[-\mathrm{i}\hat{H}_g t_1]\exp[\mathrm{i}\hat{H}_g(t+t_3)]\hat{V}_{ge}\exp[-\mathrm{i}\hat{H}_e(t+t_3)] \\ \times \exp[\mathrm{i}\hat{H}_e t]\hat{V}_{eg}\exp[-\mathrm{i}\hat{H}_g t]\hat{\rho}_g\rangle \ , \end{aligned} \tag{S5}$$

which would eventually decouple the Fourier transforms involving Ω and ω, see next equation. Since the spectrum is real, one can take the complex conjugate leading to the adjoint

operators with inverted order under the canonical average

$$S_{\mathrm{SLE}}(\Omega,\omega) = 2\mathrm{Re}\int_0^\infty \mathrm{d}t_1 \int_0^\infty \mathrm{d}t \int_0^\infty \mathrm{d}t_3 \exp[\mathrm{i}\Omega t + \mathrm{i}\omega t_1 - \mathrm{i}\omega(t+t_3)]$$
$$\times \langle \hat{\rho}_g \exp[\mathrm{i}\hat{H}_g t]\hat{V}_{ge} \exp[-\mathrm{i}\hat{H}_e t] \exp[\mathrm{i}\hat{H}_e(t+t_3)]\hat{V}_{eg} \exp[-\mathrm{i}\hat{H}_g(t+t_3)]$$
$$\times \exp[\mathrm{i}\hat{H}_g t_1]\hat{V}_{ge} \exp[-\mathrm{i}\hat{H}_e t_1]\hat{V}_{eg}\rangle \ ; \tag{S6}$$

note that it is, in principle, not necessary but leads to the same form of the final equation as in the main text. Now we can group the terms such that the time integrations are separated

$$S_{\mathrm{SLE}}(\Omega,\omega) = 2\mathrm{Re}\int_0^\infty \mathrm{d}t\, \mathrm{e}^{\mathrm{i}\Omega t}$$
$$\times \int_0^\infty \mathrm{d}t_3\, \mathrm{e}^{-\mathrm{i}\omega(t+t_3)} \langle \hat{\rho}_g \mathrm{e}^{\mathrm{i}\hat{H}_g t}\hat{V}_{ge}\mathrm{e}^{-\mathrm{i}\hat{H}_e t}\mathrm{e}^{\mathrm{i}\hat{H}_e(t+t_3)}\hat{V}_{eg}\mathrm{e}^{-\mathrm{i}\hat{H}_g(t+t_3)}$$
$$\times \int_0^\infty \mathrm{d}t_1\, \mathrm{e}^{\mathrm{i}\omega t_1}\mathrm{e}^{\mathrm{i}\hat{H}_g t_1}\hat{V}_{ge}\mathrm{e}^{-\mathrm{i}\hat{H}_e t_1}\hat{V}_{eg}\rangle \ . \tag{S7}$$

Noting that the t-integrand has the form of an equilibrium auto-correlation function (and has thus a symmetric real part and an anti-symmetric imaginary part) the imaginary part vanishes by construction and one can drop the Re symbol. Further one can remove the factor 2 and change the integration limits to $(-\infty,\infty)$, since the integrand is even.

At this point we generalize the expression to many states and set the interaction terms to be the properly polarized transition dipoles according to the RIXS process, see Fig. 1 in the main text. In order to distinguish the generalized case, the RIXS amplitude is further

referred to as $\mathcal{R}(\Omega,\omega)$

$$\begin{aligned}\mathcal{R}(\Omega,\omega) = &\int_{-\infty}^{\infty} \mathrm{d}t\, \mathrm{e}^{\mathrm{i}\Omega t} \\ &\times \int_{0}^{\infty} \mathrm{d}t_3\, \mathrm{e}^{-\mathrm{i}\omega(t+t_3)} \langle \hat{\rho}_g \mathrm{e}^{\mathrm{i}\hat{H}_g t} \hat{D}_j^{g\zeta} e_\zeta \mathrm{e}^{-\mathrm{i}H_j t} \mathrm{e}^{\mathrm{i}H_j(t+t_3)} u^\nu \hat{D}_{\nu f}^{j} \mathrm{e}^{-\mathrm{i}H_f(t+t_3)} \\ &\times \int_{0}^{\infty} \mathrm{d}t_1\, \mathrm{e}^{\mathrm{i}\omega t_1} \mathrm{e}^{\mathrm{i}H_f t_1} \hat{D}_i^{f\eta} u_\eta \mathrm{e}^{-\mathrm{i}H_i t_1} e^\xi \hat{D}_{\xi g}^{i} \rangle \ , \end{aligned} \tag{S8}$$

where $\mathbf{u}$ and $\mathbf{e}$ are the polarizations of the emitted and the absorbed light, respectively, and $\hat{D}_a^b := \langle a|\hat{d}|b\rangle$, where $\hat{d}$ is the dipole operator. The use of super- and subscripts is pictorial, since one sees in which way the excitation goes (from the subscript to the superscript). For the sake of brevity, the notation $c^\xi = c_\xi^\star$ for any indexed complex quantity is used and the Einstein convention for summing the indices that appear in a subsrcipt *and* in a superscript is employed. Note that the aforementioned embracing does not yet have the desired form of the Heisenberg time evolution, since it is performed with respect to *different* Hamiltonians. In fact, it would be convenient if the time evolution would be performed with respect to the electronic ground state $|0\rangle$, since this allows one to employ well-established ground state electronic structure methods for calculating forces for MD. In order to circumvent this issue we employ the interaction representation[S14,S15]

$$\mathrm{e}^{-\mathrm{i}\hat{H}_a t} = \mathrm{e}^{-\mathrm{i}\hat{H}_0 t} \hat{S}_a(t,0) \ , \tag{S9}$$

where the scattering operator is defined as

$$\hat{S}_a(t,t_0) := \exp_+ \left[-\mathrm{i} \int_{t_0}^{t} \mathrm{d}\tau\, \Delta\hat{E}_{a0}(\tau) \right] \ , \tag{S10}$$

with the energy gap $\Delta\hat{E}_{a0} := \hat{E}_a - \hat{E}_0$ and the symbol $\exp_+$ standing for a (positively)

time-ordered exponential. The time argument of the integrand therein corresponds to the time evolution according to the Heisenberg equation of motion with respect to the electronic ground state Hamiltonian, $\hat{H}_0$

$$\hat{A}(t) \equiv \mathrm{e}^{\mathrm{i}\hat{H}_0 t}\hat{A}\mathrm{e}^{-\mathrm{i}\hat{H}_0 t} \ . \tag{S11}$$

The result after applying the interaction representation reads

$$\begin{aligned}\mathcal{R}(\Omega,\omega) = &\int_{-\infty}^{\infty} \mathrm{d}t\, \mathrm{e}^{\mathrm{i}\Omega t} \int_{0}^{\infty} \mathrm{d}t_3\, \mathrm{e}^{-\mathrm{i}\omega(t+t_3)} \\ &\times \langle \hat{\rho}_g \hat{S}^g(t,0)\hat{D}_j^{g\zeta}(t) e_\zeta \hat{S}_j(t,0) u^\nu \hat{S}^j(t+t_3,0)\hat{D}_{\nu f}^{j}(t+t_3)\hat{S}_f(t+t_3,0) \\ &\times \int_{0}^{\infty} \mathrm{d}t_1\, \mathrm{e}^{\mathrm{i}\omega t_1} \hat{S}^f(t_1,0)\hat{D}_i^{f\eta}(t_1) u_\eta \hat{S}_i(t_1,0) e^\xi \hat{D}_{\xi g}^{i}(0)\rangle \ . \end{aligned} \tag{S12}$$

Finally, introducing the dressed dipoles

$$\hat{M}_b^a(t,0) := \hat{S}^a(t,0)\hat{D}_b^a(t)\hat{S}_b(t,0) \tag{S13}$$

and deciphering the canonical averaging $\langle \rho_g \bullet \rangle := \sum_G \langle G| \exp[-\beta \hat{H}_g(0)] \bullet |G\rangle / Z$, Z being the canonical partition function and $|G\rangle$ are nuclear states corresponding to g-th electronic level, leads to a compact form for the RIXS amplitude

$$\mathcal{R}(\Omega,\omega) = \frac{1}{Z}\int_{-\infty}^{\infty} \mathrm{d}t\, \mathrm{e}^{\mathrm{i}\Omega t} \sum_G \langle G|\mathrm{e}^{-\beta \hat{H}_g(0)} \tag{S14}$$

$$\int_{-\infty}^{\infty} \mathrm{d}t_3\, \mathrm{e}^{-\mathrm{i}\omega(t+t_3)} \hat{M}_j^{g\zeta}(t,0) e_\zeta \Delta_j(t_3) u^\nu \hat{M}_{\nu f}^{j}(t+t_3,0)$$

$$\int_{-\infty}^{\infty} \mathrm{d}t_1\, \mathrm{e}^{\mathrm{i}\omega t_1} \hat{M}_i^{f\eta}(t_1,0) u_\eta \Delta_i(t_1) e^\xi \hat{M}_{\xi g}^{i}(0,0)|G\rangle \ , \tag{S15}$$

where we have introduced phenomenological mono-exponential decay $\Delta_{i/j}(t) := \theta(t)\exp[-\Gamma_{i/j}t]$, which is equivalent to adding an imaginary part for the Hamiltonians of the intermediate

states. Note that the lower integration limits have been extended to $-\infty$ using the properties of the Heaviside step function $\theta(t)$.

The last step is to perform the dynamical classical limit for the nuclei.[S14,S15] In particular, the nuclei are represented by point particles and the operators are replaced by continuous dynamic functions. Consequently, the trace over the initial nuclear states $|G\rangle$ is substituted by an integral over the phase space

$$\frac{1}{Z}\sum_{G}\langle G|\mathrm{e}^{-\beta\hat{H}_g(0)}\bullet|G\rangle \rightarrow \frac{1}{\tilde{Z}}\sum_{g}\iint \mathrm{d}\mathbf{R}_0\,\mathrm{d}\mathbf{P}_0\mathrm{e}^{-\beta H_g}\bullet \ , \tag{S16}$$

where $\tilde{Z}$ is the classical canonical partition function. However, the goal is to formulate the averaging with respect to the electronic ground state Hamilton function, i.e. $\langle\bullet\rangle = \iint \mathrm{d}\mathbf{R}_0\mathrm{d}\mathbf{P}_0 \exp\left[-\beta H_0(0)\right]/Z_0\bullet$, where Z_0 is the partition function of the electronic ground state. Multiplying and dividing $\tilde{Z}$ by Z_0 and adding and subtracting the electronic ground state Hamilton function, $H_g(0) = H_0(0) + \Delta E_{g0}(0)$, one can write

$$\begin{aligned}
\tilde{Z} &= \sum_g \iint \mathrm{d}\mathbf{R}_0\mathrm{d}\mathbf{P}_0\mathrm{e}^{-\beta H_g(0)} \\
&= Z_0\sum_g \iint \mathrm{d}\mathbf{R}_0\mathrm{d}\mathbf{P}_0\frac{\mathrm{e}^{-\beta H_g(0)}}{Z_0} \\
&= Z_0\iint \mathrm{d}\mathbf{R}_0\mathrm{d}\mathbf{P}_0\frac{\mathrm{e}^{-\beta H_0(0)}}{Z_0}\sum_g \mathrm{e}^{-\beta\Delta E_{g0}(0)} \qquad \text{(S17)} \\
&= Z_0\left\langle\sum_g \mathrm{e}^{-\beta\Delta E_{g0}(0)}\right\rangle \ . \qquad \text{(S18)}
\end{aligned}$$

Finally, the classical canonical average becomes

$$\begin{aligned}
\sum_g \iint \mathrm{d}\mathbf{R}_0\mathrm{d}\mathbf{P}_0 \exp\left[-\beta H_g(0)\right]/Z\ \bullet &= \iint \mathrm{d}\mathbf{R}_0\mathrm{d}\mathbf{P}_0\frac{\mathrm{e}^{-\beta H_0(0)}}{Z_0}\mathcal{W}_g(0)\bullet \qquad \text{(S19)} \\
&= \left\langle\mathcal{W}_g(0)\ \bullet\right\rangle \ , \qquad \text{(S20)}
\end{aligned}$$

with $\mathcal{W}_g(0)$ defined in Eq. (4) of the main text.

According to the correspondence principle, the Heisenberg time evolution for a general operator $\hat{A}$ becomes the dynamic function $A(t) \equiv A(\mathbf{R}(t), \mathbf{P}(t))$, with the time evolution induced by the Hamilton function $H_0(\mathbf{R}, \mathbf{P})$. Naturally, the time-ordering of exponentials in Eq. (S10) becomes irrelevant and disappears. Performing all these replacements leads to the final time-domain expression for the RIXS amplitude, Eq. (2) in the main text, that reads

$$\mathcal{R}(\Omega,\omega) = \int_{-\infty}^{\infty} \mathrm{d}t\, \mathrm{e}^{\mathrm{i}\Omega t} \int_{-\infty}^{\infty} \mathrm{d}t_3\, \mathrm{e}^{-\mathrm{i}\omega(t+t_3)} \int_{-\infty}^{\infty} \mathrm{d}t_1\, \mathrm{e}^{\mathrm{i}\omega t_1} \left\langle \mathcal{W}_g(0) M_j^{g\zeta}(t,0) e_\zeta \Delta_j(t_3) u^\nu M_{\nu f}^j(t+t_3,0) M_i^{f\eta}(t_1,0) u_\eta \Delta_i(t_1) e^\xi M_{\xi g}^i(0,0) \right\rangle \ . \tag{S21}$$

Note that in the main text the second argument of the dressed dipoles has been skipped, since it is always zero in the developed formalism.

3 Derivation of the time-domain expression from the linear response function

The derivation of the expression for the XAS amplitude follows the same line of reasoning as presented for the RIXS one in the previous section. Here, the starting point is the linear response function $J(t_1)$, see Eq. (7.4a) on p. 190 of Ref. S14

$$J(t_1) = \langle \exp[\mathrm{i}\hat{H}_g t_1] \hat{V}_{ge} \exp\left[-\mathrm{i}\hat{H}_e t_1\right] \hat{V}_{eg} \hat{\rho}_g \rangle \ . \tag{S22}$$

In order to obtain the spectrum that depends on the excitation frequency Ω, the response function is Fourier-transformed. After the generalization to a many-level system and employing the interaction representation via Eqs. (S9,S10), the absorption spectrum can be written

in terms of a time-correlation function of the dressed dipole moments, Eq. (S13),

$$\mathcal{X}(\Omega) = \frac{1}{Z}\int_{-\infty}^{\infty} \mathrm{d}t_1\, \mathrm{e}^{\mathrm{i}\Omega t_1} \sum_G \langle G|\mathrm{e}^{-\beta \hat{H}_g(0)} \hat{M}_f^{g\eta}(t_1,0) e_\eta e^\xi \hat{M}_{\xi g}^f(0,0)|G\rangle \ , \tag{S23}$$

where the symbols from Ref. S14 have been replaced by our notation as it has been done for RIXS. In the next step, the nuclei are subjected to the dynamical classical limit leading finally to the XAS amplitude obtained from classical ground-state dynamics and the corresponding classical canonical average

$$\mathcal{X}(\Omega) = \int_{-\infty}^{\infty} \mathrm{d}t_1\, \mathrm{e}^{\mathrm{i}\Omega t_1} \left\langle \mathcal{W}_g(0) M_f^{g\eta}(t_1,0) e_\eta e^\xi M_{\xi g}^f(0,0) \right\rangle \tag{S24}$$

which coincides with Eq. (1) in the main text after dropping the second time argument for the dressed dipoles.

4 Expression for RIXS in Fourier space

Firstly an additional integration along an MD trajectory with the length T is performed in Eq. (S21), owing to the stationarity of the canonical density

$$\begin{aligned}\mathcal{R}(\Omega,\omega) = \Bigg\langle \frac{1}{T}\int_0^T \mathrm{d}\tau\, \mathcal{W}_g(\tau) \int_{-\infty}^{\infty} \mathrm{d}t\, \mathrm{e}^{\mathrm{i}\Omega t} \\ \int_{-\infty}^{\infty} \mathrm{d}t_3\, \mathrm{e}^{-\mathrm{i}\omega(\tau+t+t_3)} M_j^{g\zeta}(\tau+t,\tau) e_\zeta \Delta_j(t_3) u^\nu M_{\nu f}^j(\tau+t+t_3,\tau) \\ \int_{-\infty}^{\infty} \mathrm{d}t_1\, \mathrm{e}^{\mathrm{i}\omega(\tau+t_1)} M_i^{f\eta}(\tau+t_1,\tau) u_\eta \Delta_i(t_1) e^\xi M_{\xi g}^i(\tau,\tau) \Bigg\rangle \ ,\end{aligned} \tag{S25}$$

where also $1 = \exp[-\mathrm{i}\omega\tau]\exp[\mathrm{i}\omega\tau]$ has been inserted. One can show that if the dressed dipoles' product has a cyclic structure of indices, then the *starting* time can be chosen

arbitrarily. A relevant example is the expression from Eq. (S25)

$$M_j^{g\zeta}(\tau+t,\tau)M_{\nu f}^j(\tau+t+t_3,\tau)M_i^{f\eta}(\tau+t_1,\tau)M_{\xi g}^i(\tau,\tau) \equiv$$
$$M_j^{g\zeta}(\tau+t,0)M_{\nu f}^j(\tau+t+t_3,0)M_i^{f\eta}(\tau+t_1,0)M_{\xi g}^i(\tau,0) \ . \tag{S26}$$

For a sufficiently large T one may extend formally the τ-integration interval to $(-\infty,\infty)$. Subsequently, one substitutes $\tau' := \tau + t$ yielding

$$\mathcal{R}(\Omega,\omega) = \Big\langle \frac{1}{T}\int\limits_{-\infty}^{\infty} \mathrm{d}\tau \mathrm{e}^{-\mathrm{i}\Omega\tau} \int\limits_{-\infty}^{\infty} \mathrm{d}\tau' \, \mathrm{e}^{\mathrm{i}\Omega\tau'}$$
$$\int\limits_{-\infty}^{\infty} \mathrm{d}t_3 \, \mathrm{e}^{-\mathrm{i}\omega(\tau'+t_3)} M_j^{g\zeta}(\tau',0) e_\zeta \Delta_j(t_3) u^\nu M_{\nu f}^j(\tau'+t_3,0)$$
$$\int\limits_{-\infty}^{\infty} \mathrm{d}t_1 \, \mathrm{e}^{\mathrm{i}\omega(\tau+t_1)} M_i^{f\eta}(\tau+t_1,0) u_\eta \Delta_i(t_1) e^\xi M_{\xi g}^i(\tau,0) \mathcal{W}_g(\tau) \Big\rangle \ . \tag{S27}$$

Now, one can replace the damping function by its Fourier transform via

$$\Delta_a(\tau) = \int\limits_{-\infty}^{\infty} \mathrm{d}\omega' \mathrm{e}^{\mathrm{i}\omega'\tau} \check{\Delta}_a(\omega') \equiv \int\limits_{-\infty}^{\infty} \mathrm{d}\omega' \mathrm{e}^{-\mathrm{i}\omega'\tau} \check{\Delta}_a(-\omega') \ . \tag{S28}$$

where $\check{\Delta}_a(\omega') := 1/(2\pi)\sqrt{\Gamma_a/\pi}(\Gamma_a + \mathrm{i}\omega')^{-1}$. By rearranging the integrations one gets a product of two very similar constructs

$$\mathcal{R}(\Omega,\omega) =$$
$$\Big\langle \frac{1}{T} \int\limits_{-\infty}^{\infty} \mathrm{d}\omega_1 \int\limits_{-\infty}^{\infty} \mathrm{d}\tau' \, \mathrm{e}^{\mathrm{i}\Omega\tau'} \int\limits_{-\infty}^{\infty} \mathrm{d}t_3 \, \mathrm{e}^{-\mathrm{i}\omega(\tau'+t_3)} M_j^{g\zeta}(\tau',0) e_\zeta \check{\Delta}_j(\omega_1) \mathrm{e}^{\mathrm{i}\omega_1 t_3} u^\nu M_{\nu f}^j(\tau'+t_3,0)$$
$$\int\limits_{-\infty}^{\infty} \mathrm{d}\omega_2 \int\limits_{-\infty}^{\infty} \mathrm{d}\tau \mathrm{e}^{-\mathrm{i}\Omega\tau} \int\limits_{-\infty}^{\infty} \mathrm{d}t_1 \, \mathrm{e}^{\mathrm{i}\omega(\tau+t_1)} \ M_i^{f\eta}(\tau+t_1,0) u_\eta \check{\Delta}_i(-\omega_2) \mathrm{e}^{-\mathrm{i}\omega_2 t_1} e^\xi M_{\xi g}^i(\tau,0) \mathcal{W}_g(\tau) \Big\rangle \ . \tag{S29}$$

The form of the time arguments of the dressed dipoles suggests two additional variable substitutions: $\tau_1' := \tau' + t_3$ and $\tau_2' := \tau + t_1$ that yield

$$\begin{aligned}&\mathcal{R}(\Omega,\omega) = \\ &\left\langle \frac{1}{T} \int_{-\infty}^{\infty} \mathrm{d}\omega_1 \int_{-\infty}^{\infty} \mathrm{d}\tau' \, \mathrm{e}^{\mathrm{i}\Omega\tau'} \int_{-\infty}^{\infty} \mathrm{d}\tau_1' \, \mathrm{e}^{-\mathrm{i}\omega\tau_1'} M_j^{g\zeta}(\tau',0) e_\zeta \check{\Delta}_j(\omega_1) \mathrm{e}^{\mathrm{i}\omega_1(\tau_1'-\tau')} u^\nu M_{\nu f}^j(\tau_1',0) \right. \\ &\left. \int_{-\infty}^{\infty} \mathrm{d}\omega_2 \int_{-\infty}^{\infty} \mathrm{d}\tau \mathrm{e}^{-\mathrm{i}\Omega\tau} \int_{-\infty}^{\infty} \mathrm{d}\tau_2' \, \mathrm{e}^{\mathrm{i}\omega\tau_2'} \, M_i^{f\eta}(\tau_2',0) u_\eta \check{\Delta}_i(-\omega_2) \mathrm{e}^{-\mathrm{i}\omega_2(\tau_2'-\tau)} e^\xi M_{\xi g}^i(\tau,0) \mathcal{W}_g(\tau) \right\rangle \ ,\end{aligned} \tag{S30}$$

which becomes after rearranging the integrals

$$\begin{aligned}&\mathcal{R}(\Omega,\omega) = \\ &\left\langle \frac{1}{T} \int_{-\infty}^{\infty} \mathrm{d}\,\omega_1 \check{\Delta}_j(\omega_1) \int_{-\infty}^{\infty} \mathrm{d}\tau' \, \mathrm{e}^{-\mathrm{i}(\omega_1-\Omega)\tau'} M_j^{g\zeta}(\tau',0) e_\zeta \int_{-\infty}^{\infty} \mathrm{d}\tau_1' \, \mathrm{e}^{-\mathrm{i}(\omega-\omega_1)\tau_1'} u^\nu M_{\nu f}^j(\tau_1',0) \right. \\ &\left. \int_{-\infty}^{\infty} \mathrm{d}\omega_2 \, \check{\Delta}_i(-\omega_2) \int_{-\infty}^{\infty} \mathrm{d}\tau \mathrm{e}^{-\mathrm{i}(\Omega-\omega_2)\tau} e^\xi M_{\xi g}^i(\tau,0) \mathcal{W}_g(\tau) \int_{-\infty}^{\infty} \mathrm{d}\tau_2' \, \mathrm{e}^{-\mathrm{i}(\omega_2-\omega)\tau_2'} M_i^{f\eta}(\tau_2',0) u_\eta \right\rangle \ .\end{aligned} \tag{S31}$$

Here, one recognizes the Fourier transforms of the dressed transition dipole moments

$$\check{M}_g^f(\Omega) := \int_{-\infty}^{\infty} \mathrm{d}t \, \mathrm{e}^{-\mathrm{i}\Omega t} M_g^f(t,0) \tag{S32}$$

and

$$\check{\mathcal{M}}_g^i(\Omega) := \int_{-\infty}^{\infty} \mathrm{d}t \, \mathrm{e}^{-\mathrm{i}\Omega t} M_g^i(t,0) \mathcal{W}_g(\tau) \tag{S33}$$

leading to a compact expression

$$\mathcal{R}(\Omega,\omega) = \left\langle \frac{1}{T}\int_{-\infty}^{\infty} \mathrm{d}\omega_1 \check{M}_j^{g\zeta}(\omega_1-\Omega)\, e_\zeta \check{\Delta}_j(\omega_1) u^\nu \check{M}_{\nu f}^{j}(\omega-\omega_1) \right. \\ \left. \int_{-\infty}^{\infty} \mathrm{d}\omega_2 \check{M}_i^{f\eta}(\omega_2-\omega)\, u_\eta \check{\Delta}_i(-\omega_2) e^\xi \check{\mathcal{M}}_{\xi g}^{i}(\Omega-\omega_2) \right\rangle \quad . \tag{S34}$$

Finally, defining the gap fluctuation $U_{fg}(\tau) := \Delta E_{fg}(\tau) - \bar{\omega}_{fg}$, where $\bar{\omega}_{fg} := 1/T \int_0^T \mathrm{d}\tau \Delta E_{fg}(\tau)$ is the mean transition frequency along the MD trajectory, enables the definition of

$$\bar{M}_g^f(t,0) \;\; := \;\; D_g^f(t) \exp\left[\mathrm{i}\int_0^t \mathrm{d}\tau U_{fg}(\tau)\right] \quad . \tag{S35}$$

Since this quantity evolves exclusively on the nuclear timescale, its Fourier transform $\check{\bar{M}}_g^f(\Omega)$ can be calculated numerically by standard routines using the MD time step. It is straightforward to show the relation

$$\check{M}_g^f(\Omega) = \check{\bar{M}}_g^f(\Omega - \bar{\omega}_{fg}) \tag{S36}$$

which is used to obtain the RIXS amplitude, Eq. (S34), via numerical available data.

5 Expression for XAS in Fourier space

The derivation follows the logic of that for the RIXS amplitude. After performing an additional integration along an MD trajectory in Eq. (S24), one can exploit the cyclic structure of indices in the dressed dipoles analogously to Eq. (S26), and subsequently the XAS amplitude takes the form

$$\mathcal{X}(\Omega) = \left\langle \frac{1}{T}\int_0^T \mathrm{d}\tau \int_{-\infty}^{\infty} \mathrm{d}t_1\, \mathrm{e}^{\mathrm{i}\Omega t_1} \mathcal{W}_g(\tau) M_f^{g\eta}(t_1+\tau,0) e_\eta e^\xi M_{\xi g}^f(\tau,0) \right\rangle \quad . \tag{S37}$$

If the length T of the trajectory is sufficiently long, one may extend the τ-integration and substitute $\tau' := \tau + t_1$ yielding after rearranging

$$\mathcal{X}(\Omega) = \left\langle \frac{1}{T} \int_{-\infty}^{\infty} \mathrm{d}\tau \, \mathrm{e}^{\mathrm{i}\Omega\tau'} M_f^{g\eta}(\tau', 0) e_\eta \int_{-\infty}^{\infty} \mathrm{d}\tau \mathrm{e}^{-\mathrm{i}\Omega\tau} \mathcal{W}_g(\tau) e^\xi M_{\xi g}^f(\tau, 0) \right\rangle \quad . \tag{S38}$$

With the definitions of the Fourier transform and the mean transition frequency $\bar{\omega}_{fg}$ the XAS amplitude takes the compact form

$$\mathcal{X}(\Omega) = \left\langle \frac{1}{T} \check{M}_f^{g\eta}(\bar{\omega}_{fg} - \Omega) e_\eta e^\xi \check{\mathcal{M}}_{\xi g}^f(\Omega - \bar{\omega}_{fg}) \right\rangle \tag{S39}$$

which can be calculated using available numerical data.

References

(S1) Hess, B.; Kutzner, C.; van der Spoel, D.; Lindahl, E. GROMACS 4: Algorithms for highly efficient, load-balanced, and scalable molecular simulation. *J. Chem. Theory Comput.* **2008**, *4*, 435–447.

(S2) Paesani, F.; Zhang, W.; Case, D. A.; Cheatham, T. E.; Voth, G. A. An accurate and simple quantum model for liquid water. *J. Chem. Phys.* **2006**, *125*, 184507.

(S3) Ivanov, S. D.; Witt, A.; Marx, D. Theoretical spectroscopy using molecular dynamics: theory and application to CH_5^+ and its isotopologues. *Phys. Chem. Chem. Phys.* **2013**, *15*, 10270–10299.

(S4) Perdew, J. P.; Burke, K.; Ernzerhof, M. Generalized gradient approximation made simple. *Phys. Rev. Lett.* **1996**, *77*, 3865–3868.

(S5) Neese, F. The ORCA program system. *Wiley Interdiscip. Rev. Comput. Mol. Sci.* **2012**, *2*, 73–78.

(S6) Weigend, F.; Ahlrichs, R. Balanced basis sets of split valence, triple zeta valence and quadruple zeta valence quality for H to Rn: Design and assessment of accuracy. *Phys. Chem. Chem. Phys.* **2005**, *7*, 3297–3305.

(S7) Almlöf, J.; Taylor, P. R. General contraction of Gaussian basis sets. I. Atomic natural orbitals for first- and second-row atoms. *J. Chem. Phys.* **1987**, *86*, 4070–4077.

(S8) Roos, B. O.; Andersson, K.; Fülscher, M. P.; Malmqvist, P.-Å.; Serrano-Andrés, L.; Pierloot, K.; Merchán, M. *New Methods in Computational Quantum Mechanics*; Adv. Chem. Phys. 93; John Wiley & Sons, Inc., 1996; pp 219–331.

(S9) Kaufmann, K.; Baumeister, W.; Jungen, M. Universal Gaussian basis sets for an optimum representation of Rydberg and continuum wavefunctions. *Journal of Physics B: Atomic, Molecular and Optical Physics* **1989**, *22*, 2223.

(S10) Lee, N.; Petrenko, T.; Bergmann, U.; Neese, F.; DeBeer, S. Probing valence orbital composition with iron Kß X-ray emission spectroscopy. *J. Am. Chem. Soc.* **2010**, *132*, 9715–9727.

(S11) Milne, C.; Penfold, T.; Chergui, M. Recent experimental and theoretical developments in time-resolved X-ray spectroscopies. *Coord. Chem. Rev.* **2014**, *277-278*, 44–68.

(S12) Hjelte, I.; Piancastelli, M. N.; Fink, R. F.; Feifel, R.; Giertz, A.; Wang, H.; Wiesner, K.; Ausmees, A.; Miron, C.; Sorensen, S. L.; Svensson, S. Evidence for ultra-fast dissociation of molecular water from resonant Auger spectroscopy. *Chem. Phys. Lett.* **2001**, *334*, 151–158.

(S13) Lange, K. M.; Aziz, E. F. The hydrogen bond of water from the perspective of soft X-ray spectroscopy. *Chem. Asian J.* **2013**, *8*, 318–327.

(S14) Mukamel, S. *Principles of nonlinear optical spectroscopy*; Oxford University Press, Oxford, 1995.

(S15) May, V.; Kühn, O. *Charge and energy transfer dynamics in molecular systems*; Wiley-VCH, Weinheim, 2011.

[SK2] A time-correlation function approach to nuclear dynamical effects in X-ray spectroscopy

SVEN KARSTEN, SERGEY I. BOKAREV, SAADULLAH G. AZIZ, SERGEI D. IVANOV, and OLIVER KÜHN

Reproduced from S. KARSTEN, S. I. BOKAREV, S. G. AZIZ, S. D. IVANOV, and O. KÜHN, *Journal of Chemical Physics* **146**, 224203 (2017), with the permission of AIP Publishing.

THE JOURNAL OF CHEMICAL PHYSICS **146**, 224203 (2017)

A time-correlation function approach to nuclear dynamical effects in X-ray spectroscopy

Sven Karsten,[1] Sergey I. Bokarev,[1,a)] Saadullah G. Aziz,[2] Sergei D. Ivanov,[1,b)] and Oliver Kühn[1]
[1]*Institute of Physics, Rostock University, Universitätsplatz 3, 18055 Rostock, Germany*
[2]*Chemistry Department, Faculty of Science, King Abdulaziz University, 21589 Jeddah, Saudi Arabia*

(Received 9 February 2017; accepted 19 May 2017; published online 12 June 2017)

Modern X-ray spectroscopy has proven itself as a robust tool for probing the electronic structure of atoms in complex environments. Despite working on energy scales that are much larger than those corresponding to nuclear motions, taking nuclear dynamics and the associated nuclear correlations into account may be of importance for X-ray spectroscopy. Recently, we have developed an efficient protocol to account for nuclear dynamics in X-ray absorption and resonant inelastic X-ray scattering spectra [Karsten *et al.*, J. Phys. Chem. Lett. **8**, 992 (2017)], based on ground state molecular dynamics accompanied with state-of-the-art calculations of electronic excitation energies and transition dipoles. Here, we present an alternative derivation of the formalism and elaborate on the developed simulation protocol using gas phase and bulk water as examples. The specific spectroscopic features stemming from the nuclear motions are analyzed and traced down to the dynamics of electronic energy gaps and transition dipole correlation functions. The observed tendencies are explained on the basis of a simple harmonic model, and the involved approximations are discussed. The method represents a step forward over the conventional approaches that treat the system in full complexity and provides a reasonable starting point for further improvements. *Published by AIP Publishing.* [http://dx.doi.org/10.1063/1.4984930]

I. INTRODUCTION

Understanding complex phenomena arising in physical chemistry requires unraveling the underlying processes on an atomistic level. Due to the energetic separation of the core levels of different elements and the compact nature of the corresponding orbitals, X-ray spectroscopy can reveal highly local and element-specific information on the electronic structure of an absorbing atom and on its interaction with the environment.[1] In particular, X-ray absorption spectra (XAS) probe those electronic transitions, where a core electron is excited to the unoccupied molecular orbitals (MOs), whereas resonant inelastic X-ray scattering (RIXS) detects the emission signal resulting from the refill of the core hole by electrons from occupied MOs. Thus, the combination of both approaches provides detailed information on the electronic structure of a sample in different aggregation states.[2,3]

Along with the improvement of the instrumental resolution in X-ray spectroscopic studies, not only electronic but also the vibrational transitions have recently attracted growing attention.[4,5] In Ref. 6, RIXS has been even regarded to be a complementary technique to the conventional vibrational infrared and Raman spectroscopies. Although X-ray scattering processes occur during few femtoseconds due to the typically short lifetimes of core-excited states, indications of ultrafast nuclear dynamics could be observed. For instance, the inclusion of vibronic effects in RIXS spectra as well as coherences between vibrational levels has been found essential for the correct assignment of spectral features in simple model systems.[7,8] Further, dissociative dynamics on the timescale of the RIXS scattering process[9–11] has also been detected. The RIXS spectra of liquid water and alcohols initiated active debates in the last decade due to the splitting of the $1b_1$ band, which is not observed in the photoelectron spectra.[12–15] Remarkably, this peculiar effect received controversial interpretation resulting in six hypotheses,[16] with four of them involving different aspects of nuclear dynamics, such as ultrafast dissociation and H-bond dynamics. Thus, the necessity for a robust theoretical treatment of nuclear vibrational effects becomes apparent.

Since solving the electronic-nuclear Schrödinger equation is feasible only for rather small model systems,[17] different approximate schemes are commonly applied. Frequently, electronic spectra are obtained via single point electronic structure calculations combined with phenomenological broadening for the vibrational environmental effects, thereby neglecting peculiarities of the underlying microscopic dynamics, see, e.g., Ref. 18. A popular extension to this approach that explicitly includes nuclear vibrations is to assume the shifted harmonic potentials for the initial and final electronic states, leading to the analytical Franck-Condon description.[7,19–22] However, this approach is not appropriate for cases where strong anharmonicities, bond formation or cleavage, and/or pronounced conformational changes are present. Here,

a) Electronic mail: sergey.bokarev@uni-rostock.de
b) Electronic mail: sergei.ivanov@uni-rostock.de

real-time propagation of a nuclear wavepacket on pre-calculated potential energy surfaces improves on the purely harmonic description.[8,21,23,24] Nevertheless, the construction of such multidimensional potentials as well as the wavepacket propagation itself is practically unfeasible for large numbers of highly-excited electronic states (relevant for RIXS spectra) and nuclear degrees of freedom.

Trajectory-based approaches have become very popular in the last two decades in theoretical chemistry.[25,26] In this context, classical molecular dynamics (MD) method employing forces according to the electronic ground state has proven itself as a versatile approach to incorporate and analyze the spectral fingerprints of nuclear dynamics in (non-)linear infrared to ultraviolet spectroscopies.[19,25,27,28] Extending this methodology to the X-ray range and performing quantum-chemical static point calculations for each MD snapshot allows one to utilize nuclear distributions in the phase space, leading to a more realistic description of conformational and environmental effects.[18,29–31] However, this sampling approach is capable of describing a distribution of structural motifs only, without any (time-ordered) nuclear correlation, and a truly time-domain approach is needed to account for both statical and dynamical effects. Interestingly, these effects could be disentangled from each other experimentally, employing RIXS with excitation pulses strongly detuned from the resonance.[14]

Recently, we have suggested a trajectory-based time-domain approach for calculating XAS and RIXS amplitudes, which is an improvement on the state-of-the-art sampling approaches. The method employs the nuclear time evolution provided by electronic ground state MD simulations. With the help of the developed protocol, we were able to demonstrate the importance of nuclear correlation effects on the example of a gas phase water molecule.[32] Here, we present an alternative but still rigorous derivation for the formalism, starting from Fermi's golden rule and the Kramers-Heisenberg expression for XAS and RIXS amplitudes, respectively, followed by employing the interaction representation picture and the dynamical classical limit[19,33] as is described in Sec. II. To retain nuclear correlations, one has to trace the entire manifold of relevant electronic levels along the MD trajectory in order to eliminate possible order and phase alterations. A fully-automated procedure serving this purpose has been developed as is illustrated in Secs. III and IV. The established protocol is exemplified by oxygen K-edge XAS and RIXS of gas phase and bulk water. However, in the present article we mainly focus on methodological aspects rather than on the particular application and, thus, the obtained results have been compared against those of the sampling approach, not focusing on the peculiarities of water X-ray spectra, see Sec. V. Importantly, the sources of the observed differences have been extensively analyzed.

The developed correlation-function technique provides a step forward in the description of nuclear dynamical effects in various X-ray spectroscopies. It can be applied to generally anharmonic systems treating them in full dimensionality, that is, without scanning potential energy surfaces. The limitations of the method are summarized in Sec. V C, and conclusions are presented in Sec. VI.

II. THEORY

A. Setting the stage

Let us consider a molecular system consisting of electrons represented by Cartesian positions $\hat{\mathbf{r}}$ and momenta $\hat{\mathbf{p}}$ and nuclei described, respectively, by $\hat{\mathbf{R}}$ and $\hat{\mathbf{P}}$. In the framework of the Born-Oppenheimer approximation (BOA), an eigenstate of the total Hamiltonian, having the energy ϵ_α, factorizes as $|\alpha\rangle = |a\rangle|A\rangle$; here and in the following nuclear states denoted with a capital letter correspond to an electronic state indicated with the same small letter, e.g., a set of nuclear states $|A\rangle$ belongs to the electronic state $|a\rangle$. The respective electronic energies are given as the solutions of the electronic time-independent Schrödinger equation (TISE)

$$\hat{H}_{\mathrm{el}}(\hat{\mathbf{r}}, \hat{\mathbf{p}}, \hat{\mathbf{R}})|a\rangle = \hat{E}_a(\hat{\mathbf{R}})|a\rangle, \tag{1}$$

where $\hat{H}_{\mathrm{el}}$ is the electronic Hamiltonian, see, e.g., Ref. 19. Finally, the nuclear state $|A\rangle$ is an eigenstate of the Hamiltonian $\hat{H}_a(\hat{\mathbf{R}}, \hat{\mathbf{P}}) := \hat{H}_{\mathrm{nuc}}(\hat{\mathbf{R}}, \hat{\mathbf{P}}) + \hat{E}_a(\hat{\mathbf{R}})$ with the eigenvalue ϵ_A

$$\hat{H}_a|A\rangle = \epsilon_A|A\rangle, \tag{2}$$

with $\hat{H}_{\mathrm{nuc}}$ consisting of the nuclear kinetic and potential (Coulomb) energy operators.[19]

In the following, atomic units will be used and the arguments of the operators will be skipped unless the dependency has to be emphasized. In general, the indices stemming from electronic bra-states appear in superscript, whereas the subscript ones correspond to the ket-states. For the sake of brevity, the notation $c^\xi := c^*_\xi$ for any indexed complex quantity and $\hat{A}^\xi := \hat{A}^\dagger_\xi$ for any indexed operator (vector) is used throughout the manuscript. Furthermore, the Einstein notation is employed; that is, indices that appear as a subscript *and* as a superscript are summed over.

B. The XAS amplitude

In this section, the derivation of a time-domain expression for the XAS amplitude is presented in detail. We opted to present it because of its relative simplicity, rather than the derivation of a perhaps more interesting but cumbersome expression for the RIXS amplitude. Still the present derivation contains all the necessary steps and can thus serve as a roadmap for deriving the RIXS amplitude in the time domain. The latter is presented here only schematically with all the details left for the supplementary material. In contrast to the derivation presented in the supplementary material of Ref. 32, we do not employ optical response functions here.

1. The quantum expression

The process under study consists of exciting the system from an initial state $|\gamma\rangle$ to a final state $|\phi\rangle$ by absorbing light with angular frequency Ω and polarization vector with the Cartesian components e_ξ, see the left panel in Fig. 1. Following Fermi's golden rule, the X-ray absorption spectrum is proportional to the XAS amplitude that can be written down with the help of the notations introduced in Sec. II A as

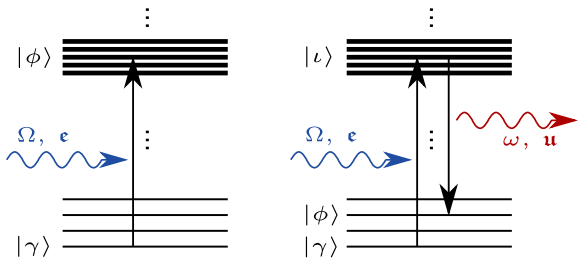

FIG. 1. Schematic sketch of XAS (left) and RIXS (right) processes.

$$\mathcal{X}(\Omega) = \sum_{\gamma,\phi} \frac{\mathrm{e}^{-\beta\epsilon_\gamma}}{Z} \left|\langle\phi|\mathrm{e}^{\xi}\hat{d}_\xi|\gamma\rangle\right|^2 \delta\left(\Omega - (\epsilon_\phi - \epsilon_\gamma)\right), \quad (3)$$

where $\beta := 1/(k_\mathrm{B}T)$ is the inverse temperature, k_B is the Boltzmann constant, $Z := \sum_\gamma \exp[-\beta\epsilon_\gamma]$ is the canonical partition function, and $\hat{d}_\xi$ is the ξ-th component of the dipole operator. The Dirac δ-function ensures the energy conservation during the process.

In order to formulate the time-domain version of Eq. (3), the δ-function is represented as the time integral

$$\delta\left(\Omega - \Omega_0\right) = \frac{1}{2\pi}\int_{-\infty}^{\infty} \mathrm{d}t\, \mathrm{e}^{\mathrm{i}(\Omega-\Omega_0)t}, \quad (4)$$

yielding

$$\mathcal{X}(\Omega) = \frac{1}{2\pi Z}\sum_{\gamma,\phi}\int_{-\infty}^{\infty} \mathrm{d}t\, \mathrm{e}^{\mathrm{i}(\Omega-(\epsilon_\phi-\epsilon_\gamma))t} \times \mathrm{e}^{-\beta\epsilon_\gamma}\langle\gamma|\hat{d}^\eta \mathrm{e}_\eta|\phi\rangle\langle\phi|\mathrm{e}^{\xi}\hat{d}_\xi|\gamma\rangle \quad (5)$$

in the fashion similar to the derivation of the infrared and UV/Vis spectroscopies.[19,34–37] Alternatively, this expression follows from time-dependent perturbation theory as is exercised in Ref. 33, see also Ref. 32. Note that in order to keep notations as compact as possible the transition dipoles are assumed to be projected on the polarization vector and the corresponding coordinate indices ξ and η are dropped throughout the theory section without any loss of generality. They will be restored in the final expressions.

Applying the BOA leads to the aforementioned factorization of the states: $|\gamma\rangle = |g\rangle|G\rangle$ and $|\phi\rangle = |f\rangle|F\rangle$, which after rearranging the complex exponential in Eq. (5) yields

$$\mathcal{X}(\Omega) = \frac{1}{2\pi Z}\sum_{G,F}\int_{-\infty}^{\infty} \mathrm{d}t\, \mathrm{e}^{\mathrm{i}\Omega t} \times\langle G|\mathrm{e}^{-\beta\epsilon_G}\mathrm{e}^{\mathrm{i}\epsilon_G t}\hat{D}_f^g\mathrm{e}^{-\mathrm{i}\epsilon_F t}|F\rangle\langle F|\hat{D}_g^f|G\rangle, \quad (6)$$

where $\hat{D}_b^a(\hat{\mathbf{R}}) := \langle a|\hat{d}(\hat{\mathbf{r}},\hat{\mathbf{R}})|b\rangle$ is the electronic transition dipole moment that remains an operator in the nuclear space. In order to obtain the time evolution for the dipole operator, one may substitute the energies ϵ_F and ϵ_G, being the eigenvalues of $\hat{H}_f$ and $\hat{H}_g$, correspondingly, see Eq. (2), by the operators themselves. Since after this substitution there is no dependence on the final nuclear states left in Eq. (6), one may employ the closure for $|F\rangle$ to eliminate the projectors $|F\rangle\langle F|$, leading to

$$\mathcal{X}(\Omega) = \frac{1}{2\pi Z}\int_{-\infty}^{\infty} \mathrm{d}t\, \mathrm{e}^{\mathrm{i}\Omega t}\sum_G \langle G|\mathrm{e}^{-\beta\hat{H}_g}\mathrm{e}^{\mathrm{i}\hat{H}_g t}\hat{D}_f^g\mathrm{e}^{-\mathrm{i}\hat{H}_f t}\hat{D}_g^f|G\rangle. \quad (7)$$

The mission to obtain a practical time-domain analogue of Eq. (3) would be accomplished if $\hat{H}_f$ coincided with $\hat{H}_g$. This difference can be circumvented by the following steps. First, one rewrites $\hat{H}_f = \hat{H}_0 + \Delta\hat{E}_{f0}$, $\Delta\hat{E}_{f0} := \hat{E}_f - \hat{E}_0$ with the index 0 standing for the electronic ground state. Second, the energy gap is treated as a perturbation operator that enables switching to the interaction representation[19,33]

$$\mathrm{e}^{-\mathrm{i}\hat{H}_f t} = \mathrm{e}^{-\mathrm{i}\hat{H}_0 t}\hat{S}_f(t,0), \quad (8)$$

where the scattering operator is defined as

$$\hat{S}_f(t,t_0) := \exp_+\left[-\mathrm{i}\int_{t_0}^{t}\mathrm{d}\tau\,\Delta\hat{E}_{f0}(\tau)\right]. \quad (9)$$

The symbol $\exp_+$ in Eq. (9) represents a (positively) time-ordered exponential. The time argument of the integrand therein stands for the time evolution according to the Heisenberg equation of motion with respect to the electronic ground state Hamiltonian, $\hat{H}_0$. The equations for $|g\rangle$ can be obtained by taking the adjoint from Eqs. (8) and (9) and substituting f by g. Importantly, the choice of the electronic ground state as the reference is motivated by the initial condition before absorbing a photon and is beneficial in view of potential use of classical MD methods, which are available mostly for the ground state.

Utilizing the interaction representation, Eq. (8), for the XAS amplitude yields

$$\mathcal{X}(\Omega) = \frac{1}{2\pi Z}\int_{-\infty}^{\infty} \mathrm{d}t\, \mathrm{e}^{\mathrm{i}\Omega t}\sum_G \Big\langle G|\mathrm{e}^{-\beta\hat{H}_g(0)}\hat{S}^g(t,0) \times\hat{D}_f^g(t)\hat{S}_f(t,0)\hat{D}_g^f(0)|G\Big\rangle. \quad (10)$$

Introducing the "dressed" dipole moment

$$\hat{M}_b^a(t,0) := \hat{S}^a(t,0)\hat{D}_b^a(t)\hat{S}_b(t,0) \quad (11)$$

leads to a compact form for the XAS amplitude

$$\mathcal{X}(\Omega) = \frac{1}{2\pi Z}\int_{-\infty}^{\infty} \mathrm{d}t\, \mathrm{e}^{\mathrm{i}\Omega t}\sum_G \Big\langle G|\mathrm{e}^{-\beta\hat{H}_g(0)}\hat{M}_f^g(t,0)\hat{M}_g^f(0,0)|G\Big\rangle, \quad (12)$$

where we have used that $\hat{M}_g^f(0,0) \equiv \hat{D}_g^f(0)$.

2. The dynamical classical limit

In order to utilize well-established classical MD methods in combination with state-of-the-art quantum chemistry tools, the quantum mechanical expression for the XAS amplitude, Eq. (12), is subjected to the dynamical classical limit for the nuclei.[19,33] In particular, the nuclei are represented by point particles and the operators are replaced by continuous dynamical functions. Consequently, the trace over the initial nuclear states $|G\rangle$ is substituted by an integral over the phase

space and time-evolved operators become dynamic functions. Naturally, the time ordering of exponentials in Eq. (9) becomes irrelevant and disappears.

Performing all these replacements in Eq. (12) results in

$$\mathcal{X}(\Omega) = \frac{1}{2\pi Z}\int_{-\infty}^{\infty} \mathrm{d}t\, \mathrm{e}^{\mathrm{i}\Omega t} \times \iint \mathrm{d}\mathbf{R}_0 \mathrm{d}\mathbf{P}_0 \mathrm{e}^{-\beta H_g(0)} M_f^g(t,0) M_g^f(0,0), \tag{13}$$

where Z becomes the sum of *classical* partition functions corresponding to potential energy surfaces of all electronic states in question, $Z = \sum_g \iint \mathrm{d}\mathbf{R}_0 \mathrm{d}\mathbf{P}_0 \exp[-\beta H_g(0)]$. Since the aim is to use classical MD methods, the observables should have the form of a canonical ensemble average, $\langle \bullet \rangle$, with respect to the Hamilton function of the electronic ground state

$$\langle A \rangle := \frac{1}{Z_0} \iint \mathrm{d}\mathbf{R}_0 \mathrm{d}\mathbf{P}_0\, \mathrm{e}^{-\beta H_0(\mathbf{R}_0,\mathbf{P}_0)} A(\mathbf{R}_0,\mathbf{P}_0), \tag{14}$$

where $Z_0 := \iint \mathrm{d}\mathbf{R}_0 \mathrm{d}\mathbf{P}_0 \exp[-\beta H_0(\mathbf{R}_0,\mathbf{P}_0)]$. Using the standard trick of adding and subtracting H_0 and performing some simple algebra leads to

$$\mathcal{X}(\Omega) = \frac{1}{2\pi}\int_{-\infty}^{\infty} \mathrm{d}t\, \mathrm{e}^{\mathrm{i}\Omega t} \left\langle \mathcal{W}_g(0) M_f^{g\eta}(t,0) \mathrm{e}_\eta \mathrm{e}^{\xi} M_{\xi g}^f(0,0) \right\rangle, \tag{15}$$

where the omitted polarization vectors have been restored. Here, the weighting function is

$$\mathcal{W}_g(0) := \mathrm{e}^{-\beta[\Delta E_{g0}(0)]}/\mathcal{Z} \tag{16}$$

with the normalization factor

$$\mathcal{Z} := \left\langle \sum_g \mathrm{e}^{-\beta[\Delta E_{g0}(0)]} \right\rangle, \tag{17}$$

see supplementary material. Equation (15) for the XAS amplitude has the desired form of the Fourier transform of an equilibrium time correlation function.

C. The RIXS amplitude

It was pointed out in the Introduction that the XAS spectra considered above correspond to one-photon processes, whereas more information can be obtained from a two-photon process, e.g., RIXS. Here, the system is first excited from the initial state $|\gamma\rangle$ to an intermediate state $|\iota\rangle$ by absorbing light with a frequency Ω and a polarization vector with the components e_ξ, see the right panel in Fig. 1. Second, the system transits from the state $|\iota\rangle$ to the final state $|\phi\rangle$ by emitting light with the frequency ω and the polarization vector with components u_η.

Following Kramers and Heisenberg, the RIXS amplitude reads[38]

$$\mathcal{R}(\Omega,\omega) = \sum_{\gamma,\phi} \frac{\mathrm{e}^{-\beta\epsilon_\gamma}}{Z} \left| \sum_\iota \frac{\langle\phi|\hat{d}^\eta \mathrm{u}_\eta|\iota\rangle\langle\iota|\mathrm{e}^\xi \hat{d}_\xi|\gamma\rangle}{\Omega - (\epsilon_\iota - \epsilon_\gamma) + \mathrm{i}\Gamma_\iota} \right|^2 \times \delta\left(\Omega - (\epsilon_\phi - \epsilon_\gamma + \omega)\right), \tag{18}$$

where the dephasing rate Γ_ι takes into account the finite lifetime of the state $|\iota\rangle$. This implies that intricate electron-nuclear dynamics therein, including non-radiative relaxation mechanisms, such as the Auger one, is modeled by a simple mono-exponential decay. Note that the sum in Eq. (18) is under the square; thereby, coherences are taken into account.

In order to get a classical time-domain expression for RIXS, the same pathway as for XAS is followed, as is summarized below and detailed in the supplementary material. To start, the integral representation of a δ-function, Eq. (4), is employed. Additionally, the denominator in Eq. (18) is recast into the time domain via

$$\frac{1}{\omega - \omega_0 \pm \mathrm{i}\Gamma_\alpha} = \mp\mathrm{i}\int_{-\infty}^{\infty} \mathrm{d}t\, \mathrm{e}^{\pm\mathrm{i}(\omega-\omega_0)t} \Delta_\alpha(t), \tag{19}$$

with the damping function

$$\Delta_\alpha(t) := \mathrm{e}^{-\Gamma_\alpha t}\theta(t), \tag{20}$$

where $\theta(t)$ is the Heaviside step function. The latter is introduced in order to have the integrations from $-\infty$ to ∞. Further, the BOA is applied and the lifetimes of the intermediate states are assumed to depend on the corresponding electronic level only, i.e., $\Gamma_\alpha = \Gamma_a$. Then the interaction representation is employed in order to obtain the time evolution for the dipole operators with respect to the electronic ground state, see Eqs. (8) and (9). To formulate a practical recipe involving classical MD methods, the dynamical classical limit is performed for nuclear degrees of freedom following Sec. II B 2. Finally, the resulting RIXS amplitude possesses the form of a multi-time integral over the classical canonical average with respect to the electronic ground state Hamilton function

$$\mathcal{R}(\Omega,\omega) = \frac{1}{2\pi}\int_{-\infty}^{\infty} \mathrm{d}t\, \mathrm{e}^{\mathrm{i}\Omega t} \int_{-\infty}^{\infty} \mathrm{d}\tau_1\, \mathrm{e}^{-\mathrm{i}\omega(t+\tau_1)} \int_{-\infty}^{\infty} \mathrm{d}\tau_2\, \mathrm{e}^{\mathrm{i}\omega\tau_2} \times \left\langle \mathcal{W}_g(0) M_j^{g\zeta}(t,0) \mathrm{e}_\zeta \Delta_j(\tau_1) \mathrm{u}^\nu M_{\nu f}^j(t+\tau_1,0) \times M_i^{f\eta}(\tau_2,0) \mathrm{u}_\eta \Delta_i(\tau_2) \mathrm{e}^\xi M_{\xi g}^i(0,0) \right\rangle. \tag{21}$$

This expression for the RIXS amplitude together with the one for the XAS amplitude, Eq. (15), is the central theoretical result of this work. These expressions coincide with the ones derived via optical response functions in Ref. 32. Similar to the corresponding analogues in the UV/Vis domain,[33,34,39] these expressions provide a general and unified framework for simulating XAS and RIXS amplitudes.

III. METHODOLOGY

A. Tracing the states

In this section, we aim at formulating practical recipes for evaluating the time-domain expressions for the XAS and RIXS amplitudes, Eqs. (15) and (21). One notices that both are fully determined by the time evolution of the transition dipole moments, $D_{\xi b}^a(t)$, and the electronic energies, $E_a(t)$. To reiterate, the evolution is carried out with respect to the electronic ground state potential energy surface.

Unfortunately, the functional dependence of the aforementioned ingredients on nuclear coordinates is not available for any realistic many-particle system. A possible solution is

to solve the TISE at each MD timestep independently using any established quantum-chemistry method. This, however, would lead to two problems. First, the numbering of the eigenvalues is arbitrary at any time instance. Second, the phases of the eigenstates are ambiguous. Ignoring these obstacles would ultimately destroy the dynamical correlation effects that are the essence of the developed formalism. Thus, evaluating the time correlation functions requires tracing the states along MD trajectories, in order to have a continuous evolution of the respective energies and phases. Technically, the order and phases can be fixed at $t=0$ and then followed by identifying the states of the same character at future times.

In order to find a mapping of an unordered set of states $\{|\tilde{b}(t)\rangle\}$ onto the desired ordered set $\{|a(t)\rangle\}$, one can formally make the expansion

$$|a(t)\rangle = \sum_{\tilde{b}} \langle \tilde{b}(t)|a(t)\rangle\, |\tilde{b}(t)\rangle, \tag{22}$$

assuming that both sets are complete. Then, one can define a generalized permutation matrix, $\mathbf{Y}(t)$, with elements $Y_a^{\tilde{b}}(t) := \langle \tilde{b}(t)|a(t)\rangle$ that brings any unordered observable, $\tilde{A}_{\tilde{c}}^{\tilde{d}}(t)$, to the correct order via $A_a^b(t) = Y_{\tilde{d}}^b(t)\tilde{A}_{\tilde{c}}^{\tilde{d}}(t)Y_a^{\tilde{c}}(t)$. Note that the matrix $\mathbf{Y}(t)$ contains only one non-zero (complex unity) element per column *and* row by construction.

Since the correctly ordered set of states $\{|a(t)\rangle\}$ is not available, one can start at $t=0$ and to approximate the respective matrix elements as

$$Y_a^{\tilde{b}}(\Delta t) \approx O_a^{\tilde{b}}(\Delta t, 0) := \langle \tilde{b}(\Delta t)|a(0)\rangle, \tag{23}$$

where Δt is the next time instance, e.g., next MD timestep. Since $O_a^{\tilde{b}}(\Delta t, 0)$ might contain many non-zero contributions per row/column, one finds a maximal one in each column of $\mathbf{O}(\Delta t, 0)$, normalizes this (complex) number to unity, and sets the other to zero. In order to verify the uniqueness of the result, the same procedure is performed row-wise. If this self-consistency check is failed, it implies that the MD timestep is too large and has to be reduced. The restored set of states at $t = \Delta t$ serves as a basis for ordering the states at $t = 2\Delta t$ and so on along the MD trajectory. Since similar problems arise in surface hopping methods,[40] the developed procedure might be of use there as well.

B. An efficient evaluation of XAS and RIXS amplitudes

The XAS amplitude, Eq. (15), is the Fourier transform of an equilibrium time correlation function. Moreover, the RIXS amplitude, Eq. (21), contains a multi-time correlation function and three time integrations, only one of those being decoupled from the other two. This implies calculating a two-dimensional time integral on top of evaluating the correlation functions (each being a nested time integration as well). A handy way of making this numerically efficient can be adopted from vibrational spectroscopy,[27] where the stationarity of the canonical density is utilized implying that any time instance can be considered as the starting one. Integrating over all initial times with the help of the convolution theorem leads to XAS and RIXS amplitudes in a form of products of the Fourier-transformed (indicated by the reversed hat) dressed dipole moments

$$\check{M}_g^f(\Omega) = \int_{-\infty}^{\infty} \mathrm{d}t\, \mathrm{e}^{-\mathrm{i}\Omega t} D_g^f(t) \mathrm{e}^{\mathrm{i}\int_0^t \mathrm{d}\tau \Delta E_{fg}(\tau)}, \tag{24}$$

see supplementary material for details. Note that in the dynamical classical limit, the energy gap between the excited and the electronic ground states is canceled out, and only the gap between the states f and g remains in the exponent. Since the complex exponential depending on the energy gap oscillates on the electronic timescale, which is not accessible by MD, the common recipe for separating the highly oscillating contribution is employed.[19] One defines the mean transition frequency between two electronic states f and g as the average along the trajectory of a total length T, $\bar{\omega}_{fg} := 1/T \int_0^T \mathrm{d}\tau \Delta E_{fg}(\tau)$, and the gap fluctuation as $U_{fg}(\tau) := \Delta E_{fg}(\tau) - \bar{\omega}_{fg}$. Substituting them into Eq. (24) leads to

$$\check{M}_g^f(\Omega) \equiv \check{\bar{M}}_g^f(\Omega - \bar{\omega}_{fg}), \tag{25}$$

where $\bar{M}_g^f(t,0) := D_g^f(t) \exp[\mathrm{i}\int_0^t \mathrm{d}\tau U_{fg}(\tau)]$. The bars above the quantities generally indicate that the mean electronic gap has been removed and they evolve on the nuclear time scale and, thus, can be Fourier-transformed using the data provided by MD.

Finally, with the help of the convolution theorem, the XAS amplitude can be expressed as a product

$$\mathcal{X}(\Omega) = \frac{1}{2\pi T} \left\langle \check{\bar{M}}_f^g(\bar{\omega}_{fg} - \Omega) \check{\bar{\mathcal{M}}}_g^f(\Omega - \bar{\omega}_{fg}) \right\rangle, \tag{26}$$

where $\bar{\mathcal{M}}_g^f(t,0) := \mathcal{W}_g(t) D_g^f(t) \exp[\mathrm{i}\int_0^t \mathrm{d}\tau U_{fg}(\tau)]$; note the different signs in the argument of the two functions in Eq. (26).

Following the same approach, the RIXS amplitude can be reformulated as

$$\begin{aligned}\mathcal{R}(\Omega,\omega) = \frac{1}{2\pi T} \Bigg\langle & \int_{-\infty}^{\infty} \mathrm{d}\omega_1 \check{\bar{M}}_j^g \left(\bar{\omega}_{jg} - [\Omega - \omega_1]\right) \check{\Delta}_j(\omega_1) \\ & \times \check{\bar{M}}_f^j \left([\omega - \omega_1] - \bar{\omega}_{jf}\right) \\ & \times \int_{-\infty}^{\infty} \mathrm{d}\omega_2 \check{\bar{\mathcal{M}}}_g^i \left([\Omega - \omega_2] - \bar{\omega}_{ig}\right) \check{\Delta}_i(-\omega_2) \\ & \times \check{\bar{M}}_i^f \left(\bar{\omega}_{if} - [\omega - \omega_2]\right) \Bigg\rangle, \end{aligned} \tag{27}$$

where $\check{\Delta}_j(\omega) := 1/(2\pi)\sqrt{\Gamma_j/\pi}(\Gamma_j + \mathrm{i}\omega)^{-1}$. Here, one still has to perform a convolution due to the finite lifetime of the intermediate states.

To sum up, the calculation of both spectra is accomplished by performing single-variable integrations using the MD timestep. It is worth mentioning that this structure of the final result naturally enables identifying the contribution from any particular initial, intermediate, and/or final state. Note also that identifying the contributions from the underlying geometrical motifs can be performed analogously to vibrational spectroscopy.[41,42]

C. Sampling and time-domain approaches

As it has been stated in the Introduction, the conventional approach to the X-ray amplitudes, Eqs. (3) and (18), is based

on static single point calculations for structures sampled from statistical ensembles. Note that the sampling amplitudes, which correspond to the limit of fixed nuclei of the respective time-domain expressions, can be brought to the same functional form as the latter, see supplementary material. This makes the analysis of the contributions of the nuclear dynamics, performed via comparison of the time-domain results to their sampling counterparts, convenient, see Sec. V B. In order to conduct a fair comparison, the sampling procedure and the time-domain method have employed identical large data sets.

IV. COMPUTATIONAL DETAILS

The MD simulations have been performed using the Gromacs program package ver. 4.6.5[43] employing the anharmonic qSPC/Fw water model with a Morse potential for the O–H intra-molecular potential.[44] The "standard protocol"[27] for calculating spectra in the canonical ensemble has been used, that is, a set of uncorrelated initial conditions has been generated from an *NVT* MD run with the target temperature of 300 K imposed by the Langevin thermostat. These initial conditions have been further used as starting points for simulating micro-canonical (*NVE*) trajectories, each 0.5 ps long, yielding a spectral resolution of ≈8 meV. The MD timestep of 0.1 fs has been used to provide a successful tracing of the states as described in Sec. III A. The spectra calculated along the *NVE* trajectories have been averaged to yield the result for the canonical ensemble.

Two systems have been considered: (a) an isolated water molecule, referred to as gas phase water; (b) a cubic box consisting of 466 water molecules under periodic boundary conditions with the box edge length of 2.4 nm, which corresponds to a density of 1.0 g/cm^3, referred to as bulk water.

The TISE [Eq. (1)] has been solved for each MD snapshot at the level of the ground state density functional theory with the Perdew-Burke-Ernzerhof functional[45] using the ORCA ver. 3.0.3 program package.[46] Tight convergence criteria (10^{-7} hartree) and a standard grid (ORCA grid3) have been employed. The def2-QZVPP basis set for oxygen and hydrogen[47] together with (5s5p)/[1s1p] generally contracted Rydberg functions on oxygen have been used. Rydberg contractions have been obtained as atomic natural orbitals[48,49] constructed of primitives with universal exponents (see Ref. 50). Such a small Rydberg basis does not allow one to reproduce the high-energy tail of the absorption spectrum[51] but enables description of the lowest states just above the core-excitation threshold. The energies of the singly-excited valence and core states have been approximated by the differences of the respective Kohn-Sham orbital energies; the corresponding dipole transition moments have been calculated with respect to these orbitals.[52] This approximate quasi–one-electron method could be a reasonable compromise between accuracy and efficiency, as has been demonstrated for various kinds of systems.[7,51–54] It will be shown that it still yields a satisfactory agreement with experimental data for the present case, see Secs. V and V C for a discussion.

In order to achieve a feasible treatment of the bulk system, a hybrid quantum mechanics/molecular mechanics (QM/MM) partitioning has been performed. For each snapshot *and* each selected molecule individually, the whole simulation box has been translated to the mass centre frame of that molecule which has been further treated via the QM method. The atoms of all surrounding molecules have been considered as classical point charges that enter the QM calculation via a static external potential.

Since the QM calculations here are to be performed for an isolated (hence non-periodic) system, surface effects due to the finite box have been "smoothed out" by applying a spherically symmetric cutoff function $f(r)$ to the charges, i.e.,

$$f(r) := \begin{cases} 1, r < R_{\text{in}} \\ \dfrac{2(r-R_{\text{in}})^3}{(R_{\text{out}}-R_{\text{in}})^3} - \dfrac{3(r-R_{\text{in}})^2}{(R_{\text{out}}-R_{\text{in}})^2} + 1, R_{\text{in}} \le r \le R_{\text{out}}, \\ 0, r > R_{\text{out}} \end{cases} \tag{28}$$

with a smoothing region $[R_{\text{in}}, R_{\text{out}}]$, where r is the distance from the origin to the mass center of a surrounding water molecule. We have employed the values $R_{\text{in}} = 5$ Å and $R_{\text{out}} = 8$ Å to safely include all charges in the first solvation shell. In order to preserve the charge neutrality of the entire system the same function value has been applied to all point charges belonging to the same molecule. Convergence has been reached employing 120 trajectories for gas phase water and 70 for bulk water.

In order to mimic the finite width σ of the exciting light pulse, as given by experimental conditions, the spectra, Eqs. (15) and (21), have been convoluted with normalized Gaussian functions $\exp[-\Omega^2/(2\sigma^2)]/(\sqrt{2\pi\sigma^2})$ in Ω-direction with $\sigma = 0.025$ eV and $\sigma = 0.25$ eV as typical small and large widths, respectively.[55] Naturally the effects in question should be mostly pronounced when σ is small. However, it is important to also demonstrate them for large values of σ, when vibronic features are smeared out. Additionally, the XAS amplitude has been convoluted with normalized Lorentzian functions $\Gamma_f/\pi \cdot [\Gamma_f^2 + \Omega^2]^{-1}$ taking into account the finite lifetime of the core-excited final states. For the results in Sec. V, the value $\Gamma_a = 0.25$ fs^{-1}, as a typical decay rate for core holes,[56] has been used for all final states entering the XAS amplitude as well as for all intermediate states entering the RIXS amplitude, where the finite lifetime is already accounted for by construction, see Eqs. (18) and (21).

The number of considered states that contribute to the spectra is determined by the absorption and emission frequency range of interest. Here, $\Omega \in [532.8, 540.8]$ eV and $\omega \in [509.8, 540.8]$ eV requires the consideration of 31 states for both water setups. Note that all spectra have been shifted *globally* by 24.8 eV such that the peak structure roughly matches the experimental data for bulk and gas phase water.[13] Finally, the data shown in Sec. V correspond to an average over orthogonal polarizations of the incoming and the emitted light[57,58] owing to the isotropy of the gas and liquid phases.

V. RESULTS AND DISCUSSION

The proposed methodology has been first suggested by us in Ref. 32 and applied to K-edge oxygen spectra of a gas phase

water molecule. Nuclear correlation effects have been demonstrated to be essential for second-order X-ray spectroscopy. In particular, RIXS has turned out to be a sensitive technique for the effects in question, whereas XAS exhibited almost no traces of the underlying nuclear dynamics. However, the origin of the observed phenomena has not been analyzed and will be the main concern here.

A. XAS

In this section, the results for the XAS amplitude obtained via various simulation scenarios are discussed and compared against each other. We would like to stress again that the focus is put on the differences due to nuclear dynamics rather than on the peculiarities of the water spectra themselves, see Ref. 15 and references therein.

In Fig. 2 the XAS amplitudes for the small (σ = 0.025 eV) and the large (σ = 0.25 eV) width of the excitation pulse provided by the sampling and the time-domain approach are shown for gas phase as well as for bulk water. The

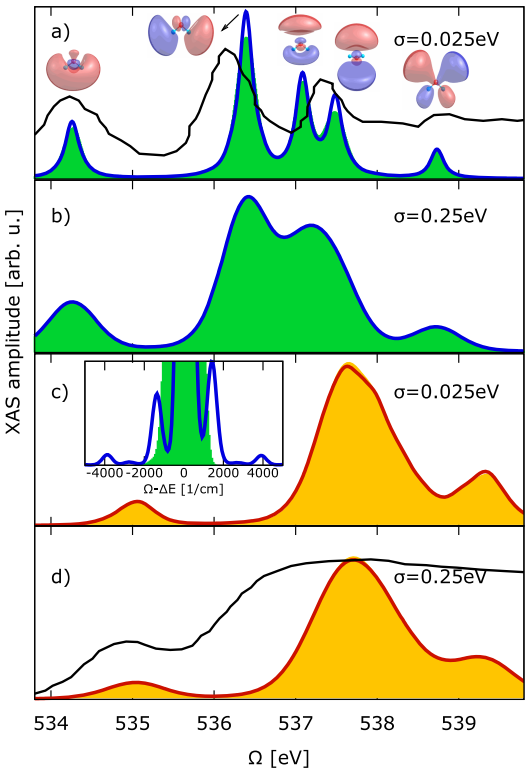

FIG. 2. XAS amplitudes of water for a small (σ = 0.025 eV) and a large (σ = 0.25 eV) pulse width are shown in panels [(a), (c)] and [(b), (d)], respectively. The gas phase spectra are presented in panels (a) and (b), whereas panels (c) and (d) are dedicated to that of bulk water. Black lines represent normalized experimental data for bulk and gas phase water from Ref. 13. Blue and red lines depict the time-domain approach results according to Eq. (26), whereas filled (green and orange) curves correspond to the sampling method. The unoccupied molecular orbitals to which the transition is performed are shown near the respective spectral peaks. Inset zooms on the $1s \rightarrow \sigma^*(2s)$ $[1a_1 \rightarrow 4a_1]$ transition in the gas phase with the imposed infinite lifetime ($\Gamma_f \rightarrow 0$), where the frequency axis is shifted by the peak position ΔE = 534.3 eV.

agreement with experimental data, depicted with solid black curves therein, is fairly good for the gas phase and qualitatively correct for the liquid; note that the widths were not fit. Before comparing the spectra, we assign the peaks in the XAS to the underlying transitions in order to connect to the energy level structure of the water molecule. The respective unoccupied molecular orbitals are exemplified near the spectral peaks. In particular, the first two peaks (534.3 eV and 536.4 eV) correspond to the $1s \rightarrow \sigma^*(2s)$ $[1a_1 \rightarrow 4a_1]$ and $1s \rightarrow \sigma^*(2p)$ $[1a_1 \rightarrow 2b_2]$ transitions, respectively. Other peaks can be attributed to the transitions from 1s to 3p Rydberg orbitals of oxygen.

Comparing the results of the sampling and correlation approaches for the gas phase water molecule with the small linewidth, Fig. 2(a), one sees that there are subtle but evident differences in intensities for all the peaks apart from the one with the highest energy. Their origin can be clearly traced back by setting the lifetime of the final core-excited states to infinity ($\Gamma_f \rightarrow 0$), see inset. Here, observed pronounced side bands can be directly related to the vibrational modes of the water molecule, in particular to the bending and stretching ones, which have the frequencies of $\approx$1500 cm^{-1} and $\approx$3800 cm^{-1}, respectively. We stress that these side bands can not be provided by the sampling approach due to its intrinsic limitations. Nonetheless, all these discrepancies disappear at the large pulse width, see Fig. 2(b). Note that the two spectra have the same area by construction, see supplementary material for a proof, and thus increasing the width of the convoluted Gaussian naturally eliminates the differences between the two approaches. Therefore, one can view this coincidence as the cross-check for the implementation.

The same comparison is performed for bulk water, see panels (c) and (d) in Fig. 2. Here, the differences between the pulse widths and especially between the methods are vanishing. Interestingly, the discrepancies are negligibly small even for infinite lifetimes, see Fig. S1 in the supplementary material. This illustrates the statement that XAS is not a very sensitive observable for nuclear correlation effects.

To sum up, nuclear correlations do not influence XAS amplitudes for bulk water under any circumstances, whereas for gas phase the (small) differences are seen only if the pulse width and/or lifetime broadening of the final states are particularly small. In principle, the RIXS amplitude contains more information and, thus, could be more promising for observing nuclear effects, as will be shown in Sec. V B.

B. RIXS

In Fig. 3 a 2D spectrum for bulk water obtained according to Eq. (27) is shown. Although it gives an overall impression about the spectral shape in the entire excitation and emission ranges, it is hard to make a quantitative analysis on its basis. Therefore, we consider a particular cut for a fixed excitation frequency Ω that corresponds to a maximum of the spectral peak assigned to the $1s \rightarrow \sigma^*(2s)$ $[1a_1 \rightarrow 4a_1]$ absorption transition, see vertical line in Fig. 3; note that the particular excitation frequencies are different for the gas phase (534.2 eV) and bulk (535.0 eV) cases. Note further

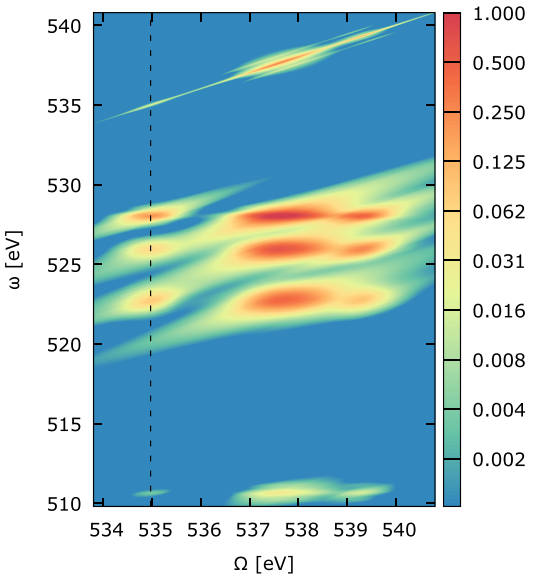

FIG. 3. 2D RIXS spectrum for bulk water (small pulse width) obtained by means of the time-correlation approach, Eq. (27). The dashed vertical line indicates the position of the cut depicted in Fig. 4.

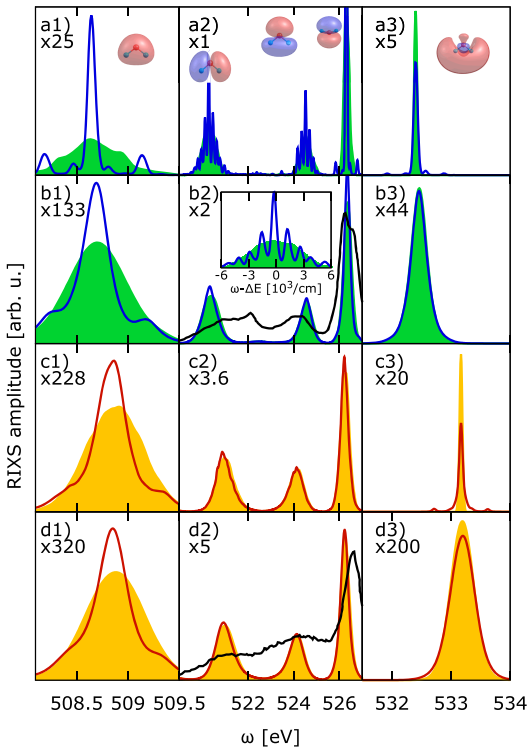

FIG. 4. Cuts through RIXS spectra for various simulation scenarios. The excitations frequencies are fixed at 534.2 eV and 535.0 eV for the gas phase and the bulk, respectively. The colour-code and the panel structure are the same as in Fig. 2. Panels (a) and (c) correspond to $\sigma = 0.025$ eV whereas (b) and (d) to $\sigma = 0.25$ eV. Each panel is split into three sub-panels according to the spectral ranges that exhibit intensity (note multiplicative factors therein), see Fig. 3. The black line represents the respective experimental data for the gas phase and for the bulk system from Refs. 59 and 13, respectively. Inset zooms on the left peak in panel (a2) with $\Delta E = 520.2$ eV, which corresponds to the maximum intensity of the $1b_2 \rightarrow 1a_1$ transition.

that the tendencies observed for cuts at different excitation frequencies are qualitatively similar, see Ref. 32 and supplementary material. The agreement with the experimental data is qualitative, given that the widths were not fit to reproduce experiment.[31]

Three spectral ranges corresponding to peaks in the aforementioned cut are shown for various simulation scenarios in Fig. 4. These peaks can be related to transitions from the intermediate (core-excited) state to final (ground or valence-excited) states, see the respective orbitals from which the emission takes place in panels (a). In particular, the peak in panel (a1) can be assigned to the $\sigma(2s) \rightarrow 1s$ $[2a_1 \rightarrow 1a_1]$ core-hole refill. In panel (a2), the peaks at 520.2, 524.6, and 526.3 eV stand for the refill from bonding $\sigma(2p)$ $[1b_2]$ and two lone-pairs n(2p) $[3a_1$ and $1b_1]$, respectively. Panel (a3) contains the elastic peak, that is, the refill from the antibonding $\sigma^*(2s)$ $[4a_1]$ orbital populated in the first step of the RIXS process. In panels (a1)-(a3) one sees pronounced differences between the methods in case of the small pulse width. A prominent vibronic structure is observed for all peaks with the frequencies easily attributed to vibrational normal modes, see, e.g., inset where the fingerprints of the bending mode can be clearly seen. Although these structures disappear for the large pulse width, see panels (b) therein, differences in intensity remain for the elastic and for the lone-pair peak with the highest energy (526.3 eV). Moreover, the energetically lowest transition in panel (b1) still exhibits a pronounced peak structure when computed with the time-correlation approach. Importantly, the results for bulk water still reveal noticeable differences between the methods for all pulse widths considered, see panels (c1), (c3), (d1), and (d3). In particular, the sampling approach overestimates the intensity of the elastic peak and underestimates the intensity of the inelastic ones and, in addition, reveals no vibronic progressions. This underlines the statement that RIXS spectra are sensitive to correlation effects in the nuclear dynamics. Most importantly, one sees clear traces of nuclear dynamics at all realistic experimental conditions considered.

In order to shed light on the origin of the observed deviations, we consider all possible sources, see Eq. (21), that is, the time correlation of the transition dipoles and that of the energy gaps. The former corresponds to the effects beyond the Condon approximation, which can be easily elucidated by setting the dipoles to their values at, e.g., $t = 0$. It turns out that the deviations due to the Condon approximation are small for inelastic peaks, see Fig. 5, and thus cannot be responsible for the substantial differences observed in RIXS spectra. This implies that these differences are caused by the time dependence of the energies involved. Interestingly, the aforementioned deviations for the elastic peak are notable only for correlated spectra computed here. Importantly, the Condon approximation increases the intensity of the elastic peak, whereas correlation effects suppress it. Since the two act in opposite directions, one can employ the Condon approximation results for the analysis, as the true non-Condon differences between the sampling and correlation methods can be only more pronounced.

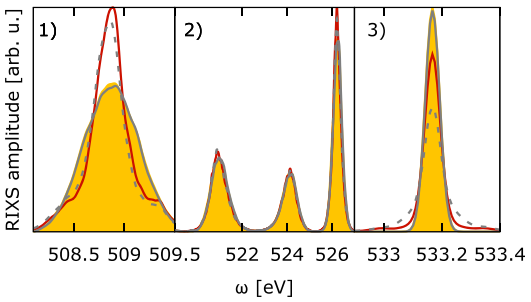

FIG. 5. The accuracy of the Condon approximation. The same cut as in Fig. 4 panels (c) is shown with the same colour code corresponding to bulk water with $\sigma = 0.025$ eV. Gray dashed and solid curves correspond to the reference results without Condon approximation for the time-domain approach and the sampling, respectively.

To investigate the role of the energy time-dependencies, we consider a particular RIXS channel, $g \to i \to f$, and impose the Condon approximation as it has been justified for inelastic peaks for the present system. The corresponding RIXS amplitudes for the sampling, $\mathcal{R}^S$, and the time-correlation approach, $\mathcal{R}^C$, taken at the mean transition frequencies $\bar{\omega}_{ig}$ and $\bar{\omega}_{if}$ can be reduced to

$$\mathcal{R}^{\mathrm{S/C}}(\bar{\omega}_{ig}, \bar{\omega}_{if}) \propto \int_0^\infty \mathrm{d}t\, C^{\mathrm{S/C}}_{gif}(t), \tag{29}$$

where

$$C^{\mathrm{S}}_{gif}(t) := \mathrm{e}^{-\sigma^2 t^2/2} \mathrm{Re}\left\langle \mathrm{e}^{\mathrm{i}U_{gf}(0)t} |\chi^{\mathrm{S}}_{if}(0)|^2 \right\rangle \tag{30a}$$

$$C^{\mathrm{C}}_{gif}(t) := \mathrm{e}^{-\sigma^2 t^2/2} \mathrm{Re}\left\langle \mathrm{e}^{\mathrm{i}\int_0^t \mathrm{d}\tau U_{gf}(\tau)} \chi^{\mathrm{C}*}_{if}(t)\chi^{\mathrm{C}}_{if}(0) \right\rangle, \tag{30b}$$

as it is shown in the supplementary material. The functions $\mathcal{R}^{\mathrm{S/C}}(\bar{\omega}_{ig}, \bar{\omega}_{if})$ approximately describe the heights of the corresponding spectral peaks at maximum. Here,

$$\chi^{\mathrm{S/C}}_{if}(t) := \int_{-\infty}^{\infty} \mathrm{d}\tau\, L^{\mathrm{S/C}}_{if}(\tau; t), \tag{31}$$

with

$$L^{\mathrm{S}}_{if}(\tau; 0) := \exp[\mathrm{i}U_{if}(0)\tau]\Delta_i(\tau) \tag{32a}$$

$$L^{\mathrm{C}}_{if}(\tau; t) := \exp[\mathrm{i}\int_t^{t+\tau} \mathrm{d}\bar{\tau}\, U_{if}(\bar{\tau})]\Delta_i(\tau), \tag{32b}$$

where Δ_i is the damping function defined in Eq. (20), and $U_{ab}(t)$ are the gap fluctuations; note that $\chi^{\mathrm{S}}_{if}(t)$ is evaluated only at $t = 0$. Importantly, $C^{\mathrm{S}}_{gif}(t)$ consists of the averaged product of the phase w.r.t. $U_{gf}(0)$ and the squared value of $\chi^{\mathrm{S}}_{if}(0)$, which is just a number. In contrast, $C^{\mathrm{C}}_{gif}(t)$ is constructed from the averaged product of the two expressions, both involving autocorrelation functions, since the phase factor in Eq. (30b) can be treated as an autocorrelation function in the framework of the cumulant expansion.[19,33] Note that the two autocorrelation functions involve *different* gap fluctuations, i.e., U_{if} and U_{gf}.

To proceed, the following approximate factorization is performed

$$C^{\mathrm{C}}_{gif}(t) \approx \mathrm{Re}\left[\mathrm{e}^{-\sigma^2 t^2/4}\left\langle \mathrm{e}^{\mathrm{i}\int_0^t \mathrm{d}\tau U_{gf}(\tau)}\right\rangle\right] \times \mathrm{Re}\left[\mathrm{e}^{-\sigma^2 t^2/4}\left\langle \chi^{\mathrm{C}*}_{if}(t)\chi^{\mathrm{C}}_{if}(0)\right\rangle\right]; \tag{33}$$

here the Gaussian has also been split into two in order to smooth both parts in a similar way. The same factorization is then performed for $C^{\mathrm{S}}_{gif}(t)$ defined in Eq. (30a). These factorizations are possible due to the absence of correlations between the two parts as can be shown numerically and seen from Fig. 6. Thus, the aforementioned averaged product of the two factors has now become the product of the averages.

The relevant quantities are summarized in Fig. 6, whose two rows correspond to the peaks exhibiting the most pronounced differences in the RIXS spectra, that is, the elastic one and the peak with the lowest emission energy, see Fig. 4; the analysis for the other three peaks is shown in the supplementary material. The first column contains $C^{\mathrm{S/C}}_{gif}$, the second and third columns depict the first and second parts in Eq. (33), respectively, as well as the corresponding sampling counterparts. The fourth column shows the averaged absolute values of the Fourier-transformed gap fluctuations, i.e., the spectral density function. The intensity differences in question are given by the difference of the *areas* under the $C^{\mathrm{S/C}}$ curves in the first column therein. To reiterate, although for the elastic peak the Condon approximation is not justified, going beyond it will make the effect in question even stronger, as becomes apparent from Fig. 5.

For elastic scattering $g = f$, and hence the first part in Eq. (33) reduces to $\exp[-\sigma^2 t^2/4]$ by construction, as $U_{gg}(\tau) \equiv 0$; the same naturally applies to its sampling counterpart, see panel (a2). Therefore, C^{S} [shaded area in panel (a1)] exhibits a Gaussian decay stemming from the excitation pulse. The solid curve therein, C^{C}, contains in addition *correlation* effects due to the second part of Eq. (33) shown in panel (a3), that shrink the area under the curve (a1), and are thus responsible for the observed intensity difference in the spectra Fig. 5 panel (3).

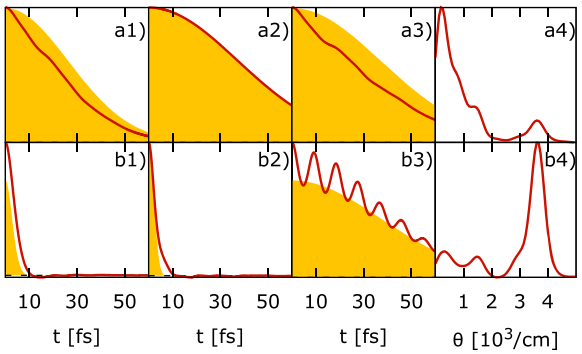

FIG. 6. The origin of different peak intensities. The colour code is the same as in Fig. 4. Row (a) corresponds to the intensity of the elastic peaks in Condon approximation, see orange and red curves in Fig. 5 panel (3). The lower row (b) is related to the $\sigma(2s) \to 1s\,[2a_1 \to 1a_1]$ transition, see Fig. 5 panel (1). The first column contains the time-dependent functions that determine the peak intensities, see Eqs. (30a) and (30b). The second and third columns feature the first and the second part of the factorization in Eq. (33), respectively, as well as the sampling counterparts. In the fourth column one can see the spectral densities (averaged absolute value of the Fourier-transformed gap fluctuations), where the results are convoluted with a normalized Gaussian ($\sigma = 0.025$ eV).

The same analysis performed for the inelastic peak immediately suggests that the shape of $C^{S/C}$, panel (b1), is dictated almost exclusively by the first part in Eq. (33) presented in panel (b2). The observed rapid decay (≈10 fs) in turn implies that the peculiarities of the time-dependence of the correlation function constituting the second part, panel (b3), are irrelevant. Thus, its value at $t = 0$, which can be notably different for the two approaches, controls the magnitude of $C^{S/C}$ and, hence, the signal intensity at maximum.

One can show on the basis of a simple harmonic model, that in the limit of fast nuclear vibrations the sampling method would underestimate $\chi^{C}_{if}(0)$ and thus $C^{S/C}(0)$, whereas the two methods coincide in the low-frequency limit, see supplementary material. This implies that *inelastic* spectral intensities would be underestimated as well. Practically one can expect this underestimation to be strong if the gap fluctuation has more contributions from high-frequency modes than from low-frequency ones. Indeed, the spectral density shown in panel (b4) strongly supports this scenario, see supplementary material for the respective contributions for other peaks. Furthermore, the similar values of $C^{S/C}(0)$ for the elastic peak in panel (a1) directly follow from the fact that the corresponding spectral density has its major contribution in the low frequency range, see panel (a4). Nonetheless, for elastic peaks not only the value at zero is important but the entire shape of $C^{S/C}(t)$, and thus the overall conclusion for elastic peaks can not be drawn on this basis.

Interestingly, the impact of the Condon approximation on spectra can be explained by the above analysis. In particular, the time-dependence of the transition dipoles, which is ignored by the approximation, serves as an additional source for dephasing, decreasing the elastic peak intensity even further, see Fig. 5. Since for inelastic peaks just the value of $C^{S/C}(0)$ matters, the faster dephasing is expected to be almost irrelevant and thus, the Condon approximation has proven itself reliable in this case.

To resume, the differences in intensities between the two approaches for the system studied are determined by the second part of Eq. (33), which is a clear trace of nuclear dynamics.

C. Limitations of the method

Let us recapitulate the approximations that have been employed on the way from the coupled nuclear-electronic Schrödinger equation to the final result, Eqs. (15) and (21). The first one is the BOA, which leads to ignoring non-adiabatic effects that can be important in a typical scenario when the density of core-excited states is substantial. In general, having the continuous time evolution of the electronic wavefunction opens the doorway for taking these effects into account, and thus this is not a principal deficiency.

The second issue is the electronic structure method employed. Here, we have used ground state Kohn-Sham orbitals for the excited states and thus inevitably neglected electronic relaxation, differential correlation, and possible multi-configurational nature of the wavefunction. Importantly, the developed approach is independent of the electronic structure method and, thus, utilizing a truly correlated technique for the excited states,[60] such as the multi-configurational self-consistent field approach, would mitigate the problem.[61–64]

The last but not the least approximation is the classical one. In particular, the classical treatment of the scattering operator, Eq. (9), which does not have in principle the correct classical limit, is, in our opinion, the most severe approximation employed. The replacement of the operator $\Delta\hat{E}_{a0}$ by a number, leads to the complete loss of information about the dynamics in the excited state $|a\rangle$, and leaves us with a simple phase factor. The consequences of the dynamical classical limit have been extensively studied by Berne *et al.*[65,66] This approximation can cause wrong frequencies and shapes of the vibronic progressions in certain physical situations, whereas the envelopes of the vibronic bands are reproduced reasonably well. Another deficiency of the limit is that for ambient temperatures the ground state trajectory is confined in a small region near the potential minimum. In contrast, in the correct quantum picture the nuclei can move far away from that minimum in a dissociative core-excited state potential.[56,67,68] However, we believe that in the case of water, which has a core-hole lifetime of ≈4 fs, the phenomenological dephasing model used, Eq. (20), is suited to describe XAS. In case of RIXS, such an ultrafast dissociation gives rise to vibronic features, which cannot be captured by our method due to a significant difference between the dynamics in the bound ground and unbound core-excited states.

Note that the classical approximation for the dipoles appears to be not so important, since the Condon approximation holds reasonably well. We believe that the observed symmetry of the vibrational progressions with respect to 0-0 vibronic transition is also due to the classical limit, which corresponds to a temperature much larger than a vibrational quantum. This can be understood in terms of a simple Huang-Rhys model, where such a symmetry emerges as a result of equally populated nuclear levels of the initial electronic state.

To resume, the only unsurmountable approximation that belongs to the method itself is the classical limit and thus is the main target for future improvements. These may be incorporating nuclear quantum effects, which is well-established for trajectory-based methods,[25,26] and improving the dynamics to take many potential surfaces into account in an Ehrenfest or averaged classical limit fashion.[69–71] An interesting possibility, combining all the improvements needed, might be provided by the non-adiabatic ring polymer molecular dynamics method.[72,73]

VI. CONCLUSIONS

In order to include correlation effects from the underlying nuclear dynamics into theoretical X-ray spectroscopy, a time-domain approach to XAS and RIXS spectra has been rigorously developed and tested on gas phase and bulk water. The derivation has been carried out here from the Schrödinger-picture expressions and in Ref. 32 from optical response functions. It has been shown that at realistic (experimental) conditions the impact of nuclear dynamical effects on XAS amplitudes of water is fairly small. However, the RIXS

spectra have turned out to exhibit pronounced signatures of the nuclear dynamics that have been traced down to the particular underlying effects in all cases studied. The difference between the sampling and the approach presented here has turned out to be caused by nuclear correlation effects. The observed intensity differences have been rationalized on the basis of a simple harmonic model and connected to the high- and low-frequency contributions to the spectral density. Such an analysis in combination with a more accurate description of the electronic structure and the nuclear dynamics might help to resolve controversial debates, e.g., the splitting of $1b_1$ band in water RIXS spectra. The practical limitations of the method and underlying approximations, with the dynamical classical limit being the most important one, have been analyzed and discussed. Despite the deficiencies of the method, it represents a step forward over the conventional approaches treating the system in full complexity and provides a reasonable starting point for further improvements.

SUPPLEMENTARY MATERIAL

See supplementary material for the complete derivations of the norm-factor, time-domain expression for RIXS, expressions for XAS and RIXS in Fourier space; the time-dependent functions used for the analysis; the graphs containing XAS amplitudes with infinite lifetimes for final states, various cuts for RIXS, and time-dependent functions for the other inelastic peaks complementary to Fig. 6; the recipes how to obtain the XAS and RIXS amplitudes from the sampling approach and to perform averaging over polarization vectors; a proof that the spectral norm is preserved in XAS; and finally a simple harmonic model that helps to understand the differences observed between $\chi_{if}^{C/S}(0)$.

ACKNOWLEDGMENTS

We acknowledge financial support by the Deanship of Scientific Research (DSR), King Abdulaziz University, Jeddah (Grant No. D-003-435), and the Deutsche Forschungsgemeinschaft [Nos. KU 952/10-1 (S.K.) and IV 171/2-1 (S.D.I.)]. Special thanks go to Fabian Gottwald for technical assistance with the MD simulations of water.

[1] J. Stöhr, *NEXAFS Spectroscopy* (Springer-Verlag, Berlin, Heidelberg, 1992).
[2] F. De Groot and A. Kotani, *Core Level Spectroscopy of Solids* (CRC Press, Boca Raton, 2008).
[3] B. Winter and M. Faubel, Chem. Rev. **106**, 1176 (2006).
[4] J. E. Rubensson, F. Hennies, and A. Pietzsch, J. Electron Spectrosc. Relat. Phenom. **188**, 79 (2013).
[5] R. Guillemin, S. Carniato, L. Journel, W. C. Stolte, T. Marchenko, L. E. Khoury, E. Kawerk, M. N. Piancastelli, A. C. Hudson, D. W. Lindle, and M. Simon, J. Electron Spectrosc. Relat. Phenom. **188**, 53 (2013).
[6] W. Dong, H. Wang, M. M. Olmstead, J. C. Fettinger, J. Nix, H. Uchiyama, S. Tsutsui, A. Q. R. Baron, E. Dowty, and S. P. Cramer, Inorg. Chem. **52**, 6767 (2013).
[7] F. Hennies, S. Polyutov, I. Minkov, A. Pietzsch, M. Nagasono, F. Gelmukhanov, L. Triguero, M.-N. Piancastelli, W. Wurth, H. Ågren, and A. Föhlisch, Phys. Rev. Lett. **95**, 163002 (2005).
[8] M. P. Ljungberg, L. G. M. Pettersson, and A. Nilsson, J. Chem. Phys. **134**, 044513 (2011).
[9] R. Bohinc, M. Žitnik, K. Bučar, M. Kavčič, L. Journel, R. Guillemin, T. Marchenko, M. Simon, and W. Cao, J. Chem. Phys. **139**, 134302 (2013).
[10] A. Pietzsch, Y.-P. Sun, F. Hennies, Z. Rinkevicius, H. O. Karlsson, T. Schmitt, V. N. Strocov, J. Andersson, B. Kennedy, J. Schlappa, A. Föhlisch, J.-E. Rubensson, and F. Gelmukhanov, Phys. Rev. Lett. **106**, 153004 (2011).
[11] F. Hennies, A. Pietzsch, M. Berglund, A. Föhlisch, T. Schmitt, V. Strocov, H. O. Karlsson, J. Andersson, and J.-E. Rubensson, Phys. Rev. Lett. **104**, 193002 (2010).
[12] L. Weinhardt, M. Blumc, O. Fuchs, A. Benkert, F. Meyerb, M. Bar, J. D. Denlinger, W. Yang, F. Reinert, and C. Heske, J. Electron Spectrosc. Relat. Phenom. **188**, 111 (2013).
[13] K. M. Lange and E. F. Aziz, Chem. - Asian J. **8**, 318 (2013).
[14] S. Schreck, A. Pietzsch, K. Kunnus, B. Kennedy, W. Quevedo, P. S. Miedema, P. Wernet, and A. Föhlisch, Struct. Dyn. **1**, 054901 (2014).
[15] T. Fransson, Y. Harada, N. Kosugi, N. A. Besley, B. Winter, J. J. Rehr, L. G. M. Pettersson, and A. Nilsson, Chem. Rev. **116**, 7551 (2016).
[16] J. A. Sellberg, T. A. Mcqueen, H. Laksmono, S. Schreck, M. Beye, D. P. Deponte, B. Kennedy, D. Nordlund, R. G. Sierra, D. Schlesinger, T. Tokushima, I. Zhovtobriukh, S. Eckert, V. H. Segtnan, H. Ogasawara, K. Kubicek, S. Techert, U. Bergmann, G. L. Dakovski, W. F. Schlotter, Y. Harada, M. J. Bogan, P. Wernet, A. Föhlisch, L. G. M. Pettersson, and A. Nilsson, J. Chem. Phys. **142**, 044505 (2015).
[17] G. K. Paramonov and O. Kühn, J. Phys. Chem. A **116**, 11388 (2012).
[18] M. Leetmaa, M. Ljungberg, A. Lyubartsev, A. Nilsson, and L. Pettersson, J. Electron Spectrosc. Relat. Phenom. **177**, 135 (2010).
[19] V. May and O. Kühn, *Charge and Energy Transfer Dynamics in Molecular Systems* (Wiley-VCH, Weinheim, 2011).
[20] M. Schröter, S. Ivanov, J. Schulze, S. Polyutov, Y. Yan, T. Pullerits, and O. Kühn, Phys. Rep. **567**, 1 (2015).
[21] M. Wächtler, J. Guthmuller, L. González, and B. Dietzek, Coord. Chem. Rev. **256**, 1479 (2012).
[22] A. Sakko, S. Galambosi, J. Inkinen, T. Pylkkänen, M. Hakala, S. Huotari, and K. Hämäläinen, Phys. Chem. Chem. Phys. **13**, 11678 (2011).
[23] P. Saek, A. Baev, F. Gel'mukhanov, and H. Ågren, Phys. Chem. Chem. Phys. **5**, 1 (2003).
[24] R. C. Couto, M. Guarise, A. Nicolaou, N. Jaouen, G. S. Chiuzbian, J. Lüning, V. Ekholm, J.-E. Rubensson, C. Såthe, F. Hennies, F. F. Guimarães, H. Ågren, F. Gel'mukhanov, L. Journel, M. Simon, and V. Kimberg, Phys. Rev. A **93**, 032510 (2016).
[25] D. Marx and J. Hutter, *Ab Initio Molecular Dynamics: Basic Theory and Advanced Methods* (Cambridge University Press, Cambridge, 2009).
[26] M. E. Tuckerman, *Statistical Mechanics: Theory and Molecular Simulation* (Oxford University Press, 2010).
[27] S. D. Ivanov, A. Witt, and D. Marx, Phys. Chem. Chem. Phys. **15**, 10270 (2013).
[28] W. Zhuang, T. Hayashi, and S. Mukamel, Angew. Chem., Int. Ed. **48**, 3750 (2009).
[29] Y.-P. Sun, F. Hennies, A. Pietzsch, B. Kennedy, T. Schmitt, V. N. Strocov, J. Andersson, M. Berglund, J.-E. Rubensson, K. Aidas, F. Gel'mukhanov, M. Odelius, and A. Föhlisch, Phys. Rev. B **84**, 132202 (2011).
[30] N. K. Jena, I. Josefsson, S. K. Eriksson, A. Hagfeldt, H. Siegbahn, O. Björneholm, H. Rensmo, and M. Odelius, Chem. - A Eur. J. **21**, 4049 (2015).
[31] L. Weinhardt, E. Ertan, M. Iannuzzi, M. Weigand, O. Fuchs, M. Bär, M. Blum, J. D. Denlinger, W. Yang, E. Umbach, M. Odelius, and C. Heske, Phys. Chem. Chem. Phys. **17**, 27145 (2015).
[32] S. Karsten, S. D. Ivanov, S. G. Aziz, S. I. Bokarev, and O. Kühn, J. Phys. Chem. Lett. **8**, 992 (2017).
[33] S. Mukamel, *Principles of Nonlinear Optical Spectroscopy* (Oxford University Press, Oxford, 1995).
[34] E. J. Heller, J. Chem. Phys. **68**, 3891 (1978).
[35] C. Lawrence and J. Skinner, J. Chem. Phys. **117**, 8847 (2002).
[36] E. Harder, J. D. Eaves, A. Tokmakoff, and B. Berne, Proc. Natl. Acad. Sci. U. S. A. **102**, 11611 (2005).
[37] D. A. McQuarrie, *Statistical Mechanics* (HARPER & ROW, New York, 1976).
[38] H. Kramers and W. Heisenberg, *Original Scientific Papers Wissenschaftliche Originalarbeiten* (Springer, 1985), pp. 354–381.
[39] S.-Y. Lee and E. J. Heller, J. Chem. Phys. **71**, 4777 (1979).
[40] A. I. Krylov, R. B. Gerber, and R. D. Coalson, J. Chem. Phys. **105**, 4626 (1996).
[41] G. Mathias and M. D. Baer, J. Chem. Theory Comput. **7**, 2028 (2011).

[42]G. Mathias, S. D. Ivanov, A. Witt, M. D. Baer, and D. Marx, J. Chem. Theory Comput. **8**, 224 (2012).
[43]B. Hess, C. Kutzner, D. van der Spoel, and E. Lindahl, J. Chem. Theory Comput. **4**, 435 (2008).
[44]F. Paesani, W. Zhang, D. A. Case, T. E. Cheatham, and G. A. Voth, J. Chem. Phys. **125**, 184507 (2006).
[45]J. P. Perdew, K. Burke, and M. Ernzerhof, Phys. Rev. Lett. **77**, 3865 (1996).
[46]F. Neese, Wiley Interdiscip. Rev.: Comput. Mol. Sci. **2**, 73 (2012).
[47]F. Weigend and R. Ahlrichs, Phys. Chem. Chem. Phys. **7**, 3297 (2005).
[48]J. Almlöf and P. R. Taylor, J. Chem. Phys. **86**, 4070 (1987).
[49]B. O. Roos, K. Andersson, M. P. Fülscher, P.-Å. Malmqvist, L. Serrano-Andrés, K. Pierloot, and M. Merchán, *New Methods in Computational Quantum Mechanics*, Advances in Chemical Physics, Vol. 93 (John Wiley & Sons, Inc., 1996), pp. 219–331.
[50]K. Kaufmann, W. Baumeister, and M. Jungen, J. Phys. B: At. Mol. Opt. Phys. **22**, 2223 (1989).
[51]L.-Å. Näslund, M. Cavalleri, H. Ogasawara, A. Nilsson, L. G. M. Pettersson, P. Wernet, D. C. Edwards, M. Sandström, and S. Myneni, J. Phys. Chem. A **107**, 6869 (2003).
[52]N. Lee, T. Petrenko, U. Bergmann, F. Neese, and S. DeBeer, J. Am. Chem. Soc. **132**, 9715 (2010).
[53]B. Lassalle-Kaiser, T. T. Boron, V. Krewald, J. Kern, M. a. Beckwith, M. U. Delgado-Jaime, H. Schroeder, R. Alonso-Mori, D. Nordlund, T. C. Weng, D. Sokaras, F. Neese, U. Bergmann, V. K. Yachandra, S. Debeer, V. L. Pecoraro, and J. Yano, Inorg. Chem. **52**, 12915 (2013).
[54]C. J. Pollock, K. Grubel, P. L. Holland, and S. Debeer, J. Am. Chem. Soc. **135**, 11803 (2013).
[55]C. Milne, T. Penfold, and M. Chergui, Coord. Chem. Rev. **277-278**, 44 (2014).
[56]I. Hjelte, M. N. Piancastelli, R. F. Fink, R. Feifel, A. Giertz, H. Wang, K. Wiesner, A. Ausmees, C. Miron, S. L. Sorensen, and S. Svensson, Chem. Phys. Lett. **334**, 151 (2001).
[57]P. Monson and W. McClain, J. Chem. Phys. **53**, 29 (1970).
[58]Y. Luo, H. Ågren, and F. Gel'mukhanov, Phys. Rev. A **53**, 1340 (1996).
[59]L. Weinhardt, A. Benkert, F. Meyer, M. Blum, R. G. Wilks, W. Yang, M. Bär, F. Reinert, and C. Heske, J. Chem. Phys. **136**, 144311 (2012).
[60]T. Helgaker, P. Jørgenson, and J. Olsen, *Molecular Electronic-Structure Theory* (John Wiley & Sons, Chichester, 2000).
[61]I. Josefsson, K. Kunnus, S. Schreck, A. Föhlisch, F. de Groot, P. Wernet, and M. Odelius, J. Phys. Chem. Lett. **3**, 3565 (2012).
[62]S. I. Bokarev, M. Dantz, E. Suljoti, O. Kühn, and E. F. Aziz, Phys. Rev. Lett. **111**, 083002 (2013).
[63]S. I. Bokarev, M. Khan, M. K. Abdel-Latif, J. Xiao, R. Hilal, S. G. Aziz, E. F. Aziz, and O. Kühn, J. Phys. Chem. C **119**, 19192 (2015).
[64]P. Wernet, K. Kunnus, I. Josefsson, I. Rajkovic, W. Quevedo, M. Beye, S. Schreck, S. Grubel, M. Scholz, D. Nordlund, W. Zhang, R. W. Hartsock, W. F. Schlotter, J. J. Turner, B. Kennedy, F. Hennies, F. M. F. de Groot, K. J. Gaffney, S. Techert, M. Odelius, and A. Fohlisch, Nature **520**, 78 (2015).
[65]S. A. Egorov, E. Rabani, and B. J. Berne, J. Chem. Phys. **108**, 1407 (1998).
[66]E. Rabani, S. A. Egorov, and B. J. Berne, J. Chem. Phys. **109**, 6376 (1998).
[67]R. Bohinc, M. Žitnik, K. Bučar, and M. Kavčič, J. Chem. Phys. **140**, 164304 (2014).
[68]Y. Harada, T. Tokushima, Y. Horikawa, O. Takahashi, H. Niwa, M. Kobayashi, M. Oshima, Y. Senba, H. Ohashi, K. T. Wikfeldt, A. Nilsson, L. G. M. Pettersson, and S. Shin, Phys. Rev. Lett. **111**, 193001 (2013).
[69]N. E. Shemetulskis and R. F. Loring, J. Chem. Phys. **97**, 1217 (1992).
[70]Q. Shi and E. Geva, J. Chem. Phys. **122**, 064506 (2005).
[71]Q. Shi and E. Geva, J. Chem. Phys. **129**, 124505 (2008).
[72]J. O. Richardson and M. Thoss, J. Chem. Phys. **139**, 031102 (2013).
[73]J. O. Richardson, P. Meyer, M.-O. Pleinert, and M. Thoss, Chem. Phys. **482**, 124 (2016).

Supplemental Information: A time-correlation function approach to nuclear dynamical effects in X-ray spectroscopy

Sven Karsten,[1] Sergey I. Bokarev,[1, a)] Saadullah G. Aziz,[2] Sergei D. Ivanov,[1, b)] and Oliver Kühn[1]

[1)] *Institute of Physics, Rostock University, Universitätsplatz 3, 18055 Rostock, Germany*

[2)] *Chemistry Department, Faculty of Science, King Abdulaziz University, 21589 Jeddah, Saudi Arabia*

(Dated: 19 May 2017)

[a)] Electronic mail: sergey.bokarev@uni-rostock.de

[b)] Electronic mail: sergei.ivanov@uni-rostock.de

CONTENTS

I. DERIVING THE NORM-FACTOR

In the following the phase space averaging with respect to all initial states

$$\sum_g \iint \mathrm{d}\mathbf{R}_0 \mathrm{d}\mathbf{P}_0 \exp\left[-\beta H_g(0)\right]/Z \bullet \tag{S1}$$

is rewritten as a canonical ensemble average with respect to the electronic ground state Hamilton function, i.e. $\langle \bullet \rangle = \iint \mathrm{d}\mathbf{R}_0 \mathrm{d}\mathbf{P}_0 \exp\left[-\beta H_0(0)\right]/Z_0 \bullet$. First, the focus is put on rewriting the partition function Z. Multiplying and dividing Z by Z_0 and employing again the trick of adding and subtracting the electronic ground state Hamilton function, $H_g(0) =$

$H_0(0) + \Delta E_{g0}(0)$, one can write

$$\begin{aligned} Z &= \sum_g \iint \mathrm{d}\mathbf{R}_0 \mathrm{d}\mathbf{P}_0 \mathrm{e}^{-\beta H_g(0)} \\ &= Z_0 \sum_g \iint \mathrm{d}\mathbf{R}_0 \mathrm{d}\mathbf{P}_0 \frac{\mathrm{e}^{-\beta H_g(0)}}{Z_0} \\ &= Z_0 \iint \mathrm{d}\mathbf{R}_0 \mathrm{d}\mathbf{P}_0 \frac{\mathrm{e}^{-\beta H_0(0)}}{Z_0} \sum_g \mathrm{e}^{-\beta \Delta E_{g0}(0)} \quad . \end{aligned} \tag{S2}$$

In the last equation one recognizes the relation between the full partition function and the norm factor given according to Eq. (17) in the main text as

$$\mathcal{Z} := \left\langle \sum_g \mathrm{e}^{-\beta \Delta E_{g0}(0)} \right\rangle \quad , \tag{S3}$$

i.e. $Z = Z_0 \mathcal{Z}$. Inserting this relation into the general phase space integration, Eq. (1), and employing once again the trick of adding and subtracting the electronic ground state Hamilton function yields

$$\begin{aligned} \sum_g \iint \mathrm{d}\mathbf{R}_0 \mathrm{d}\mathbf{P}_0 \exp\left[-\beta H_g(0)\right]/Z \bullet &= \iint \mathrm{d}\mathbf{R}_0 \mathrm{d}\mathbf{P}_0 \frac{\mathrm{e}^{-\beta H_0(0)}}{Z_0} \sum_g \frac{\mathrm{e}^{-\beta \Delta E_{g0}(0)}}{\mathcal{Z}} \bullet \\ &= \left\langle \sum_g \frac{\mathrm{e}^{-\beta \Delta E_{g0}(0)}}{\mathcal{Z}} \bullet \right\rangle \quad , \end{aligned} \tag{S4}$$

Thus, the general phase space integration can be recast into a canonical ensemble average with respect to the ground state Hamilton function, with the norm-factor given in Eq. (17) of the main text.

II. DERIVING THE TIME-DOMAIN EXPRESSION FOR RIXS

In this section the detailed derivation of the time-domain expression for RIXS amplitude from the Kramers-Heisenberg expression, Eq. (18) in the main text that reads

$$\mathcal{R}(\Omega, \omega) = \sum_{\gamma,\phi} \frac{\mathrm{e}^{-\beta\epsilon_\gamma}}{Z} \left| \sum_\iota \frac{\langle\phi|\hat{d}^\eta \mathfrak{u}_\eta|\iota\rangle\langle\iota|\mathfrak{e}^\xi \hat{d}_\xi|\gamma\rangle}{\omega - (\epsilon_\iota - \epsilon_\phi) + \mathrm{i}\Gamma_\iota} \right|^2 \delta\left(\Omega - (\epsilon_\phi - \epsilon_\gamma + \omega)\right) \quad , \tag{S5}$$

is shown. First, the absolute value squared is formulated out, yielding

$$\mathcal{R}(\Omega, \omega) = \sum_{\gamma,\iota,\iota',\phi} \frac{\mathrm{e}^{-\beta\epsilon_\gamma}}{Z} \frac{\langle\gamma|\hat{d}^\zeta \mathfrak{e}_\zeta|\iota'\rangle\langle\iota'|\mathfrak{u}^\nu \hat{d}_\nu|\phi\rangle}{\omega - (\epsilon_{\iota'} - \epsilon_\phi) - \mathrm{i}\Gamma_{\iota'}} \frac{\langle\phi|\hat{d}^\eta \mathfrak{u}_\eta|\iota\rangle\langle\iota|\mathfrak{e}^\xi \hat{d}_\xi|\gamma\rangle}{\omega - (\epsilon_\iota - \epsilon_\phi) + \mathrm{i}\Gamma_\iota} \delta\left(\Omega - (\epsilon_\phi - \epsilon_\gamma + \omega)\right) \quad . \tag{S6}$$

Second, the time-domain expressions for a δ-function, Eq. (4) in the main text that reads

$$\delta\left(\Omega-\Omega_0\right)=\frac{1}{2\pi}\int\limits_{-\infty}^{\infty}\mathrm{d}t\,\mathrm{e}^{\mathrm{i}(\Omega-\Omega_0)t}\ , \tag{S7}$$

and for a Lorentzian, Eq. (19) in the main text given as

$$\frac{1}{\omega-\omega_0\pm\mathrm{i}\Gamma_\alpha}=\mp\mathrm{i}\int\limits_{-\infty}^{\infty}\mathrm{d}\tau\,\mathrm{e}^{\pm\mathrm{i}(\omega-\omega_0)\tau}\Delta_\alpha(\tau)\ , \tag{S8}$$

are inserted, leading to

$$\begin{aligned}\mathcal{R}(\Omega,\omega)=\sum_{\gamma,\iota,\iota',\phi}\frac{\mathrm{e}^{-\beta\epsilon_\gamma}}{Z}\int\limits_{-\infty}^{\infty}\mathrm{d}t\,\mathrm{e}^{\mathrm{i}\left(\Omega-(\epsilon_\phi-\epsilon_\gamma+\omega)\right)t}\int\limits_{-\infty}^{\infty}\mathrm{d}\tau_1\,\mathrm{e}^{-\mathrm{i}\left(\omega-\left(\epsilon_{\iota'}-\epsilon_\phi\right)\right)\tau_1}\langle\gamma|\hat{d}^\zeta\mathfrak{e}_\zeta|\iota'\rangle\Delta_{\iota'}(\tau_1)\langle\iota'|\mathfrak{u}^\nu\hat{d}_\nu|\phi\rangle\\ \int\limits_{-\infty}^{\infty}\mathrm{d}\tau_2\,\mathrm{e}^{\mathrm{i}\left(\omega-\left(\epsilon_\iota-\epsilon_\phi\right)\right)\tau_2}\langle\phi|\hat{d}^\eta\mathfrak{u}_\eta|\iota\rangle\Delta_\iota(\tau_2)\langle\iota|\mathfrak{e}^\xi\hat{d}_\xi|\gamma\rangle\ .\end{aligned} \tag{S9}$$

Third, the BOA is applied, thus, the system's eigenstates factorise as $|\gamma\rangle=|g\rangle|G\rangle$, $|\iota\rangle=|i\rangle|I\rangle$, $|\iota'\rangle=|j\rangle|J\rangle$ and $|\phi\rangle=|f\rangle|F\rangle$. After rearranging the complex exponentials $\exp\left[\mathrm{i}\epsilon_{\iota'}\tau_1\right]=\exp\left[\mathrm{i}\epsilon_{\iota'}(t+\tau_1)\right]\exp\left[-\mathrm{i}\epsilon_{\iota'}t\right]$ and using the eigenvalue relation given in Eq. (2) in the main text that reads

$$\hat{H}_a|A\rangle=\epsilon_A|A\rangle\ , \tag{S10}$$

one gets

$$\begin{aligned}\mathcal{R}(\Omega,\omega)=&\frac{1}{2\pi Z}\int\limits_{-\infty}^{\infty}\mathrm{d}t\,\mathrm{e}^{\mathrm{i}\Omega t}\sum_{G,I,J,F}\\ &\int\limits_{-\infty}^{\infty}\mathrm{d}\tau_1\,\mathrm{e}^{-\mathrm{i}\omega(t+\tau_1)}\langle G|\mathrm{e}^{-\beta\hat{H}_g}\mathrm{e}^{\mathrm{i}\hat{H}_g t}\hat{D}_j^{g\zeta}\mathfrak{e}_\zeta\mathrm{e}^{-\mathrm{i}\hat{H}_j t}|J\rangle\Delta_j(\tau_1)\langle J|\mathrm{e}^{\mathrm{i}\hat{H}_j(t+\tau_1)}\mathfrak{u}^\nu\hat{D}_{\nu f}^j\mathrm{e}^{-\mathrm{i}\hat{H}_f(t+\tau_1)}|F\rangle\\ &\int\limits_{-\infty}^{\infty}\mathrm{d}\tau_2\,\mathrm{e}^{\mathrm{i}\omega\tau_2}\langle F|\mathrm{e}^{\mathrm{i}\hat{H}_f\tau_2}\hat{D}_i^{f\eta}\mathfrak{u}_\eta\mathrm{e}^{-\mathrm{i}\hat{H}_i\tau_2}|I\rangle\Delta_i(\tau_2)\langle I|\mathfrak{e}^\xi\hat{D}_{\xi g}^i|G\rangle\ ;\end{aligned} \tag{S11}$$

noting that the damping function is assumed to depend on the electronic state only.

Fourth, the summation over the nuclear states I,J,F can be carried out by using the closure relation and one can make use of interaction representation to employ the dressed

transition dipole moments, defined in Eq. (11) in the main text, for the RIXS amplitude

$$\mathcal{R}(\Omega,\omega) = \frac{1}{2\pi Z}\int_{-\infty}^{\infty} \mathrm{d}t\, \mathrm{e}^{\mathrm{i}\Omega t} \sum_G \langle G|\mathrm{e}^{-\beta \hat{H}_g(0)} \int_{-\infty}^{\infty} \mathrm{d}\tau_1\, \mathrm{e}^{-\mathrm{i}\omega(t+\tau_1)} \hat{M}_j^{g\zeta}(t,0)\mathfrak{e}_\zeta \Delta_j(\tau_1)\mathfrak{u}^\nu \hat{M}_{\nu f}^j(t+\tau_1,0) \int_{-\infty}^{\infty} \mathrm{d}\tau_2\, \mathrm{e}^{\mathrm{i}\omega\tau_2} \hat{M}_i^{f\eta}(\tau_2,0)\mathfrak{u}_\eta \Delta_i(\tau_2)\mathfrak{e}^\xi \hat{M}_{\xi g}^i(0,0)|G\rangle \ . \tag{S12}$$

Fifth, the nuclei are subjected to the dynamical classical limit, i.e. the operators are replaced by the corresponding classical dynamical functions and the trace over initial nuclear states is replaced by classical phase space integral, leading to

$$\mathcal{R}(\Omega,\omega) = \frac{1}{2\pi}\int_{-\infty}^{\infty} \mathrm{d}t\, \mathrm{e}^{\mathrm{i}\Omega t} \int_{-\infty}^{\infty} \mathrm{d}\tau_1\, \mathrm{e}^{-\mathrm{i}\omega(t+\tau_1)} \int_{-\infty}^{\infty} \mathrm{d}\tau_2\, \mathrm{e}^{\mathrm{i}\omega\tau_2} \left\langle \mathcal{W}_g(0) M_j^{g\zeta}(t,0)\mathfrak{e}_\zeta \Delta_j(\tau_1)\mathfrak{u}^\nu M_{\nu f}^j(t+\tau_1,0) M_i^{f\eta}(\tau_2,0)\mathfrak{u}_\eta \Delta_i(\tau_2)\mathfrak{e}^\xi M_{\xi g}^i(0,0)\right\rangle \ , \tag{S13}$$

which coincides with Eq. (21) in the main text. Note again that the same rearrangement for the partition functions, as was described in the previous section, has been employed in order to have the canonical averaging with respect to the ground state.

III. EXPRESSIONS FOR XAS AND RIXS IN FOURIER SPACE

In this section the XAS amplitude is recast into Fourier space, getting from Eq. (15) to Eq. (26) in the main text. Firstly an additional integration along an MD trajectory with the length T is performed in Eq. (15), owing to the stationarity of the canonical density

$$\mathcal{X}(\Omega) = \left\langle \frac{1}{2\pi T}\int_{-\infty}^{\infty} \mathrm{d}t\, \mathrm{e}^{\mathrm{i}\Omega t} \int_0^T \mathrm{d}\tau \mathcal{W}_g(\tau) M_f^{g\eta}(t+\tau,\tau)\mathfrak{e}_\eta \mathfrak{e}^\xi M_{\xi g}^f(\tau,\tau)\right\rangle \ , \tag{S14}$$

Using the form of the complex exponential stemming from the scattering operator, Eqs. (9) and (11) of the main text, respectively, one can easily show that the starting time in the product $M_f^{g\eta}(t+\tau,0)M_{\xi g}^f(\tau,0)$ can be shifted, leading to

$$M_f^{g\eta}(t+\tau,\tau)M_{\xi g}^f(\tau,\tau) = M_f^{g\eta}(t+\tau,0)M_{\xi g}^f(\tau,0) \ . \tag{S14}$$

Note that this time shift property does not apply to an arbitrary quantity, but one can still generalize it to a product of dressed dipoles with chain indices and the same starting time,

such as $M_a^b(t_1,t_0)M_b^c(t_2,t_0)\dots M_z^a(t_N,t_0)$. Shifting the starting time to zero, making the substitution $\tau' = \tau + t$ and rearranging yields

$$\mathcal{X}(\Omega) = \left\langle \frac{1}{2\pi T} \int_{-\infty}^{\infty} \mathrm{d}\tau' \, \mathrm{e}^{\mathrm{i}\Omega\tau'} M_f^{g\eta}(\tau',0)\mathfrak{e}_\eta \mathfrak{e}^\xi \int_0^T \mathrm{d}\tau \mathrm{e}^{-\mathrm{i}\Omega\tau} M_{\xi g}^f(\tau,0)\mathcal{W}_g(\tau) \right\rangle \ , \tag{S15}$$

For a sufficiently large T one may extend formally the τ-integration interval to $(-\infty,\infty)$ resulting in a negligible error. Subsequently, one recognises the Fourier transforms of the dressed dipoles, Eq. (24) in the manuscript (note the minus sign), and gets by using Eq. (25) the desired Eq. (26) as written in the main text. Note also that the mean transition frequency $\bar{\omega}_{ab} = -\bar{\omega}_{ba}$ can be negative and thus, in order to keep frequencies positive, $\bar{\omega}_{fg}$ is used in the final expression.

Now the focus is put on the RIXS amplitude and the necessary steps to get from Eq. (21) to Eq. (27) in the main text. Following the same line of reasoning as for the XAS amplitude, the additional integration over MD trajectory is applied to Eq. (21) resulting in

$$\begin{aligned}\mathcal{R}(\Omega,\omega) = \Bigg\langle \frac{1}{2\pi T} \int_0^T \mathrm{d}\tau \, \mathcal{W}_g(\tau) \int_{-\infty}^{\infty} \mathrm{d}t \, \mathrm{e}^{\mathrm{i}\Omega t} \\ \int_{-\infty}^{\infty} \mathrm{d}\tau_1 \, \mathrm{e}^{-\mathrm{i}\omega(\tau+t+\tau_1)} M_j^{g\zeta}(\tau+t,\tau)\mathfrak{e}_\zeta \Delta_j(\tau_1)\mathfrak{u}^\nu M_{\nu f}^j(\tau+t+\tau_1,\tau) \\ \int_{-\infty}^{\infty} \mathrm{d}\tau_2 \, \mathrm{e}^{\mathrm{i}\omega(\tau+\tau_2)} M_i^{f\eta}(\tau+\tau_2,\tau)\mathfrak{u}_\eta \Delta_i(\tau_2)\mathfrak{e}^\xi M_{\xi g}^i(\tau,\tau) \Bigg\rangle \ ,\end{aligned} \tag{S16}$$

where also $1 = \exp[-\mathrm{i}\omega\tau]\exp[\mathrm{i}\omega\tau]$ has been inserted. Again, since the dressed dipoles' product in Eq. (S16) has a cyclic structure of indices, the starting time can be chosen arbitrarily, that is

$$\begin{aligned}M_j^{g\zeta}(\tau+t,\tau)M_{\nu f}^j(\tau+t+\tau_1,\tau)M_i^{f\eta}(\tau+\tau_2,\tau)M_{\xi g}^i(\tau,\tau) \equiv \\ M_j^{g\zeta}(\tau+t,0)M_{\nu f}^j(\tau+t+\tau_1,0)M_i^{f\eta}(\tau+\tau_2,0)M_{\xi g}^i(\tau,0) \ .\end{aligned} \tag{S17}$$

For a sufficiently large T one may extend formally the τ-integration interval to $(-\infty,\infty)$.

Subsequently, one substitutes $\tau' = \tau + t$ yielding

$$\mathcal{R}(\Omega,\omega) = \Bigg\langle \frac{1}{2\pi T} \int\limits_{-\infty}^{\infty} \mathrm{d}\tau \mathrm{e}^{-\mathrm{i}\Omega\tau} \int\limits_{-\infty}^{\infty} \mathrm{d}\tau' \, \mathrm{e}^{\mathrm{i}\Omega\tau'} \int\limits_{-\infty}^{\infty} \mathrm{d}\tau_1 \, \mathrm{e}^{-\mathrm{i}\omega(\tau'+\tau_1)} M_j^{g\zeta}(\tau',0)\mathfrak{e}_\zeta \Delta_j(\tau_1)\mathfrak{u}^\nu M_{\nu f}^j(\tau'+\tau_1,0) \int\limits_{-\infty}^{\infty} \mathrm{d}\tau_2 \, \mathrm{e}^{\mathrm{i}\omega(\tau+\tau_2)} M_i^{f\eta}(\tau+\tau_2,0)\mathfrak{u}_\eta \Delta_i(\tau_2)\mathfrak{e}^\xi M_{\xi g}^i(\tau,0)\mathcal{W}_g(\tau) \Bigg\rangle \ . \tag{S18}$$

Now, one can replace the damping function by its Fourier transform via

$$\Delta_a(\tau) = \int\limits_{-\infty}^{\infty} \mathrm{d}\omega' \mathrm{e}^{\mathrm{i}\omega'\tau} \check{\Delta}_a(\omega') \equiv \int\limits_{-\infty}^{\infty} \mathrm{d}\omega' \mathrm{e}^{-\mathrm{i}\omega'\tau} \check{\Delta}_a(-\omega') \ . \tag{S19}$$

where $\check{\Delta}_a(\omega') := 1/(2\pi)\sqrt{\Gamma_a/\pi}(\Gamma_a + \mathrm{i}\omega')^{-1}$. By rearranging the integrations one gets

$$\mathcal{R}(\Omega,\omega) = \Bigg\langle \frac{1}{2\pi T} \int\limits_{-\infty}^{\infty} \mathrm{d}\omega_1 \int\limits_{-\infty}^{\infty} \mathrm{d}\tau' \, \mathrm{e}^{\mathrm{i}\Omega\tau'} \int\limits_{-\infty}^{\infty} \mathrm{d}\tau_1 \, \mathrm{e}^{-\mathrm{i}\omega(\tau'+\tau_1)} M_j^{g\zeta}(\tau',0)\mathfrak{e}_\zeta \check{\Delta}_j(\omega_1)\mathrm{e}^{\mathrm{i}\omega_1\tau_1}\mathfrak{u}^\nu M_{\nu f}^j(\tau'+\tau_1,0) \int\limits_{-\infty}^{\infty} \mathrm{d}\omega_2 \int\limits_{-\infty}^{\infty} \mathrm{d}\tau \mathrm{e}^{-\mathrm{i}\Omega\tau} \int\limits_{-\infty}^{\infty} \mathrm{d}\tau_2 \, \mathrm{e}^{\mathrm{i}\omega(\tau+\tau_2)} \, M_i^{f\eta}(\tau+\tau_2,0)\mathfrak{u}_\eta \check{\Delta}_i(-\omega_2)\mathrm{e}^{-\mathrm{i}\omega_2\tau_2}\mathfrak{e}^\xi M_{\xi g}^i(\tau,0)\mathcal{W}_g(\tau) \Bigg\rangle \ . \tag{S20}$$

Looking at the time arguments of the dressed dipoles suggests two more variable substitutions: $\tau_1' := \tau' + \tau_1$ and $\tau_2' := \tau + \tau_2$ that yield

$$\mathcal{R}(\Omega,\omega) = \Bigg\langle \frac{1}{2\pi T} \int\limits_{-\infty}^{\infty} \mathrm{d}\omega_1 \int\limits_{-\infty}^{\infty} \mathrm{d}\tau' \, \mathrm{e}^{\mathrm{i}\Omega\tau'} \int\limits_{-\infty}^{\infty} \mathrm{d}\tau_1' \, \mathrm{e}^{-\mathrm{i}\omega\tau_1'} M_j^{g\zeta}(\tau',0)\mathfrak{e}_\zeta \check{\Delta}_j(\omega_1)\mathrm{e}^{\mathrm{i}\omega_1(\tau_1'-\tau')}\mathfrak{u}^\nu M_{\nu f}^j(\tau_1',0) \int\limits_{-\infty}^{\infty} \mathrm{d}\omega_2 \int\limits_{-\infty}^{\infty} \mathrm{d}\tau \mathrm{e}^{-\mathrm{i}\Omega\tau} \int\limits_{-\infty}^{\infty} \mathrm{d}\tau_2' \, \mathrm{e}^{\mathrm{i}\omega\tau_2'} \, M_i^{f\eta}(\tau_2',0)\mathfrak{u}_\eta \check{\Delta}_i(-\omega_2)\mathrm{e}^{-\mathrm{i}\omega_2(\tau_2'-\tau)}\mathfrak{e}^\xi M_{\xi g}^i(\tau,0)\mathcal{W}_g(\tau) \Bigg\rangle \ , \tag{S21}$$

which becomes after rearranging the integrals

$$\mathcal{R}(\Omega,\omega) = \Bigg\langle \frac{1}{2\pi T} \int_{-\infty}^{\infty} \mathrm{d}\,\omega_1 \check{\Delta}_j(\omega_1) \int_{-\infty}^{\infty} \mathrm{d}\tau'\, \mathrm{e}^{-\mathrm{i}(\omega_1-\Omega)\tau'} M_j^{g\zeta}(\tau',0)\mathfrak{e}_\zeta \int_{-\infty}^{\infty} \mathrm{d}\tau_1'\, \mathrm{e}^{-\mathrm{i}(\omega-\omega_1)\tau_1'} \mathfrak{u}^\nu M_{\nu f}^j(\tau_1',0) \int_{-\infty}^{\infty} \mathrm{d}\omega_2\, \check{\Delta}_i(-\omega_2) \int_{-\infty}^{\infty} \mathrm{d}\tau \mathrm{e}^{-\mathrm{i}(\Omega-\omega_2)\tau} \mathfrak{e}^\xi M_{\xi g}^i(\tau,0) \mathcal{W}_g(\tau) \int_{-\infty}^{\infty} \mathrm{d}\tau_2'\, \mathrm{e}^{-\mathrm{i}(\omega_2-\omega)\tau_2'} M_i^{f\eta}(\tau_2',0)\mathfrak{u}_\eta \Bigg\rangle \ . \tag{S22}$$

Here, one recognises the Fourier transforms of the dressed transition dipole moments and one can write more compactly

$$\mathcal{R}(\Omega,\omega) = \Bigg\langle \frac{1}{2\pi T} \int_{-\infty}^{\infty} \mathrm{d}\omega_1 \check{M}_{\zeta j}^g\,(\omega_1-\Omega)\,\mathfrak{e}_\zeta \check{\Delta}_j(\omega_1)\mathfrak{u}^\nu \check{M}_f^{j\nu}\,(\omega-\omega_1) \int_{-\infty}^{\infty} \mathrm{d}\omega_2 \check{M}_i^{f\eta}\,(\omega_2-\omega)\,\mathfrak{u}_\eta \check{\Delta}_i(-\omega_2)\mathfrak{e}^\xi \check{\mathcal{M}}_{\xi g}^i\,(\Omega-\omega_2) \Bigg\rangle \tag{S23}$$

and finally, by using Eq. (25) in the main text that reads

$$\check{M}_g^f(\Omega) \equiv \check{\bar{M}}_g^f(\Omega-\bar{\omega}_{fg}) \ , \tag{S24}$$

one gets the desired expression for the RIXS amplitude in Fourier space, Eq. (27) in the main text. Note that the mean transition frequencies were always chosen positive by switching the indices: $\bar{\omega}_{ab} = -\bar{\omega}_{ba}$.

In order to calculate the quantities $\check{\bar{M}}_g^f(\Omega)$ numerically, the transition dipoles and the energy gaps between the traced electronic states have to be stored along the trajectory. Subsequently one has to construct $\bar{M}_g^f(t,0) = D_g^f(t)\exp[\mathrm{i}\int_0^t \mathrm{d}\tau U_{fg}(\tau)]$ as defined in the main text. Importantly, the functions $\bar{M}_g^f(t,0)$ change only on the nuclear time scale, thus the Fourier transforms, yielding $\check{\bar{M}}_g^f(\Omega)$, can be performed numerically via standard routines employing the MD time step size.

IV. THE SAMPLING VERSUS THE TIME-DOMAIN APPROACH.

In this section it is presented how one obtains the XAS and RIXS amplitudes from the sampling approach and which assumptions and approximations are involved. The XAS am-

plitude should serve again as a template since all performed manipulations can be transferred to the more complicated RIXS amplitude.

The starting point is Eq.(3) (in the manuscript) as a result of Fermi's Golden rule. After applying the BOA, the nuclei are subjected to a statical classical limit, that is in contrast to the derivation Sec. 2.2.2 in the main text. In other words, the nuclear degrees of freedom are assumed to be in a fixed configuration $\mathbf{R}_0$, producing a static external potential. Subsequently, the states $|\alpha\rangle$ of the molecular system are identified with the electronic states $|a\rangle$ that depend parametrically on that particular configuration $\mathbf{R}_0$ and the trace over nuclear states is transferred in to a phase space integral. Inserting the definition of the weighting factor, Eq. (17) in the main text, and performing simple algebra as described in Sec. 1 in the Supplement one obtains the XAS amplitude from sampling via

$$X^{\mathrm{S}}(\Omega) = \left\langle \mathcal{W}_g(\mathbf{R}_0) D_f^{g\eta}(\mathbf{R}_0) \mathfrak{e}_\eta \mathfrak{e}^\xi D_{\xi g}^f(\mathbf{R}_0) \delta\left(\Omega - \Delta E_{fg}(\mathbf{R}_0)\right) \right\rangle \quad . \tag{S25}$$

Applying the same assumptions, one gets the sampled RIXS amplitude from the expression

$$R^{\mathrm{S}}(\Omega,\omega) = \left\langle \mathcal{W}_g(\mathbf{R}_0) \frac{D_j^{g\zeta}(\mathbf{R}_0)\mathfrak{e}_\zeta \mathfrak{u}^\nu D_{\nu f}^j(\mathbf{R}_0)}{\omega - \Delta E_{jf}(\mathbf{R}_0) - \mathrm{i}\Gamma_j} \frac{D_i^{f\eta}(\mathbf{R}_0)\mathfrak{u}_\eta \mathfrak{e}^\xi D_{\xi g}^i(\mathbf{R}_0)}{\omega - \Delta E_{if}(\mathbf{R}_0) + \mathrm{i}\Gamma_i} \delta\left(\Omega - (\Delta E_{fg}(\mathbf{R}_0) + \omega)\right) \right\rangle \quad . \tag{S26}$$

Note that similar to the time-domain approach, Eqs. (15,21) in the main text, the sampled amplitudes are fully determined by the electronic energy gaps and the transition dipole moments and the canonical average is with respect to the electronic ground state Hamilton function. Thus, the sampling can be performed using the very same data as employed for the time-domain method. However, since the dipoles and energies in Eqs. (S25,S26) are evaluated at the same configuration, any phase alteration cancels and the order of summation is irrelevant. Thus, the state tracing as described in Sec. 3.2 in the main text is only obligatorily for the time-correlation function approach.

In order to examine the similarities and difference to the time-domain expression it is beneficial to write the δ-functions and the denominators in the RIXS amplitude in their integral representation, Eqs. (4,19) in the main text, respectively, leading to

$$X^{\mathrm{S}}(\Omega) = \frac{1}{2\pi} \int_{-\infty}^{\infty} \mathrm{d}t\, \mathrm{e}^{\mathrm{i}\Omega t} \left\langle \mathcal{W}_g(\mathbf{R}_0) D_f^{g\eta}(\mathbf{R}_0) \mathfrak{e}_\eta \mathrm{e}^{\mathrm{i}\Delta E_{gf}(\mathbf{R}_0)t} \mathfrak{e}^\xi D_{\xi g}^f(\mathbf{R}_0) \right\rangle \tag{S27}$$

and

$$R^{\mathrm{S}}(\Omega,\omega) = \frac{1}{2\pi}\int_{-\infty}^{\infty}\mathrm{d}t\,\mathrm{e}^{\mathrm{i}\Omega t}\int_{-\infty}^{\infty}\mathrm{d}\tau_1\,\mathrm{e}^{-\mathrm{i}\omega(t+\tau_1)}\int_{-\infty}^{\infty}\mathrm{d}\tau_2\,\mathrm{e}^{\mathrm{i}\omega\tau_2} \\ \left\langle \mathcal{W}_g(\mathbf{R}_0)D_j^{g\zeta}(\mathbf{R}_0)\mathfrak{e}_\zeta \mathrm{e}^{\mathrm{i}\Delta E_{gj}(\mathbf{R}_0)t}\Delta_j(\tau_1)\mathfrak{u}^\nu D^j_{\nu f}(\mathbf{R}_0)\mathrm{e}^{\mathrm{i}\Delta E_{jf}(\mathbf{R}_0)(t+\tau_1)} \right. \\ \left. \times D_i^{f\eta}(\mathbf{R}_0)\mathrm{e}^{\mathrm{i}\Delta E_{fi}(\mathbf{R}_0)\tau_2}\mathfrak{u}_\eta\Delta_i(\tau_2)\mathfrak{e}^\xi D^i_{\xi g}(\mathbf{R}_0)\right\rangle \ , \tag{S28}$$

where it has been used that $\Delta E_{gf}(\mathbf{R}_0)t + \Delta E_{jf}(\mathbf{R}_0)\tau_1 = \Delta E_{gj}(\mathbf{R}_0)t + \Delta E_{jf}(\mathbf{R}_0)(t+\tau_1)$. Surprisingly, the expressions obtained via sampling have a very similar structure as their time-domain counterparts. However, there are two striking differences. First, the transition dipoles are all evaluated at the same configuration: $D_a^{b\xi}(t) \to D_a^{b\xi}(\mathbf{R}_0)$. Second, the integrals in the complex exponentials become simple products: $\int_0^t \Delta E_{ab}(\tau)\mathrm{d}\tau \to \Delta E_{ab}(\mathbf{R}_0)t$. Having these relations at hand, it is straightforward to show that both sampling amplitudes can be considered as limits of the corresponding correlation function expressions if nuclear dynamics can be neglected, i.e. $\mathbf{R}(t) \approx \mathbf{R}(0) \equiv \mathbf{R}_0$.

V. AVERAGING OVER POLARIZATION VECTORS

The starting point is the Fourier space expression for the XAS amplitude

$$\mathcal{X}(\Omega) = \frac{1}{2\pi T}\left\langle \check{M}_f^{g\eta}(-\Omega)\mathfrak{e}_\eta\mathfrak{e}^\xi\check{\mathcal{M}}^f_{\xi g}(\Omega)\right\rangle \ . \tag{S28}$$

This expression, involving only a particular polarization vector of the incoming light beam, should account for the free tumbling of the molecules in the gas or liquid phases. Equivalently it can be averaged over all polarization orientations. In order to achieve this goal the normalized vector is parametrized with the angular spherical coordinates ϕ, θ as

$$\mathfrak{e}_x(\phi,\theta) = \sin(\theta)\cos(\phi), \quad \mathfrak{e}_y(\phi,\theta) = \sin(\theta)\sin(\phi), \quad \mathfrak{e}_z(\phi,\theta) = \cos(\theta) \tag{S28}$$

The average can now easily be performed as an analytical integration over the spherical angles leading to

$$\left\langle \mathfrak{e}_\eta\mathfrak{e}^\xi\right\rangle_{\mathrm{pol.}} = \frac{1}{3}\delta^\xi_\eta \tag{S28}$$

Inserting this into the expression for XAS amplitude on obtains

$$\langle\mathcal{X}(\Omega)\rangle_{\mathrm{pol.}} = \frac{1}{6\pi T}\left\langle \check{M}_f^{g\xi}(-\Omega)\check{\mathcal{M}}^f_{\xi g}(\Omega)\right\rangle \ . \tag{S28}$$

The derivation for the averaged RIXS amplitude follows the same line of reasoning as done for XAS. One starts with

$$\mathcal{R}(\Omega,\omega) = \left\langle \frac{1}{2\pi T} \int_{-\infty}^{\infty} \mathrm{d}\omega_1 \check{M}^{g}_{\zeta j}\left(\omega_1-\Omega\right) \mathfrak{e}_{\zeta} \check{\Delta}_j(\omega_1) \mathfrak{u}^{\nu} \check{M}^{j\nu}_{f}\left(\omega-\omega_1\right) \right.$$
$$\left. \int_{-\infty}^{\infty} \mathrm{d}\omega_2 \check{M}^{f\eta}_{i}\left(\omega_2-\omega\right) \mathfrak{u}_{\eta} \check{\Delta}_i(-\omega_2) \mathfrak{e}^{\xi} \check{\mathcal{M}}^{i}_{\xi g}\left(\Omega-\omega_2\right) \right\rangle \quad . \tag{S29}$$

and both polarization vectors are parametrized with the angular coordinates. The analytical integration is now performed with the constraint, given by experimental conditions, that there is a fixed angle Φ between the two vectors, i.e. for the present consideration $\Phi = 90°$. Equivalently to the results presented in Ref. 54 of the main text, the averaged expression becomes

$$\begin{aligned}
\left\langle \mathcal{R}(\Omega,\omega) \right\rangle_{\mathrm{pol.}} = & \left\langle \frac{1}{2\pi T} \right. \\
& \times F \int_{-\infty}^{\infty} \mathrm{d}\omega_1 \check{M}^{g}_{\zeta j}\left(\omega_1-\Omega\right) \check{\Delta}_j(\omega_1) \check{M}^{j\zeta}_{f}\left(\omega-\omega_1\right) \int_{-\infty}^{\infty} \mathrm{d}\omega_2 \check{M}^{f\xi}_{i}\left(\omega_2-\omega\right) \check{\Delta}_i(-\omega_2) \check{\mathcal{M}}^{i}_{\xi g}\left(\Omega-\omega_2\right) \\
& + G \int_{-\infty}^{\infty} \mathrm{d}\omega_1 \check{M}^{g}_{\xi j}\left(\omega_1-\Omega\right) \check{\Delta}_j(\omega_1) \check{M}^{j\eta}_{f}\left(\omega-\omega_1\right) \int_{-\infty}^{\infty} \mathrm{d}\omega_2 \check{M}^{f\eta}_{i}\left(\omega_2-\omega\right) \check{\Delta}_i(-\omega_2) \check{\mathcal{M}}^{i}_{\xi g}\left(\Omega-\omega_2\right) \\
& \left. + H \int_{-\infty}^{\infty} \mathrm{d}\omega_1 \check{M}^{g}_{\eta j}\left(\omega_1-\Omega\right) \check{\Delta}_j(\omega_1) \check{M}^{j\xi}_{f}\left(\omega-\omega_1\right) \int_{-\infty}^{\infty} \mathrm{d}\omega_2 \check{M}^{f\eta}_{i}\left(\omega_2-\omega\right) \check{\Delta}_i(-\omega_2) \check{\mathcal{M}}^{i}_{\xi g}\left(\Omega-\omega_2\right) \right\rangle \quad ,
\end{aligned} \tag{S30}$$

where $F = H = 3\cos^2(\Phi) - 1$, $G = 4 - 2\cos^2(\Phi)$. As an exception to the employed sum convention, the summation in the middle line still goes over ξ and η although they appear exclusively as a subscript or superscript, respectively.

VI. XAS AMPLITUDES WITH INFINITE LIFETIMES FOR FINAL STATES

Fig. S1 shows the absorption spectra obtained via Eq. (26) in the main text without additional convolution by a Lorentzian function which implies that the lifetime of the final state goes to infinity ($\Gamma \to 0$).

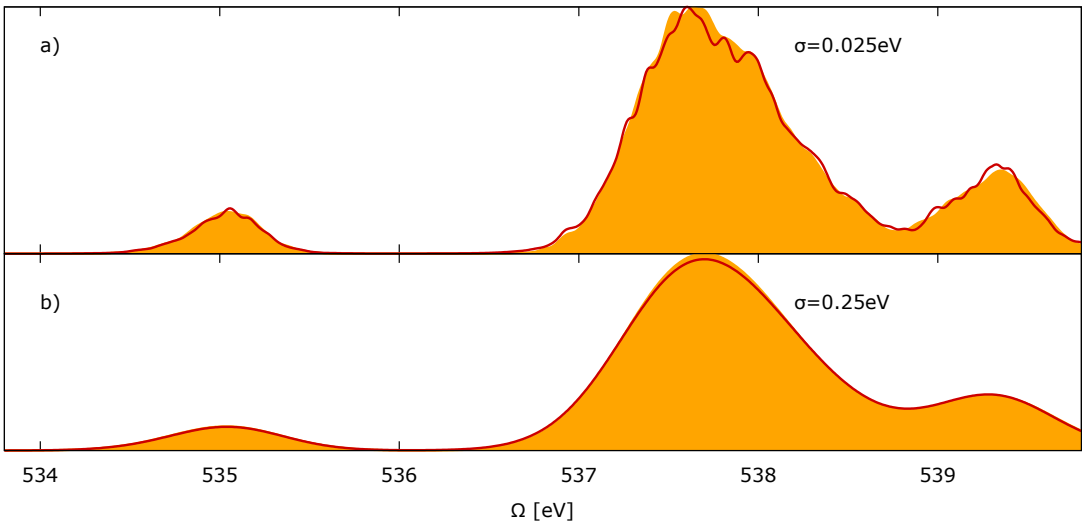

FIG. S1. XAS amplitudes with an infinite lifetimes for final states. The colour code is explained in Fig. 1 in the main text.

VII. PROOF THAT THE SPECTRAL NORM IS PRESERVED IN XAS

First, the focus is put on the XAS amplitude obtained from the sampling procedure. Again the canonical average is partially written as a time integration along an NVE trajectory yielding

$$\mathcal{X}_{\mathrm{S}}(\Omega) = \left\langle \frac{1}{T}\int_0^T \mathrm{d}\tau \mathcal{W}_g(\tau) D_f^{g\eta}(\tau)\mathfrak{e}_\eta \mathfrak{e}^\xi D_{\xi g}^f(\tau)\delta(\Omega - \Delta E_{fg}(\tau)) \right\rangle \quad . \tag{S31}$$

Using the integral representation of the delta function one gets

$$\mathcal{X}_{\mathrm{S}}(\Omega) = \left\langle \frac{1}{T}\int_{-\infty}^{\infty} \mathrm{d}\tau \mathcal{W}_g(\tau) D_f^{g\eta}(\tau)\mathfrak{e}_\eta \mathfrak{e}^\xi D_{\xi g}^f(\tau)\frac{1}{2\pi}\int_{-\infty}^{\infty} \mathrm{d}t\, \mathrm{e}^{\mathrm{i}\Omega t}\mathrm{e}^{-\mathrm{i}\Delta E_{fg}(\tau)t} \right\rangle \quad , \tag{S32}$$

Now one can carry out the integration over Ω to get the spectral norm of XAS

$$\int_{-\infty}^{\infty}\mathrm{d}\Omega\mathcal{X}_{\mathrm{S}}(\Omega) = \left\langle \frac{1}{T}\int_0^T \mathrm{d}\tau \mathcal{W}_g(\tau) \int_{-\infty}^{\infty}\mathrm{d}t\frac{1}{2\pi}\int_{-\infty}^{\infty}\mathrm{d}\Omega \mathrm{e}^{\mathrm{i}\Omega t} D_f^{g\eta}(\tau)\mathfrak{e}_\eta \mathfrak{e}^\xi D_{\xi g}^f(\tau)\mathrm{e}^{-\mathrm{i}\Delta E_{fg}(\tau)t} \right\rangle \tag{S33}$$

$$= \left\langle \frac{1}{T}\int_0^T \mathrm{d}\tau \int_{-\infty}^{\infty}\mathrm{d}t\delta(t)\mathcal{W}_g(\tau) D_f^{g\eta}(\tau)\mathfrak{e}_\eta \mathfrak{e}^\xi D_{\xi g}^f(\tau)\mathrm{e}^{-\mathrm{i}\Delta E_{fg}(\tau)t} \right\rangle \tag{S34}$$

$$= \left\langle \frac{1}{T}\int_0^T \mathrm{d}\tau \mathcal{W}_g(\tau) D_f^{g\eta}(\tau)\mathfrak{e}_\eta \mathfrak{e}^\xi D_{\xi g}^f(\tau) \right\rangle \quad . \tag{S35}$$

Now the focus is put on the XAS amplitude stemming from the time domain approach, i.e.

$$\mathcal{X}(\Omega) = \frac{1}{2\pi} \int_{-\infty}^{\infty} \mathrm{d}t\, \mathrm{e}^{\mathrm{i}\Omega t} \left\langle \frac{1}{T} \int_{0}^{T} \mathrm{d}\tau \mathcal{W}_g(\tau) M_f^{g\eta}(t+\tau,\tau) \mathfrak{e}_\eta \mathfrak{e}^\xi M_{\xi g}^f(\tau,\tau) \right\rangle \quad . \tag{S36}$$

Integrating over the excitation frequency Ω and subsequently employing the integral representation of the delta function yields

$$\int_{-\infty}^{\infty} \mathrm{d}\Omega \mathcal{X}(\Omega) = \int_{-\infty}^{\infty} \mathrm{d}t\, \delta(t) \left\langle \frac{1}{T} \int_{0}^{T} \mathrm{d}\tau \mathcal{W}_g(\tau) M_f^{g\eta}(t+\tau,\tau) \mathfrak{e}_\eta \mathfrak{e}^\xi M_{\xi g}^f(\tau,\tau) \right\rangle \quad . \tag{S37}$$

Carrying out the integration over t and noting that $M_{\xi g}^f(\tau,\tau) \equiv D_{\xi g}^f(\tau)$ leads to

$$\int_{-\infty}^{\infty} \mathrm{d}\Omega \mathcal{X}(\Omega) = \left\langle \frac{1}{T} \int_{0}^{T} \mathrm{d}\tau \mathcal{W}_g(\tau) D_f^{g\eta}(\tau) \mathfrak{e}_\eta \mathfrak{e}^\xi D_{\xi g}^f(\tau) \right\rangle \quad , \tag{S38}$$

which is identical to the spectral norm resulting from the sampling approach, Eq. (S35), if the same data has been used.

VIII. VARIOUS CUTS FOR RIXS

For the model system, as presented in the main text, the RIXS spectra for different fixed excitation frequencies show all very similar structures, compare Fig. 4 in the main text and Fig. S2. This fact is due the simplistic one-electron approximation that neglects any orbital relaxation after the excitation has happened.

IX. DERIVATION OF THE TIME-DEPENDENT FUNCTIONS

First, the focus is put on the RIXS amplitude obtained via the time-domain approach, Eq. (21) in the main text, where the additional convolution with the normalised Gaussian function has been performed, as discussed Sec. 4 in the main text. The convoluted RIXS amplitude then reads

$$\begin{aligned}\mathcal{R}(\Omega,\omega) = \frac{1}{2\pi} \int_{-\infty}^{\infty} \mathrm{d}t\, \mathrm{e}^{-t^2\sigma^2/2} \mathrm{e}^{\mathrm{i}\Omega t} \int_{-\infty}^{\infty} \mathrm{d}\tau_1\, \mathrm{e}^{-\mathrm{i}\omega(t+\tau_1)} \int_{-\infty}^{\infty} \mathrm{d}\tau_2\, \mathrm{e}^{\mathrm{i}\omega\tau_2} \\ \left\langle \mathcal{W}_g(0) M_j^{g\zeta}(t,0) \mathfrak{e}_\zeta \Delta_j(\tau_1) \mathfrak{u}^\nu M_{\nu f}^j(t+\tau_1,0) M_i^{f\eta}(\tau_2,0) \mathfrak{u}_\eta \Delta_i(\tau_2) \mathfrak{e}^\xi M_{\xi g}^i(0,0) \right\rangle \quad .\end{aligned} \tag{S39}$$

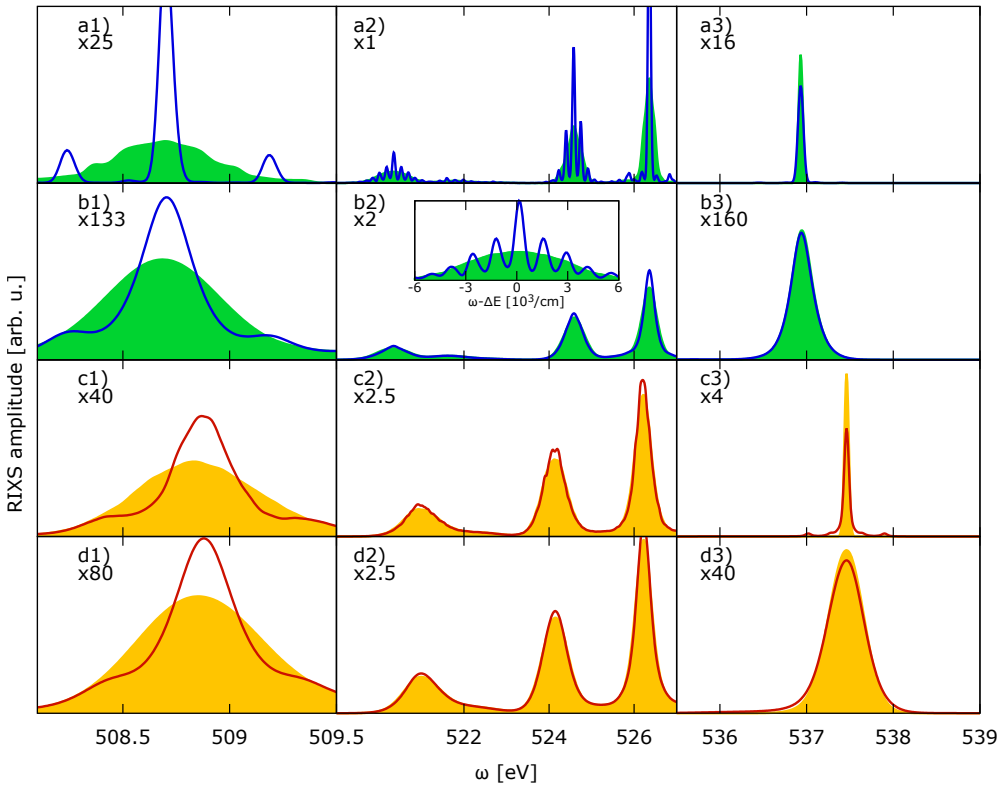

FIG. S2. Cuts through the RIXS spectrum at the highest considered resonant absorption frequencies, i.e. $\Omega = 538.7\,\mathrm{eV}$ for the gas phase and $\Omega = 539.2\,\mathrm{eV}$ for the bulk water. The inset zooms into the left peak of panel a2) with $\Delta E = 520.3\,\mathrm{eV}$.

Now the spectrum is evaluated at a certain frequency pair $(\Omega, \omega) = (\bar{\omega}_{ig}, \bar{\omega}_{if})$ related to a particular channel $g \to i \to f$. Using the definitions of the dressed dipole moments $M_a^{b\xi}(t,0)$ (Eq. (11) in the main text) and the gap fluctuation function $U_{ab}(\tau)$ (Sec. 3.2 in the main text) one can write

$$\mathcal{R}(\bar{\omega}_{ig}, \bar{\omega}_{if}) = \frac{1}{2\pi} \int_{-\infty}^{\infty} \mathrm{d}t\, \mathrm{e}^{-t^2\sigma^2/2} \mathrm{e}^{\mathrm{i}(\bar{\omega}_{ig} - \bar{\omega}_{j'g'})t} \int_{-\infty}^{\infty} \mathrm{d}\tau_1\, \mathrm{e}^{-\mathrm{i}(\bar{\omega}_{if} - \bar{\omega}_{j'f'})(t+\tau_1)} \int_{-\infty}^{\infty} \mathrm{d}\tau_2\, \mathrm{e}^{\mathrm{i}(\bar{\omega}_{if} - \bar{\omega}_{i'f'})\tau_2}$$
$$\Big\langle \mathcal{W}_{g'}(0) D_{j'}^{g'\zeta}(t) \mathrm{e}^{\mathrm{i}\int_0^t U_{g'j'}(\tau)\mathrm{d}\tau} \mathfrak{e}_\zeta \Delta_{j'}(\tau_1) \mathfrak{u}^\nu D_{\nu f'}^{j'}(t+\tau_1) \mathrm{e}^{\mathrm{i}\int_0^{t+\tau_1} U_{j'f'}(\tau)\mathrm{d}\tau}$$
$$D_{i'}^{f\eta}(\tau_2) \mathrm{e}^{\mathrm{i}\int_0^{\tau_2} U_{f'i'}(\tau)\mathrm{d}\tau} \mathfrak{u}_\eta \Delta_{i'}(\tau_2) \mathfrak{e}^\xi D_{\xi g}^{i'}(0) \Big\rangle \quad , \tag{S40}$$

where the summation goes now over the primed indices in order to distinguish them from the fixed g, i, f that are not summed over in the following. It is assumed that only one

summand contributes significantly, namely where $i' = j' = i$, $f' = f$ and $g' = g$, i.e.

$$\begin{aligned}\mathcal{R}(\bar{\omega}_{ig}, \bar{\omega}_{if}) \approx \frac{1}{2\pi} \int_{-\infty}^{\infty} \mathrm{d}t\, \mathrm{e}^{-t^2\sigma^2/2} \int_{-\infty}^{\infty} \mathrm{d}\tau_1 \int_{-\infty}^{\infty} \mathrm{d}\tau_2 \\ \Big\langle \mathcal{W}_g(0) D_i^{g\zeta}(t) \mathrm{e}^{\mathrm{i}\int_0^t \mathrm{d}\tau U_{gi}(\tau)} \mathfrak{e}_\zeta \Delta_i(\tau_1) \mathfrak{u}^\nu D^i_{\nu f}(t+\tau_1) \mathrm{e}^{\mathrm{i}\int_0^{t+\tau_1} U_{if}(\tau)\mathrm{d}\tau} \\ D_i^{f\eta}(\tau_2) \mathrm{e}^{\mathrm{i}\int_0^{\tau_2} U_{fi}(\tau)\mathrm{d}\tau} \mathfrak{u}_\eta \Delta_i(\tau_2) \mathfrak{e}^\xi D^i_{\xi g}(0) \Big\rangle \quad . \end{aligned} \tag{S41}$$

Additionally the Condon approximation is applied by setting the transition dipoles to, e.g. $D_a^{b\xi}(t) \equiv D_a^{b\xi}(0)$ leading after rearranging to

$$\begin{aligned}\mathcal{R}(\bar{\omega}_{ig}, \bar{\omega}_{if}) \approx \Big\langle \frac{1}{2\pi} \mathcal{W}_g(0) D_i^{g\zeta}(0) \mathfrak{e}_\zeta \mathfrak{u}^\nu D^i_{\nu f}(0) D_i^{f\eta}(0) \mathfrak{u}_\eta \mathfrak{e}^\xi D^i_{\xi g}(0) \int_{-\infty}^{\infty} \mathrm{d}t\, \mathrm{e}^{-t^2\sigma^2/2} \int_{-\infty}^{\infty} \mathrm{d}\tau_1 \int_{-\infty}^{\infty} \mathrm{d}\tau_2 \\ \mathrm{e}^{\mathrm{i}\int_0^t U_{gi}(\tau)\mathrm{d}\tau} \Delta_i(\tau_1) \mathrm{e}^{\mathrm{i}\int_0^{t+\tau_1} U_{if}(\tau)\mathrm{d}\tau} \mathrm{e}^{\mathrm{i}\int_0^{\tau_2} U_{fi}(\tau)\mathrm{d}\tau} \Delta_i(\tau_2) \Big\rangle \quad . \end{aligned} \tag{S42}$$

The results for the RIXS amplitude, as shown in Fig. 4 in the main text, exhibit a remarkable difference between elastic ($g = f$) and inelastic ($g \neq f$) peaks with respect to the impact of nuclear dynamics. It is therefore desirable to restructure the expression such that elastic and inelastic RIXS amplitude are easily distinguishable. This can be achieved by rewriting and combining the integrals in the complex exponents as $\int_0^{t+\tau_1} U_{if}(\tau)\mathrm{d}\tau = \int_t^{t+\tau_1} U_{if}(\tau)\mathrm{d}\tau + \int_0^t U_{if}(\tau)\mathrm{d}\tau$ and subsequently $\int_0^t U_{gi}(\tau)\mathrm{d}\tau + \int_0^t U_{if}(\tau)\mathrm{d}\tau = \int_0^t U_{gf}(\tau)\mathrm{d}\tau$ yielding

$$\begin{aligned}\mathcal{R}(\bar{\omega}_{ig}, \bar{\omega}_{if}) \propto \\ \Big\langle \int_{-\infty}^{\infty} \mathrm{d}t\, \mathrm{e}^{-t^2\sigma^2/2} \mathrm{e}^{\mathrm{i}\int_0^t U_{gf}(\tau)\mathrm{d}\tau} \int_{-\infty}^{\infty} \mathrm{d}\tau_1\, \mathrm{e}^{\mathrm{i}\int_t^{t+\tau_1} U_{if}(\tau)\mathrm{d}\tau} \Delta_i(\tau_1) \int_{-\infty}^{\infty} \mathrm{d}\tau_2\, \mathrm{e}^{\mathrm{i}\int_0^{\tau_2} U_{fi}(\tau)\mathrm{d}\tau} \Delta_i(\tau_2) \Big\rangle \quad , \end{aligned} \tag{S43}$$

where the constant prefactor $\mathcal{W}_g(0) D_i^{g\zeta}(0) \mathfrak{e}_\zeta \mathfrak{u}^\nu D^i_{\nu f}(0) D_i^{f\eta}(0) \mathfrak{u}_\eta \mathfrak{e}^\xi D^i_{\xi g}(0)/(2\pi)$ has been omitted for the sake of brevity and the integrations have been interchanged. Note that for the elastic peak the exponential $\mathrm{e}^{\mathrm{i}\int_0^t U_{gf}(\tau)\mathrm{d}\tau}$ becomes unity, since $U_{gg}(\tau) \equiv 0$ and thus the expression differs substantially in the inelastic case as it has been desired. With the definition $\chi^{\mathrm{C}}_{if}(t) := \int_{-\infty}^{\infty} \mathrm{d}\tau_1\, \mathrm{e}^{\mathrm{i}\int_t^{t+\tau_1} U_{if}(\tau)\mathrm{d}\tau} \Delta_i(\tau_1)$ one can write more compactly

$$\mathcal{R}(\bar{\omega}_{ig}, \bar{\omega}_{if}) \propto \int_{-\infty}^{\infty} \mathrm{d}t\, \mathrm{e}^{-t^2\sigma^2/2} \left\langle \mathrm{e}^{\mathrm{i}\int_0^t U_{gf}(\tau)\mathrm{d}\tau} \chi^{\mathrm{C}}_{if}(t) \chi^{\mathrm{C}*}_{if}(0) \right\rangle \quad . \tag{S44}$$

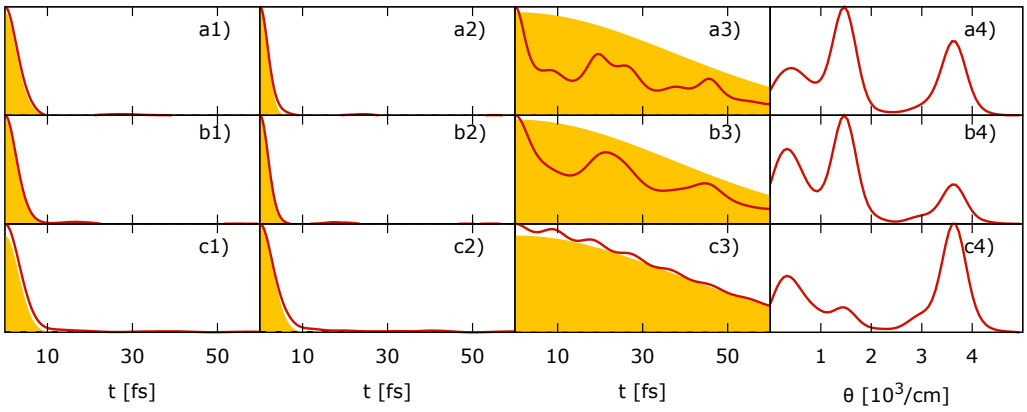

FIG. S3. Time-dependent functions corresponding to the inelastic spectral peaks in Fig. 5, panel 2) in the main text. Panels a) to c) are assigned to the peaks from the left to the right.

Since the integrand has the structure of an autocorrelation function it is symmetric and, hence, the integral reduces to

$$\mathcal{R}(\bar{\omega}_{ig},\bar{\omega}_{if}) \propto \int_0^\infty \mathrm{d}t\, \mathrm{e}^{-t^2\sigma^2/2}\mathrm{Re}\left\langle \mathrm{e}^{\mathrm{i}\int_0^t U_{gf}(\tau)\mathrm{d}\tau}\chi^{\mathrm{C}}_{if}(t)\chi^{\mathrm{C}*}_{if}(0)\right\rangle \quad . \tag{S45}$$

The respective RIXS amplitude $\mathcal{R}^{\mathrm{S}}(\bar{\omega}_{ig},\bar{\omega}_{if})$ resulting from the sampling approach can be obtained by taking the limit of static nuclei. Consequently, setting $U_{ab}(\tau) \equiv U_{ab}(0)$ leads to

$$\mathcal{R}^{\mathrm{S}}(\bar{\omega}_{ig},\bar{\omega}_{if}) \propto \int_0^\infty \mathrm{d}t\, \mathrm{e}^{-t^2\sigma^2/2}\mathrm{Re}\left\langle \mathrm{e}^{\mathrm{i}U_{gf}(0)t}|\chi^{\mathrm{S}}_{if}(0)|^2\right\rangle \quad , \tag{S46}$$

where $\chi^{\mathrm{S}}_{if}(0) := \int_{-\infty}^{\infty}\mathrm{d}\tau_1\, \mathrm{e}^{\mathrm{i}U_{if}(0)\tau_1}\Delta_i(\tau_1)$.

X. TIME-DEPENDENT FUNCTIONS FOR THE INELASTIC PEAKS

Complementary to Fig. 6 in the main text, the Fig. S3 exhibits the time-dependent functions and their ingredients belonging to the other inelastic peaks in the RIXS spectrum.

XI. SIMPLE HARMONIC MODEL

One can understand the differences for $\chi^{\mathrm{C/S}}_{if}(0)$ discussed in the main text on the basis of a simple model, where the gap fluctuation has the harmonic form $U_{if}(\tau) \approx \varepsilon_{if}\cos(\Theta\tau)$.

In this case

$$L_{if}^{\mathrm{S}}(\tau;0) = \exp\left[\mathrm{i}\varepsilon_{if}\tau\Delta_i(\tau)\right] \tag{S46a}$$

$$L_{if}^{\mathrm{C}}(\tau;0) = \exp\left[\mathrm{i}\varepsilon_{if}\frac{\sin(\Theta\tau)}{\Theta}\Delta_i(\tau)\right] \quad . \tag{S46b}$$

One immediately recognizes that $L_{if}^{\mathrm{S}}(\tau;0)$ does not depend on the vibrational frequency, Θ, in contrast to $L_{if}^{\mathrm{C}}(\tau;0)$. It is straightforward to show that in the low frequency limit

$$\lim_{\Theta\to 0}|\chi_{if}^{\mathrm{C}}(0)|^2 = \frac{1}{\varepsilon_{if}^2+\Gamma_i^2} = \lim_{\Theta\to 0}|\chi_{if}^{\mathrm{S}}(0)|^2 \tag{S46}$$

the time-domain and the sampling results coincide, as is expected from the limit of static nuclei described in Sec. IV in the supplementary information. In contrast, in the limit of fast nuclear oscillation one gets

$$\lim_{\Theta\to\infty}|\chi_{if}^{\mathrm{C}}(0)|^2 = \frac{1}{\Gamma_i^2} > \frac{1}{\varepsilon_{if}^2+\Gamma_i^2} = \lim_{\Theta\to\infty}|\chi_{if}^{\mathrm{S}}(0)|^2 \quad . \tag{S46}$$

Thus, for this simple model, the sampling method would underestimate the value $|\chi_{if}^{\mathrm{C}}(0)|^2$ and thus the intensity of the inelastic scattering if the gap strongly fluctuates with a frequency stemming from a fast nuclear mode.

[SK3] Quasi-classical approaches to vibronic spectra revisited

SVEN KARSTEN, SERGEI D. IVANOV, SERGEY I. BOKAREV, and OLIVER KÜHN

Reproduced from S. KARSTEN, S. D. IVANOV, S. I. BOKAREV, and O. KÜHN, *Journal of Chemical Physics* **148**, 102337 (2018), with the permission of AIP Publishing.

THE JOURNAL OF CHEMICAL PHYSICS **148**, 102337 (2018)

Quasi-classical approaches to vibronic spectra revisited

Sven Karsten, Sergei D. Ivanov,[a] Sergey I. Bokarev, and Oliver Kühn
Institute of Physics, Rostock University, Albert-Einstein-Str. 23-24, 18059 Rostock, Germany

(Received 2 November 2017; accepted 20 December 2017; published online 22 January 2018)

The framework to approach quasi-classical dynamics in the electronic ground state is well established and is based on the Kubo-transformed time correlation function (TCF), being the most classical-like quantum TCF. Here we discuss whether the choice of the Kubo-transformed TCF as a starting point for simulating *vibronic* spectra is as unambiguous as it is for vibrational ones. Employing imaginary-time path integral techniques in combination with the interaction representation allowed us to formulate a method for simulating vibronic spectra in the adiabatic regime that takes nuclear quantum effects and dynamics on multiple potential energy surfaces into account. Further, a generalized quantum TCF is proposed that contains many well-established TCFs, including the Kubo one, as particular cases. Importantly, it also provides a framework to construct new quantum TCFs. Applying the developed methodology to the generalized TCF leads to a plethora of simulation protocols, which are based on the well-known TCFs as well as on new ones. Their performance is investigated on 1D anharmonic model systems at finite temperatures. It is shown that the protocols based on the new TCFs may lead to superior results with respect to those based on the common ones. The strategies to find the optimal approach are discussed. *Published by AIP Publishing.* https://doi.org/10.1063/1.5011764

I. INTRODUCTION

Understanding the dynamics of complex many-body systems is the grand challenge of theoretical chemistry and molecular physics. The recent decade witnessed spectacular progress in (non-linear) experimental spectroscopic techniques[1–3] in various frequency ranges, owing to the appearance of ultra-short pulses and intense light sources.[4–7] The resulting vibrational, electronic, and vibronic spectra provide comprehensive information about the dynamical processes, when interpreted and understood with the help of proper theoretical tools.

From the theoretical standpoint, there exist two limiting strategies to simulate vibronic spectra, that is, energy- and time-domain approaches. For the former, in the simplest case, single-point electronic structure calculations are performed and broadening is included on a phenomenological level.[1,8] Further, nuclear vibrations can be treated within the Franck-Condon model assuming shifted harmonic potentials for the initial and final electronic states.[2,8–10] Still, this approach is not appropriate for cases where strong anharmonicities, bond formation or cleavage, and/or pronounced conformational changes are observed. In the time domain, arguably the best approach is to perform wavepacket quantum dynamics numerically exactly.[9,11–15] However, it usually requires an expensive pre-computation of many-dimensional potential energy surfaces (PESs) and is limited to small systems or is based on a reduction of dimensionality. Many attempts to bridge the gap between the two extrema, which are not possible to review in detail here, were made; see Refs. 16–18 and references therein for selected examples. The consensus is that it is desirable to have a method that would combine the advantages of the two limiting strategies in an optimal way. If one starts from the energy-domain approaches, a step in this direction is to sample nuclear distributions in the phase space via molecular dynamics (MD) methods.[2,19] It leads to a more realistic description of conformational and environmental effects[20–22] but still lacks information about correlated nuclear motion and thus, for instance, is not capable of reproducing vibronic progressions. Correlations can be included by recasting the quantities of interest in terms of time correlation functions (TCFs).[1,2,23–25]

Recently, we have developed such an extension to the state-of-the-art sampling approach to X-ray spectroscopy, in particular, to X-ray absorption and resonant inelastic X-ray scattering spectra.[26,27] Further improvements of the method should attack the main approximations behind it: the Born-Oppenheimer approximation and the dynamical classical limit (DCL).[2] The former leads to a neglect of non-adiabatic effects that are conventionally treated via surface hopping methods,[28,29] mean-field (Ehrenfest) dynamics,[29] multiple spawning techniques,[16,30] classical and semiclassical mapping approaches,[31–33] exact factorization perspective[34,35] and Bohmian dynamics[36] to mention but few; see, e.g., Refs. 18, 37, and 38 for review. The consequences of the DCL approximation are twofold. First, the nuclear dynamics is exclusively due to forces in the electronic ground state. It leads to the complete loss of information about the excited state dynamics and can cause wrong frequencies and shapes of the vibronic progressions in certain physical situations, although the envelopes of the vibronic bands may be reproduced reasonably well.[39,40] Furthermore, at ambient temperatures, the ground state trajectory is confined in a small region near the potential minimum, i.e., one cannot describe excited-state dynamics such as dissociation within the DCL. Further, the nuclei are treated as

[a]Electronic mail: sergei.ivanov@uni-rostock.de

point particles, sacrificing their quantum nature, in particular zero-point energy and tunneling effects. This might lead to qualitatively wrong dynamics and even sampling, if light atoms, shallow PESs, and/or isotope substitutions are involved, as have been shown on numerous examples starting from small molecules in gas phase to biomolecules.[41–44]

In order to improve on the DCL, a method that explicitly accounts for excited states' dynamics is needed. Following Ref. 45, one can derive a semiclassical approximation to the absorption cross section that leads to the dynamics that is performed on the arithmetic mean of the ground and excited state PESs, hence referred to as the averaged classical limit (ACL) method. Note that such a derivation for resonant Raman spectra leads to the known expression derived by Shi and Geva.[46,47] The authors evaluated the quality of the ACL method on simple test systems and found it satisfactory.

For inclusion of quantum effects, Feynman path integrals (PIs) provide hitherto the most elegant and robust solution for trajectory-based approaches.[19,48–50] Here, the ring polymer molecular dynamics (RPMD) method[51] enjoyed success in simulating quasi-classical dynamics; see, e.g., Refs. 52 and 53 for review. Further, two similar non-adiabatic versions of RPMD (NRPMD) were developed,[54,55] based on the mapping approach.[37,56,57] This method allows for all the aspects discussed above and is a suitable method of choice to approach vibronic spectra, given an efficient simulation protocol is provided.[58] Several PI approaches for many PESs without mapping variables were attempted,[59–63] most of them addressing non-adiabatic effects on static properties or reaction rates via surface hopping methods. However, none of them have been applied for simulating vibronic spectra. We here suggest a practical recipe for simulating optical absorption spectra in the adiabatic limit, taking nuclear quantum effects and multiple PESs into account. The heart of the method is the imaginary-time shifted TCF, given in Eq. (3), which is addressed via imaginary-time PI techniques and the interaction representation; see Sec. II C. To the best of our knowledge, such a methodology for simulating vibronic spectra is proposed for the first time.

The cornerstone of (N)RPMD is the Kubo-transformed TCF, which is the most classical-like quantum TCF since it is real-valued and symmetric with respect to time reversal. Nonetheless, when it comes to practical evaluation of *vibronic* spectra, the Kubo TCF either becomes non-tractable by MD methods or has to be decomposed into the contributions that do not have the beneficial properties of the original TCF; in particular, they are no more real functions of time; see Sec. II B for details. This poses the central question of this work, that is, whether the choice of the Kubo TCF as the starting point for simulating vibronic spectra is as unambiguous as it is in infrared spectroscopy.[25,51,64]

In anticipation of our results, we propose a generalized quantum TCF that is based on the aforementioned imaginary-time shifted one and contains most of the well-established TCFs, including Kubo, as particular cases. Moreover, it offers the possibility to construct, in principle, infinitely many other new TCFs that may or may not be numerically favorable. Importantly, the new TCFs are constructed out of the imaginary-time shifted TCF without a need to recompute it. We demonstrate numerically on 1D model systems that the best results indeed do not necessarily come from the Kubo TCF.

This paper is structured as follows. In Sec. II, the generalized TCF is introduced and the new methodology for the simulation of vibronic spectra is developed. The connections to the well-established TCFs and methods based on them are discussed in Sec. II D. The results for 1D model systems (see Sec. III) are presented in Sec. IV. In Sec. IV B, the flexibility of the formalism is taken advantage of to propose new TCFs that improve the numerical behavior for the particular models. Conclusions and outlook, containing the discussion of the optimal starting point for simulating vibronic spectra, can be found in Sec. V.

II. THEORY

A. Generalized time correlation function

The experimentally measured quantity, the absorption cross section is proportional to the lineshape function

$$S_0(\Omega) = \int_{-\infty}^{\infty} \mathrm{d}t\, \mathrm{e}^{-\mathrm{i}\Omega t} C_0(t), \tag{1}$$

which is given by the Fourier transform of the dipole autocorrelation function[2]

$$C_0(t) \equiv \frac{1}{Z}\mathrm{tr}\left[\mathrm{e}^{-\beta\hat{H}}\hat{d}(0)\hat{d}(t)\right], \tag{2}$$

and the TCFs will be denoted with C and their respective Fourier transforms with S throughout the manuscript. Here $\hat{H}$ is the full molecular Hamiltonian of the system including both electrons and nuclei, $Z = \mathrm{tr}[\exp(-\beta\hat{H})]$ is the respective partition function, $\mathrm{tr}[\bullet]$ standing for the trace with respect to both nuclear and electronic degrees of freedom, $\beta \equiv 1/k_\mathrm{B}T$ is the inverse temperature, and $\hat{d}(t)$ is the total dipole operator time-evolved with respect to $\hat{H}$.

It is well known that many quantum TCFs can be defined, all carrying the same information since their Fourier transforms have simple relations.[64] In particular, applying a shift in imaginary time to the dipole autocorrelation function, Eq. (2), leads to

$$C_\lambda(t) \equiv C_0(t + \mathrm{i}\lambda\hbar) = \frac{1}{Z}\mathrm{tr}\left[\mathrm{e}^{-(\beta-\lambda)\hat{H}}\hat{d}(0)\mathrm{e}^{-\lambda\hat{H}}\hat{d}(t)\right], \tag{3}$$

hence referred to as the imaginary-time shifted TCF. The aforementioned relation for the Fourier transforms of C_λ and C_0 reads

$$S_\lambda(\Omega) = \mathrm{e}^{-\lambda\Omega\hbar} S_0(\Omega), \tag{4}$$

as it is shown in the supplementary material. Integrating both sides of this equation over λ from 0 to β yields the relation between the absorption spectrum and the well-known Kubo-transformed TCF.[65] In an attempt to formulate a more general and flexible approach that may lead to more practical simulation protocols, we propose to employ a weighting function $w(\lambda)$ for this integration leading to

$$\underbrace{\frac{1}{\beta}\int_0^\beta \mathrm{d}\lambda\, w(\lambda) S_\lambda(\Omega)}_{\bar{S}_w(\Omega)} = \underbrace{\frac{1}{\beta}\int_0^\beta \mathrm{d}\lambda\, w(\lambda)\mathrm{e}^{-\lambda\Omega\hbar}}_{p_w(\Omega)} S_0(\Omega) \tag{5}$$

such that the absorption lineshape can be obtained as

$$S_0(\Omega) = p_w^{-1}(\Omega)\bar{S}_w(\Omega). \tag{6}$$

Naturally, setting $w(\lambda) = 1$ would yield back the Kubo-transformed TCF.

Given the flexibility provided by the arbitrary choice of the weighting function $w(\lambda)$, we attempt to find a reasonable approximation to $\bar{C}_w(t)$,

$$\bar{C}_w(t) = \frac{1}{\beta}\int_0^\beta \mathrm{d}\lambda w(\lambda) C_\lambda(t), \tag{7}$$

which is a time-domain version of $\bar{S}_w(\Omega)$, rather than to approximate the desired lineshape function, $S_0(\Omega)$, directly. The prefactor $p_w^{-1}(\Omega)$ in Eq. (6) compensates the performed shift in the imaginary time and is thus referred to as the shift correction factor (SCF). As it will become clear later, the SCF acts as a "magnifying glass" or a "filter" emphasizing certain contributions stemming from particular λ and suppressing the others. It will be also shown that Eq. (6) serves as a common starting point for several popular approximations to vibronic spectra.

B. Practical considerations

In order to formulate a reasonable approximation to $\bar{C}_w(t)$, the central object to consider is the imaginary-time shifted TCF, $C_\lambda(t)$, defined in Eq. (3). Assuming the Born-Oppenheimer approximation and evaluating the electronic part of the trace in Eq. (3) in the adiabatic basis $|a\rangle$ yields

$$C_\lambda(t) = \frac{1}{Z}\sum_{a,b}\mathrm{Tr}\left[\mathrm{e}^{-(\beta-\lambda)\hat{H}_a}\hat{D}_b^a\mathrm{e}^{-\lambda\hat{H}_b}\mathrm{e}^{\mathrm{i}\hat{H}_b t/\hbar}\hat{D}_a^b\mathrm{e}^{-\mathrm{i}\hat{H}_a t/\hbar}\right], \tag{8}$$

where the capital Tr[•] stands for a trace in the nuclear Hilbert space only, $\hat{H}_a$ corresponds to the nuclear Hamiltonian with the PES of the ath electronic eigenstate and $\hat{D}_b^a = \langle a|\hat{d}|b\rangle$ is the transition dipole moment. For the sake of brevity, a single transition from an initial electronic state g to a final state f of a two-level system is considered in the following. The generalization to the case of many states is straightforward.

Spelling out the electronic trace in Eq. (8) leads to

$$C_\lambda(t) = \frac{1}{Z}\mathrm{Tr}\left[\mathrm{e}^{-(\beta-\lambda)\hat{H}_g}\hat{D}_f^g\mathrm{e}^{-\lambda\hat{H}_f}\mathrm{e}^{\mathrm{i}\hat{H}_f t/\hbar}\hat{D}_g^f\mathrm{e}^{-\mathrm{i}\hat{H}_g t/\hbar} + \mathrm{e}^{-(\beta-\lambda)\hat{H}_f}\hat{D}_g^f\mathrm{e}^{-\lambda\hat{H}_g}\mathrm{e}^{\mathrm{i}\hat{H}_g t/\hbar}\hat{D}_f^g\mathrm{e}^{-\mathrm{i}\hat{H}_f t/\hbar}\right]. \tag{9}$$

It is possible to shift the final state Hamiltonian as $\hat{H}_f \equiv \hat{\tilde{H}}_f + \varepsilon_{fg}$ such that the eigenvalues of $\hat{H}_g$ and shifted $\hat{\tilde{H}}_f$ are in the same energy range, and thus, the respective frequencies are on the same (nuclear) timescale. Such a shift is needed for practical purposes since the TCF would otherwise oscillate on the electronic timescales that are unresolvable by means of nuclear MD methods.[26,27] To reiterate, the shift is equal to zero by construction when purely vibrational transitions are concerned and this issue does not occur.

Applying the shift to Eq. (9) and evaluating the trace in the nuclear eigenstates, $\hat{H}_g|G\rangle = E_G|G\rangle$ and $\hat{\tilde{H}}_f|F\rangle = \tilde{E}_F|F\rangle$ yield

$$C_\lambda(t) = \frac{1}{Z}\sum_{G,F}\mathrm{e}^{-(\beta-\lambda)E_G}\mathrm{e}^{-\lambda(\tilde{E}_F+\varepsilon_{fg})}|\langle G|\hat{D}_f^g|F\rangle|^2\mathrm{e}^{\mathrm{i}(\varepsilon_{fg}+\tilde{E}_F-E_G)t/\hbar} + \frac{1}{Z}\sum_{G,F}\mathrm{e}^{-(\beta-\lambda)(\tilde{E}_F+\varepsilon_{fg})}\mathrm{e}^{-\lambda E_G}|\langle G|\hat{D}_f^g|F\rangle|^2 \times \mathrm{e}^{-\mathrm{i}(\varepsilon_{fg}+\tilde{E}_F-E_G)t/\hbar}. \tag{10}$$

Note the different sign in front of ε_{fg} in the phase factors. The transitions due to the first and second summands group near the shift frequencies $\Omega = \pm\varepsilon_{fg}$. It becomes apparent that the two spectral features are completely isolated if $\varepsilon_{fg} \gg \tilde{E}_F - E_G$; see Fig. 1. This makes MD methods unsuitable for the present purpose as the spectrum covers frequency ranges inaccessible to them. Consequently both summands have to be considered individually in practice. However, the TCFs described by the individual terms do not have the properties of the common TCFs described by Eq. (9). For instance, the respective terms for Kubo TCF would become complex when treated this way, as can be easily seen by choosing $w(\lambda) = 1$. Therefore the terms themselves do not constitute an obvious choice for an approximation by (quasi-)classical methods. In a nutshell, for a practical application, one cannot approximate the TCF given by Eq. (9) directly, as it requires treating the dynamics on the electronic timescales, whereas approximating the summands therein individually does not favor the Kubo-transformed TCF because the summands are not real functions of time. In the following, only the first term in Eq. (9) is considered since only the feature on the positive part of the frequency axis is important for absorption spectroscopy.

C. Vibronic spectra via imaginary-time PI methods

In the spirit of RPMD techniques, it is useful to consider the quantity of interest, $C_\lambda(t)$, at time zero for any given λ.[51] To reiterate, only the summand that leads to absorption spectra is kept in the expression for $C_\lambda(t)$, Eq. (9). The nuclear trace therein is evaluated in the coordinate representation, and the shift in imaginary time is equidistantly discretized, i.e., $\lambda = l\beta/P$, where $l \in [0, P]$ is an integer number and $P > 0$ is a natural number which will become later the number of beads in the ring polymer. The result has the form of a configuration-space average

$$C_\lambda(0) = \frac{1}{Z}\int \mathrm{d}\mathbf{R}_0\,\langle\mathbf{R}_0|\,\mathrm{e}^{-(P-l)\beta\hat{H}_g/P}\hat{D}_f^g\mathrm{e}^{-l\beta\hat{H}_f/P}\hat{D}_g^f\,|\mathbf{R}_0\rangle, \tag{11}$$

where $\mathbf{R}$ describes the positions of all the nuclei in the system; note that since l is a discretized version of λ, we use both interchangeably to simplify the notation. Following the standard imaginary-time path integral approach,[50,66] each exponential term $\exp(-j\beta\hat{H}_a/P)$, where $a = g, f$ and $j = P - l, l$, can

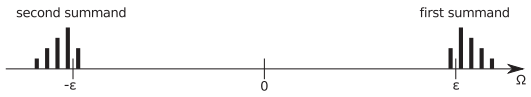

FIG. 1. Schematic picture of a spectrum resulting from the two summands in Eq. (10). Note that the SCF, which would lead to different relative intensities at $\pm\varepsilon$, is not applied.

be written as a product of j identical factors $\exp(-\beta\hat{H}_a/P)$. Further, in total, $P-2$ spatial closures $\int \mathrm{d}\mathbf{R}_k\,|\mathbf{R}_k\rangle\langle\mathbf{R}_k| = 1$, with $k = 1, \ldots, l-1$ and $k = l+1, \ldots, P-1$ for $a = f$ and $a = g$, respectively, are inserted in between those factors. One additional closure with $k = l$ is put right next to $\hat{D}_f^g$ yielding the corresponding eigenvalue $\hat{D}_f^g\,|\mathbf{R}_l\rangle = D_f^g(\mathbf{R}_l)\,|\mathbf{R}_l\rangle$ as it happens for $\hat{D}_g^f\,|\mathbf{R}_0\rangle$ as well. The resulting matrix elements $\langle\mathbf{R}_{k+1}|\exp(-\beta\hat{H}_a/P)\,|\mathbf{R}_k\rangle$ are approximated via the symmetric Trotter factorization in order to separate position- and momentum-dependent terms. The former result in the respective eigenvalues, whereas the latter are supplied by the momenta closures leading after some straightforward algebra to the well-known kinetic (spring) terms. These terms stand for harmonic springs connecting adjacent beads of the resulting ring polymer; note that they are state-independent and thus coincide for $\hat{H}_g$ and $\hat{H}_f$. Finally, the value $C_\lambda(0)$ gets the form of a configuration integral over the ring polymer coordinate space

$$C_\lambda(0) \approx \frac{1}{Z}\int \mathrm{d}\mathbb{R}\,\mathrm{e}^{-\beta U_l(\mathbb{R})} D_f^g(\mathbf{R}_l) D_g^f(\mathbf{R}_0), \tag{12}$$

where $\mathbb{R} = (\mathbf{R}_0, \ldots, \mathbf{R}_{P-1})^{\mathrm{T}}$ is the ring polymer configuration obeying the cyclic condition $\mathbf{R}_P = \mathbf{R}_0$ and the effective ring polymer potential

$$U_l(\mathbb{R}) = K(\mathbb{R}) + \frac{1}{P}\left[\sum_{k=0}^{l}\eta_k V_f(\mathbf{R}_k) + \sum_{k=l}^{P}\eta_k V_g(\mathbf{R}_k)\right], \tag{13}$$

$$K(\mathbb{R}) = \sum_{k=0}^{P-1}\frac{P}{2\beta^2\hbar^2}(\mathbf{R}_k - \mathbf{R}_{k+1})^{\mathrm{T}}\mathbb{M}(\mathbf{R}_k - \mathbf{R}_{k+1}). \tag{14}$$

Here K denotes the kinetic spring term, $\mathbb{M}$ is the nuclear mass matrix, and η_k is equal to 1/2 if k corresponds to the first or the last summand, to 0 if there is only one summand, which is the case if $l = 0, P$, and to 1 in all other cases. Importantly each value of l defines a particular PES and thus a particular *realization* of the ring polymer, undergoing different dynamics as will become clear later; see Eq. (21). An example of such a realization of the ring polymer is illustrated in Fig. 2. One sees that there are two sets of beads, which "feel" either the upper or the lower PES as is indicated by the blue or the red color,

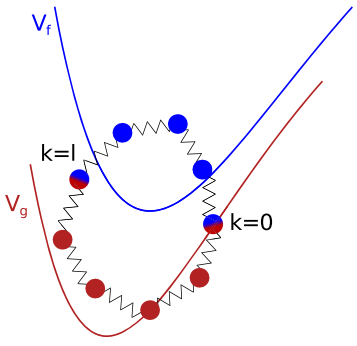

FIG. 2. Sketch of the effective ring polymer potential, Eq. (13), for the case $P = 9$ and $l = 4$, where the 0-th and the lth bead are marked. The PESs V_g and V_f are shown in red and blue, respectively. The color of the beads that "feel" one of the PESs is chosen accordingly.

respectively. Note that there are two "boundary" beads that distinguish one set of beads from the other and are influenced by the averaged potential (hence depicted with both colors). The presence of the two distinguishable sets of beads breaks the cyclic symmetry of the ring polymer. Remarkably, in the classical limit, $P = 1$, l can be equal to 0 and 1, and thus there would be *two* realizations of the ring polymer according to Eq. (13). This can be viewed as a consequence of the broken cyclic symmetry of the ring polymer; note that when the PESs are the same, the two potential energy terms in Eq. (13) coincide, yielding the standard PIMD expression for the ground state dynamics. Equation (12) remains exact in the limit $P \to \infty$.

In order to evaluate the configuration integral in Eq. (12) correctly via the standard sampling methods, the partition function that appears in the expression has to normalize the density $\exp[-\beta U_l(\mathbb{R})]$. Thus, the expression is multiplied and divided by

$$Z_\lambda = \mathrm{Tr}\left[\mathrm{e}^{-(\beta-\lambda)\hat{H}_g}\mathrm{e}^{-\lambda\hat{H}_f}\right] \propto \int \mathrm{d}\mathbb{R}\,\mathrm{e}^{-\beta U_l(\mathbb{R})} \tag{15}$$

leading to a prefactor $\xi_\lambda \equiv Z_\lambda/Z$ that has to be calculated. As it is derived in the supplementary material, this prefactor can be conveniently and still numerically exactly extracted as

$$\xi_\lambda = \frac{\exp\left[-\int_0^\lambda \left\langle \hat{V}_f - \hat{V}_g\right\rangle_\mu \mathrm{d}\mu\right]}{1 + \exp\left[-\int_0^\beta \left\langle \hat{V}_f - \hat{V}_g\right\rangle_\mu \mathrm{d}\mu\right]}, \tag{16}$$

where the average is defined as

$$\langle\bullet\rangle_\lambda = \frac{1}{Z_\lambda}\mathrm{Tr}\left[\mathrm{e}^{-(\beta-\lambda)\hat{H}_g}\mathrm{e}^{-\lambda\hat{H}_f}\bullet\right]. \tag{17}$$

Finally, putting together all the obtained results leads to a relation for $\bar{C}_w(0)$,

$$\bar{C}_w(0) \approx \frac{1}{P}\sum_{l=0}^{P}\eta_l w(\lambda)\xi_\lambda\left\langle D_f^g(\mathbf{R}_l) D_g^f(\mathbf{R}_0)\right\rangle_\lambda, \tag{18}$$

where the imaginary-time integration in Eq. (7) has been discretized via the trapezoidal rule. It becomes apparent at this point that one has to independently simulate each summand in Eq. (18), which corresponds to the respective realization of the ring polymer defined by a particular value λ. The factor $w(\lambda)$ provides an external weight to the realizations and can be chosen arbitrarily, whereas the factors ξ_λ are *intrinsic* weights that are dictated by quantum statistical mechanics; note that we consider distinguishable particles only.

The remaining question is how to approximate the nuclear dynamics, in particular, how to estimate the non-classical time evolution in Eq. (8), i.e., $\exp[-\mathrm{i}\hat{H}_f t/\hbar]\hat{D}_g^f \exp[\mathrm{i}\hat{H}_g t/\hbar]$. First, an effective Hamiltonian $\hat{H}_\lambda$ is defined for each point in the imaginary time $\lambda = l\beta/P$ that corresponds to the effective potential $U_l(\mathbb{R})$, Eq. (13). Second, the Hamiltonian of the ath state is rewritten as $\hat{H}_a = \hat{H}_\lambda + \hat{H}_a - \hat{H}_\lambda$ for $a = g, f$ in order to switch to the interaction representation[1,2] that yields

$$\mathrm{e}^{-\mathrm{i}\hat{H}_a t/\hbar} = \mathrm{e}^{-\mathrm{i}\hat{H}_\lambda t/\hbar}\exp_+\left\{-\frac{\mathrm{i}}{\hbar}\int_0^t [\hat{H}_a(\tau) - \hat{H}_\lambda]\mathrm{d}\tau\right\}, \tag{19}$$

where the time arguments indicate a time evolution with respect to $\hat{H}_\lambda$. Third, the dynamics induced by $\hat{H}_\lambda$ are approximated by the quasi-classical dynamics of the ring polymer with respect to

$$H_\lambda(\mathbb{R},\mathbb{P}) = \frac{1}{2P}\mathbb{P}^{\mathrm{T}}\mathbb{M}^{-1}\mathbb{P} + U_l(\mathbb{R}) \tag{20}$$

and the operators are replaced by their classical counterparts. The momenta of the ring polymer $\mathbb{P}$ are introduced as conjugate variables to the coordinates $\mathbb{R}$ in the usual fashion. Finally, the desired TCF is approximated as

$$\bar{C}_w(t) \approx \frac{1}{P}\sum_{l=0}^{P}\eta_l w(\lambda)\xi_\lambda \times \left\langle D_f^g(\mathbf{R}_l)D_g^f(\mathbf{R}_0(t))\mathrm{e}^{\mathrm{i}/\hbar\int_0^t[V_f(\mathbf{R}_0(\tau))-V_g(\mathbf{R}_0(\tau))]\mathrm{d}\tau}\right\rangle_\lambda . \tag{21}$$

Equation (21) is the main theoretical result of this work. It should be stressed that this approximation leaves the density stationary at all times and excludes problems such as the infamous zero-point energy leakage.[67] Additionally, this stationarity enables averaging along trajectories, on top of the averaging with respect to the initial conditions, thereby greatly improving the statistical convergence. The generalization to a larger number of states amounts to considering each transition separately according to Eq. (21) and summing the results over.

D. Limiting cases

The formalism presented in Sec. II C as well as several important limiting cases are sketched in Fig. 3. The starting point is Eq. (5), where a specific choice of the, in principle, arbitrary weighting function, $w(\lambda)$, is made. This choice defines the SCF and leads to a particular TCF, including most of the well-established ones. For instance, choosing $w(\lambda) = \delta(\lambda)$, see the left column therein, defines a constant SCF equal to β and corresponds to the standard dipole autocorrelation function, Eq. (2). Approximating the dynamics according to Eq. (21) would lead to the dynamics with respect to the ground state *only*, as it is done in the DCL, but taking nuclear quantum effects into account, hence termed PI-DCL. The pure DCL limit can be straightforwardly obtained by setting the number of beads $P = 1$. The neglect of dynamics leads to sampling approaches and further sacrifice of nuclear degrees of freedom as such results in single-point calculation methods as it was discussed in the Introduction.

For the case $w(\lambda) = \delta(\lambda)$, there exists also a completely different route to approximate the dynamics,[45] starting from Eq. (8) with $\lambda = 0$ in the Wigner representation and taking the semiclassical limit. This results in the ACL dynamics, that is, the dynamics on the averaged PES $U_{1/2} \equiv 1/2[V_g + V_f]$. In contrast to the approximation suggested in this work, the initial conditions for the ACL are sampled with respect to the PES of the ground state, U_0, thereby making the density non-stationary. The presence of these non-equilibrium dynamics causes unphysical negativities in the spectrum as it is discussed in Sec. IV A and is proven in the supplementary material.

Interestingly, the same approximation to the dynamics can be obtained within the presented formalism by setting $w(\lambda) = \delta(\lambda - \beta/2)$, see the second column in Fig. 3, which results in the Schofield TCF,[68] being another TCF that has the desired symmetry properties for quasi- or semi-classical approximations.[69,70] Then the $P \to 1$ limit of the corresponding ring polymer potential can be interpreted as the averaged PES, $U_{1/2}$, defined above. Thus, the dynamics in this case would be identical to the ACL one with the big advantage that the density is stationary. Since it stems from the Schofield TCF, it is referred to as Schofield ACL (SACL) in the following. It is worth mentioning that analogous to ACL, one can obtain SACL by starting from the Schofield TCF and following the semiclassical route described in Ref. 45.

Choosing $w(\lambda) = 1$, which corresponds to a democratic average over all possible ring polymer realizations, results in the Kubo TCF. For this choice of the weighting function and restricting to the *adiabatic* regime, it has been suggested in Ref. 58 that in the limit of an infinite number of mapping variables, the NRPMD method[54,58] evokes dynamics similar

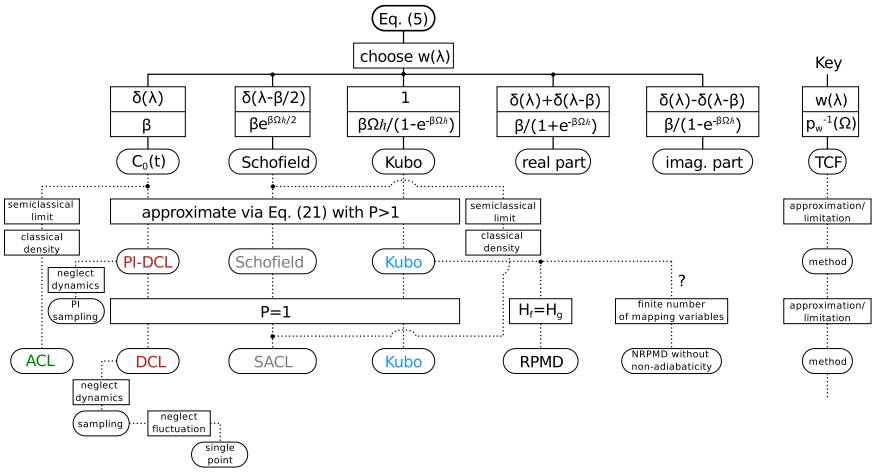

FIG. 3. Sketch of the developed formalism with several examples of the weighting function $w(\lambda)$ that lead to the well-established TCFs. The legend on the right-hand side deciphers the employed convention.

to that in Eq. (21). Further, setting $\hat{H}_f = \hat{H}_g$ yields the standard Kubo-transformed TCF, which serves as the basis for the state-of-the-art RPMD method.[51,53] Note that the real as well as the imaginary part of $C_0(t)$ can be obtained by setting $w(\lambda) = \delta(\lambda) \pm \delta(\lambda - \beta)$, respectively.

III. COMPUTATIONAL DETAILS

In order to probe a chemically relevant regime, the presented protocol was applied to a diatomic that mimics the OH bond of a gas-phase water molecule. The PESs for the states, V_g and V_f, were represented by a Morse potential $V_a(r) = E_a(1 - \exp[-\alpha_a(r - r_a^{\mathrm{eq}})])^2$, where the ground state parameters $E_g = 0.185$ a.u., $\alpha_g = 1.21$ a.u.$^{-1}$, and $r_g^{\mathrm{eq}} = 1.89$ a.u. were taken from the qSPC/Fw water model and r is the distance between O and H atoms.[71] To have non-trivial spectra, the frequency and the position of the minimum for the (final) excited state PES were chosen to be different from the ground state ones, whereas the dissociation energy was set the same $E_f = E_g \equiv E$. The particular values for the parameters α_f and r_f^{eq} for the cases considered are given in Sec. IV. Further, the Condon approximation for the dipoles was used, and the spectra were broadened with a Gaussian function with the dispersion $\sigma = 0.002$ a.u. to account for dephasing due to the interactions with an environment.

Spectra were simulated according to Eq. (21), with 500 uncorrelated initial conditions for each summand therein (that is, each realization of the ring polymer with respect to λ); ACL required 5000 trajectories due to non-stationarity of the dynamics. MD with a Langevin thermostat was employed at two different temperatures. One was the ambient $T = 300.0$ K corresponding to $\beta\hbar\omega_g = 18.6$, where ω_g is the harmonic frequency of the ground state. The other higher $T = 1117.6$ K implied $\beta\hbar\omega_g = 5$. As a side product of this sampling, the prefactors ξ_λ were obtained via the gap average $\langle \hat{V}_f - \hat{V}_g \rangle_\lambda$ according to Eq. (16). An MD trajectory according to H_λ with a length of 12 000.0 a.u. and a timestep of 3.0 a.u. was performed using the velocity-Verlet algorithm, starting from each initial condition. The time evolution resulting from the kinetic spring term was carried out analytically as described in Ref. 72. The desired TCF was calculated as an ensemble average combined with the time average. The former was realized as an average over the swarm of trajectories. The latter was carried out as an average along each trajectory, which is legitimate owing to the stationarity of the density. Exact results were obtained in the basis of 50 eigenstates of the harmonic oscillator with the frequency ω_g. Note that in view of the generalization to multi-state cases, where all transitions have to be considered separately and then summed up, an individual normalization of the TCFs would lead to wrong intensity ratios between the transitions. Hence, a normalization of the spectra was not performed.

IV. RESULTS AND DISCUSSION

A. Common weighting functions

The performance of all the aforementioned methods, namely, PI-DCL, DCL, ACL, Schofield, SACL, and Kubo, is compared against the numerically exact quantum-mechanical (QM) reference in Fig. 4 for the two shifted Morse oscillators. The shifts were chosen to be $r_f^{\mathrm{eq}} - r_g^{\mathrm{eq}} = 0.22$ a.u. (left) and $r_f^{\mathrm{eq}} - r_g^{\mathrm{eq}} = 0.5$ a.u. (right), with a moderate ratio $\alpha_f/\alpha_g = 0.86$ and using ambient temperature. In Fig. 4(a1) the convergence of intrinsic weights, ξ_λ, to the exact result is illustrated. To start, the weights for $P = 1$ (classical case) are qualitatively wrong. In this case, there are only two points corresponding to the two realizations of the classical particle being *either* in the ground *or* in the excited state; see Sec. II for a discussion. Importantly, despite being an exponential quantity, the intrinsic weights can be obtained with sufficient accuracy with $P = 16$ and completely converge at $P = 32$; note the log scale. These numbers of beads are typical for reaching convergence for ground-state properties of water at ambient conditions.[67,73] It is natural to expect the same convergence behavior when the shift between PESs is sufficiently small.

Switching to the absorption spectra depicted in Figs. 4(b1) and 4(c1), one sees that the exact solution reveals a typical Franck-Condon progression with a Huang-Rhys factor below 0.5, which implies the maximal intensity at the 0–0 transition.[2,10] For the classical case, $P = 1$, Fig. 4(b1), DCL and Kubo results are very similar since ξ_0 is much higher than ξ_β, see Fig. 4(a1), and thus the contributions stemming from the ground state play the most important role. Both methods fail completely to reproduce the exact spectrum in this parameter regime. In particular, the intensities are dramatically overestimated (note the scaling factor), and the maximum is not at the exact 0–0 transition. The vibronic progression is significantly suppressed and features wrong frequencies and almost symmetrical shapes, as it was discussed for DCL before.[26,27] The shape is more symmetrical for DCL than for Kubo because the Kubo SCF, being responsible for the detailed balance, suppresses the signal below zero frequency; the SCFs are listed in Fig. 3 and the non-trivial ones are plotted in Fig. 6(b). In contrast, ACL results satisfactorily agree with the exact ones, apart from a slight difference in the fundamental frequency. Nonetheless, the infamous negativities, which are intrinsic to the method, can be observed to the left of the 0–0 transition. Finally, the spectral intensities resulting from SACL grow uncontrollably due to the SCF. To illustrate, the SCF that reads $\exp[\hbar\beta\Omega/2]$ would yield approximately 3000, $9{\cdot}10^6$, and $2.7{\cdot}10^{10}$ for the first, second, and third overtones of the characteristic frequency ω_f, respectively; note that whereas the frequency is growing linearly with the vibrational quantum number in vibronic progression, the SCF grows exponentially. This suggests that a more suitable choice of the SCF can yield better numerical results, as is discussed in Sec. IV B.

When it comes to more beads, that is, $P = 32$ in Fig. 4(c1), PI-DCL exhibits reasonable amplitudes but still yields fairly symmetric wrong spectral shapes. This is a manifestation of the fact that the ground-state dynamics only cannot reproduce the spectra which are significantly dependent on the peculiarities of the excited state. The Kubo results improve a lot with respect to the spectral structure, as they include contributions from the beads evolving on the PES of the excited state, included due to the intrinsic weights in the proper way. The shape is still not correct which is presumably due to

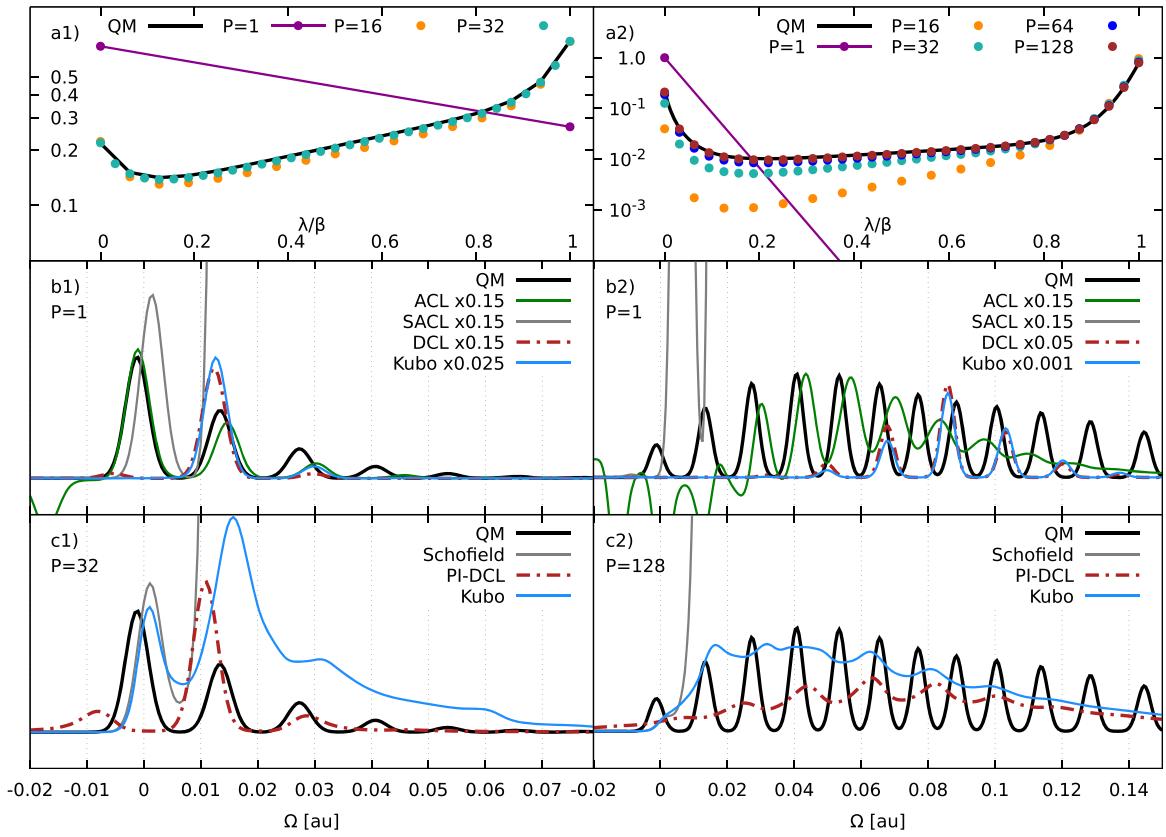

FIG. 4. The two-level system with the parameters $\alpha_f/\alpha_g = 0.86$ at 300 K, left: $r_f^{\mathrm{eq}} - r_g^{\mathrm{eq}} = 0.22$ a.u. and right: $r_f^{\mathrm{eq}} - r_g^{\mathrm{eq}} = 0.5$ a.u.; see the text. Top: intrinsic weights, ξ_λ, and middle and bottom: absorption spectra for $P = 1, 32, 128$.

over-pronounced contributions from large values of λ, which in principle can be healed by a proper choice of the SCF; see Sec. IV B. Schofield spectra still grow uncontrollably with frequency due to the SCF, which does not depend on the number of beads.

In order to test a different regime, where the vibronic progressions are more pronounced, the same system with the displacement of the PESs increased to $r_f^{\mathrm{eq}} - r_g^{\mathrm{eq}} = 0.5$ a.u. was considered; see right panels in Fig. 4. Following the same structure of the discussion, the curve for intrinsic weights is an order of magnitude lower, is much steeper at the imaginary-time borders, and converges slower to the exact result. The latter is intuitively expected since a larger number of beads are needed to account for the increased displacement of the PESs as can be understood from Fig. 2. The difference between ξ_0 and ξ_β for $P = 1$ suggests that the results for Kubo and DCL would match even closer than it was observed in Fig. 4(b1). Indeed, the difference between the two is barely visible; see Fig. 4(b2); note that they are still not identical due to the different SCFs. Again, both show dramatically overestimated intensities and rather symmetric lineshapes, whereas the ACL spectra are qualitatively better, though they suffer increasingly from the negativities. When the number of beads is increased to $P = 128$ in Fig. 4(c2), the Kubo spectrum improves over that from DCL with respect to the envelop but the peaks are still much broader than in the QM reference and are not at the correct positions, whereas the Schofield spectra diverge again. The PI-DCL amplitudes are getting more reasonable, but the shape and peak positions still do not fit to the QM result. Practically, there is no qualitative difference in terms of the performance of each method for the two regimes considered.

Yet another possible regime can be accessed via increasing the temperature (or, equivalently, by decreasing the frequencies) while keeping the (other) parameters of the ground and excited PESs the same; see Fig. 5. Starting with the system with moderate shift in the left panels, one can see that the intrinsic weights, ξ_λ, are converged at $P = 32$. Switching to the classical spectra in Fig. 4(b1), one sees that DCL and Kubo again fail to describe the exact spectrum. The ACL spectrum reveals small negativities and slightly incorrect peak positions but overall demonstrates the best agreement among the methods considered. Interestingly in this regime, the Schofield spectrum remains bound which can be explained by a more moderate SCF as a consequence of the higher temperature. However the intensities are still strongly overestimated especially for higher frequencies.

By increasing the number of beads, panels (c), the PI-DCL results do not improve over pure DCL ones although the amplitudes become better. The Kubo spectrum loses the fine structure whereas the envelop resembles the shape of the exact

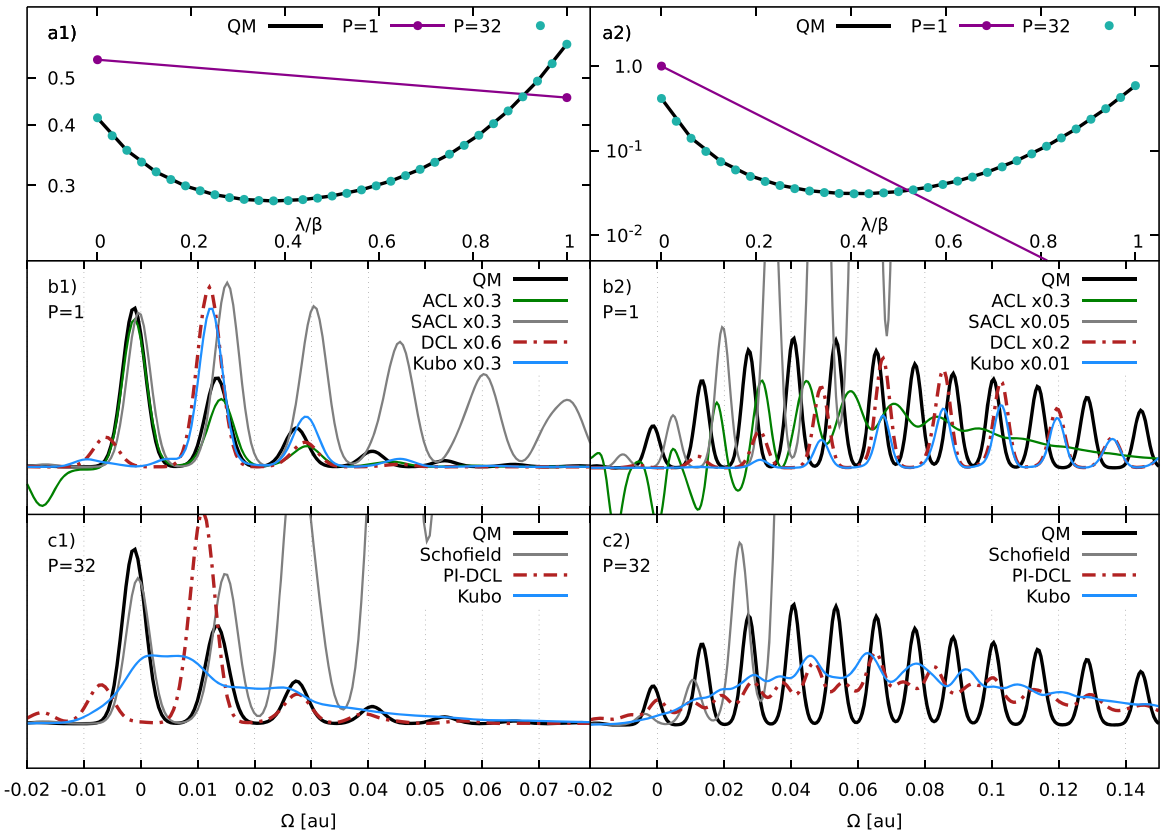

FIG. 5. The structure of the figure coincides with that of Fig. 4 with the only difference being the higher temperature $T = 1117.6$ K ($\beta\hbar\omega_g = 5$).

result. The Schofield spectrum again becomes unbound as it was for the lower temperature.

The conclusions for the other system are the same apart from the exploding SACL spectra in Fig. 5(b2) as the interested reader can figure out.

B. Possible improvements

As it was shown in Sec. IV A, ACL performs generally quite well with respect to the lineshapes but reveals negativities due to non-equilibrium dynamics, which is a rather severe problem. The equilibrium version of ACL, which does not have this deficiency, stems from the Schofield correlation function, hence termed SACL in Sec. II D. Unfortunately, the respective SCF is enormously large in the relevant frequency regions [Fig. 6(b)] thereby leading to a numerical instability (large times small number) for spectra. It is thus desirable to preserve the dynamics of SACL having a more "gentle" SCF. To reiterate, in contrast to intrinsic weights ξ_λ dictated by statistics, external weighting function $w(\lambda)$ can be chosen arbitrarily. One possibility is to choose

$$w(\lambda) = \mathrm{e}^{-|\lambda-\beta/2|\epsilon}, \tag{22}$$

which "smooths" the delta peak around $\beta/2$ (corresponding to the Schofield TCF), with the smoothing being controlled by the value of ϵ. It can be clearly seen in Fig. 6(b) that the resulting SCFs (green curves) indeed exhibit a significantly more moderate growth with frequency. Another possibility logically follows from the conclusion that Kubo performs reasonably well but suffers from overestimated intensities for higher frequencies. It is supposed that this deficiency is due to over-pronounced contributions with large λ, thus, suggesting

$$w(\lambda) = \mathrm{e}^{-\lambda\epsilon}. \tag{23}$$

This constitutes a low-pass filter that suppresses the unwanted contributions to spectra. The respective filtered intrinsic weights, $\xi_\lambda \cdot w(\lambda)$, are shown in the upper panels of Fig. 6. One sees that the smoothed Schofield includes all the contributions keeping the emphasis on the middle one, whereas the low-pass filter indeed suppresses the contributions with large λ. To reiterate, Kubo and Schofield can be viewed as two limiting cases, the former taking all the contributions into account democratically and the latter picking only a single ($\lambda = \beta/2$) one.

The respective spectra for the system with the small shift are shown in the lower panels of Fig. 6; the results for the other system are given in the supplementary material. One sees that at lower temperatures (larger β), Fig. 6(c1) the low-pass filter appears to be the better choice. In particular, it removes the over-pronounced high frequency contributions that the Kubo results suffer from, whereas the smoothed Schofield filter emphasizes these contributions even more. However, the low-pass filter results in the dynamical features that are washed out with respect to the exact spectrum. In contrast, for the higher temperature case, low-pass performs as badly as the

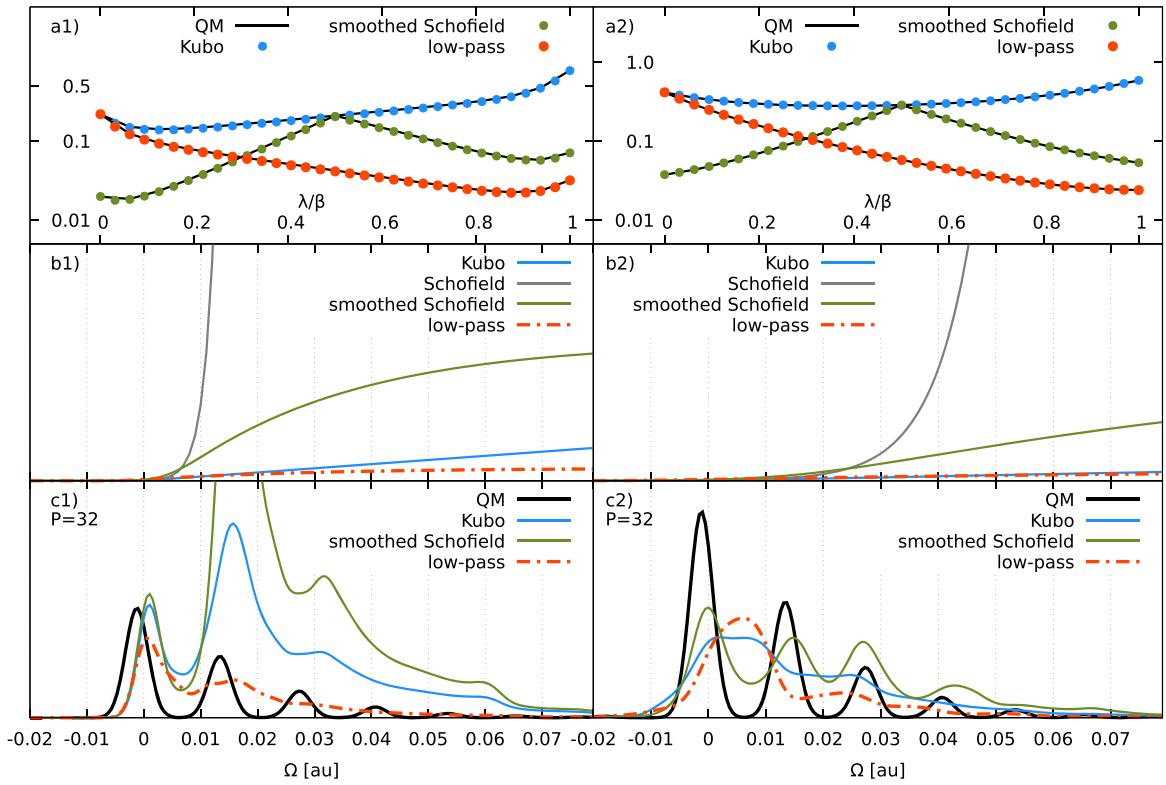

FIG. 6. The two-level system with the parameters $\alpha_f/\alpha_g = 0.86$, $r_f^{\mathrm{eq}} - r_g^{\mathrm{eq}} = 0.22$ a.u.; left: at $T = 300$ K and right: at $T = 1117.6$ K; see the text. The smoothing for the Schofield function $\beta\varepsilon = 4.8$ and for the low-pass filter $\beta\varepsilon = 3.2$. Panels (a) filtered intrinsic weights, $\xi_\lambda \cdot w(\lambda)$, (b) SCFs, and (c) absorption spectra for $P = 32$.

Kubo does, whereas the smoothed Schofield filter reveals the fine spectral structure with a decent quality. In both cases, the smoothed Schofield spectra remain bound, as it is implied by the choice of the external weight. Unfortunately the suggested weights did not improve the results for the system with the larger shift; see supplementary material.

To summarize, the present study suggests that a non-standard form of $w(\lambda)$ *can* be beneficial in comparison to the common choices with respect to quality and numerical stability. However, a universal recipe for choosing the weighting function is hard to formulate for the general case and requires further investigations.

V. CONCLUSIONS AND OUTLOOK

The central question of this work was whether the common TCFs employed for approximations to nuclear dynamics on a single PES are still preferable for vibronic spectroscopy. To reiterate, the Kubo-transformed TCF enjoyed success in describing the ground state dynamics due to fundamental symmetry properties that make it the most classical-like quantum TCF.[51,64] Unfortunately, the direct practical application of the Kubo TCF to *vibronic* transitions leads to either numerical or conceptual deficiencies, namely, it is either intractable numerically or becomes a complex function. Therefore in the present work, we suggested a generalized form of quantum time correlation functions and several approximations based on it that can be used, e.g., for the linear vibronic absorption spectroscopy. The generalization is done via employing a shift in imaginary time and introducing a weighting function, thereby uniting many TCFs that have been reported in the literature before. Furthermore, it is possible to construct new TCFs that might outperform the common ones when it comes to quasi-classical approximations to vibronic spectroscopy. Here we employed imaginary-time PI techniques and the interaction representation to develop a method that allows for dynamics on multiple potential energy surfaces and nuclear quantum effects.

Absorption spectra resulting from various weighting functions and thereby from different TCFs were compared against the exact results, which can be straightforwardly obtained for 1D two-level model system considered here. As it was already shown in the previous studies,[26,27] DCL-based methods typically exhibit (incorrectly) symmetrical spectral shapes with possibly wrong frequencies, when the ground and excited PESs differ significantly. Apart from the negativities which stem from the non-equilibrium dynamics, the results of the ACL method agree well with exact spectra in terms of frequencies and intensity ratios in vibronic progressions. We would like to stress that these negativities are not trivial artifacts that can be manually removed from the spectra. A possible solution based on the Schofield TCF, which leads to an equilibrium dynamics, suffers from an unhealthy growth of the shift correction factor for both low- and high-temperature regimes. The

performance of the popular Kubo TCF is in most cases not superior with respect to the aforementioned ones that treat excited-state dynamics explicitly, exhibiting washed-out fine spectral structures and/or incorrect frequencies and intensities. The results could be improved upon choosing a more complicated weighting function form, however staying unsatisfactory for systems with a large shift between ground and excited state PESs.

To summarize, a successful method should employ dynamics, which accounts for the involved PESs simultaneously. The imaginary-time PI approach in combination with the generalized TCF, as it is presented here, not only incorporates nuclear quantum effects but also yields the possibility to construct more practical numerical protocols than those based on the state-of-the-art Kubo TCF. Nonetheless, the presented formalism neglects non-adiabatic effects; to allow for them, NRPMD[54,55] is hitherto the method of choice.

The existing freedom for the choice of the SCF provides attractive possibilities for finding an optimal one suited for a particular problem as well as, if possible, for a class of problems or even for the general case. A criterion for the optimality may be the match of the spectra in terms of peak positions and spectral shapes to the exact ones simulated for prototypical model systems. Practically, such an investigation can be done in an automated manner, e.g., using machine learning techniques. Importantly, it can be performed *a posteriori* based on the existing dynamical results without recomputing them. Ideally, this should be supported by a physical motivation that can specify the particular form of the weighting function or explain the numerically obtained one. This requires a general understanding of the reasons behind the success or failure of a particular weighting function, which may be obtained at minimum via an extensive analysis for various systems (beyond 1D) in different parameter regimes. This is clearly a project on its own and is thus a subject for future research.

SUPPLEMENTARY MATERIAL

See supplementary material for the relation between $S_\lambda(\Omega)$ and the absorption lineshape $S_0(\Omega)$, the derivation of the expression for the intrinsic weights, Eq. (16), the proof that the negativities in the spectra are due to non-equilibrium dynamics, and the results of applying the filters to the system with the large PES shift.

ACKNOWLEDGMENTS

We acknowledge financial support by the Deutsche Forschungsgemeinschaft [KU 952/10-1 (S.K.), IV 171/2-1 (S.D.I.), and BO 4915/1-1 (S.I.B.)].

[1]S. Mukamel, *Principles of Nonlinear Optical Spectroscopy* (Oxford University Press, Oxford, 1995).
[2]V. May and O. Kühn, *Charge and Energy Transfer Dynamics in Molecular Systems* (Wiley-VCH, Weinheim, 2011).
[3]P. Hamm and M. Zanni, *Concepts and Methods of 2D Infrared Spectroscopy* (Cambridge University Press, Cambridge, 2011).
[4]H. Y. Hwang, S. Fleischer, N. C. Brandt, B. G. Perkins, Jr., M. Liu, K. Fan, A. Sternbach, X. Zhang, R. D. Averitt, and K. A. Nelson, J. Mod. Opt. **62**, 1447 (2015).
[5]M. Cho, Chem. Rev. **108**, 1331 (2008).
[6]C. Milne, T. Penfold, and M. Chergui, Coord. Chem. Rev. **277-278**, 44 (2014).
[7]S. M. Teichmann, F. Silva, S. L. Cousin, M. Hemmer, and J. Biegert, Nat. Commun. **7**, 11493 (2016).
[8]S. Grimme, in *Reviews in Computational Chemistry*, edited by K. B. Lipkowitz, R. Larter, and T. R. Cundari (John Wiley & Sons, Inc., 2004), Chap. 3, Vol. 20.
[9]M. Wächtler, J. Guthmuller, L. González, and B. Dietzek, Coord. Chem. Rev. **256**, 1479 (2012).
[10]M. Schröter, S. Ivanov, J. Schulze, S. Polyutov, Y. Yan, T. Pullerits, and O. Kühn, Phys. Rep. **567**, 1 (2015).
[11]E. J. Heller, J. Chem. Phys. **68**, 3891 (1978).
[12]S. Lee and E. J. Heller, J. Chem. Phys. **71**, 4777 (1979).
[13]K. Giese, M. Petković, H. Naundorf, and O. Kühn, Phys. Rep. **430**, 211 (2006).
[14]R. Schinke, *Photodissociation Dynamics* (Cambridge University Press, 1995).
[15]H.-D. Meyer, F. Gatti, and G. A. Worth, *Multidimensional Quantum Dynamics: MCTDH Theory and Applications* (Wiley-VCH Verlag GmbH & Co. KGaA, 2009).
[16]M. Ben-Nun, J. Quenneville, and T. J. Martínez, J. Phys. Chem. A **104**, 5161 (2000).
[17]G. A. Worth, M. A. Robb, and I. Burghardt, Faraday Discuss. **127**, 307 (2004).
[18]I. Tavernelli, Acc. Chem. Res. **48**, 792 (2015).
[19]D. Marx and J. Hutter, *Ab Initio Molecular Dynamics: Basic Theory and Advanced Methods* (Cambridge University Press, Cambridge, 2009).
[20]M. Ončák, L. Scistik, and P. Slavíček, J. Chem. Phys. **133**, 174303 (2010).
[21]N. K. Jena, I. Josefsson, S. K. Eriksson, A. Hagfeldt, H. Siegbahn, O. Björneholm, H. Rensmo, and M. Odelius, Chem. Eur. J. **21**, 4049 (2015).
[22]L. Weinhardt, E. Ertan, M. Iannuzzi, M. Weigand, O. Fuchs, M. Bär, M. Blum, J. D. Denlinger, W. Yang, E. Umbach, M. Odelius, and C. Heske, Phys. Chem. Chem. Phys. **17**, 27145 (2015).
[23]C. Lawrence and J. Skinner, J. Chem. Phys. **117**, 8847 (2002).
[24]E. Harder, J. D. Eaves, A. Tokmakoff, and B. Berne, Proc. Natl. Acad. Sci. U. S. A. **102**, 11611 (2005).
[25]S. D. Ivanov, A. Witt, and D. Marx, Phys. Chem. Chem. Phys. **15**, 10270 (2013).
[26]S. Karsten, S. D. Ivanov, S. G. Aziz, S. I. Bokarev, and O. Kühn, J. Phys. Chem. Lett. **8**, 992 (2017).
[27]S. Karsten, S. I. Bokarev, S. G. Aziz, S. D. Ivanov, and O. Kühn, J. Chem. Phys. **146**, 224203 (2017).
[28]J. C. Tully and R. K. Preston, J. Chem. Phys. **55**, 562 (1971).
[29]J. C. Tully, Faraday Discuss. **110**, 407 (1998).
[30]B. G. Levine and T. J. Martínez, Annu. Rev. Phys. Chem. **58**, 613 (2007).
[31]H. Meyer and W. H. Miller, J. Chem. Phys. **70**, 3214 (1979).
[32]G. Stock and M. Thoss, Phys. Rev. Lett. **78**, 578 (1997).
[33]S. Bonella and D. F. Coker, Chem. Phys. **268**, 189 (2001).
[34]A. Abedi, N. T. Maitra, and E. K. U. Gross, Phys. Rev. Lett. **105**, 123002 (2010).
[35]F. Agostini, S. K. Min, A. Abedi, and E. K. U. Gross, J. Chem. Theory Comput. **12**, 2127 (2016).
[36]B. F. Curchod and I. Tavernelli, J. Chem. Phys. **138**, 184112 (2013).
[37]G. Stock and M. Thoss, Adv. Chem. Phys. **131**, 243 (2005).
[38]J. C. Tully, J. Chem. Phys. **137**, 22A301 (2012).
[39]S. A. Egorov, E. Rabani, and B. J. Berne, J. Chem. Phys. **108**, 1407 (1998).
[40]E. Rabani, S. A. Egorov, and B. J. Berne, J. Chem. Phys. **109**, 6376 (1998).
[41]S. D. Ivanov, O. Asvany, A. Witt, E. Hugo, G. Mathias, B. Redlich, D. Marx, and S. Schlemmer, Nat. Chem. **2**, 298 (2010).
[42]A. Witt, S. D. Ivanov, and D. Marx, Phys. Rev. Lett. **110**, 083003 (2013).
[43]M. H. M. Olsson, P. E. M. Siegbahn, and A. Warshel, J. Am. Chem. Soc. **126**, 2820 (2004).
[44]J. Gao and D. G. Truhlar, Annu. Rev. Phys. Chem. **53**, 467 (2002).
[45]N. E. Shemetulskis and R. F. Loring, J. Chem. Phys. **97**, 1217 (1992).
[46]Q. Shi and E. Geva, J. Chem. Phys. **122**, 064506 (2005).
[47]Q. Shi and E. Geva, J. Chem. Phys. **129**, 124505 (2008).
[48]R. P. Feynman and A. R. Hibbs, *Quantum Mechanics and Path Integrals* (McGraw-Hill, New York, 1965).
[49]L. Schulman, *Techniques and Applications of Path Integration* (Dover Publications, Inc., Mineola, New York, 2005).
[50]M. E. Tuckerman, *Statistical Mechanics: Theory and Molecular Simulation* (Oxford University Press, Oxford, 2010).

[51]I. R. Craig and D. E. Manolopoulos, J. Chem. Phys. **121**, 3368 (2004).
[52]S. Habershon, D. E. Manolopoulos, T. E. Markland, and T. F. Miller III, Annu. Rev. Phys. Chem. **64**, 387 (2013).
[53]M. Ceriotti, W. Fang, P. G. Kusalik, R. H. McKenzie, A. Michaelides, M. A. Morales, and T. E. Markland, Chem. Rev. **116**, 7529 (2016).
[54]J. O. Richardson and M. Thoss, J. Chem. Phys. **139**, 031102 (2013).
[55]N. Ananth, J. Chem. Phys. **139**, 124102 (2013).
[56]M. Thoss and G. Stock, Phys. Rev. A **59**, 64 (1999).
[57]N. Ananth and T. F. Miller III, J. Chem. Phys. **133**, 234103 (2010).
[58]J. O. Richardson, P. Meyer, M.-O. Pleinert, and M. Thoss, Chem. Phys. **482**, 124 (2016).
[59]C. D. Schwieters and G. A. Voth, J. Chem. Phys. **111**, 2869 (1999).
[60]M. H. Alexander, Chem. Phys. Lett. **347**, 436 (2001).
[61]J. Schmidt and J. C. Tully, J. Chem. Phys. **127**, 094103 (2007).
[62]P. Shushkov, R. Li, and J. C. Tully, J. Chem. Phys. **137**, 22A549 (2012).
[63]J. Lu and Z. Zhou, J. Chem. Phys. **146**, 154110 (2017).
[64]R. Ramirez, T. López-Ciudad, P. P. Kumar, and D. Marx, J. Chem. Phys. **121**, 3973 (2004).
[65]R. Kubo, J. Phys. Soc. Jpn. **12**, 570 (1957).
[66]D. Chandler and P. Wolynes, J. Chem. Phys. **74**, 4078 (1981).
[67]S. Habershon, T. E. Markland, and D. E. Manolopoulos, J. Chem. Phys. **131**, 024501 (2009).
[68]P. Schofield, Phys. Rev. Lett. **4**, 239 (1960).
[69]M. Monteferrante, S. Bonella, and G. Ciccotti, J. Chem. Phys. **138**, 054118 (2013).
[70]J. Beutier, D. Borgis, R. Vuilleumier, and S. Bonella, J. Chem. Phys. **141**, 084102 (2014).
[71]F. Paesani, W. Zhang, D. A. Case, T. E. Cheatham, and G. A. Voth, J. Chem. Phys. **125**, 184507 (2006).
[72]M. Ceriotti, M. Parrinello, T. E. Markland, and D. E. Manolopoulos, J. Chem. Phys. **133**, 124104 (2010).
[73]S. D. Ivanov, A. Witt, M. Shiga, and D. Marx, J. Chem. Phys. **132**, 031101 (2010).

Quasi-classical approaches to vibronic spectra revisited

Sven Karsten, Sergei D. Ivanov,[a] Sergey I. Bokarev, and Oliver Kühn

Institute of Physics, Rostock University, Albert-Einstein-Str. 23-24, 18059 Rostock, Germany

(Dated: 18 December 2017)

[a] Electronic mail: sergei.ivanov@uni-rostock.de

CONTENTS

I. RELATION BETWEEN THE FOURIER TRANSFORMS

To show the relation between $S_\lambda(\Omega)$ for a given λ and the absorption line shape $S_0(\Omega)$ as given by Eq. (4) in the main text, one can evaluate Eq. (3) therein in the basis of the molecular energy eigenstates and apply the Fourier transform

$$\int_{-\infty}^{\infty} \mathrm{d}t\, \mathrm{e}^{-\mathrm{i}\Omega t} C_\lambda(t) = \frac{1}{Z} \int_{-\infty}^{\infty} \mathrm{d}t\, \mathrm{e}^{-\mathrm{i}\Omega t} \sum_{\gamma,\phi} \mathrm{e}^{-(\beta-\lambda)\varepsilon_\gamma} \langle\gamma|\hat{d}|\phi\rangle \mathrm{e}^{-\lambda\varepsilon_\phi} \mathrm{e}^{\mathrm{i}\varepsilon_\phi t/\hbar} \langle\phi|\hat{d}|\gamma\rangle \mathrm{e}^{-\mathrm{i}\varepsilon_\gamma t/\hbar} \ . \tag{S1}$$

Rearranging the factors and performing the time integration yields

$$S_\lambda(\Omega) = \frac{2\pi}{Z} \sum_{\gamma,\phi} \mathrm{e}^{-\lambda(\varepsilon_\phi-\varepsilon_\gamma)} \mathrm{e}^{-\beta\varepsilon_\gamma} \langle\gamma|\hat{d}|\phi\rangle\langle\phi|\hat{d}|\gamma\rangle \delta(\Omega - (\varepsilon_\phi - \varepsilon_\gamma)/\hbar) \ . \tag{S2}$$

Due to the delta-function one can replace the energy gap appearing in the left exponential by the energy quantum carried by the incoming photon, i.e. $\varepsilon_\phi - \varepsilon_\gamma = \hbar\Omega$,

$$S_\lambda(\Omega) = \mathrm{e}^{-\lambda\hbar\Omega} \frac{2\pi}{Z} \sum_{\gamma,\phi} \mathrm{e}^{-\beta\varepsilon_\gamma} \langle\gamma|\hat{d}|\phi\rangle\langle\phi|\hat{d}|\gamma\rangle \delta(\Omega - (\varepsilon_\phi - \varepsilon_\gamma)/\hbar) \ . \tag{S3}$$

Due to this substitution the exponential containing λ became independent on the indices γ, ϕ and could be pulled out of the sum. Recognizing the remaining sum to be the absorption line shape $S_0(\Omega)$ (in accordance to Fermi's golden rule) yields directly Eq. (4) in the main text.

II. DERIVING THE INTRINSIC WEIGHTS

In order to derive a working expression for the intrinsic weights, Eq. (16) in the main text, the full partition function is written as

$$Z = \mathrm{Tr}[\mathrm{e}^{-\beta\hat{H}_g}] + \mathrm{Tr}[\mathrm{e}^{-\beta\hat{H}_f}] = Z_0 + Z_\beta \ , \tag{S4}$$

where the latter equality follows from the definition of Z_λ, Eq. (15) in the main text. It turns out to be beneficial to multiply and divide ξ_λ by $1/Z_0$ yielding

$$\xi_\lambda = \frac{Z_\lambda}{Z} = \frac{Z_\lambda}{Z_0 + Z_\beta} = \frac{Z_\lambda/Z_0}{1 + Z_\beta/Z_0} \ , \tag{S5}$$

thus the remaining task is to evaluate Z_λ/Z_0 for $\lambda = 0, \dots \beta$. The direct evaluation of the fraction would require the sampling of an observable depending exponentially on the phase-space variables leading to an uncontrollable fluctuation and, hence, to a poor convergence behavior. In order to circumvent this issue one can consider first the logarithm of the fraction and subsequently its derivative with respect to the imaginary time λ

$$\frac{\mathrm{d}}{\mathrm{d}\lambda} \ln \frac{Z_\lambda}{Z_0} = \frac{1}{Z_\lambda} \frac{\mathrm{d}Z_\lambda}{\mathrm{d}\lambda} = -\frac{1}{Z_\lambda} \mathrm{Tr} \left[\mathrm{e}^{-(\beta-\lambda)\hat{H}_g} \mathrm{e}^{-\lambda \hat{H}_f} (\hat{V}_f - \hat{V}_g) \right] = -\left\langle \hat{V}_f - \hat{V}_g \right\rangle_\lambda \ . \tag{S6}$$

The remaining quantity to be evaluated is the quantum mechanical average of the potential gap which can be calculated efficiently and numerically exact by means of imaginary time path integral methods. To invert the differentiation one has to integrate the gap over the imaginary time

$$\ln \frac{Z_\lambda}{Z_0} = -\int_0^\lambda \left\langle \hat{V}_f - \hat{V}_g \right\rangle_\mu \mathrm{d}\mu + \ln \frac{Z_{\lambda=0}}{Z_0} \ . \tag{S7}$$

Exponentiating and noting that $\ln(1) = 0$ yields Eq. (16) in the main text.

III. NEGATIVITIES IN THE SPECTRUM DUE TO NON-EQUILIBRIUM DYNAMICS

Consider a general auto-correlation function in terms of a phase-space integral

$$C(t) = \int \mathrm{d}\Gamma \, \rho A(t) A^*(0) \ , \tag{S8}$$

where ρ and A are functions of the considered phase-space variables collectively described by Γ and the asterisk represents the complex conjugation. One can now insert a unity as

$$1 = \lim_{T\to\infty} \frac{1}{2T} \int_{-T}^{T} \mathrm{d}\tau \, \mathrm{e}^{-\hat{\mathcal{L}}\tau} \mathrm{e}^{\hat{\mathcal{L}}\tau} \ , \tag{S9}$$

in between ρ and $A(t)$, where $\hat{\mathcal{L}}$ is the Liouvillian that generates the dynamics in $A(t)$. After acting with the time-evolution operators to the left and to the right, respectively, the expression for the auto-correlation function becomes

$$C(t) = \lim_{T\to\infty} \frac{1}{2T} \int \mathrm{d}\Gamma \int_{-T}^{T} \mathrm{d}\tau\, \rho(\tau) A(t+\tau) A^*(\tau) \ , \tag{S10}$$

where the density ρ is not necessarily stationary and the Liouville theorem is employed, i.e. $\exp[\hat{\mathcal{L}}\tau]\mathrm{d}\Gamma = \mathrm{d}\Gamma$. Switching to the corresponding spectrum $S(\Omega) = \int_{-\infty}^{\infty} \mathrm{d}t\, \exp[-\mathrm{i}\Omega t] C(t)$ and making a variable substitution $t \to t + \tau$ yields

$$S(\Omega) = \lim_{T\to\infty} \frac{1}{2T} \int \mathrm{d}\Gamma \int_{-\infty}^{\infty} \mathrm{d}t\, \mathrm{e}^{-\mathrm{i}\Omega t} A(t) \int_{-T}^{T} \mathrm{d}\tau\, \mathrm{e}^{\mathrm{i}\Omega\tau} \rho(\tau) A^*(\tau) \ . \tag{S11}$$

If T becomes sufficiently large, the τ-integration limits may be extended to infinity and one can recognize the Fourier transforms of the corresponding time-dependent functions

$$S(\Omega) = \lim_{T\to\infty} \frac{1}{2T} \int \mathrm{d}\Gamma\, S_A(\Omega) S^*_{\rho^* A}(\Omega) \ . \tag{S12}$$

Assuming now that ρ is real, positive semi-definite and obeys stationarity, as given in most (quasi-)classical equilibrium dynamics, it can be pulled out of the Fourier transform, yielding

$$S(\Omega) = \lim_{T\to\infty} \frac{1}{2T} \int \mathrm{d}\Gamma\, \rho |S_A(\Omega)|^2 \ , \tag{S13}$$

which represents a spectrum without negativities. Since the stationarity of the density was the only assumption involved, the presence of non-equilibrium (quasi-)classical dynamics is a *necessary* requirement for negativities in an absorption spectrum.

IV. APPLYING THE FILTERS TO THE SYSTEM WITH THE LARGE PES SHIFT

Figure 1 reveals that the filter techniques presented in the main text, i.e. the smoothed Schofield and the low-pass filter do not improve the results for the system with the large PES shift.

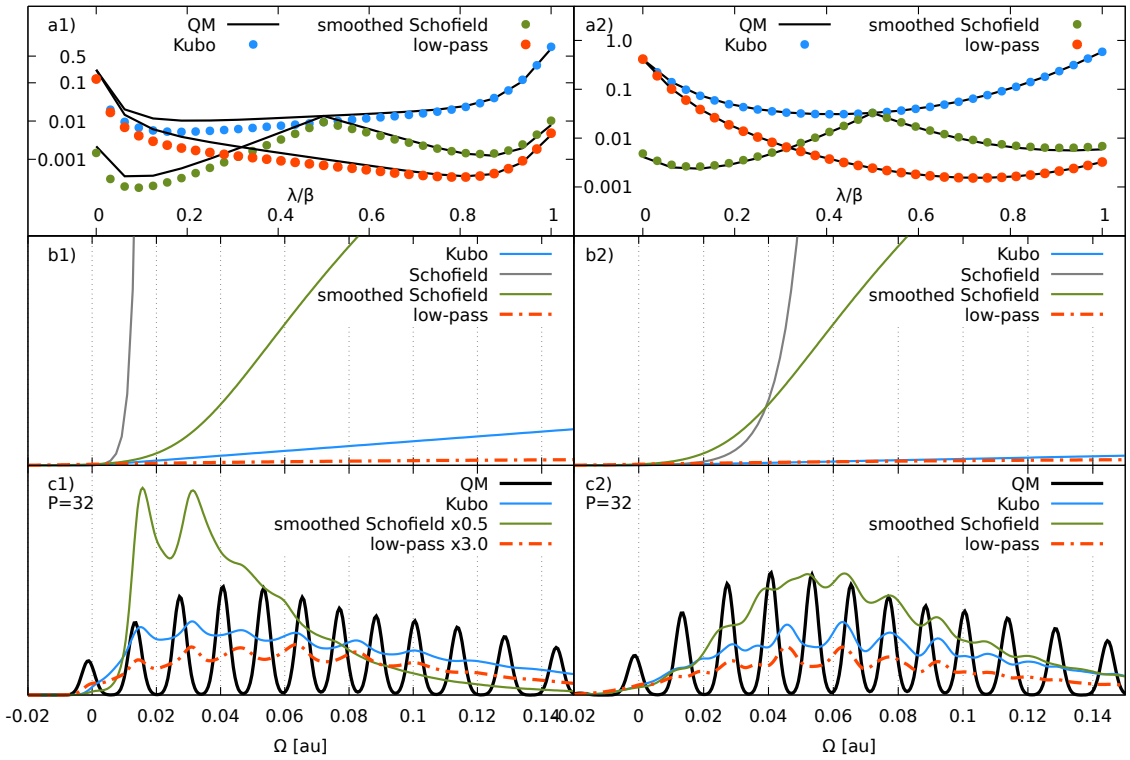

FIG. 1. The two-level system with the parameters $\alpha_f/\alpha_g = 0.86$, $r_f^{\mathrm{eq}} - r_g^{\mathrm{eq}} = 0.5\,\mathrm{au}$ at $T = 300\,\mathrm{K}$ and 1117.6 K in the left and in the right panels, respectively. The PES parameters coincide with those of the right panels in Fig. 4 and Fig. 5 in the main text and the structure is the same as in Fig. 6 therein. Panels a) filtered intrinsic weights, $\xi_\lambda w(\lambda)$, b) SCFs, c) absorption spectra for $P = 32$. The smoothing parameter for the Schofield function is $\beta\varepsilon = 9.2$ and for the low-pass $\beta\varepsilon = 5.2$.

C Additional manuscripts

[SK4] Simulating vibronic spectra via Matsubara dynamics: coping with the sign problem

SVEN KARSTEN, SERGEI D. IVANOV, SERGEY I. BOKAREV, and OLIVER KÜHN

Reprinted from S. KARSTEN, S. D. IVANOV, S. I. BOKAREV, and O. KÜHN, e-print *arXiv:* 1805.06195 [physics.chem-ph] (2018).

Simulating vibronic spectra via Matsubara dynamics: coping with the sign problem

Sven Karsten, Sergei D. Ivanov,[a] Sergey I. Bokarev, and Oliver Kühn

Institute of Physics, Rostock University, Albert-Einstein-Str. 23-24, 18059 Rostock, Germany

(Dated: 17 May 2018)

Measuring the vibronic spectrum probes dynamical processes in molecular systems. When interpreted via suitable theoretical tools, the experimental data provides comprehensive information about the system in question. For complex many-body problems, such an approach usually requires the formulation of proper classical-like approximations, which is particularly challenging if multiple electronic states are involved. In this manuscript, we express the imaginary-time shifted time correlation function (TCF) and, thus, the vibronic spectrum in terms of the so-called Matsubara dynamics, which combines quantum statistics and classical-like dynamics. In contrast to the existing literature, we invoke a local harmonic approximation to the potential allowing an analytical evaluation of integrals. By subsequently applying the Matsubara approximation, we derive a generalization of the existing Matsubara method to multiple potential energy surfaces (PESs), which, however, suffers from the sign problem as its single-PES counterpart does. The mathematical analysis for two shifted harmonic oscillators suggests a new modified method to simulate the standard correlation function via classical-like dynamics. Importantly, this modified method samples the thermal Wigner function without suffering from the sign problem and it yields an accurate approximation to the vibronic absorption spectrum, not only for the harmonic system, but also for an anharmonic one.

[a]Electronic mail: sergei.ivanov@uni-rostock.de

I. INTRODUCTION

Spectroscopic methods constitute the cornerstone of experimental molecular physics and physical chemistry.[1–3] Constant sharpening of the energy and time resolution provides increasingly detailed insight into photophysical and photochemical processes. Complementing measurements by proper theoretical tools enables understanding of the underlying microscopic phenomena. Simple models,[1,2] on the one hand, often fail to capture essential features, whereas solving the time-dependent Schödinger equation numerically exactly,[4] on the other hand, is not feasible for large systems due to the infamous curse of dimensionality. Therefore, compromises between the both extremes are to be found. A remarkable pathway is to approximate the exact quantum dynamics via (quasi-)classical methods motivated by the provided intuitive access into the atomistic picture. For instance, imaginary-time path integral (PI) techniques have proven themselves to rigorously account for static quantum effects profiting from the classical-like equations of motion (EOMs).[5–8] These approaches are successfully employed for electronic ground-state properties and purely vibrational spectra.[9–12] Here, the quantum time evolution has a direct classical analogue since only a single electronic PES is of relevance. In contrast, vibronic spectra are intrinsically more quantum due to electronic degrees of freedom (DOFs) undergoing transitions between discrete levels. Thus in a simulation, at least two PESs need to be explicitly accounted for; such a situation has no classical analogue.

A number of trajectory-based methods treating dynamics on several PESs has been suggested (see, e.g., Refs. 13–15 for review), mostly addressing the rates of non-adiabatic transitions, while leaving the problem of vibronic spectra aside. Further, nonadiabatic ring polymer molecular dynamics (NRPMD) techniques have been developed,[16,17] which are based on the mapping approach introduced by Stock and Thoss.[13,18,19] Although these methods are suitable for vibronic spectra, given an efficient simulation protocol is provided,[20] such an application has not been commonly discussed. Similarly, PI approaches for many PESs without mapping variables[21–25] have addressed mostly non-adiabatic effects on static properties or reaction rates but not vibronic spectra.

In a recent publication, Ref. 26, we have suggested a generalized formalism to address the vibronic spectra of complex systems. Within this approach, many commonly known correlation functions such as the Kubo[27] or Schofield[28] TCFs as well as the more pragmatic

dynamical classical limit (DCL) one[29–32] are naturally recovered. Additionally, this formulation enables constructing completely new TCFs and it has been demonstrated for model systems that some newly suggested TCFs can yield numerical protocols that outperform the well-established ones. This has led to the conclusion that there is no unambiguously favorable TCF when it comes to a practical consideration of the vibronic spectrum, which is in contrast to infra-red (IR) spectroscopy, where the Kubo TCF is to be preferred.[33,34] In Ref. 26, an adiabatic quasi-classical approximation to the imaginary-time shifted TCF, which is the main ingredient of the generalized formalism, has been carried out. In the spirit of the standard ring polymer molecular dynamics (RPMD) method,[34] a numerically exact expression for the TCF at time zero has been derived. The subsequent dynamics has been constructed to conserve the quantum Boltzmann density, but it suffers from infamous artificial harmonic spring oscillations, intrinsic to quasi-classical PI techniques.[35]

During the last years, several attempts have been performed to develop improved approximations to vibrational quantum dynamics based on the so-called Matsubara dynamics.[36–38] This methodology starts from the observation that only smooth imaginary-time paths contribute to canonical thermal averages, whereas jagged or discontinuous paths are sufficiently suppressed by the Boltzmann operator. Assuming that the path remains smooth even if it undergoes dynamics, i.e. the Matsubara approximation, one can rigorously derive classical-like EOMs leaving the initial density unchanged. Although the Matsubara dynamics ansatz yields a reasonable approximation to the Kubo TCF for small systems, it is not yet applicable to high-dimensional problems due to the infamous sign problem. Still, it has been shown that popular methods such as RPMD, thermostatted RPMD (TRPMD)[39] as well as centroid molecular dynamics (CMD)[40] can be viewed as feasible approximations to the Matsubara dynamics. Thus, it is natural to expect that other even more powerful approximations to nuclear quantum dynamics can be derived on its basis, making this approach particularly promising.

However, so far the Matsubara dynamics method has not been employed for vibronic spectra. In this manuscript, we present how this spectroscopic observable can be approximately evaluated making use of the Matsubara dynamics. First, the exact imaginary-time shifted TCF is rigorously reformulated in terms of a phase-space integration, see Sec. II A. Second, alternatively to existing literature, a local harmonic approximation to the potential is involved in Sec. II B. Together with the Matsubara approximation itself, this leads to

a generalization of the established Matsubara method to multiple PESs. Third, classical-like EOMs are derived in Sec. II C, leaving a flexibility for a choice of Hamilton function generating the dynamics. Two reasonable variants are motivated in Sec. II E, followed by a discussion of common approaches to circumvent the sign problem in Sec. II F. Finally, favorable simulation scenarios are suggested, based on the mathematical analysis for an analytically solvable system consisting of two shifted harmonic oscillators in Sec. IV. Moreover, a modified method to simulate the standard correlation function without suffering from the sign problem is outlined. Importantly, this method samples directly the thermal Wigner function of the harmonic oscillator. All considered approaches are subsequently applied to a one-dimensional model system at ambient temperature, see Sec. IV A 2. In Sec. IV B 1, the modified method is generalized to anharmonic systems and is demonstrated to sample accurately the thermal Wigner function for a quartic expansion of the Morse potential. Interestingly, although designed for the harmonic case, the modified method yields vibronic spectra very similar to those obtained with the Matsubara dynamics method for the general case, see Sec. IV B 2. In Sec. V, the manuscript is concluded and some perspectives for future research are given.

II. THEORY

Traditionally, the heart of (N)RPMD methodologies is the Kubo-transformed TCF, however, we have shown recently that when vibronic spectra are addressed, the choice of the correlation function is not as unambiguous as it is for vibrational dynamics.[26] The cornerstone of the generalized TCF suggested therein is the formally exact imaginary-time shifted TCF, $C_\lambda(t)$ (see Eq. (1)). Here, we generalize the well-established Matsubara dynamics[36] to vibronic spectroscopy and derive it from $C_\lambda(t)$ by means of a local harmonic approximation to the potential.

A. Setting the stage

The starting point is the imaginary-time shifted correlation function for a particular $\lambda \in [0, \beta]$[26]

$$C_\lambda(t) = \frac{1}{Z}\mathrm{Tr}\left[\mathrm{e}^{-(\beta-\lambda)\hat{H}_g}\hat{D}_f^g \mathrm{e}^{-\lambda\hat{H}_f}\mathrm{e}^{\mathrm{i}\hat{H}_f t/\hbar}\hat{D}_g^f \mathrm{e}^{-\mathrm{i}\hat{H}_g t/\hbar}\right] \ , \tag{1}$$

where the Born-Oppenheimer approximation (BOA) is assumed, Tr[•] stands for a trace in the nuclear Hilbert space, $\hat{H}_a$ corresponds to the nuclear Hamiltonian with the PES $\hat{V}_a$ of the a-th adiabatic state, where $a = g, f$ and $\hat{D}_f^g \equiv (\hat{D}_g^f)^*$ is the transition dipole moment. Note that for $\lambda = 0$, the standard correlation function $C_0(t)$ is recovered, whose Fourier transform directly yields the absorption spectrum. For the sake of brevity, we restrict ourselves to a 1D system, described by position and momentum operators $\hat{x}$ and $\hat{p}$ in nuclear space and two discrete electronic states g and f; the generalization to a many-dimensional multi-level system is straightforward. To start, the shift in imaginary time is equidistantly discretized, i.e. $\lambda = l\beta/P$, where $P > 0$ is a natural number and λ and l are used synonymously throughout the manuscript. The nuclear trace in Eq. (1) is performed in the eigenstate basis of $\hat{x}$ over coordinates x_0^- and an additional spatial closure, i.e. an integral over x_0^+, is inserted. Subsequently, a canonical variable substitution to midpoint and difference variables is performed, i.e. $x_0 := (x_0^+ + x_0^-)/2$ and $\Delta_0 := x_0^+ - x_0^-$, respectively, see Fig. 1 for a sketch. The resulting expression reads

$$C_\lambda(t) = \frac{1}{Z} \int \mathrm{d}x_0 \int \mathrm{d}\Delta_0 \langle x_0^- | \mathrm{e}^{-(P-l)\beta\hat{H}_g/P} \hat{D}_f^g \mathrm{e}^{-l\beta\hat{H}_f/P} | x_0^+ \rangle \langle x_0^+ | \mathrm{e}^{\mathrm{i}\hat{H}_f t/\hbar} \hat{D}_g^f \mathrm{e}^{-\mathrm{i}\hat{H}_g t/\hbar} | x_0^- \rangle \ . \quad (2)$$

Following the standard imaginary-time PI approach,[8,41] each exponential term $\exp(-j\beta\hat{H}_a/P)$, with $j = P-l, l$ can be expressed as a product of j identical factors $\exp(-\beta\hat{H}_a/P)$. Further, unity operators in the form

$$\hat{1} = \int \mathrm{d}x_i \int \mathrm{d}\Delta_i |x_i^+\rangle\langle x_i^+| \mathrm{e}^{\mathrm{i}\hat{\mathcal{H}}_i t/\hbar} \mathrm{e}^{-\mathrm{i}\hat{\mathcal{H}}_i t/\hbar} |x_i^-\rangle\langle x_i^-| \quad (3)$$

are inserted in between those factors, where the coordinates $x_i^\pm$ correspond to the sum and difference variables x_i and Δ_i, respectively, as it is visualized in Fig. 1. The $\hat{\mathcal{H}}_i$ are, in principle, arbitrary Hermitian operators, $i = 1, \ldots, P-1$. However, for the present purpose they are limited to a non-relativistic Hamiltonian form $\hat{\mathcal{H}}_i = \hat{p}^2/2m + \hat{\mathcal{V}}_i(\hat{x})$, where m is the nuclear mass and particular choices for the potentials $\hat{\mathcal{V}}_i$ are suggested in Sec. II E. To obtain the structure of the Wigner transform,[42,43] which will be of use later, scalar unities are inserted

$$1 = \int \mathrm{d}\Delta_i' \, \delta(\Delta_i' - \Delta_i) = \frac{1}{2\pi\hbar} \int \mathrm{d}\Delta_i' \int \mathrm{d}p_i \, \mathrm{e}^{\mathrm{i}p_i(\Delta_i' - \Delta_i)/\hbar} \quad (4)$$

for each i. Finally, time-(in)dependent parts can be singled out, leading to the compact

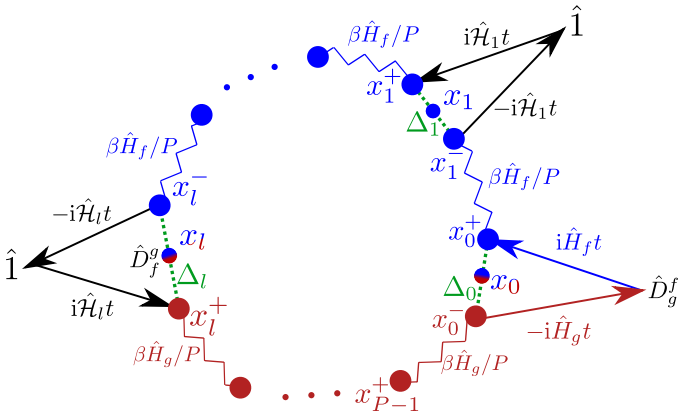

FIG. 1. Visualization of the structure of the correlation function in Eqs. (5-7). The jagged lines and straight arrows represent imaginary- and real-time propagations with length β/P and t, respectively. The red and the blue color indicates initial and final electronic state, correspondingly.

form of a classical-like phase-space integral

$$C_\lambda(t) = \int \mathrm{d}\mathbf{x} \int \mathrm{d}\mathbf{p}\, A_l(\mathbf{x},\mathbf{p}) B_l(\mathbf{x},\mathbf{p},t) \ . \tag{5}$$

Here, the time-independent part reads

$$A_l(\mathbf{x},\mathbf{p}) := \frac{1}{Z(2\pi\hbar)^P} \int \mathrm{d}\boldsymbol{\Delta}\, \mathrm{e}^{\mathrm{i}\mathbf{p}^{\mathrm{T}}\boldsymbol{\Delta}/\hbar} \frac{1}{2}[D_f^g(x_l^+) + D_f^g(x_l^-)] \prod_{i=l}^{P-1} \langle x_{i+1}^- | \mathrm{e}^{-\beta\hat{H}_g/P} | x_i^+ \rangle \prod_{i=0}^{l-1} \langle x_{i+1}^- | \mathrm{e}^{-\beta\hat{H}_f/P} | x_i^+ \rangle \ , \tag{6}$$

where $\mathbf{x} := (x_0, \ldots, x_{P-1})^{\mathrm{T}}$ (likewise for $\boldsymbol{\Delta}$ and $\mathbf{p}$) and all the vectors obey the cyclic condition $P \mapsto 0$. Note that the dipole is evaluated at both $x_l^\pm$ since the unity with the index l, Eq. (3), can be inserted on the both sides of the dipole operator. Having Fig. 1 at hand, it becomes clear that the midpoint coordinates x_i form a continuous path in the limit $P \to \infty$. Analogously to common imaginary-time PI approaches, these midpoints will be referred to as beads in the following.

The time-dependent part takes the form

$$B_l(\mathbf{x},\mathbf{p},t) := \int \mathrm{d}\boldsymbol{\Delta}\, \mathrm{e}^{-\mathrm{i}\mathbf{p}^{\mathrm{T}}\boldsymbol{\Delta}/\hbar} \prod_{i=0}^{P-1} \langle x_i^+ | \mathrm{e}^{\mathrm{i}\hat{\mathcal{H}}_i t/\hbar} \hat{\mathcal{O}}_i \mathrm{e}^{-\mathrm{i}\hat{\mathcal{H}}_i' t/\hbar} | x_i^- \rangle \ , \tag{7}$$

where $\hat{\mathcal{O}}_i = \hat{1}, \forall i > 0$ and $\hat{\mathcal{O}}_0 := \hat{D}_g^f$. Importantly, for $i = 0$ the Hamiltonians are fixed $\hat{\mathcal{H}}_0' := \hat{H}_g$ and $\hat{\mathcal{H}}_0 := \hat{H}_f$, whereas the $\hat{\mathcal{H}}_i' \equiv \hat{\mathcal{H}}_i, \forall i > 0$ remain arbitrary. Note further that

at time zero the expression collapses to $B_l(\mathbf{x},\mathbf{p},0) \equiv D_g^f(x_0)$ as it can be easily proven. The Eqs. (5-7) remain exact and possible approximations to them are discussed in Sec. II B and II C.

B. The time-independent part

First, each density matrix element in the time-independent part is evaluated via the symmetric Trotter factorization in the usual imaginary-time PI fashion, yielding

$$\langle x_{i+1}^-|\mathrm{e}^{-\beta\hat{H}_a/P}|x_i^+\rangle = \lim_{P\to\infty}\left(\frac{\beta m\Omega_P^2}{2\pi}\right)^{1/2}\exp\left\{-\frac{\beta}{2P}\left[V_a(x_{i+1}^-)+V_a(x_i^+)\right]-\beta\frac{m\Omega_P^2}{2}\left[x_{i+1}^- - x_i^+\right]^2\right\}\ , \tag{8}$$

where $\Omega_P := \sqrt{P}/\beta\hbar$ is the standard ring-polymer chain frequency. Now the *first* approximation is employed, namely that the potential is assumed to be *locally* harmonic

$$V_a(x_i^\pm) \approx V_a(x_i) \pm \frac{\partial V_a}{\partial x_i}\frac{\Delta_i}{2} + \frac{1}{2}\frac{\partial^2 V_a}{\partial x_i^2}\left(\frac{\Delta_i}{2}\right)^2 \tag{9}$$

and the transition dipole to be locally linear

$$\frac{1}{2}[D_f^q(x_l^+)+D_f^q(x_l^-)] \approx D_f^q(x_l)\ . \tag{10}$$

These assumptions enable the analytical integration over the difference variables, see Supplement for a detailed derivation. It is useful to employ the normal mode coordinates of the free-particle ring polymer,[8,35] $\mathbf{Q} := \mathbb{T}\mathbf{x}/\sqrt{P}$ and $\mathbf{\Pi} := \mathbb{T}\mathbf{p}/\sqrt{P}$, where the orthogonal transformation matrix $\mathbb{T}$ represents the discrete Fourier transform with respect to the imaginary time[36] and the matrix elements are given explicitly in Sec. I of the Supplement. For notational convenience later on, the normal modes have the index r that runs over $r = -(P-1)/2,\ldots,0,\ldots,(P-1)/2$; in contrast, the bead indices take the values $i = 0,\ldots,P-1$, see Fig. 2. Since the formulas are slightly different depending on the parity of P, it is chosen to be an odd number to get more symmetric expressions. Importantly, taking the limit $P\to\infty$, which makes the Trotter factorization exact, is problematic due to the appearance of diverging terms. These divergences can be, however, healed by an additional approximation that is described in the following.

The *second* approximation is to restrict the normal modes to the so-called Matsubara modes, i.e. to discard all higher normal modes with $|r| > \bar{M}$, where $\bar{M} := (M-1)/2$ with

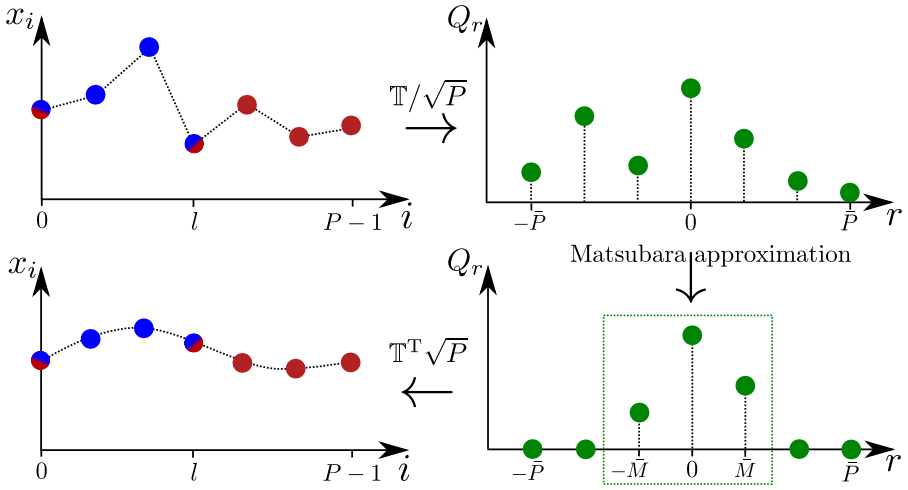

FIG. 2. A sketch illustrating how the Matsubara approximation affects an imaginary-time path. An arbitrary jagged imaginary-time path (upper left) is transformed to the normal modes' coordinates via the matrix $\mathbb{T}$ (upper right). After restricting to the M lowest modes (bottom right), i.e. the Matsubara approximation, one obtains a smooth path via the back transform (bottom left). Note that the normal mode index r runs over $-\bar{P},\ldots,\bar{P}$, where, similarly to $\bar{M}$, $\bar{P} := (P-1)/2$.

$M \ll P$, see Fig. 2 for a sketch. Subsequently, the dependency of all physical quantities, in particular, the potential, the transition dipole moment as well as the time-dependent part on these higher "non-Matsubara" modes is neglected. Practically, it implies that only smooth imaginary-time paths significantly contribute to the TCF for all times t. Under this assumption, the integrals corresponding to the non-Matsubara modes in Eq. (5) possess a Gaussian form and can be thus performed analytically, see Sec. II in the Supplement. The resulting approximate time-independent part can be written down compactly as

$$\tilde{A}_l(\mathbf{Q},\mathbf{\Pi}) \approx \frac{\bar{M}!^2}{2\pi\hbar^M Z} D_f^g(x_l(\mathbf{Q}))\mathrm{e}^{-\beta\left[\tilde{H}_l(\mathbf{Q},\mathbf{\Pi})+\mathrm{i}\mathbf{\Pi}^{\mathrm{T}}\mathbb{W}\mathbf{Q}\right]} \ , \tag{11}$$

where the anti-symmetric anti-diagonal matrix $(\mathbb{W})_{r,s} := \omega_r \delta_{r,-s}$ contains the well-known Matsubara frequencies $\omega_r := 2\pi r/\beta\hbar$. For the sake of brevity, $\mathbf{Q}$ and $\mathbf{\Pi}$ represent the Matsubara modes only and $\tilde{A}_l(\mathbf{Q},\mathbf{\Pi}) := P^P A_l(\mathbf{x}(\mathbf{Q}),\mathbf{p}(\mathbf{\Pi}))$ with P^P stemming from the substitution of the Cartesian volume element by the normal mode one. Note that we will define $\tilde{X}(\mathbf{Q},\mathbf{\Pi}) := X(\mathbf{x}(\mathbf{Q}),\mathbf{p}(\mathbf{\Pi}))$ *without* the P^P factor for any other arbitrary phase-space

function X in the following. The classical Hamilton function in Eq. (11)

$$\tilde{H}_l(\mathbf{Q},\mathbf{\Pi}) := \frac{1}{2m}\mathbf{\Pi}^{\mathrm{T}}\mathbf{\Pi} + \tilde{U}_l(\mathbf{Q}) \tag{12}$$

is determined by the effective ring polymer potential for multiple PESs[26]

$$U_l(\mathbf{x}) := \frac{1}{P}\sum_{i=0}^{l}\kappa_i V_f(x_i) + \frac{1}{P}\sum_{i=l}^{P}\kappa_i V_g(x_i) \ , \tag{13}$$

where κ_i is equal to $1/2$ if i corresponds to the first or the last summand, to 0 if there is only one summand, which is the case if $l = 0, P$, and to 1 in all other cases. Note that the harmonic spring term that is usually present in imaginary-time PI methods has vanished upon applying the Matsubara approximation, see Sec. II in the Supplement. Note further that in the case $\lambda \in \{0, \beta\}$, with $\{\bullet\}$ representing a set, the effective potential is exclusively assembled from the initial and final state potentials, respectively. Having Eq. (13) at hand, it becomes clear that the effective potential remains discontinuous at the points x_0 and x_l in the limit $P \to \infty$ for $\lambda \in]0, \beta[$, where $]\bullet, \bullet[$ refers to an open interval. The question arises whether this is in the spirit of the Matsubara approximation which permits only smooth and continuous imaginary-time paths, see Sec. IV for a discussion.

Importantly, after integrating out the non-Matsubara modes, the time-independent part does not feature any divergence as $P \to \infty$. This is a direct consequence of the Matsubara approximation and will be particularly relevant for the consideration of the time-dependent part in Sec. II C. Interestingly, setting $V_g(x) = V_f(x)$, i.e. considering a single-PES problem, and integrating Eq. (1) over λ from 0 to β yielding the Kubo transform, leads to the expression derived in Ref. 36, even though the local harmonic approximation to the PES and the linear approximation to the dipole, Eqs. (9,10), were not utilized therein.

C. The time-dependent part

In order to evaluate the time-dependent part, we first consider its time derivative. Since the factors in Eq. (7) are uncoupled, it is sufficient to consider them individually. The time derivative of the i-th factor reads

$$\dot{B}_l^i(x_i, p_i, t) = \frac{\mathrm{i}}{\hbar}\int \mathrm{d}\Delta_i \ \mathrm{e}^{-\mathrm{i}p_i\Delta_i/\hbar}\langle x_i^+|[\hat{\mathcal{H}}_i\hat{\mathcal{O}}_i(t) - \hat{\mathcal{O}}_i(t)\hat{\mathcal{H}}_i']|x_i^-\rangle \ , \tag{14}$$

where $\hat{\mathcal{O}}_i(t) := \exp[\mathrm{i}\hat{\mathcal{H}}_i t/\hbar]\hat{\mathcal{O}}_i \exp[-\mathrm{i}\hat{\mathcal{H}}'_i t/\hbar]$ with $\hat{\mathcal{O}}_i$ defined in Sec. II A. Recognizing the Wigner transform in Eq. (14), the time derivative can be *exactly* rewritten in terms of a quantum Liouvillian, see e.g. Ref. 44, as $\dot{B}^i_l(x_i,p_i,t) = \hat{\mathcal{L}}^i_l(x_i,p_i)B^i_l(x_i,p_i,t)$, where

$$\hat{\mathcal{L}}^i_l(x_i,p_i) := \frac{p_i}{m}\frac{\partial}{\partial x_i} - \frac{1}{\hbar}[\mathcal{V}_i(x_i)+\mathcal{V}'_i(x_i)]\sin\left(\frac{\hbar}{2}\frac{\overleftarrow{\partial}}{\partial x_i}\frac{\overrightarrow{\partial}}{\partial p_i}\right) + \frac{\mathrm{i}}{\hbar}[\mathcal{V}_i(x_i)-\mathcal{V}'_i(x_i)]\cos\left(\frac{\hbar}{2}\frac{\overleftarrow{\partial}}{\partial x_i}\frac{\overrightarrow{\partial}}{\partial p_i}\right) \tag{15}$$

and the arrows on top of the partial derivatives imply the direction of their action. Importantly, all terms $\mathcal{V}_i(x_i) - \mathcal{V}'_i(x_i)$ vanish apart from the case $i = 0$, where $\mathcal{V}_0(x_0) - \mathcal{V}'_0(x_0) = V_f(x_0) - V_g(x_0)$, see definitions of $\hat{\mathcal{H}}_i$ below Eq. (7). After summing up the individual parts and noting that mixed derivatives with respect to different indices i vanish, one gets the derivative of the complete time-dependent part as $\dot{B}_l(\mathbf{x},\mathbf{p},t) = \hat{\mathcal{L}}_l(\mathbf{x},\mathbf{p})B_l(\mathbf{x},\mathbf{p},t)$, with the full and still exact quantum Liouvillian

$$\hat{\mathcal{L}}_l(\mathbf{x},\mathbf{p}) := \frac{1}{m}\mathbf{p}^{\mathrm{T}}\boldsymbol{\nabla}_{\mathbf{x}} - \frac{2P}{\hbar}\mathcal{U}_l(\mathbf{x})\sin\left(\frac{\hbar}{2}\overleftarrow{\boldsymbol{\nabla}}^{\mathrm{T}}_{\mathbf{x}}\overrightarrow{\boldsymbol{\nabla}}_{\mathbf{p}}\right) + \frac{\mathrm{i}}{\hbar}[V_f(x_0)-V_g(x_0)]\cos\left(\frac{\hbar}{2}\overleftarrow{\boldsymbol{\nabla}}^{\mathrm{T}}_{\mathbf{x}}\overrightarrow{\boldsymbol{\nabla}}_{\mathbf{p}}\right) \ , \tag{16}$$

where

$$\mathcal{U}_l(\mathbf{x}) := \frac{1}{2P}[V_f(x_0)+V_g(x_0)] + \frac{1}{P}\sum_{i=1}^{P-1}\mathcal{V}_i(x_i) \ . \tag{17}$$

Following the same line of reasoning as in the previous section, the normal mode transform is employed leading to $\overleftarrow{\boldsymbol{\nabla}}^{\mathrm{T}}_{\mathbf{x}}\overrightarrow{\boldsymbol{\nabla}}_{\mathbf{p}} = \overleftarrow{\boldsymbol{\nabla}}^{\mathrm{T}}_{\mathbf{Q}}\overrightarrow{\boldsymbol{\nabla}}_{\boldsymbol{\Pi}}/P$, where it is important to note the downscaling by P. Restricting the normal modes to the Matsubara modes and bearing in mind that the limit $P \to \infty$ of the time-*independent* part exists, we can consider this limit for the time-dependent part as well. Keeping only the leading terms in the Taylor series of sine and cosine in Eq. (16) yields

$$\lim_{P\to\infty}\hat{\tilde{\mathcal{L}}}_l(\mathbf{Q},\boldsymbol{\Pi}) = \frac{1}{m}\boldsymbol{\Pi}^{\mathrm{T}}\boldsymbol{\nabla}_{\mathbf{Q}} - [\boldsymbol{\nabla}^{\mathrm{T}}_{\mathbf{Q}}\tilde{\mathcal{U}}_l(\mathbf{Q})]\boldsymbol{\nabla}_{\boldsymbol{\Pi}} + \frac{\mathrm{i}}{\hbar}[V_f(x_0(\mathbf{Q}))-V_g(x_0(\mathbf{Q}))] \ , \tag{18}$$

which is a *classical*-like Liouvillian containing a scalar imaginary inhomogeneity that depends on the energy gap between the initial and final electronic states. Importantly, neither an additional approximation nor any $\hbar \to 0$ limit has been applied; note that the latter would be a non-trivial task since the time-independent part still depends on $\hbar$. Having the

particular form of the Liouvillian at hand, one can write down the time-dependent part explicitly as

$$\tilde{B}_l(\mathbf{Q},\mathbf{\Pi},t) = \mathrm{e}^{\hat{\tilde{\mathcal{L}}}_l(\mathbf{Q},\mathbf{\Pi})t}\tilde{B}_l(\mathbf{Q},\mathbf{\Pi},0) = D_g^f(x_0(t))\exp\left\{\frac{\mathrm{i}}{\hbar}\int_0^t [V_f(x_0(\tau)) - V_g(x_0(\tau))]\mathrm{d}\tau\right\} \ , \tag{19}$$

where $x_0(t) := \mathrm{e}^{\mathrm{Re}\hat{\tilde{\mathcal{L}}}_l(\mathbf{Q},\mathbf{\Pi})t}x_0(\mathbf{Q})$ with $\mathrm{Re}\hat{\tilde{\mathcal{L}}}_l$ meaning the real part of $\hat{\tilde{\mathcal{L}}}_l$. Alternatively to the formulation with Liouville operators, one could now define a classical Hamilton function that generates the trajectory $x_0(t)$ with $x_0(0) = x_0(\mathbf{Q})$ via Hamilton's EOMs for $\mathbf{Q}$ and $\mathbf{\Pi}$ as it is spelled out explicitly in the following section.

D. The Matsubara approximation to the imaginary-time shifted TCF

Putting together the results presented in the last two sections leads to the Matsubara approximation to the imaginary-time shifted correlation function

$$\begin{aligned} C_\lambda(t) \approx & \frac{\bar{M}!^2}{2\pi\hbar^M Z}\int \mathrm{d}\mathbf{Q}\int \mathrm{d}\mathbf{\Pi} \\ & \times \mathrm{e}^{-\beta\left[\tilde{H}_l(\mathbf{Q},\mathbf{\Pi})+\mathrm{i}\mathbf{\Pi}^{\mathrm{T}}\mathbb{W}\mathbf{Q}\right]} D_f^g(x_l(0))D_g^f(x_0(t))\exp\left\{\frac{\mathrm{i}}{\hbar}\int_0^t [V_f(x_0(\tau)) - V_g(x_0(\tau))]\mathrm{d}\tau\right\} \ , \end{aligned} \tag{20}$$

where the dynamics follows from the EOMs

$$\dot{\mathbf{Q}} = \frac{\mathbf{\Pi}}{m}, \quad \dot{\mathbf{\Pi}} = -\boldsymbol{\nabla}_{\mathbf{Q}}\tilde{\mathcal{U}}_l(\mathbf{Q}) \ . \tag{21}$$

The last two equations constitute one of the main theoretical results of this manuscript and the starting point for simulating the vibronic spectra of complex systems (after a straightforward generalization to a many-dimensional many-body case). However, a few concerns are yet unresolved. First, it is not clear which particular form of the potential $\tilde{\mathcal{U}}_l(\mathbf{Q})$ is reasonable. As it is discussed in the next section, this freedom might be beneficial. Second and a more severe one, is the presence of the imaginary part $\mathbf{\Pi}^{\mathrm{T}}\mathbb{W}\mathbf{Q}$ in the exponent in Eq. (20), which is responsible for the infamous sign problem, leading to an unsufficient statistical convergence, see Sec. II F.

E. Choosing the dynamics

As it has been stated in Sec. II A, the Hermitian operators $\hat{\mathcal{H}}_i$ that determine the dynamics are, in principle, completely arbitrary. However, one can think of two choices aiming at a reasonable simulation protocol.

First, in an attempt to avoid problems such as zero-point energy leakage,[45] it would be desirable to keep the density stationary. Thus, one can define the Hamiltonians

$$\hat{\mathcal{H}}_i := \begin{cases} \hat{H}_f \ , & 1 \leq i < l \\ \hat{H}_{\mathrm{av}} := (\hat{H}_g + \hat{H}_f)/2 \ , & 0 < l < P \, , \ l = i \\ \hat{H}_g \ , & l < i \leq P - 1 \ , \end{cases} \tag{22}$$

such that, at first glance, the equality $U_l(\mathbf{Q}) = \mathcal{U}_l(\mathbf{Q})$ (see Eqs. (13,17) for their definitions) would lead to favorable equilibrium dynamics, since the density and the EOMs are determined by the same potential. Unfortunately, for $\lambda \in \{0, \beta\}$, the equality $U_l(\mathbf{Q}) = \mathcal{U}_l(\mathbf{Q})$ *cannot* be achieved, since U_0 and U_β are exclusively assembled from the initial and the excited state potential, respectively, whereas $\mathcal{U}_0$ and $\mathcal{U}_\beta$ will *always* feature the averaged potential for x_0, see Eq. (17). Further, for $\lambda \in]0, \beta[$, the Matsubara phase ($\mathbf{\Pi}^{\mathrm{T}}\mathbb{W}\mathbf{Q}$ in Eq. (20)) varies in time and so does the density, as it is shown in the Supplement, Sec. III. In contrast, this time dependence vanishes in the continuous limit for the single PES problem and, hence, the Matsubara density becomes strictly stationary as $P \to \infty$. Eventually, it seems impossible to find any set of $\hat{\mathcal{H}}_i$ for any λ that would lead to truly stationary dynamics for a vibronic spectroscopy study. Another possible objection against this choice of the potential is the presence of the discontinuity at x_0 and x_l that contradicts the path smoothness assumed within the Matsubara approximation, see the comments to Eq. (13). Despite these facts, this particular choice of $\hat{\mathcal{H}}_i$ will be employed and referred to as the *equilibrium method* in the following.

Second, by setting all $\hat{\mathcal{H}}_i := \hat{H}_{\mathrm{av}}$ the discontinuity is avoided at the price of obviously non-stationary dynamics. This choice, dubbed as the *average method*, is more compatible with smooth paths assembled from the Matsubara modes. Importantly, both the equilibrium and the average setups recover the usual Matsubara dynamics for the single-PES problem, i.e. $V_g(x) = V_f(x)$. Moreover, in contrast to known classical(-like) approaches to vibronic spectra such as the DCL, the averaged classical limit (ACL)[44] and the method presented in

Ref. 26, both choices of the dynamics recover the exact imaginary-time shifted TCF of a harmonic oscillator model, as it is shown in Sec. IV.

Here, we have considered only the two aforementioned logically sound choices for the potentials. Nonetheless, the presented formalism offers in principle infinitely many possible approaches to vibronic spectroscopy that might or might not lead to efficient simulation protocols.

F. Circumventing the sign problem

1. The conventional ansatz

As it has been already stated, the Matsubara approximation to the quantum TCF suffers from the sign problem due to the presence of the imaginary part $\mathbf{\Pi}^{\mathrm{T}}\mathbb{W}\mathbf{Q}$ in the exponent in Eq. (20). However, this imaginary part can be removed by transforming the Matsubara momentum to the complex plane, independently on the form of the physical potential[36]

$$\mathbf{\Pi} \mapsto \mathbf{\Pi} + \mathrm{i}m\mathbb{W}\mathbf{Q} \ . \tag{23}$$

It is straightforward to show that the exponent then becomes

$$\tilde{H}_l(\mathbf{Q},\mathbf{\Pi}) + \mathrm{i}\mathbf{\Pi}^{\mathrm{T}}\mathbb{W}\mathbf{Q} \mapsto \tilde{H}_l(\mathbf{Q},\mathbf{\Pi}) + \frac{1}{2}m\mathbf{Q}^{\mathrm{T}}\mathbb{W}^{\mathrm{T}}\mathbb{W}\mathbf{Q} \ , \tag{24}$$

which is purely real and thus there is no sign problem occurring. Unfortunately, the new Liouvillian

$$\mathrm{Re}\hat{\tilde{\mathcal{L}}}_l(\mathbf{Q},\mathbf{\Pi}) \mapsto \mathrm{Re}\hat{\tilde{\mathcal{L}}}_l(\mathbf{Q},\mathbf{\Pi}) - m\mathbf{Q}^{\mathrm{T}}\mathbb{W}^{\mathrm{T}}\mathbb{W}\nabla_{\mathbf{\Pi}} + \mathrm{i}[\mathbf{\Pi}^{\mathrm{T}}\mathbb{W}\nabla_{\mathbf{\Pi}} - \mathbf{Q}^{\mathrm{T}}\mathbb{W}\nabla_{\mathbf{Q}}] \tag{25}$$

would generate unstable complex trajectories yielding similar statistical convergence issues as the sign problem itself.

One common ansatz to ultimately avoid the sign problem is to simply discard the imaginary part of the Liouvillian.[36] Applying this approximation to Eq. (25) leads to a RPMD-like method for multiple PESs, since the additional terms on the right hand sides of Eqs. (24,25) correspond to the well-known spring terms.[8] Importantly, if one picks the equilibrium choice for the dynamics and considers only $\lambda \in]0,\beta[$, then the resulting approximation to $C_\lambda(t)$ coincides with the one presented in Ref. 26 in the limit $M, P \to \infty$. Hence, the method

carried out therein can be viewed as an approximation to the Matsubra dynamics presented here. Nevertheless, this relation does not hold at the imaginary-time borders, i.e. $\lambda \in \{0, \beta\}$ since the bead located at x_0 experiences the averaged potential, see Eq. (17), which is not present in Ref. 26. We note in passing that other common approximations circumventing the sign problem, such as TRPMD[39] and CMD,[40] would be equally transferable to the multiple PESs case, starting from the developed Matsubara dynamics ansatz.

2. The modified method

Utilizing the harmonic model system introduced in Sec. III allows one to write down explicit expressions for various TCFs. In particular, a comparison of the RPMD expression for the standard TCF, $C_0(t)$, to its Matsubara counterpart suggests an interesting though *ad hoc* modification of the simulation protocol, see Sec. IV of the Supplement. Substituting the exponent of the complex density from Eq. (20) as

$$\frac{1}{2m}\mathbf{\Pi}^{\mathrm{T}}\mathbf{\Pi} + \frac{1}{2}m\omega^2\mathbf{Q}^{\mathrm{T}}\mathbf{Q} + \mathrm{i}\mathbf{\Pi}^{\mathrm{T}}\mathbb{W}\mathbf{Q} \mapsto \frac{1}{2m}\mathbf{\Pi}^{\mathrm{T}}(1 + \mathbb{W}^{\mathrm{T}}\mathbb{W}/\omega^2)\mathbf{\Pi} + \frac{1}{2}m\omega^2\mathbf{Q}^{\mathrm{T}}(1 + \mathbb{W}^{\mathrm{T}}\mathbb{W}/\omega^2)\mathbf{Q} \tag{26}$$

and keeping the EOMs given in Eq. (21) unchanged, recovers the analytical Matsubara expression for the harmonic oscillator model considered. Consequently, this *modified method* recovers the exact TCF in the $M, P \to \infty$ limit as the Matsubara method does. However, since the resulting modified density is real and non-negative, there is no sign problem and thus the suggested modification leads to a strikingly more efficient protocol than the Matsubara approximation, see Sec. IV. Interestingly, in contrast to the RPMD-like protocol, this modified method features dynamics *without* springs, which can cause artificial resonances with physical modes that may ruin the correct description of dynamical properties, as is well-known in vibrational spectroscopy.[35,46] Instead, there is an additional spring term, which connects the momenta of the beads in the density but does not affect the dynamics.

Although being constructed in an *ad-hoc* fashion, the modified density is directly related to the thermal Wigner function for the harmonic oscillator case, as it is shown in Sec. IV A 2. The proposed modification is based exclusively on the expressions for $\lambda = 0$ and, thus it expectedly fails for any case, where $\lambda \in]0, \beta[$, see Sec. V in the Supplement. Inventing analogous modifications for these cases is non-obvious and, therefore, a rigorous justification of the replacement would be desirable to identify the missing ingredients.

In order to go beyond purely harmonic systems, the modified method has to be generalized to an anharmonic system. We suggest to perform the following modification

$$\frac{1}{2m}\mathbf{\Pi}^{\mathrm{T}}\mathbf{\Pi} + \tilde{U}_0(\mathbf{Q}) - \mathrm{i}\mathbf{\Pi}^{\mathrm{T}}\mathbb{W}\mathbf{Q} \mapsto \frac{1}{2m}\mathbf{\Pi}^{\mathrm{T}}(1 + \mathbb{W}^{\mathrm{T}}\mathbb{Y}^{-1}(\mathbf{Q})\mathbb{W})\mathbf{\Pi} + \tilde{U}_0(\mathbf{Q}) + \frac{1}{2}m\mathbf{Q}^{\mathrm{T}}\mathbb{W}^{\mathrm{T}}\mathbb{W}\mathbf{Q} \ , \tag{27}$$

while keeping again the original EOMs from Eq. (21). The key quantity is the position-dependent matrix $\mathbb{Y}(\mathbf{Q})$, which maps the curvature of the ground-state potential along the imaginary-time path onto the Matsubara modes, i.e.

$$\mathbb{Y}(\mathbf{Q}) := \frac{1}{m}\mathbb{T}\left(\frac{\partial^2 V_g}{\partial x_i^2}\delta_{ij}\right)\mathbb{T}^{\mathrm{T}} \ . \tag{28}$$

This seems to us as the most flexible generalization to anharmonic systems, while keeping the structure as close as possible to that in Eq. (26) and having it as the limiting case if $V_g(x)$ is perfectly quadratic. As a word of caution, it should be noted that the inverse $\mathbb{Y}^{-1}$ becomes ill-defined at the turning points of the ground-state PES and that the modified density can become unbound if $V_g(x)$ possesses regions with a negative curvature. However, for the present study these problems are avoided owing to the particular form of the quartic potential as given in Sec. III. It remains to be seen whether this new but heuristic simulation protocol can be viewed as a systematic approximation to the orignal Matsubara method or if there is any relation to the Feynman-Kleinert Quasi-Classical Wigner method.[47] Note that in case of $\lambda = 0$ all aforementioned methods tend to the well-known ACL one[29,30,44] as $P \to 1$. This is in contrast to Ref. 26, where the $\lambda = 0$ and $P = 1$ case coincides with the DCL method.

III. COMPUTATIONAL DETAILS

In order to analyze the methodology presented in Sec. II, we consider in Sec. IV A a rather simple but still non-trivial model system consisting of two shifted harmonic PESs, $V_a(x) = m\omega^2(x - x_a)^2/2$ with $a = g, f$ and the same harmonic frequency ω. Consequently the energy gap $V_f(x) - V_g(x)$ is a linear function of the coordinate. The exact quantum-mechanical (QM) imaginary-time shifted TCF for such a system in the Condon approximation, i.e. $D_g^f(x) \approx 1$, is known and is compared to its approximations in Sec. IV A 1.

For practical simulations performed in Sec. IV A 2, the parameters for the OH diatomic adopted from the qSPC/Fw model[48] are employed, that is $m = m_{\mathrm{OH}} = 1728.0\,\mathrm{au}$, $\omega = \omega_{\mathrm{OH}} = 0.0177\,\mathrm{au}$, $x_g = 0$ and $x_f = 0.5\,\mathrm{au}$.

In order to investigate a more realistic scenario in Sec. IV B, we have modeled the OH-diatomic by two displaced anharmonic oscillators, where

$$V_a(x) = E_a \left[\alpha_a^2 (x - x_a)^2 - \alpha_a^3 (x - x_a)^3 + \frac{7}{12} \alpha_a^4 (x - x_a)^4 \right] \tag{29}$$

is a quartic expansion of the Morse potential. The parameters for the electronic ground state, $E_g = 0.185\,\mathrm{au}$ and $\alpha_g = 1.21\,\mathrm{au}$, are again adopted from the qSPC/Fw model for water[48] with $x_g = 0$. Similarly to the choice made in Ref. 26, the excited state differs from the ground state by a displacement of $x_f - x_g = 0.22\,\mathrm{au}$ and a lower stiffness of $\alpha_f = 0.86\alpha_g$, whereas the dissociation energies $E_f = E_g$ are the same. The equilibration as well as the sampling have been performed at 300 K using a standard Langevin thermostat[49] and the EOMs have been integrated employing the velocity-Verlet algorithm. A reasonably large number of 10000 microcanonical trajectories starting from uncorrelated initial conditions has been used for all the methods and systems. Only the Matsubara method with $P = 9$ has required 10 times more trajectories to converge, see below. The quantum results have been obtained in the harmonic basis of the electronic ground state potential using 50 eigenstates. In order to avoid artifacts of the finite Fourier transform, the spectra have been convoluted with a Gaussian window $\exp[-\omega^2/2\sigma^2]$, where $\sigma = 0.002\,\mathrm{au}$.

Although setting $M = P$ contradicts the Matsubara approximation, where $M \ll P$ is implied, see Sec. II B, this choice still yields reasonable results for various simulation protocols, as it will be discussed in Sec. IV. In such a scenario, the correlation function originates from purely classical dynamics of P *independent* particles that are only connected via the Matsubara phase in the density, Eq. (20). In the following discussion, we will therefore make the distinction between this dynamics of independent classical particles, i.e. $M = P$, and the *true* Matsubara dynamics, involving only smooth imaginary-time paths, i.e. $M < P$. Note that for the RPMD-like method the beads are coupled via the spring term in any case.

IV. RESULTS AND DISCUSSION

A. Analysis for the harmonic oscillator model

For the harmonic system introduced in Sec. III, the exact QM imaginary-time shifted TCF, the corresponding Matsubara approximation as well as the expression resulting from the RPMD-like ansatz and the modified method can be written down explicitly as functions of M and P. These analytical expressions, written down in Sec. IV of the Supplement, serve as a basis for the following discussion that suggests several favorable simulation scenarios, subsequently employed in Sec. IV A 2 and Sec. IV B.

1. Analytical results

The developed mathematical expressions are utilized for an applicability analysis of the considered methods, with respect to the relation between M and P and a choice of λ, see Table. I. The criterion for the applicability is the correct limit of the TCF as $M, P \to \infty$ for the aforementioned harmonic oscillator system. To reiterate, common classical(-like) approaches to vibronic spectroscopy, such as the DCL and the ACL do not yield the correct TCF and thus spectrum with any parameter setup.[26]

approximation	Matsubara				RPMD-like				modified	
EOMs	equilibrium		average		equilibrium		average		equilibrium	average
$\lambda \in$	$\{0,\beta\}$	$]0,\beta[$	$\{0,\beta\}$	$]0,\beta[$	$\{0,\beta\}$	$]0,\beta[$	$\{0,\beta\}$	$]0,\beta[$	$\{0\}$	$\{0\}$
$M = P$	+	+	+	+	−	−	−	−	+	+
$M < P$	−	−	+	−	−	−	−	−	−	+

TABLE I. Applicability of the considered methods summarized in the first two rows to recover the exact result for the shifted harmonic oscillators in the limit $M, P \to \infty$. Green plus signs mark the success, whereas red minus signs represent a failure. In the third row, the curly braces indicate a set, while $]\bullet,\bullet[$ refers to an open interval.

Let us start with the Matsubara dynamics, that is Eqs. (20,21), carried out via average and equilibrium methods, as is discussed in Sec. II E. Both methods yield the exact imaginary-time shifted TCF for any λ only for $M = P$, which contradicts the original idea of the

Matsubara approximation. However, since the equilibrium method is not exact for $M < P$ irrespectively of the value of λ, $M = P$ remains the only reasonable setting for this choice of the EOMs, see Sec. IV A 2 and IV B 2 for a discussion of its ability to approximate the quantum TCF. The only combination that still yields exact results with $M < P$ is the average method with $\lambda \in \{0, \beta\}$. Solely for this choice, true Matsubara dynamics (with $M < P$) yields the exact quantum TCF for the harmonic oscillator. Importantly, for $\lambda \in]0, \beta[$ none of the considered choices for the dynamics leads to the exact result if $M < P$. This indicates that the Matsubara approximation, i.e. taking only smooth imaginary-time paths into account, is incompatible with with the discontinuity in the potential for the points x_0 and x_l, see Sec. II B and Sec. II E.

2. Numerical results

In this section, the findings from Sec. IV A 1 are supplemented by a performance comparison between all the methods via numerical simulations at ambient temperature for a harmonic oscillator system, which mimics an isolated OH bond of a water molecule, see Sec. III. The focus is on on the convergence with respect to statistics and the number of beads and Matsubara modes, i.e. P and M, respectively.

Let us first examine probability densities for the bead positions and momenta sampled by the modified method, Eq. (26), see Fig. 3. Interestingly, they tend to the exact result given by the well-known thermal Wigner function of the harmonic oscillator, not only for positions, which is natural for PI methods, but also for momenta. Nonetheless, it is clear that such a correspondence cannot be general, as i) Wigner functions can become negative, which cannot be achieved by the suggested protocol; ii) the harmonic frequency ω appearing on the r.h.s. of Eq. (26) cannot be unambiguously defined for a general system, see Sec. IV B for suggestions.

Switching to the TCFs, we first restrict ourselves to $\lambda = 0$ and $M = P$, see Fig. 4, where the left/right column corresponds to the equilibrium/average method. For each method, the degree of statistical convergence is visualized by transparent areas representing the 95 % confidence interval around the mean values that are depicted as lines and points; note that for most of the methods these areas are within the thickness of the line.

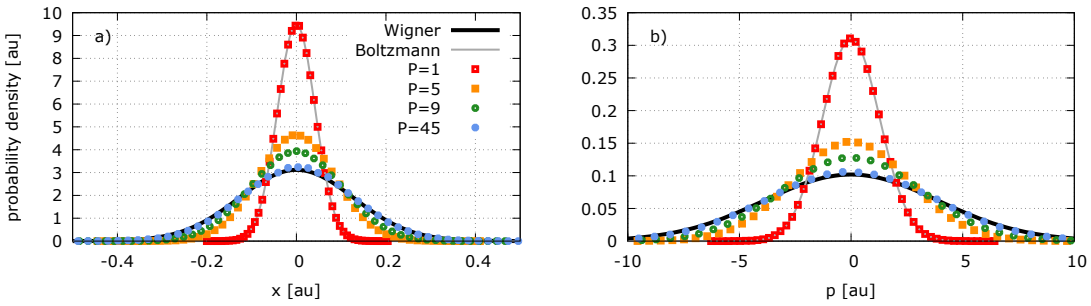

FIG. 3. Histograms of the positions, panel a), and momenta, panel b), as sampled by the modified method for various values of P. The classical Boltzmann and the QM Wigner functions are plotted as solid lines. Note that the full two-dimensional Wigner function can be constructed as the Cartesian product of both curves.

Independent classical dynamics. Starting from the common classical ($P = 1$) approaches, one sees that both DCL, Fig. 4 panel 1a), and ACL, panel 1b), fail to reproduce the correlation function, although the ACL TCF captures more features of the QM curve. For $P = 5$, still panels 1) therein, one can see that the curves resulting from the Matsubara and the modified method coincide as expected and improve qualitatively over the ACL TCF, which is their common $P \to 1$ limit. In case of the RPMD ansatz, the average method performs much better than the equilibrium one, see panels 1a) and 1b), correspondingly.

When the number of beads is further increased to nine, panels 2) in Fig. 4, the first traces of the sign problem in the Matsubara method appear, as is manifested by red areas therein. In contrast, the modified method still features an excellent statistical convergence and the curve gets closer to the exact QM result. Apart from the vicinity of the first minimum of the TCF, both RPMD-like methods do not improve, which underlines that RPMD is a short-time approximation to the exact QM dynamics.

Finally, taking a large number of beads ($P = 45$), which is a typical value to reach convergence for an OH diatomic at 300 K, as is confirmed in Fig. 3, both versions of the Matsubara method exhibit severe problems with respect to statistical convergence, see insets in panels 3). This illustrates the well-known fact that the Matsubara method is not directly applicable in practical numerical simulations. In contrast, the modified method converges to the exact result without any issues and, importantly, without any additional costs with respect to the RPMD-like method that in turn exhibits no further improvement

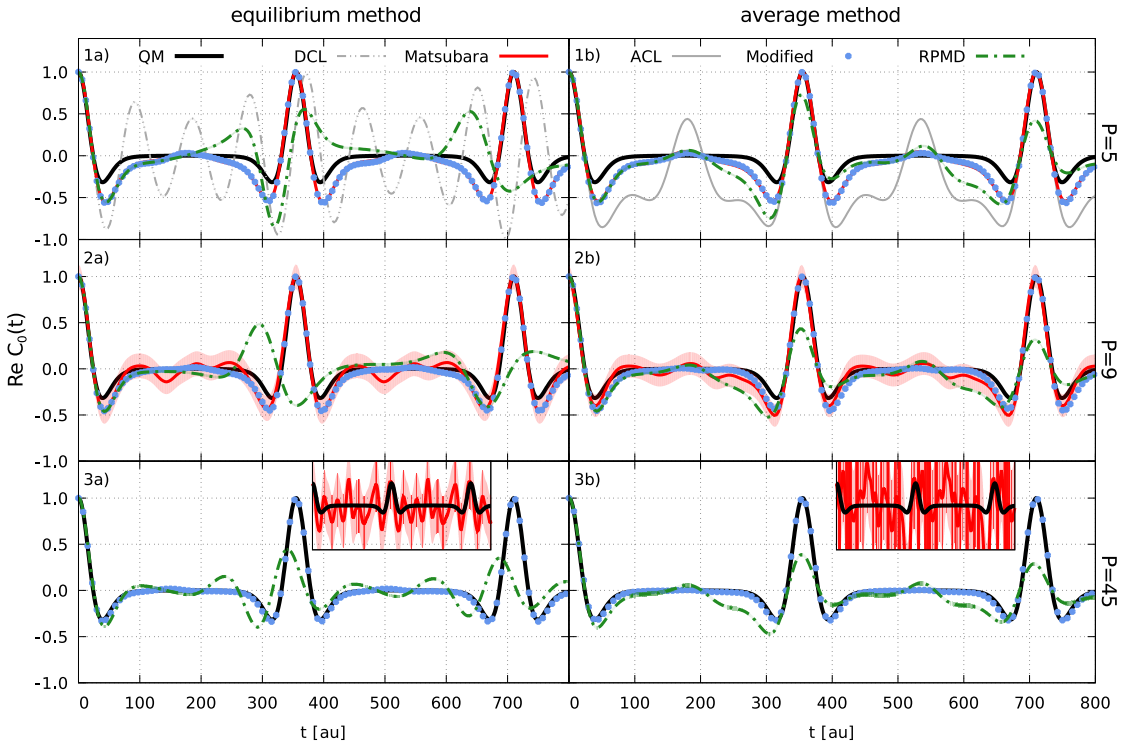

FIG. 4. The real part of standard correlation functions, $C_0(t)$, for the harmonic system, see Sec. III. The left column, panels a), exhibits the results of the equilibrium methods, whereas panels b) contain the results of the average methods for $M = P$. The first row, panels 1), correspond to the case $M = P = 5$, apart from the DCL and ACL curves which naturally imply $M = P = 1$. The second row, panels 2), features $M = P = 9$ and panels 3) show $M = P = 45$ data, with insets exhibiting the results of the Matsubara method. Transparent areas indicate the 95% confidence intervals (which are not visible for most of the curves) and the lines and points represent the statistical mean.

with increasing P.

True Matsubara dynamics. The Matsubara approximation implies that $M < P$, thus TCFs with $M/P \approx 0.5$ for all the methods are shown in Fig. 5, which has the same layout as Fig. 4. The equilibrium Matsubara and the modified method (which coincide by construction) exhibit a phase shift with respect to the exact QM curve for $M = 3, P = 5$, see panel 1a). This bad performance is anticipated on the basis of the analysis presented in Sec. IV A 1. The RPMD-like method fails in a similar way. In contrast, the curves obtained

by the average methods, panel 1b), are in phase with the QM one. Especially, the average RPMD TCF reveals much better agreement with the exact result than the equilibrium one. Note that for the classical methods ($P = 1$), the number of Matsubara modes cannot be smaller than the number of beads, thus ACL and DCL results are not shown.

Turning to a larger number of modes and beads, $M = 5, P = 9$ in panels 2) of Fig. 5, one notices immediately that in contrast to Fig. 4 the Matsubara methods do not feature issues with the statistical convergence. However, this is only due to the fact that the Matsubara density is assembled by 5 modes only, thus, the statistical behavior is effectively the same as for the case $M = P = 5$. Importantly, all the average versions approximate the QM curve much better, which is especially true for the RPMD-like method, compare panel 2a) and 2b).

Approaching the convergence with respect to the number of Matsubara modes and beads, i.e. for $M = 25, P = 45$, panels 3) in Fig. 5, the Matsubara method suffers again from the sign problem, see insets. The average version of the modified method converges to the exact result without any issues, however, as expected, the equilibrium one as well as the RPMD method do not.

To conclude, the suggested modification strikingly outperforms the Matsubara method with respect to the statistical convergence, while yielding the same results for the case $\lambda = 0$. Moreover, the modified method surpasses the RPMD-like ansatz with respect to the quality of the results. As it has been anticipated from the mathematical analysis, the equilibrium versions of the Matsubara and the modified methods lead to reasonable results only if $M = P$. The average methods outperform the equilibrium ones if $M < P$, which is especially true for the RPMD ansatz. At this point there is no pratical advantage of the quasi-classical dynamics ($M < P$) with respect to the independent classical dynamics ($M = P$). However, since the considered system consists of two one-dimensional harmonic oscillators this is not surprising. Whether such a statement can be transferred to a more realistic anharmonic case is discussed in Sec. IV B.

Finally, none of the presented methods can practically reproduce the exact imaginary-time shifted TCF for the case $\lambda \in]0, \beta[$, see Sec. V in the Supplement. In particular, the equilibrium Matsubara method converges formally to the exact result if $M = P$ but is suffering from the sign problem. The RPMD-like method does not lead to an acceptable approximation to the quantum TCF, as in all the other cases considered. Unfortunately,

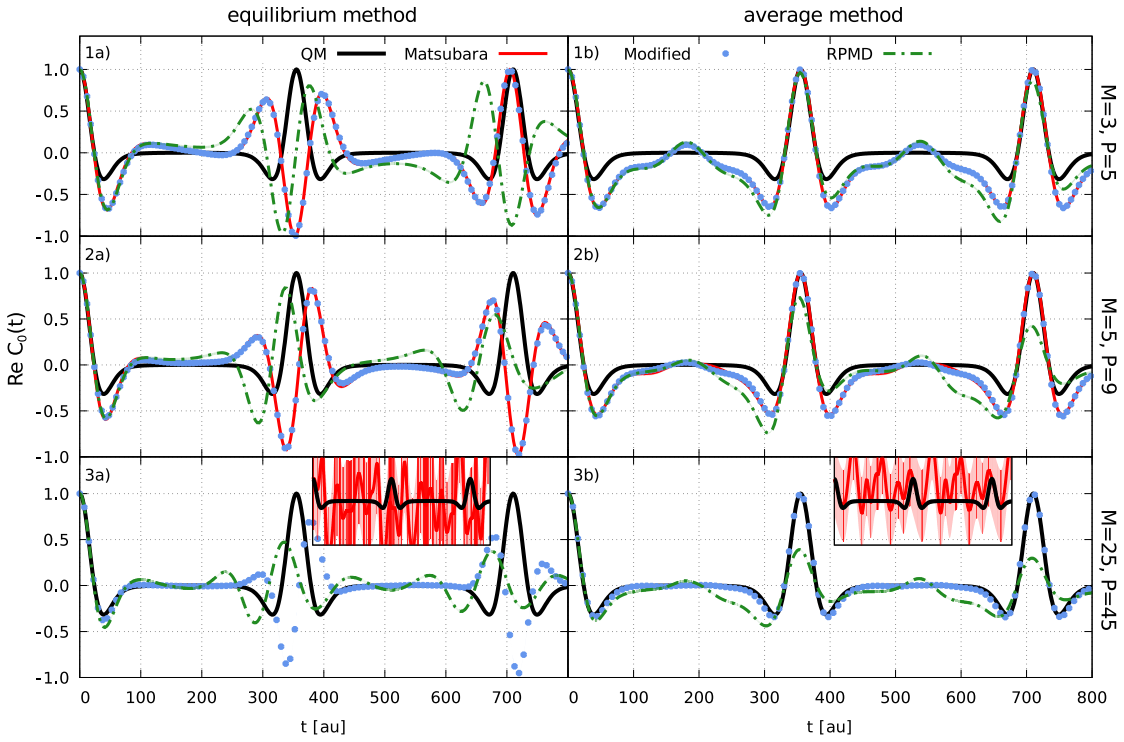

FIG. 5. Same scenario and color code as in Fig. 4 but with the first row, panels 1), exhibiting the results for $M = 3, P = 5$. The second row, panels 2), features $M = 5, P = 9$ and panels 3) show $M = 25, P = 45$.

the modified method was derived just for $\lambda = 0$ and naive use of this modification for $\lambda > 0$ expectedly fails. Still, the expressions that have been derived in Sec. II for a general value of λ might serve as a basis for future work and finally may lead to a powerful simulation protocol in combination with the generalized TCF formalism.[26]

B. Anharmonic oscillators

1. *Generalization of the modified method*

Since the modified density tends to the exact Wigner function for the harmonic oscillator, see Fig. 3, we investigate the ability of the generalized modified method to reproduce the exact Wigner function of the anharmonic system introduced in Sec. III. In Fig. 6a) one can see the classical Boltzmann function for the electronic ground state, which is the common

limit for all methods if $P = 1$. It is not surprising that the classical density is much more localized than the exact Wigner function seen in panel d); note the different scales for the color bars in the different panels. In panel b), the absolute value of the complex density corresponding to the Matsubara method, Eq. (20), is shown for $P = 45$. This is effectively nothing else than the classical Boltzmann distribution but for a temperature that is P times higher than in the classical case, panel a). For the present model this would correspond to a temperature of 13500 K and, hence, the density covers a phase-space volume that is much larger than the classical one and significantly larger than the correct QM one. Only the cancellation due to the complex phase in the Matsubara density, removes the irrelevant contributions to the observables. This *indirect* sampling of the correct distribution is at the heart of the sign problem and is thus responsible for the poor convergence of the Matsubara method. In contrast, the generalized method, Eq. (27), approximates the exact thermal Wigner function *directly* with a remarkable accuracy, see panel c). Importantly, it is even able to reproduce the "egg shape" of the correct Wigner function, which is an inherently quantum-statistical effect, since it requires the coupling of position and momenta in the density, which is not present in the classical case.

In resume, the suggested generalization captures important quantum statistics even for the anharmonic case, although any negativity in the Wigner function remains outside reach and the numerical instabilities in the regions of a vanishing or negative curvature of the potential are still awaiting for a proper treatment.

2. Vibronic absorption spectra for the anharmonic system

After discussing static properties of the methods, the dynamical observables, i.e. vibronic absorption spectra are considered for the anharmonic system. With the parameters given in Sec. III, simulations have been performed yielding the results depicted in Fig. 7, which has the same structure as Fig. 4 but now showing the Fourier transforms of $C_0(t)$.

Starting with the description of the QM spectrum, one recognizes a typical Franck-Condon progression with a Huang-Rhys factor smaller than 0.5, meaning that the maximal intensity is located at the 0-0 transition. Switching to the approximations in panel 1a), the common DCL method neither yields the correct spectral shape nor the correct peak positions, as has been observed before.[26,29,30] In contrast, the result obtained with the ACL

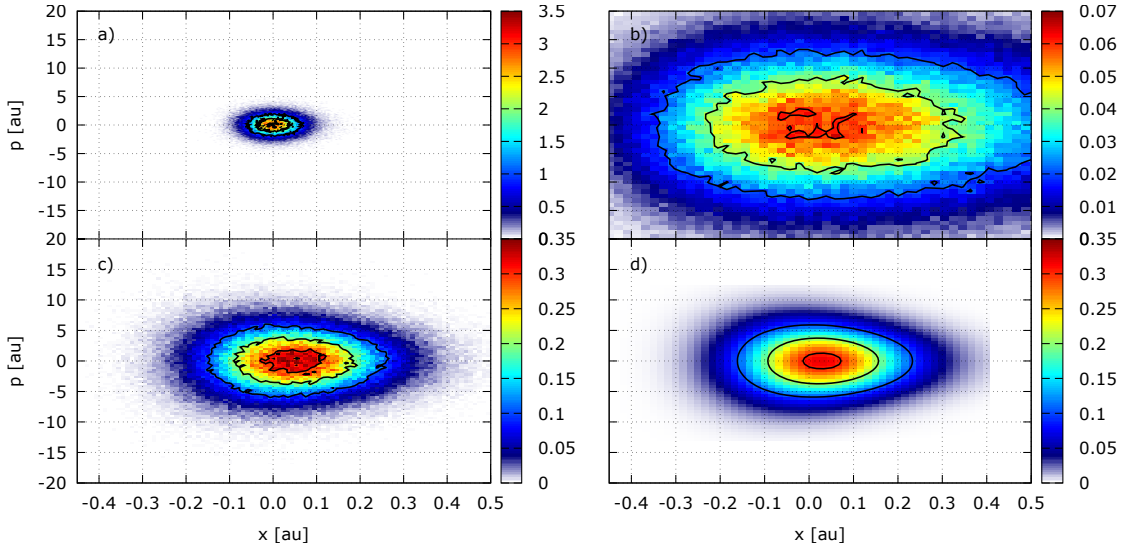

FIG. 6. Phase-space probability densities for the anharmonic model system sampled by the considered methods. Panel a) the classical Boltzmann distribution; panel b) the absolute value of the complex Matsubara density and panel c) the modified density, both with $P = 45$; panel d) the exact Wigner function.

method, see panel 1b), is in much better agreement with the QM one, though a significant negative intensity below the 0-0 transition is present. This is a consequence of the non-stationary dynamics, possibly leading to all kinds of unphysical artifacts in spectra of more complex systems.[26]

When it comes to more modes and beads, i.e. $M = P = 5$ in panels 1) of Fig. 7, the modified method still coincides with the Matsubara method although this is generally not expected for an anharmonic case. Both methods cannot completely avoid a negative intensity below the 0-0 transition, but the amplitude of the artifact is smaller than the ones produced by the ACL and RPMD-like methods. For the latter, the average method, see panel 1b), performs significantly better than its equilibrium counterpart depicted in panel 1a).

Increasing M and P to nine improves the quality of the modified and the Matsubara method, which are still surprisingly similar, as it can be seen in panels 2) of Fig. 7. However, the Matsubara method has required ten times more trajectories than the modified one to yield statistically converged results. Importantly, the artificial negativity is smaller by a factor of two than that for the case $M = P = 5$. The average version of the RPMD-like

approach, see panel 2b), improves further with respect to the peak intensities, whereas the negative intensity has not changed notably. The opposite can be observed in panel 2a) for the equilibrium RPMD-like method, where the negativity completely disappears, whereas the overall agreement with the QM curve becomes worse.

It appears to be impossible to reach statistical convergence for the Matsubara method, if the number of beads and modes is increased to 45, even employing 10^6 trajectories and, thus, no results are shown. The average version of the RPMD method does not improve significantly in this case and the quality of its equilibrium counterpart becomes even worse, see panels 3). The modified method convergences again without any issues, while coming quite close to the exact QM curve. Importantly, the artificial negativity vanishes almost completely. Finally, one can see that there is again no significant difference between the cases $M = P = 45$ and $M = 25, P = 45$ when considering the modified average methods, see the solid line in panel 3b). The equilibrium method fails again if $M < P$, as it can be seen in panel 3a).

To conclude, the Matsubara and the modified methods nearly coincide for all cases, where the Matsubara method statistically converges. One can therefore expect that both would converge to very similar results in the limit $M, P \to \infty$. In comparison to the more common methods, i.e. DCL, ACL and finally the RPMD ansatz, the modified method yields much more accurate results, especially with respect to the negativities below the 0-0 transition. These statements are additionally supported by the results for a similar anharmonic system possessing a larger displacement between the potentials, see Sec. V in the Supplement. Interestingly, even for such a notably anharmonic system, the truly quasi-classical dynamics with $M < P$ yields no benefit if compared to the methods with $M = P$. However, this is by no means the ultimate conclusion and the impact of having continuous imaginary-time paths within the dynamics has to be investigated carefully, in particular using more complex systems featuring problems such as zero-point energy leakage.

V. CONCLUSIONS AND OUTLOOK

The Matsubara dynamics has been generalized to the multi-PES case and thereby to vibronic spectroscopy. It has been shown that the Matsubara dynamics can be derived from the imaginary-time shifted TCF, assuming that the potential is locally harmonic and the

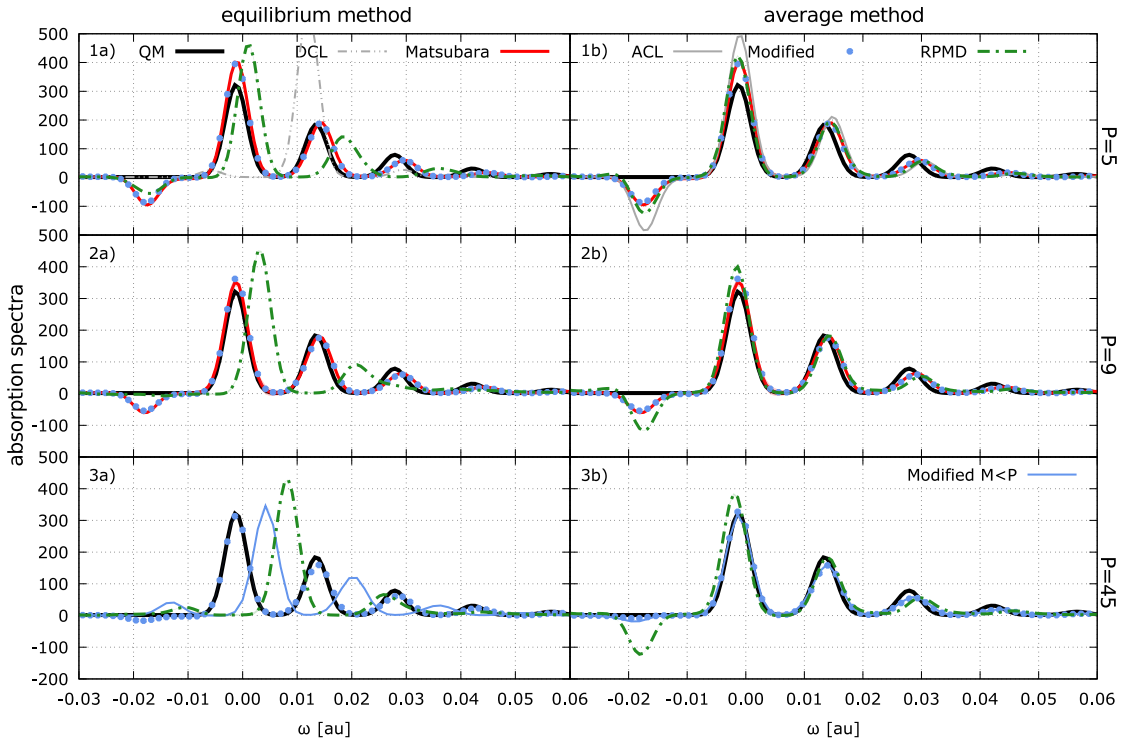

FIG. 7. Absorption spectra for two displaced anharmonic oscillators, see Eq. (29). Same color code as in Fig. 4 but with the thin blue lines in the lower row representing the setup $M = 25, P = 45$.

transition dipole moment is locally linear. The performed derivation left certain flexibility in choosing the Hamiltonians responsible for the real-time propagation. Practically, this enables infinitely many possible simulation protocols, whereas we have employed two particular ones, termed equilibrium and average methods, which have physical foundation. In order to circumvent the infamous sign problem plaguing the Matsubara-based methods, an RPMD-like ansatz has been employed. The comparison of the Matsubara expressions to the QM TCF for a system of two shifted harmonic oscillators has singled out cases that lead to numerically exact results in the limit of infinitely many Matsubara modes. Note that common classical-like approaches to the vibronic spectrum, such as the DCL and the ACL, do not yield exact results for this system with any set of parameters. Further comparison of the RPMD expressions to the exact ones has suggested an *ad hoc* but meaningful modification of the density and its generalization to the anharmonic regime has been developed. In both scenarios, the harmonic and the anharmonic one, the sampled density reproduced the exact

thermal Wigner function of the electronic ground state with remarkable accuracy. Although it cannot reproduce the negativities of the Wigner function by construction, it still may be a reasonable and very convenient method to sample Wigner densities, which is a common task in quasi- and semiclassical methods.[50] When it comes to approximating the absorption spectra, the modified method outperforms the Matsubara method with respect to the statistical convergence, while it surpasses the RPMD-like ansatz with respect to the quality of the results. Further, if true Matsubara dynamics with smooth imaginary-time paths is considered, all of the presented average methods lead to significantly better results than the equilibrium ones. Although the advantage of quasi-classical dynamics over independent classical dynamics has not become apparent for the considered one-dimensional systems, the importance of taking only smooth paths into account has to be investigated carefully for more complex systems. Unfortunately, for imaginary-time shifted TCFs, $C_\lambda(t)$ with $\lambda > 0$, none of the methods is directly applicable to realistic systems. To improve on the last point, future work might be dedicated to find a more rigorous justification of the modified method and finally to combine the generalized TCF formalism[26] with the methodology presented here. Another interesting perspective could be the application of the suggested modified method to single-PES studies such as IR spectroscopy. In contrast to the more common RPMD and CMD methods, one would expect that problems with spurious resonances or with the curvature of the ring polymer[35] could be avoided by the modified ansatz.

ACKNOWLEDGMENTS

S. K. acknowledges financial support by the Deutsche Forschungsgemeinschaft (KU 952/10-1).

REFERENCES

[1]S. Mukamel, *Principles of nonlinear optical spectroscopy* (Oxford University Press, Oxford, 1995).

[2]V. May and O. Kühn, *Charge and energy transfer dynamics in molecular systems* (Wiley-VCH, Weinheim, 2011).

[3]P. Hamm and M. Zanni, *Concepts and methods of 2D infrared spectroscopy* (Cambridge University Press, Cambridge, 2011).

[4]H.-D. Meyer, F. Gatti, and G. A. Worth, *Multidimensional Quantum Dynamics: MCTDH Theory and Applications* (Wiley-VCH, Weinheim, 2009).

[5]R. P. Feynman and A. R. Hibbs, *Quantum Mechanics and Path Integrals* (McGraw-Hill, New-York, 1965).

[6]L. Schulman, *Techniques and Applications of Path Integration* (Dover Publications, Inc., Mineola, New York, 2005).

[7]D. Marx and J. Hutter, *Ab initio molecular dynamics: basic theory and advanced methods* (Cambridge University Press, Cambridge, 2009).

[8]M. E. Tuckerman, *Statistical mechanics: theory and molecular simulation* (Oxford University Press, Oxford, 2010).

[9]S. D. Ivanov, O. Asvany, A. Witt, E. Hugo, G. Mathias, B. Redlich, D. Marx, and S. Schlemmer, Nat. Chem. **2**, 298 (2010).

[10]A. Witt, S. D. Ivanov, and D. Marx, Phys. Rev. Lett. **110**, 083003 (2013).

[11]M. H. M. Olsson, P. E. M. Siegbahn, and A. Warshel, J. Am. Chem. Soc. **126**, 2820 (2004).

[12]J. Gao and D. G. Truhlar, Annu. Rev. Phys. Chem. **53**, 467 (2002).

[13]G. Stock and M. Thoss, Adv. Chem. Phys. **131**, 243 (2005).

[14]J. C. Tully, J. Chem. Phys. **137**, 22A301 (2012).

[15]I. Tavernelli, Acc. Chem. Res. **48**, 792 (2015).

[16]J. O. Richardson and M. Thoss, J. Chem. Phys. **139**, 031102 (2013).

[17]N. Ananth, J. Chem. Phys. **139**, 124102 (2013).

[18]M. Thoss and G. Stock, Phys. Rev. A **59**, 64 (1999).

[19]N. Ananth and T. F. Miller III, J. Chem. Phys. **133**, 234103 (2010).

[20]J. O. Richardson, P. Meyer, M.-O. Pleinert, and M. Thoss, Chem. Phys. **482**, 124 (2016).

[21]C. D. Schwieters and G. A. Voth, J. Chem. Phys. **111**, 2869 (1999).

[22]M. H. Alexander, Chem. Phys. Lett. **347**, 436 (2001).

[23]J. Schmidt and J. C. Tully, J. Chem. Phys. **127**, 094103 (2007).

[24]P. Shushkov, R. Li, and J. C. Tully, J. Chem. Phys. **137**, 22A549 (2012).

[25]J. Lu and Z. Zhou, J. Chem. Phys. **146**, 154110 (2017).

[26]S. Karsten, S. D. Ivanov, S. I. Bokarev, and O. Kühn, J. Chem. Phys. **148**, 102337 (2018).

[27]R. Kubo, J. Phys. Soc. Jpn. **12**, 570 (1957).

[28]P. Schofield, Phys. Rev. Lett. **4**, 239 (1960).

[29]E. Rabani, S. A. Egorov, and B. J. Berne, J. Chem. Phys. **109**, 6376 (1998).

[30]S. A. Egorov, E. Rabani, and B. J. Berne, J. Chem. Phys. **108**, 1407 (1998).

[31]S. Karsten, S. D. Ivanov, S. G. Aziz, S. I. Bokarev, and O. Kühn, J. Phys. Chem. Lett. **8**, 992 (2017).

[32]S. Karsten, S. I. Bokarev, S. G. Aziz, S. D. Ivanov, and O. Kühn, J. Chem. Phys. **146**, 224203 (2017).

[33]R. Ramirez, T. López-Ciudad, P. Kumar P, and D. Marx, J. Chem. Phys. **121**, 3973 (2004).

[34]I. R. Craig and D. E. Manolopoulos, J. Chem. Phys. **121**, 3368 (2004).

[35]A. Witt, S. D. Ivanov, M. Shiga, H. Forbert, and D. Marx, J. Chem. Phys. **130**, 194510 (2009).

[36]T. J. H. Hele, M. J. Willatt, A. Muolo, and S. C. Althorpe, J. Chem. Phys. **142**, 134103 (2015), arXiv:1504.02227.

[37]T. J. Hele, M. J. Willatt, A. Muolo, and S. C. Althorpe, J. Chem. Phys. **142**, 191101 (2015).

[38]T. J. Hele, Mol. Phys. **114**, 1461 (2016).

[39]M. Rossi, M. Ceriotti, and D. E. Manolopoulos, J. Chem. Phys. **140**, 234116 (2014).

[40]J. Cao and G. A. Voth, J. Chem. Phys. **99**, 10070 (1993).

[41]D. Chandler and P. Wolynes, J. Chem. Phys. **74**, 4078 (1981).

[42]E. Wigner, Phys. Rev. **40**, 749 (1932).

[43]A. M. de Almeida, Phys. Rep. **295**, 265 (1998).

[44]N. E. Shemetulskis and R. F. Loring, J. Chem. Phys. **97**, 1217 (1992).

[45]S. Habershon, T. E. Markland, and D. E. Manolopoulos, J. Chem. Phys. **131**, 024501 (2009).

[46]S. Habershon, G. S. Fanourgakis, and D. E. Manolopoulos, J. Chem. Phys. **129**, 074501 (2008).

[47]K. K. Smith, J. A. Poulsen, G. Nyman, and P. J. Rossky, J. Chem. Phys. **142**, 244112 (2015).

[48]F. Paesani, W. Zhang, D. A. Case, T. E. Cheatham, and G. A. Voth, J. Chem. Phys. **125**, 184507 (2006).

[49]G. Bussi and M. Parrinello, Phys. Rev. E **75**, 056707 (2007).

[50]J. Beutier, D. Borgis, R. Vuilleumier, and S. Bonella, J. Chem. Phys. **141**, 084102 (2014).

Supplemental Information: Simulating vibronic spectra via Matsubara dynamics: coping with the sign problem

Sven Karsten, Sergei D. Ivanov,[a)] Sergey I. Bokarev, and Oliver Kühn

Institute of Physics, Rostock University, Albert-Einstein-Str. 23-24, 18059 Rostock, Germany

(Dated: 17 May 2018)

[a)]Electronic mail: sergei.ivanov@uni-rostock.de

CONTENTS

I. APPLYING THE LOCAL HARMONIC APPROXIMATION

In this section the structure of the time-independent part, is further evaluated under the assumption of locally harmonic potentials. The starting point is the symmetric Trotter factorization employed to obtain the matrix elements of the Boltzmann operator, see Eq. (8) in the main text. Applying this to each factor of the product in Eq. (6) in the main text yields

$$\prod_{i=l}^{P-1}\langle x_{i+1}^{-}|\mathrm{e}^{-\beta\hat{H}_g/P}|x_i^{+}\rangle\prod_{i=0}^{l-1}\langle x_{i+1}^{-}|\mathrm{e}^{-\beta\hat{H}_f/P}|x_i^{+}\rangle = \lim_{P\to\infty}\left(\frac{\beta m\Omega_P^2}{2\pi}\right)^{P/2}$$
$$\times\exp\left\{-\frac{\beta}{2P}\left[\sum_{i=0}^{l-1}V_f(x_{i+1}^{-})+V_f(x_i^{+})+\sum_{i=l}^{P-1}V_g(x_{i+1}^{-})+V_g(x_i^{+})\right]-\beta\frac{m\Omega_P^2}{2}\sum_{i=0}^{P-1}\left[x_{i+1}^{-}-x_i^{+}\right]^2\right\}\ , \tag{S1}$$

where $\Omega_P := \sqrt{P}/\beta\hbar$ is the standard ring-polymer chain frequency. By assuming that the potentials are quadratic in the difference variable Δ_i, see Eq. (9) in the main text, and

writing out explicitly $x_i^{\pm} = x_i \pm \Delta_i/2$, one obtains for the exponent in Eq. (S1)

$$
\begin{aligned}
&- \frac{\beta}{2P}\left[\sum_{i=0}^{l-1} V_f(x_{i+1}) + V_f(x_i) + \sum_{i=l}^{P-1} V_g(x_{i+1}) + V_g(x_i)\right] \\
&- \frac{\beta}{2P}\left[\sum_{i=0}^{l-1} \frac{\partial V_f}{\partial x_i}\frac{\Delta_i}{2} - \frac{\partial V_f}{\partial x_{i+1}}\frac{\Delta_{i+1}}{2} + \sum_{i=l}^{P-1} \frac{\partial V_g}{\partial x_i}\frac{\Delta_i}{2} - \frac{\partial V_g}{\partial x_{i+1}}\frac{\Delta_{i+1}}{2}\right] \\
&- \frac{\beta}{2P}\left[\sum_{i=0}^{l-1} \frac{\partial^2 V_f}{\partial x_i^2}\frac{\Delta_i^2}{8} + \frac{\partial^2 V_f}{\partial x_{i+1}^2}\frac{\Delta_{i+1}^2}{8} + \sum_{i=l}^{P-1} \frac{\partial^2 V_g}{\partial x_i^2}\frac{\Delta_i^2}{8} + \frac{\partial^2 V_g}{\partial x_{i+1}^2}\frac{\Delta_{i+1}^2}{8}\right] \\
&- \beta\frac{m\Omega_P^2}{2}\sum_{i=0}^{P-1}\left[(x_{i+1}-x_i)^2 + \frac{1}{4}(\Delta_{i+1}+\Delta_i)^2 - (x_{i+1}\Delta_i - x_i\Delta_{i+1})\right] \quad . \qquad \text{(S2)}
\end{aligned}
$$

The examination of each line yields the following. The term in braces in the first line represents the effective ring polymer potential

$$
U_l(\mathbf{x}) := \frac{1}{P}\sum_{i=0}^{l} \kappa_i V_f(x_i) + \frac{1}{P}\sum_{i=l}^{P} \kappa_i V_g(x_i) \quad . \qquad \text{(S3)}
$$

with κ_i ensuring the trapezoidal rule. In the second line all terms vanish apart from the summation borders, i.e. $i = 0, l$. The summands in the third line can be rewritten in terms of the second derivatives $\partial^2 U_l/\partial x_i^2$ of the effective potential and the last line stemming from the kinetic energy operator couples the sum and difference variables. In order to profit from a more compact matrix vector notation, one can introduce the matrices $(\mathbb{A})_{i,j} := 2\delta_{i,j} - \delta_{i,j+1} - \delta_{i,j-1}$, $(\mathbb{B}_l(\mathbf{x}))_{i,j} := \partial^2 U_l/\partial x_i^2 \delta_{i,j}$, $(\mathbb{C})_{i,j} := \delta_{i,j+1} - \delta_{i+1,j}$ and $(\mathbb{D}_l)_{i,j} := (\delta_{i,0}\delta_{0,j} - \delta_{i,l}\delta_{l,j})/4$ and the gradient vector

$$
\mathbf{g}(\mathbf{x}) := \boldsymbol{\nabla}_{\mathbf{x}} \frac{1}{P}\sum_{i=0}^{P-1}(V_f(x_i) - V_g(x_i)) \quad , \qquad \text{(S4)}
$$

all obeying the cyclic condition $P \mapsto 0$ for the indices i, j. The exponent then becomes

$$
-\beta\left[U_l(\mathbf{x}) + \boldsymbol{\Delta}^{\mathrm{T}}\mathbb{D}_l\mathbf{g}(\mathbf{x}) + \frac{1}{8}\boldsymbol{\Delta}^{\mathrm{T}}\mathbb{B}_l(\mathbf{x})\boldsymbol{\Delta} + \frac{m\Omega_P^2}{2}\left(\mathbf{x}^{\mathrm{T}}\mathbb{A}\mathbf{x} + \frac{1}{4}\boldsymbol{\Delta}^{\mathrm{T}}(4-\mathbb{A})\boldsymbol{\Delta} + \mathbf{x}^{\mathrm{T}}\mathbb{C}\boldsymbol{\Delta}\right)\right] \quad , \qquad \text{(S5)}
$$

which yields after rearranging for the time-independent part

$$
A_l(\mathbf{x},\mathbf{p}) = \frac{(\beta m\Omega_P^2)^{P/2} D_f^g(x_l)}{Z(4\pi^2\hbar)^{P/2}} \mathrm{e}^{-\beta[m\Omega_P^2\mathbf{x}^{\mathrm{T}}\mathbb{A}\mathbf{x}/2 + U_l(\mathbf{x})]} \int \mathrm{d}\boldsymbol{\Delta}\, \mathrm{e}^{\mathrm{i}\mathbf{p}^{\mathrm{T}}\boldsymbol{\Delta}/\hbar} \mathrm{e}^{-\beta K_l(\mathbf{x},\boldsymbol{\Delta})} \quad , \qquad \text{(S6)}
$$

where the term $K_l(\mathbf{x},\boldsymbol{\Delta})$ connects the midpoint and difference variables, i.e.

$$
K_l(\mathbf{x},\boldsymbol{\Delta}) := \frac{m\Omega_P^2}{2}\left[\frac{1}{4}\boldsymbol{\Delta}^{\mathrm{T}}\left(4 - \mathbb{A} + \frac{\mathbb{B}_l(\mathbf{x})}{m\Omega_P^2}\right)\boldsymbol{\Delta} + \mathbf{x}^{\mathrm{T}}\mathbb{C}\boldsymbol{\Delta}\right] + \boldsymbol{\Delta}^{\mathrm{T}}\mathbb{D}_l\mathbf{g}(\mathbf{x}) \quad . \qquad \text{(S7)}
$$

One can easily prove that the contribution from the matrix $\mathbb{D}_l$ is negligible in the limit $P \to \infty$. Moreover, the matrix $4 - \mathbb{A}$ is positive definite and so is $4 - \mathbb{A} + \mathbb{B}_l(\mathbf{x})/m\Omega_P^2$, since the part with $\mathbb{B}_l(\mathbf{x})$ becomes arbitrarily small in the limit $P \to \infty$ and is thus irrelevant. This allows performing the Fourier transform in Eq. (S6) analytically, since the appearing integrals over the variables Δ_i possess a Gaussian form and are well defined, leading to the following result

$$A_l(\mathbf{x},\mathbf{p}) = \frac{D_f^g(x_l)\left|\det \mathbb{S}_l^{-1}\right|^{1/2}}{Z(2\pi\hbar)^P} \mathrm{e}^{-\beta[m\Omega_P^2 \mathbf{x}^{\mathrm{T}}\mathbb{A}\mathbf{x}/2 + U_l(\mathbf{x})]} \mathrm{e}^{-\frac{\beta}{2mP}\mathbf{p}^{\mathrm{T}}\mathbb{S}_l^{-1}\mathbf{p} + \frac{\mathrm{i}}{2\hbar}\mathbf{p}^{\mathrm{T}}\mathbb{S}_l^{-1}\mathbb{C}^{\mathrm{T}}\mathbf{x} + \beta\frac{m\Omega_P^2}{8}\mathbf{x}^{\mathrm{T}}\mathbb{C}\mathbb{S}_l^{-1}\mathbb{C}^{\mathrm{T}}\mathbf{x}}, \tag{S8}$$

where $\mathbb{S}_l = \mathbb{S}_l(\mathbf{x}) := (4 - \mathbb{A} + \mathbb{B}_l(\mathbf{x})/m\Omega_P^2)/4$.

In the next step we will introduce the normal mode coordinates of the free ring polymer, i.e. $\mathbf{Q} := \mathbb{T}\mathbf{x}/\sqrt{P}$ and $\mathbf{\Pi} := \mathbb{T}\mathbf{p}/\sqrt{P}$, where the orthogonal transformation matrix $\mathbb{T}$ diagonalizes $\mathbb{T}\mathbb{A}\mathbb{T}^{\mathrm{T}} = \tilde{\mathbb{A}}$, where $(\tilde{\mathbb{A}})_{r,s} = 4\sin^2(\pi r/P)\delta_{r,s}$ contains the eignenvalues of the ring polymer coupling matrix. The elements of $\mathbb{T}$ are analytically known to be

$$(\mathbb{T})_{r,i} = \begin{cases} 1/\sqrt{P}, & r = 0 \\ \sqrt{2/P}\cos(2\pi r i/P), & r < 0 \\ \sqrt{2/P}\sin(2\pi r i/P), & r > 0 \end{cases} \tag{S9}$$

with $-(P-1)/2 \leq r \leq (P-1)/2$ and $i = 0, \ldots, P-1$, see e.g. Ref. 1. Note that the normal mode indices are defined such that they run over $r, s = -(P-1)/2, \ldots, 0, \ldots, (P-1)/2$. Further we have specified P as an odd number without loosing generality since this number should tend to infinity anyway. Inserting these new variables leads after rearranging to

$$\tilde{A}_l(\mathbf{Q},\mathbf{\Pi}) = \frac{P^P D_f^g(x_l(\mathbf{Q}))\left|\det \tilde{\mathbb{S}}_l^{-1}\right|^{1/2}}{Z(2\pi\hbar)^P} \mathrm{e}^{-\beta\left[\frac{1}{2m}\mathbf{\Pi}^{\mathrm{T}}\tilde{\mathbb{S}}_l^{-1}\mathbf{\Pi} + \tilde{U}_l(\mathbf{Q})\right]} \mathrm{e}^{\frac{\mathrm{i}P}{2\hbar}\mathbf{\Pi}^{\mathrm{T}}\tilde{\mathbb{S}}_l^{-1}\tilde{\mathbb{C}}^{\mathrm{T}}\mathbf{Q} - \beta m\Omega_P^2 P\mathbf{Q}^{\mathrm{T}}(\tilde{\mathbb{A}} - \tilde{\mathbb{C}}\tilde{\mathbb{S}}_l^{-1}\tilde{\mathbb{C}}^{\mathrm{T}}/4)\mathbf{Q}/2}, \tag{S10}$$

where $\tilde{A}_l(\mathbf{Q},\mathbf{\Pi}) := P^P A_l(\mathbf{x}(\mathbf{Q}),\mathbf{p}(\mathbf{\Pi}))$ with P^P stemming from the substitution of the Cartesian volume element by the normal mode one, $\tilde{U}_l(\mathbf{Q}) := U_l(\mathbf{x}(\mathbf{Q}))$ and all matrices with a tilde are the normal mode versions of their Cartesian counterparts, see e.g. for $\tilde{\mathbb{A}}$ above.

II. INTEGRATING OUT THE NON-MATSUBARA MODES

In order to evaluate the time-independent part further, we assume that all physical quantities, in particular, the potential, the transition dipole moment as well as the time-dependent part do not significantly depend one the non-Matsubara modes. This assumption allows us to separate them from the Matsubara modes in the time-independent part and finally to integrate out the non-Matsubara modes as it will be shown in the following.

We start with the correlation function that becomes

$$C_\lambda(t) = \int \mathrm{d}\mathbf{Q} \int \mathrm{d}\mathbf{\Pi}\, \tilde{A}_l(\mathbf{Q},\mathbf{\Pi})\tilde{B}_l(\mathbf{Q}_M,\mathbf{\Pi}_M,t) \ , \tag{S11}$$

where $Q = Q_M + Q'$ stands for all modes whereas Q_M and Q' contain only the Matsubara modes and the non-Matsubara modes, respectively, which holds likewisely for the momenta. The time-independent part then reads

$$\begin{aligned}\tilde{A}_l(\mathbf{Q},\mathbf{\Pi}) = &\frac{P^P D_f^g(x_l(\mathbf{Q}_M))}{Z(2\pi\hbar)^P}\mathrm{e}^{-\beta\tilde{U}_l(\mathbf{Q}_M)} \\ &\times \left|\det\tilde{\mathbb{S}}_l^{-1}\right|^{1/2}\mathrm{e}^{-\frac{\beta}{2m}\mathbf{\Pi}^{\mathrm{T}}\tilde{\mathbb{S}}_l^{-1}\mathbf{\Pi}+\frac{\mathrm{i}P}{2\hbar}\mathbf{\Pi}^{\mathrm{T}}\tilde{\mathbb{S}}_l^{-1}\tilde{\mathbb{C}}^{\mathrm{T}}\mathbf{Q}-\beta m\Omega_P^2 P\mathbf{Q}^{\mathrm{T}}(\tilde{\mathbb{A}}-\tilde{\mathbb{C}}\tilde{\mathbb{S}}_l^{-1}\tilde{\mathbb{C}}^{\mathrm{T}}/4)\mathbf{Q}/2} \ ,\end{aligned} \tag{S12}$$

where each of the appearing matrices will now be examined.

First, one can show that $\tilde{\mathbb{S}}^{-1}$ is of diagonal form as $P\to\infty$ if all terms are neglected that decrease at least as $1/P^2$. The elements of the matrix $\tilde{\mathbb{S}}$ can be written down as $(\tilde{\mathbb{S}})_{r,s} = (4-4\sin^2(\pi r/P)\delta_{r,s} + (\tilde{\mathbb{B}}_l)_{r,s}/m\Omega_P^2)/4$, where $(\tilde{\mathbb{B}}_l)_{r,s} = \sum_i(\mathbb{T})_{r,i}(\mathbb{T})_{s,i}\partial^2 U_l(\mathbf{x})/\partial x_i^2 \propto 1/P$ which is a consequence of the $1/\sqrt{P}$ in the elements of $\mathbb{T}$ and the $1/P$ in the definition of $U_l(\mathbf{x})$. Due to the additional factor $\Omega_P^2 \propto P$ in the denominator, the term with $\tilde{\mathbb{B}}_l$ tends to zero as $1/P^2$ and is thus negligible if P grows to infinity. The remaining term is then $(\tilde{\mathbb{S}})_{r,s} = \cos^2(\pi r/P)\delta_{r,s}$, where we have used a trigonometric identity. The inverse is consequently $(\tilde{\mathbb{S}}^{-1})_{r,s} = \cos^{-2}(\pi r/P)\delta_{r,s}$ which becomes $(\tilde{\mathbb{S}}^{-1})_{r,s} = \delta_{r,s}$ in the case that $|r|,|s| \ll (P-1)/2$, i.e. for the Matsubara modes. Owing to the diagonal form of $\tilde{\mathbb{S}}^{-1}$ the kinetic part can be now separated into $\mathbf{\Pi}^{\mathrm{T}}\tilde{\mathbb{S}}_l^{-1}\mathbf{\Pi} = \mathbf{\Pi}_M^{\mathrm{T}}\mathbf{\Pi}_M + \mathbf{\Pi}'^{\mathrm{T}}\tilde{\mathbb{S}}_l'^{-1}\mathbf{\Pi}'$, where $\tilde{\mathbb{S}}_l'^{-1}$ is a $(P-M)\times(P-M)$ matrix containing only elements that correspond to non-Matsubara modes. Moreover, one can write $\det\tilde{\mathbb{S}}_l^{-1} = 1^M\det\tilde{\mathbb{S}}_l'^{-1} = \det\tilde{\mathbb{S}}_l'^{-1}$.

Second, the elements of $P\cdot\tilde{\mathbb{C}}$ are analysed. Immediately one can see that all diagonal elements must vanish, since $(\mathbb{C})_{i,j} = \delta_{i,j+1} - \delta_{i+1,j}$ is anti-symmetric and so is the orthogonal

transformation

$$(\tilde{\mathbb{C}})_{r,s} = \sum_{i=0}^{P-1} (\mathbb{T})_{r,i}[(\mathbb{T})_{s,i-1} - (\mathbb{T})_{s,i+1}] \ . \tag{S13}$$

For the elements $P \cdot \tilde{\mathbb{C}}_{0,s}$ with $s < 0$ one gets via inserting $(\mathbb{T})_{0,i} = 1/\sqrt{P}$ and $(\mathbb{T})_{s,i-1} - (\mathbb{T})_{s,i+1} = \sqrt{2/P}[\cos(2\pi s(i-1)/P) - \cos(2\pi s(i+1)/P)] = 2\sqrt{2/P}\sin(2\pi s/P)\sin(2\pi si/P)$

$$P \cdot \tilde{\mathbb{C}}_{0,s} = 2P\sin(2\pi s/P)\sum_{i=0}^{P-1}\sqrt{\frac{1}{P}}\sqrt{\frac{2}{P}}\sin(2\pi si/P) = \tag{S14}$$

$$= 2P\sin(2\pi s/P)(\mathbb{T}\mathbb{T}^{\mathrm{T}})_{0,-s} = 2P\sin(2\pi s/P)\delta_{0,-s} \tag{S15}$$

$$= 0 \tag{S16}$$

since $\mathbb{T}$ is orthogonal and $s < 0$ and, thus, the Kronecker delta is never equal to one. Following the same line of reasoning one obtains for $s > 0$

$$P \cdot \tilde{\mathbb{C}}_{0,s} = -2P\sin(2\pi s/P)\delta_{0,-s} = 0 \tag{S17}$$

For the next combination, $r < 0$ and $s < 0$, with $(\mathbb{T})_{r,i} = \sqrt{2/P}\cos(2\pi ri/P)$ one obtains

$$P \cdot \tilde{\mathbb{C}}_{r,s} = 2P\sin(2\pi s/P)\sum_{i=0}^{P-1}\sqrt{\frac{2}{P}}\cos(2\pi ri/P)\sqrt{\frac{2}{P}}\sin(2\pi si/P) = \tag{S18}$$

$$= 2P\sin(2\pi s/P)\delta_{r,-s} = 0 \ , \tag{S19}$$

since r and s have the same sign. Similarly we get for $r > 0$ and $s > 0$

$$P \cdot \tilde{\mathbb{C}}_{r,s} = -2P\sin(2\pi s/P)\sum_{i=0}^{P-1}\sqrt{\frac{2}{P}}\sin(2\pi ri/P)\sqrt{\frac{2}{P}}\cos(2\pi si/P) = \tag{S20}$$

$$= -2P\sin(2\pi s/P)\delta_{r,-s} = 0 \ . \tag{S21}$$

Lastly, for $r < 0$, $s > 0$ one obtains

$$P \cdot \tilde{\mathbb{C}}_{r,s} = 2P\sin(2\pi s/P)\sum_{i=0}^{P-1}\sqrt{\frac{2}{P}}\cos(2\pi ri/P)\sqrt{\frac{2}{P}}\sin(2\pi si/P) = \tag{S22}$$

$$= 2P\sin(2\pi s/P)\delta_{r,-s} \ , \tag{S23}$$

which can now be non-vanishing since r and s have opposite signs. Similarly, one gets for the remaining case, i.e. $r > 0$, $s < 0$,

$$P \cdot \tilde{\mathbb{C}}_{r,s} = -2P\sin(2\pi s/P)\delta_{r,-s} = 2P\sin(2\pi r/P)\delta_{r,-s} \ . \tag{S24}$$

Finally, the matrix $P\cdot\tilde{\mathbb{C}}_{r,s}$ turns out to be an anti-diagnonal with elements tending to $P\cdot\tilde{\mathbb{C}}_{r,s}=4\pi r\delta_{r,-s}$ if $|r|,|s|\ll(P-1)/2$. Importantly, the matrix $P\cdot\tilde{\mathbb{C}}$ does not couple Matsubara and non-Matsubara modes which still holds for the products

$$P\cdot(\tilde{\mathbb{S}}_l^{-1}\tilde{\mathbb{C}}^{\mathrm{T}})_{r,s}=-\frac{2P\sin(2\pi r/P)}{\cos^2(\pi r/P)}\delta_{r,-s} \tag{S25}$$

and

$$P^2\cdot(\tilde{\mathbb{C}}\tilde{\mathbb{S}}_l^{-1}\tilde{\mathbb{C}}^{\mathrm{T}})_{r,s}=\frac{4P^2\sin^2(2\pi r/P)}{\cos^2(\pi r/P)}\delta_{r,s} \tag{S26}$$

as it can be easily verified. Interestingly, if we restrict ourselves to the Matsubara modes, i.e. $|r|,|s|\ll(P-1)/2$, the first product matrix tends to $P\cdot(\tilde{\mathbb{S}}_l^{-1}\tilde{\mathbb{C}}^{\mathrm{T}})_{r,s}=-4\pi r\delta_{r,-s}$ which corresponds up to prefactor of $-2/\beta\hbar$ to the Matsubara frequencies $\omega_r=2\pi r/\beta\hbar$. Whereas, the second products tends to $P^2\cdot(\tilde{\mathbb{C}}\tilde{\mathbb{S}}_l^{-1}\tilde{\mathbb{C}}^{\mathrm{T}})_{r,s}=16\pi^2r^2\delta_{r,s}$ which corresponds to $4\tilde{\mathbb{A}}$ in the Matsubara space, consequently, the term $\tilde{\mathbb{A}}-\tilde{\mathbb{C}}\tilde{\mathbb{S}}_l^{-1}\tilde{\mathbb{C}}^{\mathrm{T}}/4$ vanishes for the Matsubara modes.

The analysis has shown that none of matrices couples the Matsubara and the non-Matsubara modes, which allows us to separate them from each other and ultimately to integrate out the non-Matsubara ones. We can now write $\tilde{A}_l(\mathbf{Q},\mathbf{\Pi})=\tilde{A}'_l(\mathbf{Q}',\mathbf{\Pi}')\tilde{A}_l^M(\mathbf{Q}_M,\mathbf{\Pi}_M)$, where

$$\tilde{A}'_l(\mathbf{Q}',\mathbf{\Pi}'):=\frac{P^P\left|\det\tilde{\mathbb{S}}_l'^{-1}\right|^{1/2}}{(2\pi\hbar)^P}\mathrm{e}^{-\frac{\beta}{2m}\mathbf{\Pi}'^{\mathrm{T}}\tilde{\mathbb{S}}_l'^{-1}\mathbf{\Pi}'+\frac{\mathrm{i}P}{2\hbar}\mathbf{\Pi}'^{\mathrm{T}}\tilde{\mathbb{S}}_l'^{-1}\tilde{\mathbb{C}}'^{\mathrm{T}}\mathbf{Q}'-\beta m\Omega_P^2P\mathbf{Q}'^{\mathrm{T}}(\tilde{\mathbb{A}}'-\tilde{\mathbb{C}}'\tilde{\mathbb{S}}_l'^{-1}\tilde{\mathbb{C}}'^{\mathrm{T}}/4)\mathbf{Q}'/2}\ . \tag{S27}$$

and

$$\tilde{A}_l^M(\mathbf{Q}_M,\mathbf{\Pi}_M)=\frac{D_f^g(x_l(\mathbf{Q}_M))}{Z}\mathrm{e}^{-\beta[\frac{1}{2m}\mathbf{\Pi}_M^{\mathrm{T}}\mathbf{\Pi}_M+\tilde{U}_l(\mathbf{Q}_M)+\mathrm{i}\mathbf{\Pi}_M^{\mathrm{T}}\mathbb{W}\mathbf{Q}_M]}\ , \tag{S28}$$

with $\mathbb{W}:=-P\tilde{\mathbb{S}}_l^{-1}\tilde{\mathbb{C}}^{\mathrm{T}}/2\hbar\beta$ containing the Matsubara frequencies $(\mathbb{W})_{r,s}=\omega_r\delta_{r,-s}$. First, we integrate out the $P-M$ momentum variables of the non-Matsubara modes using standard Gaussian integrals

$$\frac{P^P\left|\det\tilde{\mathbb{S}}_l'^{-1}\right|^{1/2}}{(2\pi\hbar)^P}\int\mathrm{d}\mathbf{\Pi}'\,\mathrm{e}^{-\frac{\beta}{2m}\mathbf{\Pi}'^{\mathrm{T}}\tilde{\mathbb{S}}_l'^{-1}\mathbf{\Pi}'+\frac{\mathrm{i}P}{2\hbar}\mathbf{\Pi}'^{\mathrm{T}}\tilde{\mathbb{S}}_l'^{-1}\tilde{\mathbb{C}}'^{\mathrm{T}}\mathbf{Q}'} \tag{S29}$$

$$=\frac{P^P\left|\det\tilde{\mathbb{S}}_l'^{-1}\right|^{1/2}}{(2\pi\hbar)^P}\frac{(2m\pi/\beta)^{(P-M)/2}}{\left|\det\tilde{\mathbb{S}}_l'^{-1}\right|^{1/2}}\mathrm{e}^{-\frac{\beta}{4}mP^2\mathbf{Q}'^{\mathrm{T}}\tilde{\mathbb{C}}'\tilde{\mathbb{S}}_l'^{-1}\tilde{\mathbb{C}}'^{\mathrm{T}}\mathbf{Q}'/2\hbar^2\beta^2} \tag{S30}$$

$$=\frac{P^P(2m\pi/\beta)^{(P-M)/2}}{(2\pi\hbar)^P}\mathrm{e}^{-\frac{\beta}{8}m\Omega_P^2P\mathbf{Q}'^{\mathrm{T}}\tilde{\mathbb{C}}'\tilde{\mathbb{S}}_l'^{-1}\tilde{\mathbb{C}}'^{\mathrm{T}}\mathbf{Q}'}\ . \tag{S31}$$

Since the terms with $\tilde{\mathbb{C}}'\tilde{\mathbb{S}}_l'^{-1}\tilde{\mathbb{C}}'^{\mathrm{T}}$ exactly cancel each other, only the term with $\tilde{\mathbb{A}}$ remains for the spatial non-Matsubara modes, which becomes after integration

$$\int \mathrm{d}\mathbf{Q}' \, \frac{P^P (2m\pi/\beta)^{(P-M)/2}}{(2\pi\hbar)^P} \mathrm{e}^{-\frac{\beta}{2} m\Omega_P^2 P \mathbf{Q}'^{\mathrm{T}} \tilde{\mathbb{A}} \mathbf{Q}'} = \frac{P^P (2m\pi/\beta)^{(P-M)/2}}{(2\pi\hbar)^P} \frac{(2\pi\beta\hbar^2)^{(P-M)/2}}{(mP^2)^{(P-M)/2}\sqrt{\det \tilde{\mathbb{A}}'}} \tag{S32}$$

$$= \frac{P^M}{(2\pi\hbar)^M \sqrt{\det \tilde{\mathbb{A}}'}} \ . \tag{S33}$$

Since $\tilde{\mathbb{A}}$ is diagonal one can immediately write down with $\bar{P} := (P-1)/2$ and $\bar{M} := (M-1)/2$

$$\sqrt{\det \tilde{\mathbb{A}}'} = \sqrt{\prod_{r=-\bar{P}}^{-(\bar{M}+1)} 4\sin^2(\pi r/P) \prod_{r=\bar{M}+1}^{\bar{P}} 4\sin^2(\pi r/P)} \tag{S34}$$

$$\overset{\sin^2(x) \text{ is even}}{=} 4^{\bar{P}-\bar{M}} \left[\prod_{r=\bar{M}+1}^{\bar{P}} \sin(\pi r/P)\right]^2 = 4^{\bar{P}-\bar{M}} \left[\prod_{r=1}^{\bar{P}} \sin(\pi r/P) / \prod_{r=1}^{\bar{M}} \sin(\pi r/P)\right]^2 \tag{S35}$$

$$\overset{\text{sine symmetric around } \bar{\mathrm{P}}}{=} 4^{\bar{P}-\bar{M}} \prod_{r=1}^{P-1} \sin(\pi r/P) / \left[\prod_{r=1}^{\bar{M}} \sin(\pi r/P)\right]^2 \tag{S36}$$

$$\overset{M \ll P}{=} 4^{\bar{P}-\bar{M}} \frac{P}{2^{P-1}} / \left[\prod_{r=1}^{\bar{M}} \pi r/P\right]^2 = 4^{\bar{P}-\bar{M}} \frac{P}{2^{P-1}} P^{2\bar{M}} / \pi^{2\bar{M}} \bar{M}!^2 = 2\pi \frac{P^M}{(2\pi)^M \bar{M}!^2} \ , \tag{S37}$$

$$\tag{S38}$$

where the last line is obtained by employing the identity $\prod_{r=1}^{P-1} \sin(\pi r/P) = P/2^{P-1}$, see e.g. Ref. 1. Bringing everything together yields

$$\int \mathrm{d}\mathbf{Q}' \mathrm{d}\mathbf{\Pi}' \, \tilde{A}_l'(\mathbf{Q}', \mathbf{\Pi}') = \frac{\bar{M}!^2}{2\pi\hbar^M} \ . \tag{S39}$$

III. TIME EVOLUTION OF THE MATSUBARA PHASE

In contrast to the single electronic state problem, the Matsubara phase is not trivially constant as it will become clear by considering its time derivative

$$\frac{\mathrm{d}}{\mathrm{d}\tau} \mathbf{\Pi}(\tau)^{\mathrm{T}} \mathbb{W} \mathbf{Q}(\tau) = \frac{1}{m} \mathbf{\Pi}(\tau)^{\mathrm{T}} \mathbb{W} \mathbf{\Pi}(\tau) - [\boldsymbol{\nabla}_{\mathbf{Q}(\tau)}^{\mathrm{T}} \tilde{\mathcal{U}}_l(\mathbf{Q}(\tau))] \mathbb{W} \mathbf{Q}(\tau) \tag{S40}$$

where we have used Hamilton's equations of motion (EOMs) that correspond to the equilibrium method. Although it is straightforward to show that the momentum part vanishes, since $\mathbb{W}$ is antisymmetric, one can find that the potential part does not vanish as it is demonstrated in the following.

The term $[\boldsymbol{\nabla}_{\mathbf{Q}}^{\mathrm{T}}\tilde{\mathcal{U}}_l(\mathbf{Q})]\mathbb{W}\mathbf{Q}$ can be rewritten as

$$[\boldsymbol{\nabla}_{\mathbf{Q}}^{\mathrm{T}}\tilde{\mathcal{U}}_l(\mathbf{Q})]\mathbb{W}\mathbf{Q} = \lim_{P\to\infty}\frac{1}{P}[\boldsymbol{\nabla}_{\mathbf{Q}}^{\mathrm{T}}\tilde{\mathcal{U}}_l(\mathbf{Q})]\mathbb{T}P\mathbb{T}^{\mathrm{T}}\mathbb{W}\mathbf{Q} \tag{S41}$$

$$= \lim_{P\to\infty}\frac{1}{P}\sum_{i=0}^{P-1}(\sqrt{P}\mathbb{T}^{\mathrm{T}}\boldsymbol{\nabla}_{\mathbf{Q}}\tilde{\mathcal{U}}_l(\mathbf{Q}))_i(\sqrt{P}\mathbb{T}^{\mathrm{T}}\mathbb{W}\mathbf{Q})_i \ , \tag{S42}$$

which holds for any time τ and, thus, the time argument is skipped. First, one can recognize that the left term represents

$$(\sqrt{P}\mathbb{T}^{\mathrm{T}}\boldsymbol{\nabla}_{\mathbf{Q}}\tilde{\mathcal{U}}_l(\mathbf{Q}))_i = \frac{\partial\mathcal{V}_l(x_i)}{\partial x_i} \ . \tag{S43}$$

where we have used $\sqrt{P}\mathbb{T}^{\mathrm{T}}\boldsymbol{\nabla}_{\mathbf{Q}} = \boldsymbol{\nabla}_{\mathbf{x}}$ and $\mathcal{V}_l(x_i)$ stands for $V_f(x_i)$ if $0 < i < l$, $V_g(x_i)$ if $l < i \leq P-1$ and $(V_g(x_i)+V_f(x_i))/2$ if $i = 0, l$. Second, the right term can be written down as

$$(\sqrt{P}\mathbb{T}^{\mathrm{T}}\mathbb{W}\mathbf{Q})_i = \sum_{r=-\bar{M}}^{-1}\sqrt{2}\omega_r\cos(\omega_r i\beta\hbar/P)Q_{-r} + \sum_{r=1}^{\bar{M}}\sqrt{2}\omega_r\sin(\omega_r i\beta\hbar/P)Q_{-r} \ , \tag{S44}$$

where the definition of $\mathbb{T}$ and $\mathbb{W}$ has been used. By comparing the last expression to the imaginary time derivative

$$\frac{\partial x_\mu}{\partial\mu} = \frac{\partial}{\partial\mu}\lim_{P\to\infty}x_i = \frac{\partial}{\partial\mu}\left[Q_0 + \sum_{r=-\bar{M}}^{-1}\sqrt{2}\cos(\omega_r\mu\hbar)Q_r + \sum_{r=1}^{\bar{M}}\sqrt{2}\sin(\omega_r\mu\hbar)Q_r\right] \tag{S45}$$

$$= \hbar\left[-\sum_{r=-\bar{M}}^{-1}\sqrt{2}\omega_r\sin(\omega_r\mu\hbar)Q_r + \sum_{r=1}^{\bar{M}}\sqrt{2}\omega_r\cos(\omega_r\mu\hbar)Q_r\right] \tag{S46}$$

$$= \hbar\left[-\sum_{r=1}^{\bar{M}}-\sqrt{2}\omega_r\sin(-\omega_r\mu\hbar)Q_{-r} - \sum_{r=-\bar{M}}^{-1}\sqrt{2}\omega_r\cos(-\omega_r\mu\hbar)Q_{-r}\right] \tag{S47}$$

$$= -\hbar\left[\sum_{r=1}^{\bar{M}}\sqrt{2}\omega_r\sin(\omega_r\mu\hbar)Q_{-r} + \sum_{r=-\bar{M}}^{-1}\sqrt{2}\omega_r\cos(\omega_r\mu\hbar)Q_{-r}\right] \tag{S48}$$

$$= -\hbar\lim_{P\to\infty}(\sqrt{P}\mathbb{T}^{\mathrm{T}}\mathbb{W}\mathbf{Q})_i \ , \tag{S49}$$

where $\mu = i\beta/P$ is imposed, we see that both coincide up to a constant prefactor. Bringing both parts together yields

$$[\boldsymbol{\nabla}_{\mathbf{Q}}^{\mathrm{T}}\tilde{\mathcal{U}}_l(\mathbf{Q})]\mathbb{W}\mathbf{Q} = -\frac{1}{\beta\hbar}\int_0^\beta \mathrm{d}\mu \frac{\partial \mathcal{V}_\lambda(x_\mu)}{\partial x_\mu}\frac{\partial x_\mu}{\partial \mu} \ , \tag{S50}$$

where $\mathcal{V}_\lambda(x_\mu) = V_f(x_\mu)\theta(\lambda-\mu) + V_g(x_\mu)\theta(\mu-\lambda)$ is the continuous counterpart of $\mathcal{V}_l(x_i)$ with $\theta(\mu)$ being the Heaviside step function. Employing now the properties of the step function one obtains

$$\int_0^\beta \mathrm{d}\mu \frac{\partial \mathcal{V}_\lambda(x_\mu)}{\partial x_\mu}\frac{\partial x_\mu}{\partial \mu} = \int_0^\lambda \mathrm{d}\mu \frac{\partial V_f(x_\mu)}{\partial x_\mu}\frac{\partial x_\mu}{\partial \mu} + \int_\lambda^\beta \mathrm{d}\mu \frac{\partial V_g(x_\mu)}{\partial x_\mu}\frac{\partial x_\mu}{\partial \mu} \ . \tag{S51}$$

Since $V_f(x)$ and $V_g(x)$ are assumed to be smooth functions of the coordinate, one can use the chain rule of differentiation twice, which leads to

$$[\boldsymbol{\nabla}_{\mathbf{Q}}^{\mathrm{T}}\tilde{\mathcal{U}}_l(\mathbf{Q})]\mathbb{W}\mathbf{Q} = -\frac{1}{\beta\hbar}\left(V_f(x_l) - V_f(x_0) + V_g(x_0) - V_g(x_l)\right) \ , \tag{S52}$$

where the cyclicality of the imaginary-time path has been used and $x_l = x_\lambda$. Finally one can write the time derivative of the Matsubara phase as

$$\frac{\mathrm{d}}{\mathrm{d}\tau}\boldsymbol{\Pi}(\tau)^{\mathrm{T}}\mathbb{W}\mathbf{Q}(\tau) = \frac{1}{\beta\hbar}\left(V_f(x_l(\tau)) - V_g(x_l(\tau)) - [V_f(x_0(\tau)) - V_g(x_0(\tau))]\right) \tag{S53}$$

where the time arguments have been restored. In order to invert the time derivative one can integrate over time yielding

$$\boldsymbol{\Pi}(\tau)^{\mathrm{T}}\mathbb{W}\mathbf{Q}(\tau) = \boldsymbol{\Pi}^{\mathrm{T}}\mathbb{W}\mathbf{Q} + \frac{1}{\beta\hbar}\int_0^\tau \left(V_f(x_l(t')) - V_g(x_l(t')) - [V_f(x_0(t')) - V_g(x_0(t'))]\right)\mathrm{d}t' \ . \tag{S54}$$

Since the gap between the potentials is not vanishing, the phase varies in time and so does the density. If, in contrast, $V_g = V_f$, the phase and, thus, the density remain constant.

IV. CORRELATION FUNCTIONS FOR TWO SHIFTED HARMONIC OSCILLATORS

In this section the analytical results for the model system consisting of two shifted harmonic potential energy surfaces (PESs) will be derived for various methods. Specifically, we choose $V_g(x) = m\omega^2 x^2/2$ and $V_f(x) = m\omega^2(x-x_f)^2/2$, where both PESs have the same harmonic frequency ω. Consequently the energy gap is a linear function of the coordinate

and can be written as $V_f(x) - V_g(x) = ax + \varepsilon$. If the Condon approximation is valid, i.e. $D_g^f(x) \approx 1$, then the exact quantum mechanical (QM) imaginary time shifted correlation function for such a system reads

$$C_\lambda(t) = \exp\left\{ -\frac{\mathrm{i}a^2}{2m\hbar\omega^2}t + \frac{a^2}{2m\omega^2}\lambda + \frac{\mathrm{i}\varepsilon}{\hbar}t - \varepsilon\lambda - \frac{a^2\coth(\beta\hbar\omega/2)}{2m\hbar\omega^3} \right.$$
$$\left. + \frac{\mathrm{i}a^2}{2m\hbar\omega^3}\sin(\omega t)\frac{\sinh(\beta\hbar\omega/2 - \omega\lambda\hbar)}{\sinh(\beta\hbar\omega/2)} + \frac{a^2}{2m\hbar\omega^3}\cos(\omega t)\frac{\cosh(\beta\hbar\omega/2 - \omega\lambda\hbar)}{\sinh(\beta\hbar\omega/2)} \right\} . \tag{S55}$$

Note that this expression can be obtained e.g. from Ref. 2 by substituting $t \to t + \mathrm{i}\lambda\hbar$ in the standard correlation function, $C_0(t)$, and subsequently using addition theorems for (hyperbolic) sine and cosine functions.

A. Matsubara dynamics

First, the correlation function resulting from the Matsubara approximation is examined which takes the form

$$C_\lambda(t) \approx \frac{\bar{M}!^2}{2\pi\hbar^M Z}\int \mathrm{d}\mathbf{Q}\int \mathrm{d}\mathbf{\Pi}\, \mathrm{e}^{-\beta\left[\frac{1}{2m}\mathbf{\Pi}^{\mathrm{T}}\mathbf{\Pi} + U_l(\mathbf{Q}) + \mathrm{i}\mathbf{Q}^{\mathrm{T}}\mathbb{W}\mathbf{\Pi}\right]}\mathrm{e}^{\frac{\mathrm{i}}{\hbar}\int_0^t a x_0(\tau)\mathrm{d}\tau}\mathrm{e}^{\mathrm{i}\varepsilon t/\hbar} , \tag{S56}$$

where the potential in the density is

$$U_l(\mathbf{x}) = \frac{1}{P}\sum_{i=0}^{l}\kappa_i V_f(x_i) + \frac{1}{P}\sum_{i=l}^{P}\kappa_i V_g(x_i) = \frac{1}{2}m\omega^2\mathbf{Q}^{\mathrm{T}}\mathbf{Q} + \frac{a}{2P}\mathbf{G}_l^{\mathrm{T}}\mathbf{Q} + \varepsilon\frac{l}{P} = \tilde{U}_l(\mathbf{Q}) , \tag{S57}$$

with

$$\mathbf{G}_l = 2\sqrt{P}\mathbb{T}(\underbrace{1/2}_{i=0}, 1, \ldots, 1, \underbrace{1/2}_{i=l}, 0, \ldots, \underbrace{0}_{i=P-1})^{\mathrm{T}} \tag{S58}$$

$$= 2(\underbrace{\ldots, \sqrt{2}\sum_{i=0}^{l}\kappa_i\cos(2\pi i r/P), \ldots,}_{-\bar{M}\le r<0} \underbrace{l}_{r=0} \underbrace{, \ldots, \sqrt{2}\sum_{i=0}^{l}\kappa_i\sin(2\pi i r/P), \ldots)^{\mathrm{T}}}_{0<r\le\bar{M}} \tag{S59}$$

for $0 < l < P$ and $\mathbf{G}_0 = \mathbf{0}$, $\mathbf{G}_P = 2\sqrt{P}\mathbb{T}(1, \ldots, 1)^{\mathrm{T}} = (0, \ldots, 0, 2P, 0, \ldots, 0)^{\mathrm{T}}$, see definition of $\mathbb{T}$ in Eq. (S9). It is important to note that, after the restriction to the Matsubara modes, the vector $\mathbf{G}_l$ has only M elements and not P. The dynamics is generated with respect to

$$\tilde{\mathcal{U}}_l(\mathbf{Q}) = \frac{1}{2}m\omega^2\mathbf{Q}^{\mathrm{T}}\mathbf{Q} + \frac{a}{2P}\boldsymbol{\mathcal{G}}_l^{\mathrm{T}}\mathbf{Q} + \text{const.} , \tag{S60}$$

where the constant stems from the shift ε and the vector $\boldsymbol{\mathcal{G}}_l$ naturally depends on the choice of the EOMs as discussed in Sec. II E in the main text. For the equilibrium method, one gets $\boldsymbol{\mathcal{G}}_l = \mathbf{G}_l$ if $0 < l < P$, otherwise $\boldsymbol{\mathcal{G}}_0 = 2\sqrt{P}\mathbb{T}(1/2, 0, \ldots, 0)^{\mathrm{T}} = (\sqrt{2}, \ldots, \sqrt{2}, 1, 0, \ldots, 0)^{\mathrm{T}}$ and $\boldsymbol{\mathcal{G}}_P = 2\sqrt{P}\mathbb{T}(1/2, 1, \ldots, 1)^{\mathrm{T}} = (-\sqrt{2}, \ldots, -\sqrt{2}, 2P-1, 0, \ldots, 0)^{\mathrm{T}}$. In contrast, for the average method, the vector is independent on the value of l, namely $\boldsymbol{\mathcal{G}}_l = (0, \ldots, 0, P, 0, \ldots, 0)^{\mathrm{T}}$. It is straightforward to prove that for both choices of the dynamics, the resulting EOMs for the Matsubara modes have the following solution

$$\mathbf{Q}(\tau) = \mathbf{Q}\cos(\omega\tau) + \frac{\mathbf{\Pi}}{m\omega}\sin(\omega\tau) + \frac{a}{2m\omega^2 P}[\cos(\omega\tau) - 1]\boldsymbol{\mathcal{G}}_l \tag{S61}$$

This leads directly to the time evolution of $x_0(\tau) = \mathbf{F}^{\mathrm{T}}\mathbf{Q}(\tau)$, where $\mathbf{F} = 2\sqrt{P}\mathbb{T}(1/2, 0, \ldots, 0)^{\mathrm{T}} = (\sqrt{2}, \ldots, \sqrt{2}, 1, 0, \ldots, 0)^{\mathrm{T}}$, which can be integrated as

$$\int_0^t \mathrm{d}\tau \mathbf{F}^{\mathrm{T}}\mathbf{Q}(\tau) = \frac{\mathbf{F}^{\mathrm{T}}\mathbf{Q}}{\omega}\sin(\omega t) - \frac{\mathbf{F}^{\mathrm{T}}\mathbf{\Pi}}{m\omega^2}[\cos(\omega t) - 1] + \frac{a}{2Pm\omega^3}[\sin(\omega t) - \omega t]\mathbf{F}^{\mathrm{T}}\boldsymbol{\mathcal{G}}_l \ . \tag{S62}$$

After inserting this into the correlation function

$$\begin{aligned} C_\lambda(t) = & \\ & \frac{\bar{M}!^2}{2\pi\hbar^M Z}\mathrm{e}^{\mathrm{i}\varepsilon t/\hbar - \varepsilon\beta l/P}\mathrm{e}^{\mathrm{i}a^2[\sin(\omega t) - \omega t]\mathbf{F}^{\mathrm{T}}\boldsymbol{\mathcal{G}}_l/2P\hbar m\omega^3}\int \mathrm{d}\mathbf{Q}\int \mathrm{d}\mathbf{\Pi}\,\mathrm{e}^{-\beta\left[\frac{1}{2m}\mathbf{\Pi}^{\mathrm{T}}\mathbf{\Pi} + \frac{1}{2}m\omega^2\mathbf{Q}^{\mathrm{T}}\mathbf{Q} + \frac{a}{2P}\mathbf{G}_l^{\mathrm{T}}\mathbf{Q} + \mathrm{i}\mathbf{Q}^{\mathrm{T}}\mathbb{W}\mathbf{\Pi}\right]} \\ & \times \exp\left\{\frac{\mathrm{i}a\mathbf{F}^{\mathrm{T}}\mathbf{Q}}{\hbar\omega}\sin(\omega t) - \frac{\mathrm{i}a\mathbf{F}^{\mathrm{T}}\mathbf{\Pi}}{\hbar m\omega^2}[\cos(\omega t) - 1]\right\} \ , \end{aligned} \tag{S63}$$

the remaining task is to evaluate multi-dimensional Gaussian integrals. Performing the integral over the coordinates yields

$$\begin{aligned} & \int \mathrm{d}\mathbf{Q}\mathrm{e}^{-\beta\left[\frac{1}{2}m\omega^2\mathbf{Q}^{\mathrm{T}}\mathbf{Q} + \frac{a}{2P}\mathbf{G}_l^{\mathrm{T}}\mathbf{Q} + \mathrm{i}\mathbf{Q}^{\mathrm{T}}\mathbb{W}\mathbf{\Pi}\right] + \frac{\mathrm{i}a\mathbf{F}^{\mathrm{T}}\mathbf{Q}}{\hbar\omega}\sin(\omega t)} = \left(\frac{2\pi}{m\omega^2\beta}\right)^{M/2} \\ & \times \exp\left\{\frac{\beta a^2}{8P^2 m\omega^2}\mathbf{G}_l^{\mathrm{T}}\mathbf{G}_l - \frac{a^2}{2\beta m\hbar^2\omega^4}\sin^2(\omega t)\mathbf{F}^{\mathrm{T}}\mathbf{F} - \frac{\mathrm{i}a^2}{2Pm\hbar\omega^3}\mathbf{F}^{\mathrm{T}}\mathbf{G}_l\sin(\omega t)\right\} \\ & \times \exp\left\{-\frac{\beta}{2m\omega^2}\mathbf{\Pi}^{\mathrm{T}}\mathbb{W}^{\mathrm{T}}\mathbb{W}\mathbf{\Pi} + \frac{a\sin(\omega t)}{m\hbar\omega^3}\mathbf{F}^{\mathrm{T}}\mathbb{W}\mathbf{\Pi} + \frac{\mathrm{i}a\beta}{2Pm\omega^2}\mathbf{G}_l^{\mathrm{T}}\mathbb{W}\mathbf{\Pi}\right\} \ . \end{aligned} \tag{S64}$$

Subsequently one can integrate over the momenta leading to

$$\int \mathrm{d}\mathbf{\Pi} \mathrm{e}^{-\beta\left[\frac{1}{2m}\mathbf{\Pi}^{\mathrm{T}}(1+\mathbb{W}^{\mathrm{T}}\mathbb{W}/\omega^2)\mathbf{\Pi}\right]} \exp\left\{\frac{a\sin(\omega t)}{m\hbar\omega^3}\mathbf{F}^{\mathrm{T}}\mathbb{W}\mathbf{\Pi} + \frac{\mathrm{i}a\beta}{2Pm\omega^2}\mathbf{G}_l^{\mathrm{T}}\mathbb{W}\mathbf{\Pi} - \frac{\mathrm{i}a\mathbf{F}^{\mathrm{T}}\mathbf{\Pi}}{\hbar m\omega^2}[\cos(\omega t)-1]\right\} =$$
$$\left(\frac{2\pi m\omega^2}{\beta}\right)^{M/2}\left[\prod_{r=-\bar{M}}^{\bar{M}}\omega^2+\omega_r^2\right]^{-1/2}\exp\left\{\frac{a^2\sin^2(\omega t)}{4m^2\hbar^2\omega^6}\mathbf{F}^{\mathrm{T}}\mathbb{W}\mathbb{M}^{-1}\mathbb{W}^{\mathrm{T}}\mathbf{F} - \frac{a^2\beta^2}{16P^2m^2\omega^4}\mathbf{G}_l^{\mathrm{T}}\mathbb{W}\mathbb{M}^{-1}\mathbb{W}^{\mathrm{T}}\mathbf{G}_l\right\}$$
$$\times\exp\left\{-\frac{a^2}{4\hbar^2m^2\omega^4}[\cos(\omega t)-1]^2\mathbf{F}^{\mathrm{T}}\mathbb{M}^{-1}\mathbf{F} + \frac{\mathrm{i}a^2\beta}{4Pm^2\hbar\omega^5}\sin(\omega t)\mathbf{F}^{\mathrm{T}}\mathbb{W}\mathbb{M}^{-1}\mathbb{W}^{\mathrm{T}}\mathbf{G}_l\right\}$$
$$\times\exp\left\{\frac{a^2\beta}{2Pm^2\hbar\omega^4}[\cos(\omega t)-1]\mathbf{G}_l^{\mathrm{T}}\mathbb{W}\mathbb{M}^{-1}\mathbf{F}\right\}\ , \tag{S65}$$

where $\mathbb{M}=\beta(1+\mathbb{W}^{\mathrm{T}}\mathbb{W}/\omega^2)/2m$ and the cross term with $\sin(\omega t)[\cos(\omega t)-1]$ has canceled since the product $\mathbb{W}\mathbb{M}^{-1}$ is antisymmetric. In total one obtains

$$C_\lambda(t) = \frac{\bar{M}!^2}{2\pi Z}\left(\frac{2\pi}{\hbar\beta}\right)^M\left[\prod_{r=-\bar{M}}^{\bar{M}}\omega^2+\omega_r^2\right]^{-1/2}\mathrm{e}^{\mathrm{i}\varepsilon t/\hbar-\varepsilon\beta l/P}\mathrm{e}^{\mathrm{i}a^2[\sin(\omega t)-\omega t]\mathbf{F}^{\mathrm{T}}\boldsymbol{\mathcal{G}}_l/2P\hbar m\omega^3}$$
$$\times\exp\left\{\frac{\beta a^2}{8P^2m\omega^2}\mathbf{G}_l^{\mathrm{T}}\mathbf{G}_l - \frac{a^2}{2\beta m\hbar^2\omega^4}\sin^2(\omega t)\mathbf{F}^{\mathrm{T}}\mathbf{F} - \frac{\mathrm{i}a^2}{2Pm\hbar\omega^3}\mathbf{F}^{\mathrm{T}}\mathbf{G}_l\sin(\omega t)\right\}$$
$$\times\exp\left\{\frac{a^2\sin^2(\omega t)}{4m^2\hbar^2\omega^6}\mathbf{F}^{\mathrm{T}}\mathbb{W}\mathbb{M}^{-1}\mathbb{W}^{\mathrm{T}}\mathbf{F} - \frac{a^2\beta^2}{16P^2m^2\omega^4}\mathbf{G}_l^{\mathrm{T}}\mathbb{W}\mathbb{M}^{-1}\mathbb{W}^{\mathrm{T}}\mathbf{G}_l\right\}$$
$$\times\exp\left\{-\frac{a^2}{4\hbar^2m^2\omega^4}[\cos(\omega t)-1]^2\mathbf{F}^{\mathrm{T}}\mathbb{M}^{-1}\mathbf{F} + \frac{\mathrm{i}a^2\beta}{4Pm^2\hbar\omega^5}\sin(\omega t)\mathbf{F}^{\mathrm{T}}\mathbb{W}\mathbb{M}^{-1}\mathbb{W}^{\mathrm{T}}\mathbf{G}_l\right\}$$
$$\times\exp\left\{\frac{a^2\beta}{2Pm^2\hbar\omega^4}[\cos(\omega t)-1]\mathbf{G}_l^{\mathrm{T}}\mathbb{W}\mathbb{M}^{-1}\mathbf{F}\right\}\ . \tag{S66}$$

Before we further evaluate the expression in full complexity, let us consider the correlation function for the specific case $l=0$, i.e. $\lambda=0$. Since $\mathbf{G}_0=\mathbf{0}$, only a few terms remain, namely those with

$$\mathbf{F}^{\mathrm{T}}\mathbf{F} = M \tag{S67}$$
$$\mathbf{F}^{\mathrm{T}}\mathbb{W}\mathbb{M}^{-1}\mathbb{W}^{\mathrm{T}}\mathbf{F} = \frac{4m}{\beta}\sum_{r=1}^{\bar{M}}\frac{\omega_r^2}{1+\omega_r^2/\omega^2} \tag{S68}$$
$$\mathbf{F}^{\mathrm{T}}\mathbb{M}^{-1}\mathbf{F} = \frac{2m}{\beta}+\frac{4m}{\beta}\sum_{r=1}^{\bar{M}}\frac{1}{1+\omega_r^2/\omega^2}\ , \tag{S69}$$

where the definition of $\mathbb{W}$ has been used, see Sec. II B in the main text. The resulting

standard correlation function reads

$$C_0(t) = \frac{\bar{M}!^2}{2\pi Z}\left(\frac{2\pi}{\hbar\beta}\right)^M \left[\prod_{r=-\bar{M}}^{\bar{M}} \omega^2+\omega_r^2\right]^{-1/2} \mathrm{e}^{\mathrm{i}\varepsilon t/\hbar}\mathrm{e}^{\mathrm{i}a^2[\sin(\omega t)-\omega t]\mathbf{F}^{\mathrm{T}}\boldsymbol{\mathcal{G}}_0/2P\hbar m\omega^3}$$
$$\times \exp\left\{-\frac{a^2}{2\beta m\hbar^2\omega^4}\sin^2(\omega t)M + \frac{a^2\sin^2(\omega t)}{\beta m\hbar^2\omega^4}\left[\sum_{r=1}^{\bar{M}}\frac{\omega_r^2/\omega^2}{1+\omega_r^2/\omega^2}\right]\right\}$$
$$\times \exp\left\{-\frac{a^2}{4m\hbar\omega^3}[\cos(\omega t)-1]^2\left[\frac{2}{\beta\hbar\omega}+\frac{4}{\beta\hbar\omega}\sum_{r=1}^{\bar{M}}\frac{1}{1+\omega_r^2/\omega^2}\right]\right\} \quad . \tag{S70}$$

The terms with $\sin^2(\omega t)$ can be combined using $M/2 = \bar{M} + 1/2 = 1/2 + \sum_{r=1}^{\bar{M}} 1$ such that

$$\frac{a^2\sin^2(\omega t)}{4\beta m\hbar^2\omega^4}\left(4\sum_{r=1}^{\bar{M}}\left[\frac{\omega_r^2/\omega^2}{1+\omega_r^2/\omega^2}-1\right]-2\right) = -\frac{a^2\sin^2(\omega t)}{4m\hbar\omega^3}\left[\frac{2}{\beta\hbar\omega}+\frac{4}{\beta\hbar\omega}\sum_{r=1}^{\bar{M}}\frac{1}{1+\omega_r^2/\omega^2}\right] \quad . \tag{S71}$$

Using the trigonometric identity $\sin^2(x) + (\cos(x)-1)^2 = 2 - 2\cos(x)$ one obtains

$$C_0(t) = \frac{\bar{M}!^2}{2\pi Z}\left(\frac{2\pi}{\hbar\beta}\right)^M \left[\prod_{r=-\bar{M}}^{\bar{M}} \omega^2+\omega_r^2\right]^{-1/2}$$
$$\times \exp\left\{\frac{\mathrm{i}\varepsilon t}{\hbar} + \frac{\mathrm{i}a^2\mathbf{F}^{\mathrm{T}}\boldsymbol{\mathcal{G}}_0}{2Pm\hbar\omega^3}[\sin(\omega t)-\omega t] + \frac{a^2}{2m\hbar\omega^3}[\cos(\omega t)-1]\left[\frac{2}{\beta\hbar\omega}+\frac{4}{\beta\hbar\omega}\sum_{r=1}^{\bar{M}}\frac{1}{1+\omega_r^2/\omega^2}\right]\right\} \quad . \tag{S72}$$

In order to clarify the relation between the approximation and the exact result, one has to consider the limit $M \to \infty$. Using the definition of ω_r in Sec. II B of the main text and writing out the factorial, the limit of the prefactor can be explicitly written as

$$\lim_{M\to\infty}\frac{1}{Z\hbar\beta\omega}\left[\prod_{r=1}^{\bar{M}}\left(\frac{\beta\hbar\omega}{2\pi r}\right)^2+1\right]^{-1} = 1 \tag{S73}$$

where we have employed the well-known partition function of the harmonic oscillator, $Z = 2/\sinh(\beta\hbar\omega/2)$, and the product representation of the hyperbolic sine function.[3] For the term with the cosine one can employ the familiar series representation of the hyperbolic cotangens funciton

$$\lim_{M\to\infty}\frac{2}{\beta\hbar\omega}+\frac{4}{\beta\hbar\omega}\sum_{r=1}^{\bar{M}}\frac{1}{1+\omega_r^2/\omega^2} = \coth(\beta\hbar\omega/2) \quad . \tag{S74}$$

By comparing the last two expressions to Eq. (S55) with $\lambda = 0$, one can see that these two terms become exact in the limit. However, there is one remaining term in Eq. (S72) that depends explicitly on the dynamics, which is $\mathbf{F}^{\mathrm{T}}\boldsymbol{\mathcal{G}}_0 = M$ for the equilibrium method and $\mathbf{F}^{\mathrm{T}}\boldsymbol{\mathcal{G}}_0 = P$ for the average method. If M and P tend to infinity, while obeying $M \ll P$, the fraction $\mathbf{F}^{\mathrm{T}}\boldsymbol{\mathcal{G}}_0/P$ tends to zero for the equilibrium method and is constantly one for the average method. Consequently, the equilibrium method recovers the exact $C_0(t)$ only if $M = P$, whereas the average method yields accurate results for $M < P$ as it is discussed in Sec. IV of the main text. Following the same line of reasoning, one can draw the same conclusions for the case $l = P$, i.e. $\lambda = \beta$.

Switching to values $\lambda \in]0, \beta[$, we have to write out the additional terms appearing in Eq. (S66), i.e.

$$\frac{\beta}{P^2}\mathbf{G}_l^{\mathrm{T}}\mathbf{G}_l = \frac{8}{\beta}\sum_{r=-\bar{M}}^{-1}\left(\frac{\beta}{P}\sum_{i=0}^{l}\kappa_i\cos(2\pi ir/P)\right)^2 + 4\frac{\beta l^2}{P^2} + 8\sum_{r=1}^{\bar{M}}\left(\frac{\beta}{P}\sum_{i=0}^{l}\kappa_i\sin(2\pi ir/P)\right)^2 \quad , \tag{S75}$$

$$\frac{\beta}{P}\mathbf{F}^{\mathrm{T}}\mathbf{G}_l = 4\sum_{r=-\bar{M}}^{-1}\frac{\beta}{P}\sum_{i=0}^{l}\kappa_i\cos(2\pi ir/P) + 2\frac{\beta l}{P} \quad , \tag{S76}$$

$$\frac{\beta^2}{P^2}\mathbf{G}_l^{\mathrm{T}}\mathbb{W}\mathbb{M}^{-1}\mathbb{W}^{\mathrm{T}}\mathbf{G}_l = \frac{16m}{\beta}\sum_{r=1}^{\bar{M}}\frac{\omega_r^2\left(\frac{\beta}{P}\sum_{i=0}^{l}\kappa_i\sin(2\pi ir/P)\right)^2}{1+\omega_r^2/\omega^2} + \frac{16m}{\beta}\sum_{r=-\bar{M}}^{-1}\frac{\omega_r^2\left(\frac{\beta}{P}\sum_{i=0}^{l}\kappa_i\cos(2\pi ir/P)\right)^2}{1+\omega_r^2/\omega^2} \quad , \tag{S77}$$

$$\frac{\beta}{P}\mathbf{G}_l^{\mathrm{T}}\mathbb{W}\mathbb{M}^{-1}\mathbf{F} = -\frac{8m}{\beta}\sum_{r=1}^{\bar{M}}\frac{\omega_r\frac{\beta}{P}\sum_{i=0}^{l}\kappa_i\sin(2\pi ir/P)}{1+\omega_r^2/\omega^2} \quad , \tag{S78}$$

$$\frac{\beta}{P}\mathbf{F}^{\mathrm{T}}\mathbb{W}\mathbb{M}^{-1}\mathbb{W}^{\mathrm{T}}\mathbf{G}_l = \frac{8m}{\beta}\sum_{r=-\bar{M}}^{-1}\frac{\omega_k^2\frac{\beta}{P}\sum_{i=0}^{l}\kappa_i\cos(2\pi ir/P)}{1+\omega_k^2/\omega^2} \quad . \tag{S79}$$

Note that $\mathbf{F}$ "picks" only the negative modes leading to the minus sign in Eq. (S78).

First, we want to restrict ourselves to the case $M = P$. The terms in Eqs. (S75,S76) then become strikingly more compact, whereas the other terms keep their complexity. In

particular

$$\frac{\beta}{P^2}\mathbf{G}_l^{\mathrm{T}}\mathbf{G}_l = \frac{2\beta(2l-1)}{P} \ , \tag{S80}$$

$$\frac{\beta}{P}\mathbf{F}^{\mathrm{T}}\mathbf{G}_l = \beta \ , \tag{S81}$$

where we have used Eq. (S58), the Cartesian definition of $\mathbf{F}$ and that $\mathbb{T}\mathbb{T}^{\mathrm{T}} = \mathbb{T}^{\mathrm{T}}\mathbb{T} = 1$ for $M = P$. To proceed, one has to perform the limit $M = P \to \infty$ for the aforementioned terms. The summations over the index i can be written as integrals over imaginary time leading to

$$\lim_{P\to\infty}\frac{\beta}{P^2}\mathbf{G}_l^{\mathrm{T}}\mathbf{G}_l = 4\lambda \tag{S82}$$

$$\lim_{P\to\infty}\frac{\beta}{P}\mathbf{F}^{\mathrm{T}}\mathbf{G}_l = \beta \ , \tag{S83}$$

$$\begin{aligned}\lim_{P\to\infty}\frac{\beta^2}{P^2}\mathbf{G}_l^{\mathrm{T}}\mathbb{W}\mathbb{M}^{-1}\mathbb{W}^{\mathrm{T}}\mathbf{G}_l = {}& \frac{16m}{\beta\hbar^2}\sum_{r=-\infty}^{-1}\frac{\sin^2(\omega_r\lambda\hbar)}{1+\omega_r^2/\omega^2} \\ & + \frac{16m}{\beta\hbar^2}\sum_{r=1}^{\infty}\frac{\left(1-\cos(\omega_r\lambda\hbar)\right)^2}{1+\omega_r^2/\omega^2} \ ,\end{aligned} \tag{S84}$$

$$\lim_{P\to\infty}\frac{\beta}{P}\mathbf{G}_l^{\mathrm{T}}\mathbb{W}\mathbb{M}^{-1}\mathbf{F} = -\frac{8m}{\beta\hbar}\sum_{r=1}^{\infty}\frac{1-\cos(\omega_k\lambda\hbar)}{1+\omega_k^2/\omega^2} \ , \tag{S85}$$

$$\lim_{P\to\infty}\frac{\beta}{P}\mathbf{F}^{\mathrm{T}}\mathbb{W}\mathbb{M}^{-1}\mathbb{W}^{\mathrm{T}}\mathbf{G}_l = \frac{8m}{\hbar\beta}\sum_{r=-\infty}^{-1}\frac{\omega_k\sin(\omega_k\lambda\hbar)}{1+\omega_k^2/\omega^2} \ . \tag{S86}$$

Inserting these relations into the correlation function, Eq. (S66), yields after some straightforward rearranging and employing a few relations of (hyperbolic) sine and cosine functions

$$\begin{aligned}C_\lambda(t) = {}& \mathrm{e}^{\mathrm{i}\varepsilon t/\hbar-\varepsilon\lambda}\exp\left\{-\frac{\mathrm{i}a^2}{2m\hbar\omega^2}t + \frac{a^2\lambda}{2m\omega^2} + \frac{\mathrm{i}a^2\sin(\omega t)}{2m\hbar\omega^3}\left(\frac{4}{\beta\hbar\omega}\sum_{r=1}^{\infty}\frac{\sin(\omega_r\lambda\hbar)\omega_r/\omega}{1+\omega_r^2/\omega^2}\right)\right\} \\ & \times\exp\left\{\frac{a^2\cos(\omega t)}{2m\hbar\omega^3}\left[\frac{4}{\beta\hbar\omega}\sum_{r=1}^{\infty}\frac{\cos(\omega_r\lambda\hbar)}{1+\omega_r^2/\omega^2}+\frac{2}{\beta\hbar\omega}\right] - \frac{a^2}{2m\hbar\omega^3}\coth(\beta\hbar\omega/2)\right\} \ ,\end{aligned} \tag{S87}$$

where we have reused Eqs. (S73,S74) and $\mathbf{F}^{\mathrm{T}}\boldsymbol{\mathcal{G}}_l/P = 1$ for $M = P$. In Ref. 1, one can find that

$$\frac{4}{\beta\hbar\omega}\sum_{r=1}^{\infty}\frac{\cos(\omega_r\lambda\hbar)}{1+\omega_r^2/\omega^2} + \frac{2}{\beta\hbar\omega} = \frac{\cosh(\beta\hbar\omega/2-\omega\lambda\hbar)}{\sinh(\beta\hbar\omega/2)} \tag{S88}$$

and by differentiating this expression with respect to λ one readily obtains

$$\frac{4}{\beta\hbar\omega}\sum_{r=1}^{\infty}\frac{\sin(\omega_r\lambda\hbar)\omega_r/\omega}{1+\omega_r^2/\omega^2} = \frac{\sinh(\beta\hbar\omega/2-\omega\lambda\hbar)}{\sinh(\beta\hbar\omega/2)} \ , \tag{S89}$$

where the latter holds only for $0 < \lambda < \beta$. After putting these limits back into the correlation function and comparing it to the QM one, Eq. (S55), one can see that the Matsubara dynamics yields indeed the exact result for $C_\lambda(t)$ if $M = P$.

Importantly, if $M < P$, as it is imposed by the original Matsubara approximation, the exact expression cannot be recovered, since irrespectively on the chosen dynamics

$$\lim_{P\to\infty} \frac{\beta}{P^2}\mathbf{G}_l^{\mathrm{T}}\mathbf{G}_l \neq 4\lambda \ , \tag{S90}$$

$$\lim_{P\to\infty} \frac{\beta}{P}\mathbf{F}^{\mathrm{T}}\mathbf{G}_l \neq \beta \ . \tag{S91}$$

Thus, for $\lambda \in]0, \beta[$, none of the methods yields the exact result if only smooth imaginary-time paths are considered, see discussion in Sec. IV of the main text and Sec. V here.

B. The RPMD-like method

To derive the correlation function resulting from the ring polymer molecular dynamics (RPMD)-like method one has to evaluate the integral

$$C_\lambda(t) \approx \frac{\bar{M}!^2}{2\pi\hbar^M Z}\int \mathrm{d}\mathbf{Q}\int \mathrm{d}\mathbf{\Pi}\, \mathrm{e}^{-\beta\left[\frac{1}{2m}\mathbf{\Pi}^{\mathrm{T}}\mathbf{\Pi}+U_l(\mathbf{Q})+\frac{1}{2}m\mathbf{Q}^{\mathrm{T}}\mathbb{W}^{\mathrm{T}}\mathbb{W}\mathbf{Q}\right]}\mathrm{e}^{\frac{\mathrm{i}}{\hbar}\int_0^t a x_0(\tau)\mathrm{d}\tau}\mathrm{e}^{\mathrm{i}\varepsilon t/\hbar} \ , \tag{S92}$$

where $\tilde{U}_l(\mathbf{Q})$ is defined in the previous section. The dynamics that yields $x_0(\tau)$ is generated with respect to

$$\tilde{\mathcal{U}}_l(\mathbf{Q}) = \frac{1}{2}m\mathbf{Q}^{\mathrm{T}}\mathbb{W}^{\mathrm{T}}\mathbb{W}\mathbf{Q} + \frac{1}{2}m\omega^2\mathbf{Q}^{\mathrm{T}}\mathbf{Q} + \frac{a}{2P}\boldsymbol{\mathcal{G}}_l^{\mathrm{T}}\mathbf{Q} + \text{const.} \ , \tag{S93}$$

where the first summand is the well-known spring term, intrinsic to RPMD-like methods and absent in the Matsubara dynamics, and $\boldsymbol{\mathcal{G}}_l$ is the same as in the previous section. The resulting time evolution of the normal modes can be written down explicitly as

$$\mathbf{Q}(t) = \cos(\tilde{\mathbb{W}}t)\mathbf{Q} + \frac{1}{m}\tilde{\mathbb{W}}^{-1}\sin(\tilde{\mathbb{W}}t)\mathbf{\Pi} + \frac{a}{2mP}\tilde{\mathbb{W}}^{-2}[\cos(\tilde{\mathbb{W}}t) - 1]\boldsymbol{\mathcal{G}}_l \ , \tag{S94}$$

where the diagonal $\tilde{\mathbb{W}} = (\tilde{\omega}_r\delta_{r,s})$ with $\tilde{\omega}_r = \sqrt{\omega^2 + \omega_r^2}$.

Following the same line of reasoning as in the previous section, the correlation function can be further evaluated by solving multi-dimensional integrals. As it will become clear soon, it is sufficient to consider the case where $\lambda = 0$ and $M = P$, for which the final result

for the RPMD-like approximation reads

$$C_0(t) \approx \mathrm{e}^{\mathrm{i}\varepsilon t/\hbar} \exp\left\{\frac{\mathrm{i}a^2}{2\hbar m P}\left[2\sum_{r=1}^{\bar{P}}\frac{\sin(\tilde{\omega}_r t)-\tilde{\omega}_r t}{\tilde{\omega}_r^3}+\frac{\sin(\omega t)-\omega t}{\omega^3}\right]\right\} \times \exp\left\{\frac{a^2}{2m\hbar\omega^3}\left[\sum_{r=1}^{\bar{P}}\frac{4[\cos(\tilde{\omega}_r t)-1]}{\beta\hbar\omega\tilde{\omega}_r^4/\omega^4}+\frac{2[\cos(\omega t)-1]}{\beta\hbar\omega}\right]\right\} \ , \tag{S95}$$

where, for the sake of brevity, the limit for the prefactor, Eq. (S73), has been anticipated. By comparing this expression to its Matsubara counterpart, Eq. (S72), one notices a similar structure, though the frequencies appearing in the arguments of sine and cosine are not the same and, thus, the RPMD-like approximation does not tend to the correct $C_0(t)$ as $P \to \infty$. Since the $\tilde{\omega}_r$ differ from the physical frequency ω by the Matsubara frequencies, this deficiency can be directly traced back to the artificial spring forces that disturb the dynamics, which is similarly given for other values of λ and ratios of M and P.

C. The modified method

As it has been stated in the previous section, the RPMD-like ansatz fails due to the Matsubara frequencies that disturb the real-time dynamics, whereas the structure of the expression is quite close to the correct Matsubara counterpart. This suggests the *ad-hoc* modification to "remove" the Matsubara frequencies from the real-time dynamics while keeping them in the density. In particular, if one first sets all $\tilde{\omega}_r \to \omega$ in the first row of Eq. (S95), one would already obtain the correct imaginary part of the exponent, see Eq. (S72). Second, setting $\tilde{\omega}_r \to \omega$ in the cosine's argument and, third, $\tilde{\omega}_r^4 \to \tilde{\omega}_r^2\omega^2$ in the denominator would on top lead to the correct real part. The first two replacements can be readily achieved by simply removing the spring forces from the RPMD-like protocol during the real-time propagation, thereby recovering the original Matsubara dynamics. The third substitution requires additionally to *modify* the kinetic part in the density in Eq. (S92) as

$$\frac{1}{2m}\mathbf{\Pi}^{\mathrm{T}}\mathbf{\Pi} \to \frac{1}{2m}\mathbf{\Pi}^{\mathrm{T}}\tilde{\mathbb{W}}^{\mathrm{T}}\tilde{\mathbb{W}}\mathbf{\Pi}/\omega^2 = \frac{1}{2m}\mathbf{\Pi}^{\mathrm{T}}(1+\mathbb{W}^{\mathrm{T}}\mathbb{W}/\omega^2)\mathbf{\Pi} \ , \tag{S96}$$

while keeping the original physical potential as well as the usual spring term $m\mathbf{Q}^{\mathrm{T}}\mathbb{W}^{\mathrm{T}}\mathbb{W}\mathbf{Q}/2$. The combination of all three modifications leads to the modified method as it is presented in the main text in Sec. II F 2. It is straightforward to show that this method yields the exact standard correlation function, $C_0(t)$, for the equilibrium method with $M = P$ and for the average method $M \leq P$ in the limit $M, P \to \infty$.

V. COMPLEMENTARY RESULTS

A. Numerical results for imaginary-time shifted correlation functions

Fig. 1, exhibits the computed imaginary-time shifted correlation functions, $C_\lambda(t)$, with $\lambda \in]0, \beta[$ and $M = P$ for the harmonic system as introduced in Sec. III of the main text. Note that the layout is similar to that in Fig. 4 of the main text. In panels 1), one can see that the results from the Matsubara and the modified do not coincide for both, the equilibrium and the average methods if $P = 5$ and $\lambda = \beta/5$. This is expected, since the modified method is exclusively designed for the case $\lambda = 0$. Interestingly, the convergence of the Matsubara method with respect to the number of modes seems to be much slower than for the case $\lambda = 0$. An acceptable convergence could be only reached for $P = 1215$, as depicted by the corresponding analytical result, see the red dots dots. Note that such a high number of modes cannot be treated numerically in a reasonable amount of time. Note further that the statistical convergence could be improved for the equilibrium method, due to an additional integration along the trajectories, as it can be seen by the larger red areas in the right panels. The average RPMD-like method as well as the equilibrium one fail to reproduce the QM result, while both versions come closer to the results of the modified method than to the Matsubara ones.

Switching to panels 2), i.e. $P = 9, \lambda = \beta/3$, the QM result features an almost straight line that is not reasonably approximated by both Matsubara methods. An acceptable convergence with respect to the number of modes could be obtained for $P = 1215$, see the analytical results depicted by the dots. The statistical convergence of the equilibrium Matsubara method is strikingly better than for the average one, which is again due to the additional time integration. The modified method as well as the RPMD-like one fail again to approximate the QM result.

B. Anharmonic oscillators with a large shift

Fig. 2 exhibits the numerical results for two anharmonic oscillators as given in Sec. III of the main text, though featuring a larger displacement of $x_f - x_g = 0.5\,\text{au}$.

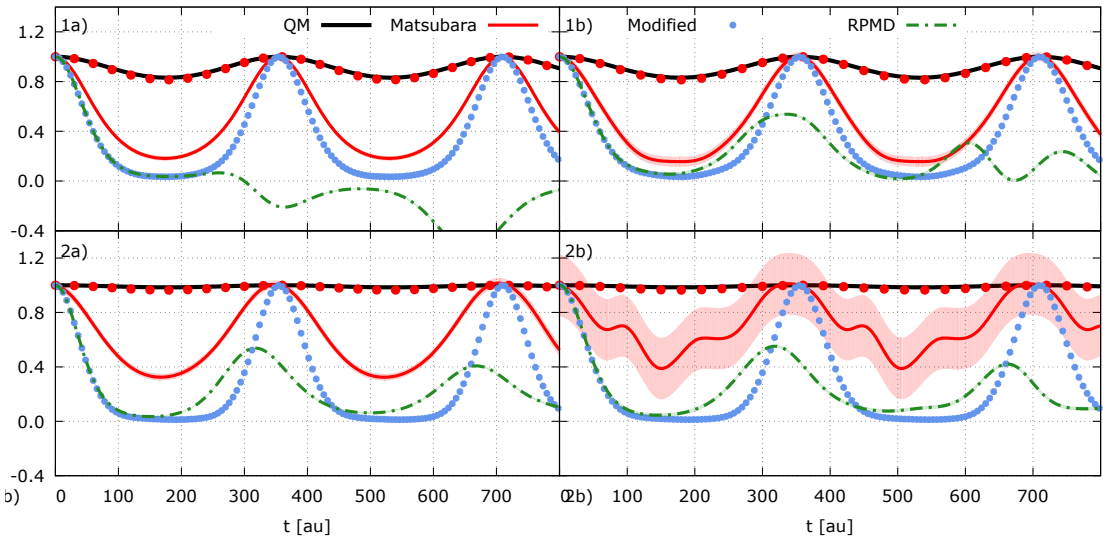

FIG. 1. Imaginary-time shifted correlation functions, $C_\lambda(t)$, with $\lambda \in]0, \beta[$ and $M = P$ for the two shifted harmonic oscillators. First row, $\lambda = \beta/5$ and the second row, $\lambda = \beta/3$. Red dots represent analytical results for the Matsubara methods with $P = M = 1215$.

REFERENCES

[1]M. J. Willatt, *Matsubara Dynamics and its Practical Implementation*, Ph.D. thesis, University of Cambridge (2017).

[2]J. O. Richardson, P. Meyer, M.-O. Pleinert, and M. Thoss, Chem. Phys. **482**, 124 (2016).

[3]Y. A. Melnikov, in *Green's Functions and Infinite Products* (Springer, 2011) pp. 17–42.

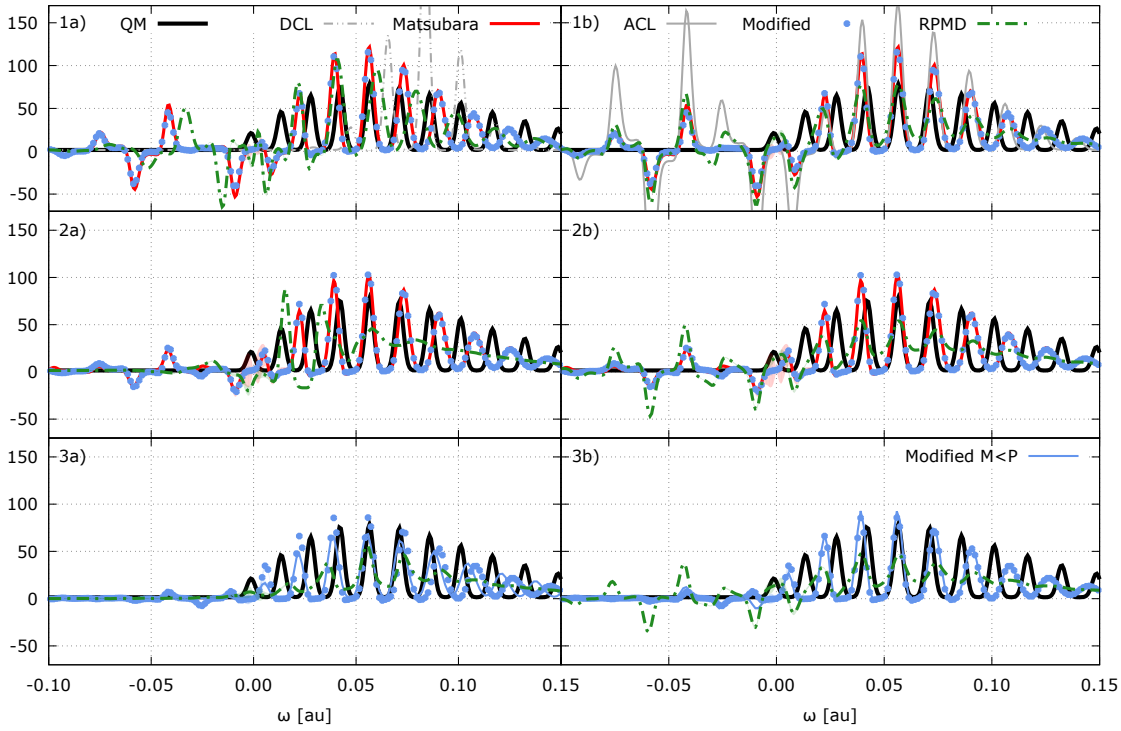

FIG. 2. Standard correlation functions, $C_0(t)$, for two displaced anharmonic oscillators with $x_f - x_g = 0.5\,\text{au}$. Same layout code as in Fig. 7 in the main text.

Danksagungen

Hier, am Ende dieser Arbeit, möchte zuallererst Prof. Oliver Kühn danken, der es mir ermöglicht hat, nicht nur während der Promotion, sondern auch schon im Bachelor- und Masterstudium in seiner Arbeitsgruppe Molekulare Quantendynamik wissenschaftlich zu arbeiten. Neben seiner Unterstützung durch inspirierende Diskussionen und die konstruktive Zusammenarbeit an den Veröffentlichungen, soll auch die von ihm geförderte freundliche Atmosphäre innerhalb der Arbeitsgruppe im Vordergrund stehen.

Ein besonderer Dank geht an Sergei Ivanov und Sergey Bokarev, die mit ihrer hingebungsvollen Art maßgeblich am Entstehen, dem Voranschreiten und der Fertigstellung dieser Arbeit beteiligt waren. Beide konnten mir in vielen Situationen mit motivierenden Worten, oder auch durch einen kritischen Blick, in wichtigen Belangen der Theorie, des Programmierens, vor allem aber des wissenschaftlichen Schreibens weiterhelfen.

Auch bei Prof. Jeremy Richardson möchte ich mich bedanken, dass er mich zur einwöchigen Mitarbeit in seiner Arbeitsgruppe ins schöne Zürich eingeladen hat. Großer Dank geht selbstverständlich an die Deutsche Forschungsgemeinschaft (KU 952/10-1) für die finanzielle Unterstützung.

Wie oben bereits angedeutet, wird die Promotionszeit als eine angenehme Erfahrung in meine Erinnerung eingehen. Eine großen Anteil haben daran meine Freunde und Kollegen Fabian Gottwald und Gilbert Grell, sowie alle anderen Mitglieder der AGQD, die mich mit allerhand (Fach-)Gesprächen oft auf neue Ideen gebracht und durch ihr technisches Knowhow so manche Simulation überhaupt erst ermöglicht haben.

Grüßen möchte ich auch meine Eltern, meine Schwestern, den Rest meiner Familie und natürlich auch meine Freunde in Rostock und in meiner Heimatstadt Wittstock. Vielen Dank für den Rückhalt und die sehr gute Ablenkung während all der Jahre des Studiums.

Den letzten und größten Dank richte ich an meine Freundin Caroline, dafür dass sie nun schon seit zwölf Jahren, auch in schweren Zeiten, immer zu mir gehalten hat und all dem hier einen Sinn gibt.